

# Rydberg Excitation of Trapped Ions

**Dissertation**

zur Erlangung des Grades  
Doktor der Naturwissenschaften

am Fachbereich 08: Physik, Mathematik und Informatik  
der Johannes Gutenberg-Universität in Mainz

von

**Thomas Feldker**

geboren in Köln

Mainz, den 30.05.2016



Erstgutachter:  
Prof. Dr. Ferdinand Schmidt-Kaler  
Zweitgutachter:  
Prof. Dr. Jochen Walz

Ich, Thomas Feldker, versichere, dass ich die vorliegende Arbeit selbstständig angefertigt und keine anderen als die angegebenen Quellen und Hilfsmittel verwendet habe.

Mainz den 30. Mai 2016

Thomas Feldker





# Abstract

In this thesis I describe the excitation of trapped  $^{40}\text{Ca}^+$  ions to Rydberg states. For the first time, the excellent experimental control over single ions in Paul traps has been combined with the unique features of highly excited Rydberg states, establishing a novel platform for experimental quantum computing and quantum simulation.

Due to the doubly charged core, and the correspondingly increased binding energy, Rydberg excitation of ions requires vacuum ultraviolet (VUV) light for single-photon excitation or multi-photon excitation with ultraviolet (UV) radiation. For the experimental work presented in this thesis, we have chosen single-photon excitation with VUV radiation near 122 nm wavelength. We have designed and built an ion trap apparatus consisting of an ultra high vacuum setup, laser sources with wavelengths in the visible and infrared spectrum, control electronics and a Paul trap and joined it with a preexisting source for continuous wave, coherent VUV radiation near 122 nm wavelength. Characterization measurements of the joined apparatus have been performed. Particularly important is the characterization of the VUV beam inside the ion trap, the compensation of residual electric fields at the ion crystal and the effects of the highly energetic VUV photons on ion trap operation. With the joined system we have successfully demonstrated photo-ionization of trapped and cold  $^{40}\text{Ca}^+$  ions.

After the presentation of this preparatory work, I describe the excitation of trapped  $^{40}\text{Ca}^+$  ions to Rydberg states. From the initial metastable  $3D$  states, we have excited ions to the Rydberg states  $22F$ ,  $52F$ ,  $53F$  and  $66F$  with light at wavelengths near 123 nm and 122 nm. Excitation wavelengths have been measured as 123.256 119(5) nm ( $3D_{5/2} \rightarrow 22F$ ), 122.041 913(5) nm ( $3D_{3/2} \rightarrow 52F$ ), 122.032 384(10) nm ( $3D_{3/2} \rightarrow 53F$ ) and 122.040 50(5) nm ( $3D_{5/2} \rightarrow 66F$ ). From these wavelengths, principle quantum numbers, quantum defect and consequently the angular momentum state of the excited states have been determined. We investigated the line shapes of the transitions to the highly sensitive Rydberg states in the oscillating potential of the Paul trap. Advanced techniques like coherent state preparation of the ion in the initial  $3D_{5/2}$  state and the addressed Rydberg excitation of single ions in one dimensional ion strings have been realized. The work presented in this dissertation paves the way towards Rydberg quantum logic applications with trapped ions.



# Zusammenfassung

In meiner Dissertation beschreibe ich die Anregung von gefangenen  $^{40}\text{Ca}^+$  Ionen in Rydbergzustände. Die exzellente Kontrollierbarkeit von einzelnen Ionen in Paulfallen wird so mit den einzigartigen Eigenschaften von hoch angeregten Rydbergzuständen kombiniert.

Aufgrund des doppelt geladenen Atomrumpfes und der damit einhergehenden hohen Bindungsenergie wird für die Rydberganregung von Ionen Licht im vakuumultravioletten (VUV) Spektralbereich benötigt. Für die hier präsentierte, experimentelle Arbeit kam VUV-Strahlung bei einer Wellenlänge von 122 nm zum Einsatz. Im Rahmen dieser Dissertation wurde ein Experiment aufgebaut, das aus einer Vakuumkammer für Ultrahochvakuum, Lasersystemen für die Erzeugung von Lichtfeldern im sichtbaren und infraroten Spektrum, Steuerungselektronik und einer Paulfalle besteht. Dieser Aufbau wurde mit einer vorhandenen Quelle für kohärente VUV-Strahlung nahe einer Wellenlänge von 122 nm kombiniert. Charakterisierungsmessungen des kombinierten Aufbaus, insbesondere des VUV-Strahls in der Ionenfalle, der elektrischen Felder in der Paulfalle und der Auswirkungen der hochenergetischen VUV-Photonen auf den Ionenfallenbetrieb, wurden durchgeführt. Durch die Photoionisation von lasergekühlten  $^{40}\text{Ca}^+$  Ionen konnte die Wechselwirkung der VUV-Strahlung mit den in der Paulfalle gefangenen Ionen nachgewiesen werden.

Im Hauptteil der Dissertation beschreibe ich die erstmalige Anregung von gefangenen  $^{40}\text{Ca}^+$  Ionen in Rydbergzustände. Von den metastabilen  $3D$ -Ausgangszuständen werden die Rydbergzustände  $22F$ ,  $52F$ ,  $53F$  und  $66F$  mit Licht der Wellenlängen 123 nm und 122 nm angeregt; die Anregungswellenlängen wurden zu 123.256 119(5) nm ( $3D_{5/2} \rightarrow 22F$ ), 122.041 913(5) nm ( $3D_{3/2} \rightarrow 52F$ ), 122.032 384(10) nm ( $3D_{3/2} \rightarrow 53F$ ) und 122.040 50(5) nm ( $3D_{5/2} \rightarrow 66F$ ) bestimmt. Mit Hilfe dieser Wellenlängen konnten wir die Hauptquantenzahlen, den Quantendefekt und dadurch den Bahndrehimpuls der erzeugten Rydbergzustände bestimmen. Im Weiteren wurde der Einfluss des oszillierenden Potentials der Paulfalle auf die empfindlichen Rydbergzustände untersucht. Aufbauend auf diese grundlegenden Experimente konnten wir komplexere Techniken wie die Präparation des Ausgangszustandes durch kohärenten Populationstransfer und die gezielte Rydberganregung einzelner Ionen aus einer Ionenkette realisieren. Damit legt diese experimentelle Arbeit die Grundlagen für Quanteninformationsanwendungen basierend auf Rydbergionen in Paulfallen.



# Contents

<b>1. Introduction</b>	<b>1</b>
<b>2. Theoretical foundations</b>	<b>11</b>
2.1. Introduction to Rydberg states . . . . .	11
2.2. Rydberg excitation of trapped, cold ions . . . . .	16
2.3. Atomic properties of $^{40}\text{Ca}^+$ ions . . . . .	27
<b>3. Experimental setup</b>	<b>33</b>
3.1. Laser sources for photo-ionization, Doppler cooling, detection and state manipulation . . . . .	33
3.2. Ion imaging . . . . .	44
3.3. Vacuum ultraviolet light source near 122 nm wavelength . . . . .	46
3.4. Ultra-high vacuum setup . . . . .	51
3.5. Magnetic field generation . . . . .	55
3.6. Computer control . . . . .	57
<b>4. Ion traps for Rydberg excitation</b>	<b>59</b>
4.1. Linear rod trap (T1) . . . . .	61
4.2. Linear segmented micro trap (T2) . . . . .	64
<b>5. Trap characterization and preparatory experiments</b>	<b>71</b>
5.1. Characterization of trap T1 . . . . .	71
5.2. Characterization of trap T2 . . . . .	77
5.3. Single ion addressing on the $4S_{1/2} \leftrightarrow 3D_{5/2}$ transition . . . . .	81
5.4. Characterization of the VUV beam . . . . .	85
5.5. Experiments with doubly ionized $^{40}\text{Ca}^{2+}$ ions . . . . .	86
<b>6. Rydberg excitation of trapped <math>^{40}\text{Ca}^+</math></b>	<b>95</b>
6.1. Rydberg excitation to the states $52F$ , $53F$ and $66F$ . . . . .	98
6.2. Excitation to the Rydberg state $22F$ . . . . .	101
6.3. Quantum defect and principal quantum numbers . . . . .	105
6.4. Line shape of the Rydberg resonance in the trap field . . . . .	107
6.5. Addressed Rydberg excitation in a linear crystal . . . . .	113
<b>7. Conclusion</b>	<b>117</b>
<b>8. Outlook</b>	<b>119</b>
8.1. Spectroscopy of Rydberg $P$ states . . . . .	119

8.2. Dispersive measurement of Rydberg states . . . . .	121
8.3. Microwave spectroscopy of Rydberg states . . . . .	122
8.4. Optimized new trap design . . . . .	123
8.5. Investigation of two-step Rydberg excitation of $^{40}\text{Ca}^+$ ions. . . . .	125
8.6. The potential of digital trap operation for Rydberg excitation of ions . . . .	127
<b>A. Assignment of Rydberg states and quantum defects</b>	<b>129</b>
<b>B. Home built external cavity diode lasers</b>	<b>131</b>
<b>C. List of publications</b>	<b>135</b>

# 1. Introduction

Rydberg states, where a single electron is excited into an orbit with large principle quantum number  $n$  [Gal94] are of great interest for many applications in quantum physics due to their remarkable properties. The long lifetime ( $\propto n^3$ ), the large polarizability in external fields ( $\propto n^7$ ) and the regular energy spectrum of Rydberg states makes them excellent candidates for spectroscopic experiments. The observation of Rydberg series of various atoms played a crucial role in understanding atomic physics [Gal94]. Spectroscopy of Rydberg states allowed for precise determination of the interaction of atomic states with external fields [Koc78,Zim78,Zim79,Rai01]. In experiments in superconducting microwave cavities, a single atom maser [Mes85,Rem90], based on the interaction of single Rb atoms excited to the state  $63P_{3/2}$  with a cavity field resonant to the transition  $61D_{3/2} \leftrightarrow 63P_{3/2}$  has been operated. On the other hand, the interaction of a single photon with atoms in circular Rydberg states has been detected [Bru94,Bru96]. The long lifetime as well as the huge dipole transition matrix element to adjacent states of the Rb atoms in the circular Rydberg state with quantum numbers  $n, l, m = 51, 50, 50$  allowed for the detection of the light shift induced by single photons in a non-resonant cavity field. The measured phase shift obtained in a Ramsey experiment is shown in Fig. 1.1.

In recent years interest has shifted from the controlled dynamics of single atoms [Rai01] to the study of multi-particle entanglement enabled by the strong dipolar interaction between Rydberg atoms [Jak00,Luk01]. At short inter atom distances  $R$  the interaction has resonant dipole-dipole character ( $\propto n^4/R^3$ ), at longer distances a transition to a van der Waals interaction is observed ( $\propto n^{11}/R^6$ ). The long-range interaction strength is increased by more than ten orders of magnitude compared to ground state atoms [Saf10], as illustrated in Fig. 1.2a. The key feature in many experiments is the Rydberg blockade [Jak00,Sin04,Ton04,Hei07]: The interaction between close Rydberg atoms becomes large enough to shift the doubly excited state out of resonance with an exciting light field. Consequently only one atom inside a certain blockade radius may be excited to the Rydberg state. The excitation rates saturate as shown in Fig. 1.2b when irradiating dense atomic sample with high intensity laser beams.

Artificially tuned Förster resonances [Vog06] lead to resonant dipole-dipole interaction even at large distances  $R$  and may significantly increase the blockade effect. Here, the Stark shift induced by an electric field shifts the pair states  $|36, P, 36, P\rangle$  and  $|36, S, 37, S\rangle$  into resonance. A resonant dipole-dipole interaction between Rydberg atoms in the  $|36, P\rangle$  state is generated in an electric field of  $E = 2.52 \text{ V/m}$  (see Fig. 1.3b).

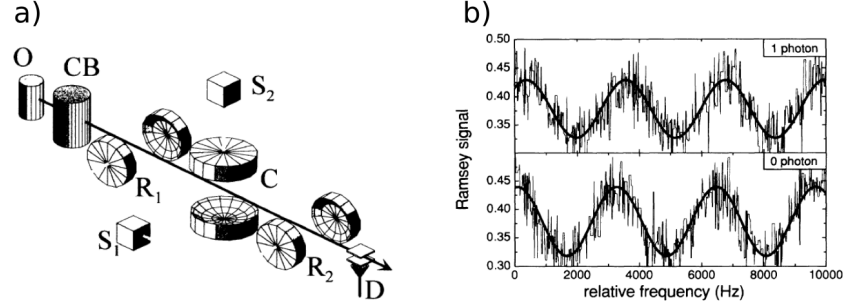


Figure 1.1.: a) Scheme of the Ramsey interferometer. A thermal beam of Rubidium atoms comes from an oven (O) before they are prepared in the Rydberg state (CB). The Ramsey pulses are applied in two microwave cavities ( $R_1$  and  $R_2$ ). In between the two Ramsey pulses, the atoms pass a superconducting non-resonant microwave cavity which induces the phase shift. b) Ramsey signal on the transition between circular Rydberg states with  $n = 50$  and  $n = 51$ . The phase shift induced by single photons in the cavity mode is clearly detected in the signal. Figure from Ref. [Bru94].

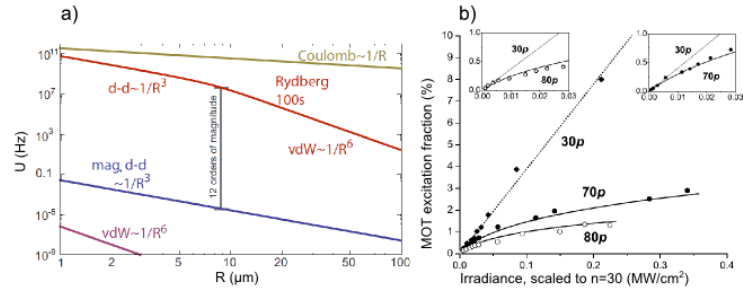


Figure 1.2.: a) Interaction strength at distance  $R$  between ions (yellow), Rydberg atoms (red) and ground state atoms (blue and purple). At a characteristic distance  $R$  the interaction changes from resonant dipole-dipole ( $\propto 1/R^3$ ) to van der Waals ( $\propto 1/R^6$ ). Figure from Ref. [Saf10]. b) Excitation saturation induced by the dipole blockade. Due to the blockade effect, only a fraction of the atoms in the magneto optical trap can be excited to Rydberg states. For the state  $30P$  no saturation is detected while the excitation to  $70P$  and  $80P$  saturates quickly. Figure from Ref. [Ton04].



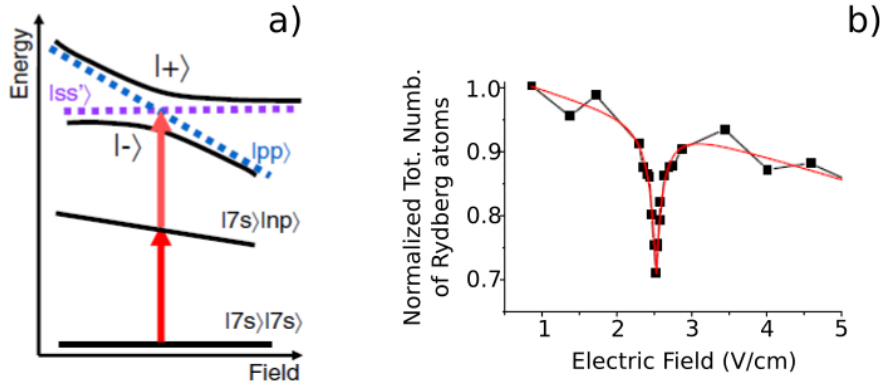


Figure 1.3.: a) Förster resonance of the two atom states  $|ss'\rangle$  and  $|pp\rangle$ . The energies of the two atom states depend on the electric field. At resonance, the dipole-dipole coupling leads to an avoided crossing. b) An artificially tuned Förster resonance at  $E = 2.52$  V/cm increases the interaction energy and results in a larger blockade radius and a lower number of excited atoms compared to the non-resonant case. Figure from Ref. [Vog06].

The dipole blockade has been used in multiple applications such as the control of light fields on the single photon level [Pey12], the simulation of spin models [Bar15, Sch15a, Sch15b] and two-qubit gate operations between two neutral atoms in optical traps [Luk01, Gaë09, Urb09, Wil10, Ise10, Mal15]. In Ref. [Ise10], a CNOT gate with fidelity  $F = 0.73$  based on the dipole blockade between two Rb atoms, trapped in individual dipole traps at a distance of  $10\text{ }\mu\text{m}$  has been demonstrated. The Rb atoms were excited to the state  $97D_{5/2}$  which results in an interaction strength of  $\Delta E/2\pi = 9.3\text{ MHz}$ . With a Rabi frequency  $\Omega_0/2\pi = 0.67\text{ MHz}$ , excitation of the target atom is strongly suppressed if the control atom is in the Rydberg state.

On the other hand, laser cooled ion crystals in Paul traps are among the most precisely controlled quantum many body systems available [Sch05, Bla08]. Hence, trapped ions have been used for a great variety of applications including quantum logic spectroscopy for optical clocks [Lud15, Cho10], quantum simulation [Bla12] and quantum information processing [Lei03a, Bla12, Kie02].

Quantum information is stored in long lived electronic states of the ion and can be manipulated by laser radiation. Typical inter-ion distances in the order of a few  $\mu\text{m}$  allow for the addressing of individual ions with laser beams [Näg99]. Due to the Coulomb repulsion, ions do not oscillate independently in the trapping potential but common vibrational modes, including all ions in the crystal, are formed. With typical vibrational frequencies of  $\omega/2\pi > 1\text{ MHz}$ , the mode structure can be resolved by laser spectroscopy and is used for the implementation of controlled interaction between qubits.

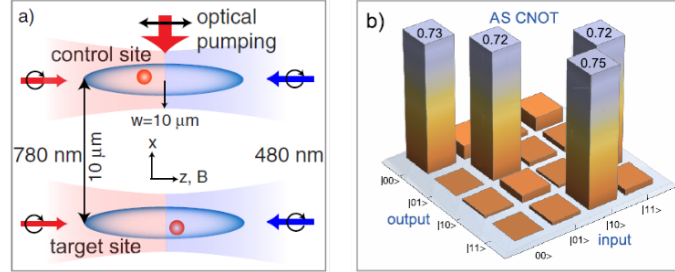


Figure 1.4.: a) Scheme of the CNOT gate based on the dipole blockade between Rb atoms excited to the state  $97D_{5/2}$ . The atoms are trapped in dipole traps at a distance of  $10 \mu\text{m}$  and individually addressed with laser beams. b) Characterization of the amplitude swap (AS) CNOT gate operation from the density matrix. A fidelity of  $F = 0.73$  is reached. Figure from Ref. [Ise10].

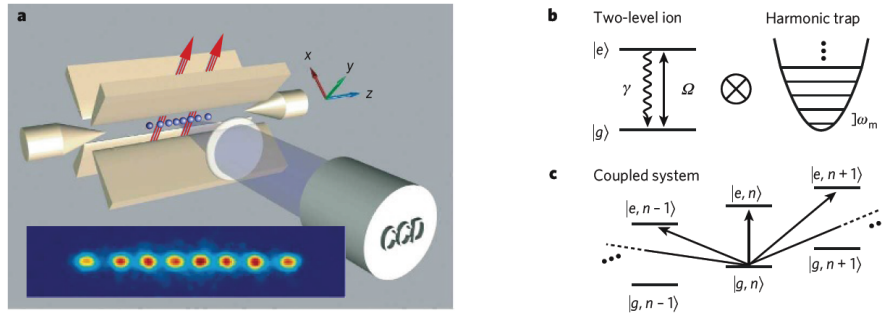


Figure 1.5.: a) A linear string of ions in a Paul trap. The distance between ions in the order of a few  $\mu\text{m}$  allows for individual excitation of ions with lasers and for resolved fluorescence detection with a camera. b) The information is stored in two long lived states  $|g\rangle$  and  $|e\rangle$  of the ion. The harmonic potential of the trap results in equally spaced energy levels for the motional modes of the Coulomb crystal. c) Laser radiation couples to electronic states as well as vibrational states. Thus internal state and motion of the ion can be entangled. Internal states of different ion can be entangled via their common motion. Figure from Ref. [Bla08].

---

Two qubit entangling gates have been proposed [Cir95], realized experimentally [SK03, Lei03b] and evolved to a fidelity of  $> 99\%$  [Ben08]. Elementary quantum algorithms like quantum teleportation [Rie04], digital quantum simulation [Lan11] or the factorization of 15 [Mon16] have been demonstrated. Further examples such as simulation of spin models [Sen15, Jur14] and relativistic quantum mechanics [Ger11, Ger10] show the great potential of trapped ions for quantum simulation.

**Rydberg excitation of trapped ions** The excitation of trapped ions to Rydberg states combines the remarkable properties of Rydberg states, particularly the large polarizability and the long-range dipolar interaction, with the experimental control offered by trapped ion crystals. In contrast to neutral atoms in dipole traps, ions in Paul traps are strongly confined even if they are excited to Rydberg states which allows for a superb level of control of all degrees of freedom. The deep potential in Paul traps omits the necessity to reload atoms for every experimental cycle, which can speed up data acquisition by orders of magnitude. The long-range interaction enables fast entangling gates independent of the vibrational modes of the Coulomb crystal. The interaction between Rydberg ions is robust with respect to thermal excitation of the ions. Thus, quantum gates based on the Rydberg blockade between ions might pave the way toward scalable and fast quantum information processing.

Additionally, the interplay of highly susceptible Rydberg states and the electric fields in the Paul trap gives rise to state-dependent forces which are unique for Rydberg ions. Compared to the commonly used state-dependent interaction with light fields, these electric forces can be huge and may allow for entanglement of spin and motion. One particularly interesting consequence is a modification of the trap potential for ions in the Rydberg state. This gives control over the potential on a single particle scale. Typical lifetimes of Rydberg states are large compared to the oscillation period of an ion in the Paul trap, consequently this modified potential may be spectroscopically resolved.

Three major challenges have to be met in order to combine the unique properties of Rydberg states with the superb experimental control offered by trapped ion crystals. First, excitation energies are large as compared to the case of neutral atoms such that either single-step excitation with vacuum ultra violet (VUV) radiation or multi-step excitation with ultra violet (UV) radiation [Hen16] is required. We opted for one photon excitation with VUV radiation near 122 nm wavelength which has the benefit of separating the complex laser system from the ion trap apparatus. Secondly, the excitation of a single ion to the Rydberg state has to be detected with high efficiency. Thirdly, Rydberg states are highly sensitive to electric fields. In Paul traps, rapidly oscillating electric fields with quadrupolar geometry and gradients of  $10^7 - 10^9 \text{ V/m}^2$  generate the potential. Ions are trapped in the node of the quadrupole where the field ideally vanishes, nevertheless residual fields might perturb the Rydberg state and lead to a shifted and broadened resonance. If not compensated carefully, these fields might cause state changing transitions and even

ionization. The spectroscopic investigation of the effects of static and oscillating fields and field-gradients on the Rydberg ion are an interesting subject and a mandatory preparatory work for quantum information applications based on Rydberg ions.

A number of proposals show the value of trapped Rydberg ions for applications in quantum simulation and quantum information processing.

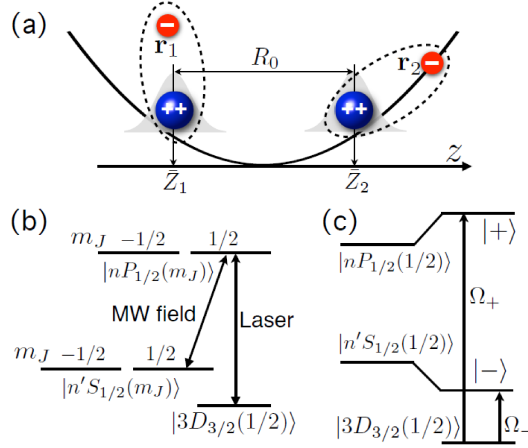


Figure 1.6.: a) Illustration of two Rydberg ions, separated by a distance  $R_0$ . The harmonic potential is indicated by the parabola b) The states  $nP_{1/2}$  and  $nS_{1/2}$  are coupled by a microwave field. Laser radiation excites the ions from the  $3D_{3/2}$  to the Rydberg state. c) The strong microwave coupling creates the dressed states  $|-\rangle$  and  $|+\rangle$  which exhibit a permanent dipole moment. Figure from Ref. [Li14].

- **Fast entanglement by dipole-blockade.** The dipole-dipole interaction allows for fast entangling operations of multiple ions independent of the vibrational modes in a Coulomb crystal. A fast two qubit gate for ions which is based on the strong dipole-dipole interaction has been proposed in Ref. [Li14]. The mechanism is similar to entangling gates for neutral atoms in optical tweezers [Wil10, Ise10]. However, the particular properties of trapped ion crystals with Rydberg excitations have to be considered. An inter ion distance of  $R_0 = 5 \mu\text{m}$  as typically found in ion crystals results in a van der Waals interaction of  $V/2\pi < 50 \text{ kHz}$  between Rydberg ions in the state  $65P_{1/2}$  [Li14] which is not sufficient for high fidelity entangling gates. Thus, one has to come up with a way to exploit resonant dipole-dipole interaction which are much stronger even on long distances [Saf10]. Tuning of Förster resonances as demonstrated in the case of neutral atoms [Vog06] requires a static electric field. This technique is not applicable in the case of trapped ions, as the field would exert a force on the ion. Instead, microwave mixing of the  $nP$  state with the nearby

$nS$  state may be used to generate dressed states  $|-\rangle$  and  $|+\rangle$  (see Fig. 1.6). These states are separated by the microwave Rabi-frequency  $\Omega_{0MW}$  and can be selectively excited by laser radiation. The states  $|-\rangle$  and  $|+\rangle$  have a permanent dipole moment which rotates with the microwave frequency  $\omega_{MW}$ . The dipole-dipole interaction between these dressed states is orders of magnitude stronger than the van der Waals interaction between the pure states (see Fig. 1.7).

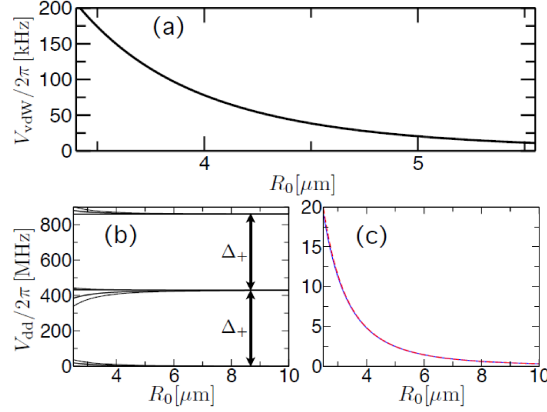


Figure 1.7.: a) Interaction strength for two ions in the  $65P_{1/2}$  state. For a typical inter ion distance of  $R_0 = 5 \mu\text{m}$ , the frequency shift is  $< 50 \text{ kHz}$ . b) and c) dipole dipole interaction between MW dressed states. The microwave coupling ( $\Omega_{0MW} = 400 \text{ MHz}$ ) is much bigger than the dipole dipole interaction, thus preserving the dressed states  $|-\rangle$  and  $|+\rangle$ . c) The interaction strength increases to about  $2 \text{ MHz}$  for a distance of  $5 \mu\text{m}$ . Figure from Ref. [Li14].

An additional feature of this scheme is used: The states  $nP$  and  $nS$  have polarizabilities  $\mathcal{P}_{nP}$  and  $\mathcal{P}_{nS}$  of opposite sign. Consequently the net polarizability of the dressed states  $|-\rangle$  and  $|+\rangle$  can be calculated as

$$\mathcal{P}_{\pm} = \frac{1}{\sqrt{1 + C_{\pm}^2}} (C_{\pm}^2 \mathcal{P}_{nP} + \mathcal{P}_{nS}). \quad (1.1)$$

For  $|C_{\pm}| \approx 0.68$  [Li14] the polarizability of the dressed state  $|-\rangle$  vanishes to first order. Thus internal and motional states of the ions are decoupled which allows for gate operations with ions in a thermal state.

- **Mode shaping by Rydberg excitations.** In large ion crystals, the mode structure becomes complex, posing a considerable challenge for the scaling of ion trap quantum computation to many qubits. Micro-structured traps with many independent regions, which allow for the transportation, splitting and merging of several small Coulomb crystals are one solution to this challenge [Kie02, Wal12, Rus14]. An

alternative is the modification of vibrational modes, tailored to a specific operation. With the state dependent potential offered by Rydberg ions, the radial vibrational frequency can be altered for individual ions: In Ref. [Li13] the authors show that Rydberg excitation of single ions in a long linear crystal leads to the emergence of localized radial modes (see Fig. 1.8). In fact, the sub-crystals between Rydberg impurities behave similar to ion crystals in independent potentials: They exhibit a simplified mode structure as only  $2N_{sub}$  radial modes exist for a sub-crystal with  $N_{sub}$  ions and, if multiple sub-crystals are generated, each one oscillates independently which allows for parallel execution of entangling gates on different sub-crystals. For an ion string consisting of 100 ions, the authors argue that the fidelity of two conditional phase flip gates, executed in parallel, may be increased to  $F > 99.9\%$ .

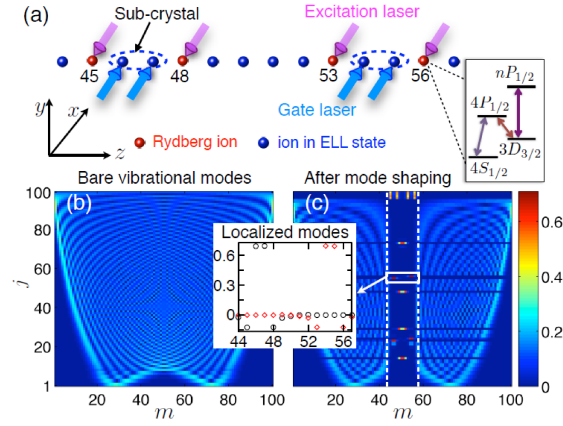


Figure 1.8.: a) Proposal for Rydberg-enabled parallel gate execution: Multiple ions in a long ion chain of 100 ions are excited to Rydberg states. The ions in between these Rydberg impurities form independent sub-crystals. Gate lasers, operating on the radial modes execute gates on multiple-sub crystals at once. b) Calculated mode structure of a 100 ion crystal, oscillation amplitudes are distributed over all ions and the spectrum is very dense. c) Calculated mode structure for a 100 ion crystal with two ions excited to the Rydberg state. In between the Rydberg ion a sub-crystal with a much simpler mode spectrum is formed. Figure from Ref. [Li13]

The technique of mode shaping can be extended to large 2D Coulomb crystals [Nat15]. Here, localized out of plane modes form around impurities as illustrated in Fig. 1.9. The oscillation amplitude of these modes is restricted to the central Rydberg ion and the six surrounding ions. Not only is this mode localized, but due to the higher oscillation frequency of the ion in the Rydberg  $P$  state, it is also well separated from all other out of plane modes in frequency space. Hence, it may be resolved by laser spectroscopy. If multiple ions are excited to Rydberg states

a regular Kagome lattice is formed which is an interesting but difficult to achieve system for quantum simulation such as the Balents-Fisher-Girvin model.

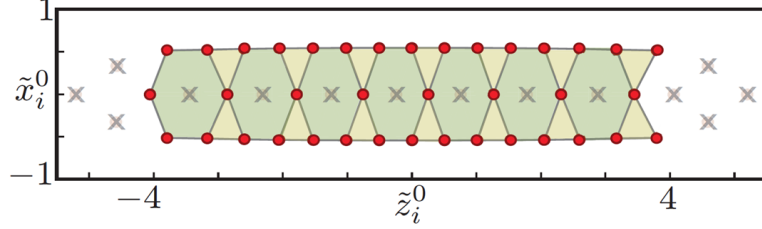


Figure 1.9.: Illustration of a 2D Coulomb crystal with Rydberg excitations on the trap axis (x's). Localized modes form on the hexagonal plaquettes consisting of the six ions (red dots) around the Rydberg ion. A plaquette spin-spin interaction can be simulated by the execution of gates on these modes. Individual plaquettes interact via the ions which are part of two of these rings (red dot; on axis). Figure from Ref. [Ber12]

- **Phase transitions driven by Rydberg excitations.** Due to the state dependent potential, excitation of Rydberg states can drive structural phase transitions [Li12]. The authors of Ref. [Li12] describe the situation of a three ion crystal in zigzag configuration, with a trap anisotropy  $\omega_r/\omega_z$  close to the critical value for a phase transition to a linear structure [Enz00]. Excitation of the central ion to a Rydberg  $nP$  state increases the potential felt by this ion and consequently induces a phase transition to a linear configuration. Structural phase transitions in ion crystals have been used to simulate spontaneous symmetry breaking described by the Kibble-Zureck effect [Ulm13, Pyk13]. Driving these transition with Rydberg excitation would open up interesting possibilities such as the generation of superposition states between different spacial configurations [Bal12].

**In this thesis, the Rydberg excitation of trapped  $^{40}\text{Ca}^+$  ions is presented.** I have built an apparatus for trapping and cooling of  $^{40}\text{Ca}^+$  ions, consisting of a Paul trap, a setup for the generation of ultra high vacuum, and multiple lasers with wavelength in the visible and infrared region of the electromagnetic spectrum. This apparatus is joined with an existing source for continuous wave, coherent vacuum ultra violet (VUV) radiation. We trapped and cooled ions in this joined setup, and finally excited them to Rydberg states by coherent VUV radiation near wavelengths of 123 nm and 122 nm. This experimental work paves the way to a novel platform of Rydberg matter, where state-dependent electric forces as well as long-range dipole-dipole interactions are combined with the outstanding control over quantum states in trapped ion crystals.

Chapter 2 summarizes the theoretical foundations which determine the behavior of Ry-

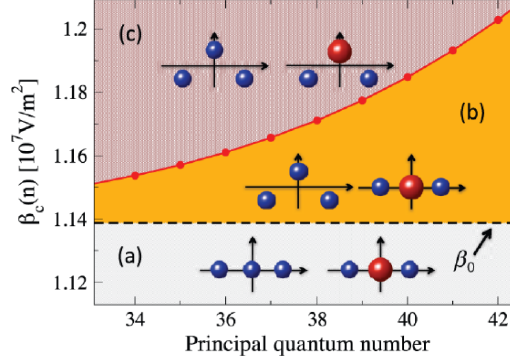


Figure 1.10.: Proposal for a Rydberg induced phase transition from linear to zigzag configuration for a three ion crystal. In parameter region a), the ions form a linear string, while in region c) they are in zigzag configuration. In between these two regions b) the spacial structure depends on the internal state of the central ion, the ions form a zigzag crystal if it is in the ground state. Rydberg excitation (red) of the central ion results in a linear crystal. Region b) gets broader for higher principle quantum numbers  $n$  as the effect of the state dependent potential gets more pronounced. Figure from Ref. [Li12].

Rydberg ions confined in Paul traps. In addition to the individual aspects of Rydberg states and trapped ions, new and unique features arise from the interplay of the Rydberg state with the electric field of the trap [Mül08,SK11]. This chapter is followed by a detailed discussion of the experimental setup of which the main building blocks are the VUV source, the combined vacuum vessel for VUV source and ion trap, the laser system for cooling, optical pumping, coherent manipulation and detection of  $^{40}\text{Ca}^+$  and the two Paul traps. In chapter 5, preparatory experiments are presented. This includes measurements for the characterization of the ion traps and the VUV source as well as experiments with  $^{40}\text{Ca}^{2+}$  ions generated by photo ionization of  $^{40}\text{Ca}^+$  with VUV radiation near 121 nm wavelength (published in Ref. [Fel14]). Rydberg excitation to the states  $22F$ ,  $52F$ ,  $53F$  and  $66F$  is presented in chapter 6. Excitation wavelengths of all transitions are determined and the resonance shapes of the transitions to  $22F$  and  $52F$  are analyzed. We combined the excitation of Rydberg state with the coherent manipulation of the optical qubit transition in  $^{40}\text{Ca}^+$  and succeeded in the addressed Rydberg excitation of single ions in linear crystals. The results are published in Ref. [Fel15,Bac16]. In the outlook, I sketch future improvements for the experiment which will enable the experimental realization of the proposed applications for fast gate operations, mode shaping in large Coulomb crystals and spin-dependent phase transitions.



## 2. Theoretical foundations

In this chapter the theoretical foundations for the Rydberg excitation of trapped ions are summarized. First, an introduction to Rydberg states is given [Gal88]. We are particularly interested in the polarizability, the radiative lifetime and the dipolar interactions between Rydberg states. In the second section the unique features of trapped ions excited to Rydberg states are discussed. The pseudo-potential of the Paul trap is derived, before its implications to Rydberg states of trapped ions are investigated in detail [Mül08, SK11]. At last, the atomic properties of  $^{40}\text{Ca}^+$  are summarized.

The dynamics of ions in an electronically low lying state in the Paul trap, laser-ion interaction in the pseudo potential and different cooling methods are not discussed in this thesis. An elaborate discussion can be found in Ref. [Lei03a, Roo00].

### 2.1. Introduction to Rydberg states

The properties of Rydberg atoms are dominated by one electron in an orbit with high principle quantum number  $n > 10$  [Gal88, Gal94]. At large distances from the nucleus ( $r \gg a_0$  with Bohr radius  $a_0$ ), the potential experienced by this valence electron is similar to the potential experienced by an electron in hydrogen. The core electrons shield the charge of the nucleus so that a Coulomb potential corresponding to a single elementary charge remains. The Coulomb potential  $V(r) \propto 1/r$  depends on the absolute value of  $r$  only. Consequently, the hydrogen wave functions can be separated into an angular part and a radial part. The radial part of the differential equation for the Coulomb potential can be written in atomic units as [Gal94]

$$\frac{\partial^2 \rho}{\partial r^2} + \left( 2W + \frac{2}{r} + \frac{l(l+1)}{r^2} \right) \rho = 0. \quad (2.1)$$

Here,  $r$  denotes the radius,  $W$  the binding energy and  $l$  the angular momentum. Equation 2.1 has two linear independent solutions,  $\rho(r) = f(W, l, r)$  and  $\rho(r) = g(W, l, r)$ .  $f$  and  $g$  are oscillatory functions with a phase difference of  $\pi/2$  in the classical allowed region given by

$$W + 2/r - l(l+1)/(2r) > 0 \quad (2.2)$$

and exponentially decreasing or increasing functions outside of that region. Only the regular coulomb function  $f(W, l, r)$  [Fan70] fulfills the boundary conditions  $\rho(0) \neq \infty$  and  $\rho(\infty) = 0$ . Hence,  $f(W, l, r)$  is the physical solution for the hydrogen atom.

At small distance  $r$ , the potential of a Rydberg atom is modified compared to the hydrogen atom by the core electrons. The overlap of the wave function of the valence electron with the core electrons decreases the potential in this inner region. This modification can be taken into account by a quantum defect  $\delta_l$  [Sea83]. The quantum defect is approximately independent of the principal quantum number  $n$  but depends strongly on the angular momentum quantum number  $l$ . Typically, only low  $l$  states exhibit a significant quantum defect, as only these states overlap with the inner core electrons. The outer part of the wave function is similar to hydrogen but shifted in phase by  $\delta_l\pi$  due to the modified inner part. Consequently, the wave function of a Rydberg state in the outer region of the potential can be described by a linear combination of the solutions to Eq. 2.1,  $f(W, l, r)$  and  $g(W, l, r)$ . The complete wave function for the Rydberg state reads [Gal94]

$$\psi(\theta, \Phi, r) = \frac{Y_{lm}(\theta, \Phi, r) (f(W, l, r) \cos \pi\delta_l - g(W, l, r) \sin \pi\delta_l)}{r}, \quad (2.3)$$

with the angular part  $Y_{lm}$  equal to the hydrogen wave function. Specific wave functions can be calculate numerically using the Numerov method [Bla67]. For the normalization constant  $\mathcal{N}$  of these wave functions one obtains

$$\mathcal{N} = \sqrt{\frac{2}{\pi n^3}}. \quad (2.4)$$

The allowed energies are modified by the quantum defect  $\delta_l$  compared to the energies in hydrogen.

$$W = \frac{-1}{2(n - \delta_l)^2}. \quad (2.5)$$

The classical inner and outer turning points of the electron can be calculated from Eq. 2.5 and Eq. 2.1 to

$$r_{min} \approx l(l + 1) \times a_0 \quad (2.6)$$

and

$$r_{max} = 2(n - \delta)^2 \times a_0. \quad (2.7)$$

From the allowed energies (Eq. 2.5), the normalization constant (Eq. 2.4) as well as inner and outer classical turning point of the electron (Eq. 2.6 and Eq. 2.7), the scaling laws for key properties of Rydberg states can be derived. From Eq. 2.5 follows the existence of distinct Rydberg manifolds with an energy spacing of  $\Delta E(n) = E(n + 1) - E(n) \propto n^{-3}$  in between states of the same manifold (see Fig. 2.1). The energy shift of each manifold compared to the hydrogen energies is determined by the respective quantum defect.

The  $n$  dependence of the radiative lifetime  $\tau$  of a Rydberg state is derived as follows:

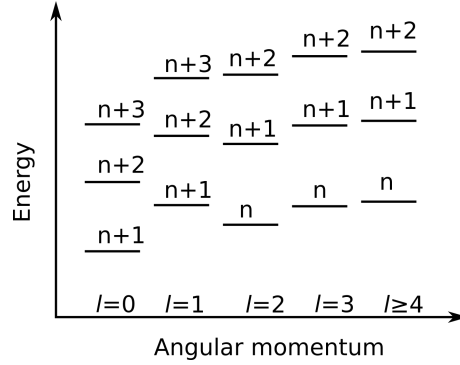


Figure 2.1.: Schematic illustration of excitation energies of Rydberg states. Within a  $l$  manifold the energy spacing is regular and scales with  $1/n^3$ . The energy shift between different  $l$  manifolds is determined by the quantum defect  $\delta(l)$ . Typically states with  $l \geq 4$  have negligible quantum defects.

The inverse lifetime of an atomic state  $n$  is given by the sum over the Einstein A coefficient for the decay to energetically lower lying state [Bet08]

$$\frac{1}{\tau} = \sum_m A_{nm}. \quad (2.8)$$

with

$$A_{nm} \propto \omega_{nm}^3 \times \mu_{nm}^2. \quad (2.9)$$

Here,  $\omega_{nm}$  denotes the resonance frequency of the transition and  $\mu_{nm}$  the transition dipole matrix element  $\langle \Psi_n | r | \Psi_m \rangle$ . For a decay to the low lying state,  $\omega_{nm}$  depends only marginally on  $n$  (see Eq. 2.5). The matrix element  $\mu_{nm}$  is determined by the expectation value of the wave function at small distances of the core. With  $r_{min} \approx l(l+1) \times a_0$  independent of  $n$  this expectation value is given by the normalization constant of the wave function which is proportional to  $n^{-3/2}$ . Thus the decay to low lying states scales with  $\mu_{nm}^2 \propto n^{-3}$ . Looking at the decay to the next  $n$  state on the other hand, the transition frequency scales with  $n^{-3}$ . The transition dipole matrix element scales with the size of the Rydberg orbital ( $n^2$ ) resulting in a Einstein A coefficient proportional to  $n^{-5}$ . Consequently the lifetime of low angular momentum states is dominated by decay to low lying state and scales as  $\tau \propto n^3$ . For high angular momentum states, dipole allowed transitions exist only to adjacent  $n$  states which results in a radiative lifetime proportional to  $n^5$ .

Due to the small energy gap  $\Delta E$  and the huge dipole moment  $\mu$  between adjacent states, Rydberg atoms are extremely sensitive to electric fields. In case of low electric fields such that the coupling of states is small compared to their energy difference, the polarizability scales as  $\alpha \propto \mu^2 / \Delta E \propto n^7$ . Thus, an extremely well controlled electric field is required

Property	scaling
binding energy $E$	$n^{-2}$
energy difference between adjacent $n$ states $\Delta E$	$n^{-3}$
orbital radius $r$	$n^2$
dipole moment $\mu_{(nl,nl\pm1)}$	$n^2$
radiative lifetime $\tau$ (low $l$ -states)	$n^3$
polarizability $\alpha$	$n^7$

Table 2.1.: Scaling of key properties of Rydberg states with principal quantum number  $n$ .

for laser excitation of Rydberg states to avoid resonance broadening. The  $n$  scaling of key properties of Rydberg states is summarized in Tab. 2.1.

**Interactions between atoms in Rydberg states** So far, the properties of single Rydberg states have been discussed. However, the key feature for many applications is the strong, long-range interaction between two or more Rydberg atoms. This interaction stems directly from the single atom properties, particularly the polarizability and can be derived as follows [Saf10]: For distances  $R \gg n^2 \times a_0$  between two Rydberg atoms, the electron orbitals do not overlap and the leading term of the interaction is the dipole-dipole interaction

$$V_{dd} = \frac{e^2}{R^3}(\vec{r}_{e1} \times \vec{r}_{e2} - 3\vec{r}_{e1} \times \hat{R}\hat{R} \times \vec{r}_{e2}), \quad (2.10)$$

with the elementary charge  $e$  and the electrons position vectors  $\vec{r}_{e1}$ ,  $\vec{r}_{e2}$  measured from their respective nuclei. Limiting our description to the case of both atoms excited to the same Rydberg state<sup>1</sup>, the two-atom state can be written as

$$|\psi_{pair}\rangle = |\psi_1\psi_2\rangle = |nl, nl\rangle. \quad (2.11)$$

Here  $|\psi_1\rangle$  and  $|\psi_2\rangle$  denote the quantum states of atoms one and two. The dipole interaction induces transitions to other pair states with  $\Delta l = \pm 1$ . One finds that the interaction is dominated by transitions to the closest two-atom states (with respect to  $n$  and energy) with opposite parity, e.g.  $|np, np\rangle \rightarrow |ns, n+1s\rangle$  [Saf10]. For these pair states the dipole moment  $\mu$  is largest and the energy difference  $\delta$  compared to the initial pair state is small. Transitions to other states with larger difference in  $n$  may feature even smaller energy gaps  $\delta$  but much smaller dipole moments. Thus the coupling of only two pair states by the dipole operator  $V_{dd}$  gives a good approximation of the total interaction energy. In the interaction picture, the dipole coupling is given by [Saf10]

---

<sup>1</sup>A more extensive summary of Rydberg interactions also discussing the case of different Rydberg states can be found in [Nab12]

$$\begin{pmatrix} \delta & V_{dd} \\ V_{dd} & 0 \end{pmatrix} \begin{pmatrix} |\chi\rangle \\ |\phi\rangle \end{pmatrix} = \Delta \begin{pmatrix} |\chi\rangle \\ |\phi\rangle \end{pmatrix}. \quad (2.12)$$

Here,  $|\chi\rangle = |ns, n+1s\rangle$  and  $|\phi\rangle = |np, np\rangle$  are the wave functions of the two coupled pair-states while  $\delta$  is the energy difference between those states. Solving for the eigenenergies  $\Delta$  yields

$$\Delta = \frac{\delta}{2} \pm \sqrt{\frac{\delta^2}{4} + \frac{C_3^2}{R^6}}, \quad (2.13)$$

with  $C_3 \propto \mu^2 \propto n^4$ . Looking at the  $R$  and  $n$  dependence of the interaction strength, there are two distinct regimes. If  $\delta^2 > C_3^2/R^6$ ,  $\Delta$  can be approximated by

$$\Delta_{vdW} \approx \frac{2C_3^2}{R^6\delta}. \quad (2.14)$$

In this regime the interaction is of van-der-Waals (vdW) form and scales as  $\Delta_{vdW} \propto n^{11}/R^6$ . On the other hand, the case of  $\delta^2 < C_3^2/R^6$  is called Förster resonance [För65] and the interaction becomes

$$\Delta_{dd} \approx \frac{C_3}{R^3}. \quad (2.15)$$

This equation resembles the interaction between two permanent dipoles and scales as  $\Delta_{dd} \propto n^4/R^3$ . The interaction energy is illustrated in Fig.2.2. For each state, the transition between resonant dipole-dipole and vdW interaction takes place at a specific inter atom distance  $R$ . Typically the transition occurs at a distance in the order of  $1\ \mu\text{m}$ .

**Interaction in external fields** Various techniques, all involving the use of external fields, exist to generate dipole-dipole interactions with a  $1/R^3$  behavior for larger inter atom distances. The dependence of the polarizability on the angular momentum state  $l$  results in a differential energy shift for the two pair states  $|n, l, n, l\rangle$  and  $|n', l', m', l'\rangle$  with  $l = l' \pm 1$ . Consequently it allows for Stark tuning of the energy gap  $\delta$  between two pair states. Thus, artificial Förster resonances can be generated in an electric field, which feature  $1/R^3$  dependence even for large inter atom distances.

Alternatively one may generate Rydberg states with permanent dipole moment for which the interactions is proportional to  $1/R^3$ . Eigenstates of the Coulomb potential do not have a permanent dipole moment. In an external electric field however, the electron orbit is shifted with respect to the nucleus which gives rise to a permanent anisotropic dipole-dipole interaction at any distance.

With a resonant microwave, Rydberg states of opposite parity can be mixed. This way a rotating dipole moment in phase with the microwave is generated. This method results in an interaction similar to the interaction of permanent dipoles.

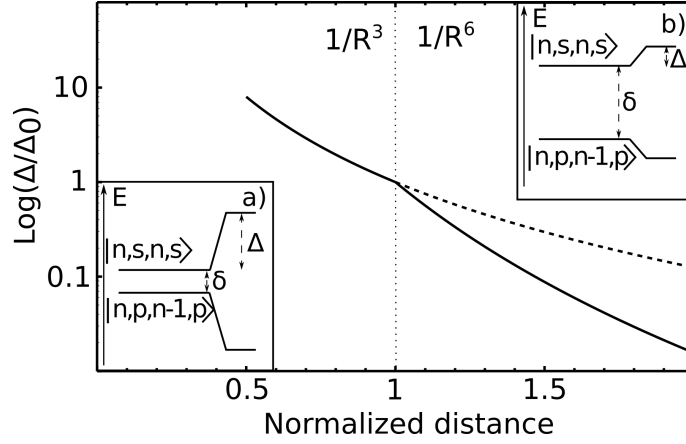


Figure 2.2.: Interaction strength  $\Delta$  as a function of the distance  $R$  between Rydberg atoms. For small distances, the energy defect  $\delta$  between pair states  $|n, S, n, S\rangle$  and  $|n, P, n-1, P\rangle$  is small compared to the energy shift  $\Delta$  and the interaction scales with  $1/R^3$ . At larger distances the interaction is weaker and a transition to a  $1/R^6$  scaling occurs. With an external electric field, the two pair states can be shifted into resonance, giving rise to an interaction energy scaling as  $1/R^3$  even for large distances (dashed line).

**Dipole blockade** The dipole-dipole interaction between Rydberg atoms can easily exceed 1 MHz at distances of a few  $\mu\text{m}$ . The interaction can be switched in a controlled way by coherent excitation of long lived Rydberg states with laser pulses. These features make it an excellent tool for many applications in quantum mechanics where a controlled interaction between otherwise isolated atoms is required. However, due to the strong  $R$  dependence of the interaction it is difficult to precisely control the strength of the interaction. Here, the concept of the dipole-blockade presents a solution: Two atoms with ground state  $|g\rangle$  and Rydberg state  $|e\rangle$  are positioned at a distance  $R$ , a laser with frequency  $\omega_0$  resonantly couples  $|g\rangle$  and  $|e\rangle$ . While the energy of the pair-states  $|gg\rangle$  and  $|ge\rangle$  is independent of  $R$ , the doubly excited state  $|ee\rangle$  is shifted by the interaction energy  $\Delta(R)$ . Consequently the state  $|ee\rangle$  is not excited by the laser with frequency  $\omega_0$  if the interaction energy is larger than the line width  $\Gamma$  of the transition. A  $\pi$ -rotation on both atoms generates the entangled state  $1/\sqrt{2}(|ge\rangle + |eg\rangle)$ . For  $\Delta > \Gamma$  this effect is independent of the exact value of the interaction strength and thus independent of  $R$ . The dipole-blockade is illustrated in Fig. 2.3.

## 2.2. Rydberg excitation of trapped, cold ions

Rydberg states of ions are very similar to Rydberg states of neutral atoms, discussed in section 2.1. The only notable difference, the doubly charged core, increases the binding

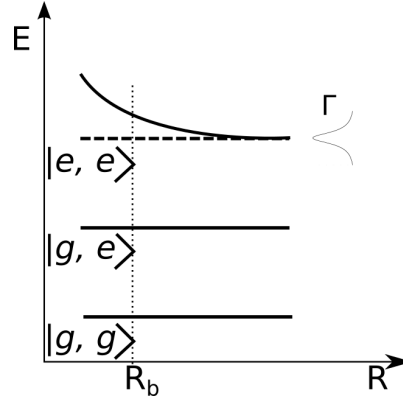


Figure 2.3.: Illustration of blockade of laser excitation of nearby Rydberg atoms. At large distances the energies of the pair states  $|g, g\rangle$ ,  $|g, e\rangle$  and  $|e, e\rangle$  are evenly spaced. All states can be coupled by a light field with frequency  $\nu_0$ . At close distances, the state  $|e, e\rangle$  is shifted due to the dipole interaction. If the shift is larger than the resonance width  $\Gamma$  the state  $|e, e\rangle$  can not be excited.

energy of the states. While this shifts the transitions to Rydberg states to even shorter wavelength and consequently poses a major experimental challenge, it does not change the properties of Rydberg states qualitatively. The unique feature of trapped ions excited to Rydberg states stem from the interplay of the electric trapping fields with the highly susceptible Rydberg state.

In order to investigate the behavior of a Rydberg ion in a Paul trap, first the electric fields present in the trap are analyzed. Subsequently the interaction of the Rydberg ion with the dynamic potential is derived. The features which arise from this interaction and their consequences for experimental applications are discussed.

### 2.2.1. Trapping ions with electric fields

In Paul traps, ions are confined by a combination of static and dynamic electric quadrupole fields [Lei03a]

$$\Phi(\mathbf{r}, t) = \cos(\Omega_{rf}t) \times \sum_i \alpha_i r_i^2 + \sum_i \beta_i r_i^2. \quad (2.16)$$

In this equation  $\mathbf{r}$  denotes the distance from the trap center,  $\alpha_i$  and  $\beta_i$  are the dynamic respectively static components of the quadrupole potential in directions  $i = (x, y, z)$  and  $\Omega_{rf}$  is the oscillation frequency of the dynamic part of the potential. From the Laplace equation  $\Delta\Phi = 0$  follows

$$\sum_i \alpha_i = 0 \text{ and } \sum_i \beta_i = 0 \quad (2.17)$$

which prevents stable trapping in all dimensions with a static electric field only. However, particles with charge  $Q$  and mass  $m$  can be trapped in an oscillating field where  $\alpha_i$  oscillates at a frequency  $\Omega_{rf}$ . The equation of motion for such a potential can be transformed into the standard form of the Mathieu equation [Lei03a]

$$\frac{d^2 \mathbf{r}}{d\xi^2} + (a_i - 2q_i \cos(2\xi)) \mathbf{r} = 0, \quad (2.18)$$

with

$$a_i = \frac{8\beta_i Q}{m\Omega_{rf}^2}, \quad q_i = \frac{4\alpha_i Q}{m\Omega_{rf}^2}, \quad \xi = \frac{\Omega_{rf} t}{2}. \quad (2.19)$$

In general, the Mathieu equation has stable solutions for various parameter regimes, however for the operation of a linear Paul trap, only the lowest stability region with  $(q_i, a_i) < 1$  is of interest. For the condition  $(|a_i|, q_i^2) \ll 1$  the motion of the ion consists of a slow secular motion at frequency

$$\omega_i = \sqrt{\frac{2\beta_i Q}{m} + \frac{2\alpha_i^2 Q^2}{m^2 \Omega_{rf}^2}} \quad (2.20)$$

and a superposed driven oscillation at frequency  $\Omega_{rf}$  with an amplitude smaller by  $q_i/2$ . This is the well known pseudo potential approximation of the Paul trap potential. For the geometry of a linear Paul trap the field gradients are simplified to

$$\alpha_z = 0, \quad \alpha_x = -\alpha_y \quad \text{and} \quad \beta_z = -2\beta_x = -2\beta_y. \quad (2.21)$$

The driven oscillation at  $\Omega_{rf}$  (micro motion) corresponds to an oscillating electric field at the ion. For ions in Rydberg states this field does not only influence the center of mass motion but, due to the high polarizability, also the internal state of the ion. The interaction between the oscillating field and the Rydberg ion is both, a major challenge and a key feature of ions excited to Rydberg states. Hence, a detailed analysis of this interaction is required.

### 2.2.2. Rydberg states of alkali-earth ions in the pseudo-potential

Alkali-earth ions like  $^{40}\text{Ca}^+$  possess a single valence electron while the remaining electrons form closed shells, leading to an effective two body system. For electronically low lying states, the valence electron is tightly bound to the two-fold ionized core, thus the trapped ion can be treated as a single particle with elementary charge  $e$  and mass  $m$  in an external electric field. For Rydberg states the electronic orbit  $a_{Ry}$  is larger than the typical oscillator length  $x_{ho}$  of an ion in the harmonic potential of a Paul trap while at the same time the binding force between core and electron is significantly reduced. In this situation the perturbation of the electron orbit by the trapping field can not longer be neglected and



the ion has to be treated as a composite object made out of a doubly ionized atomic core and a loosely bound electron, each interacting with the electric trapping field. This leads to a state dependent interaction with the external trapping fields, giving rise to complicated dynamics in the trap.

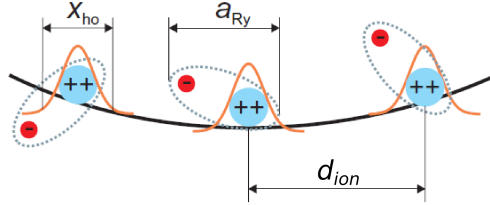


Figure 2.4.: Rydberg ion in the pseudo potential of a Paul trap. For typical trap parameters and Rydberg states accessible in the experiment, the distance between ions is large as compared to the electronic orbit which is again larger than the wave function of a ground state ion in the potential of the Paul trap ( $d_{ion} > a_{Ry} > x_{ho}$ ). Figure taken from [Mül08]

In a qualitative way, the behavior of a Rydberg ion in a Paul trap can be understood as follows: The electronic orbit of the Rydberg state reaches into the oscillating quadrupole field of the trap. The Rydberg state is polarized by the oscillating field which leads to a time dependent energy shift, oscillating with  $2\Omega_{rf}$  due to the quadratic Stark effect. This does not only influence the internal state's energy but also the trapping potential. The electric field increases linearly with the distance to the trap axis. This leads to an additional harmonic potential which can be either trapping or anti-trapping depending on the sign of the state's polarizability. Consequently the potential is modified for an ion in a Rydberg state as compared to an ion in the ground state.

A detailed quantitative analyzes of these effects [Mül08, SK11] is required. The description is limited to situations where the electron orbit is much smaller than the inter ion distance  $d_{ion}$  as depicted in Fig. 2.4. Furthermore, the frequencies attributed to the external dynamics, trap drive frequency  $\Omega_{rf}/2\pi \approx 10$  MHz and vibrational frequencies  $\omega_i/2\pi \approx 1$  MHz should be small compared to the energy differences  $\nu$  between adjacent Rydberg levels of opposite parity in order to avoid resonant coupling:

$$\nu \gg \Omega_{rf} > \omega_i. \quad (2.22)$$

A single Rydberg ion is treated as a composite object consisting of the doubly ionized core and the loosely bound electron, in the dynamic fields of the Paul trap. The two-body-Hamiltonian thus has to take into account the coupling of the doubly ionized core and the valence electron to the trapping field as well as the interaction between core and electron:

$$H = \frac{p_I^2}{2m_I} + \frac{p_e^2}{2m_e} + V(|r_e - r_I|) + V_{ls}(r_e - r_I) + 2e\Phi(r_I, t) - e\Phi(r_e, t) \quad (2.23)$$

Here,  $p_{I,e}$  and  $m_{I,e}$  are the momentum and mass of the ionic core and the electron,  $r_{I,e}$  is the position of the Ion and electron with respect to the trap center and  $e$  is the elementary charge. The interaction between the ionic core and the electron is given by a model potential  $V(|r_e - r_I|)$  and the spin-orbit coupling  $V_{ls}(r_e - r_I)$ ,  $\Phi$  is the trapping potential. It is convenient to change to a center of mass frame,

$$r_I = R - \frac{m_e}{m_I + m_e}r \approx R, \quad r_e = R + \frac{m_I}{m_I + m_e}r \approx R + r. \quad (2.24)$$

With center of mass coordinate  $R$  and relative coordinate  $r$ , the Hamiltonian becomes

$$H = \frac{p_I^2}{2m_I} + \frac{p_2^2}{2m_e} + V(|r|) + V_{ls}(r) + 2e\Phi(R, t) - e\Phi(R + r, t). \quad (2.25)$$

A Taylor expansion for  $e\Phi(R + r, t)$  around  $R$  yields

$$-e\Phi(R + r, t) = -e\Phi(R, t) - e \frac{\partial \Phi(R, t)}{\partial R} \times r - \frac{e}{2} \sum_{kl} x_k \frac{\partial^2 \Phi(R, t)}{\partial X_k \partial X_l} x_l, \quad (2.26)$$

with  $R = (X, Y, Z)$  and  $r = (x, y, z)$ . Thus the Hamiltonian reads

$$H_I = \frac{p_I^2}{2m_I} + e\Phi(R, t) \quad (2.27)$$

$$H_e = \frac{p_e^2}{2m_e} + V(|r|) + V_{ls}(r) - e\Phi(r, t) \quad (2.28)$$

$$H_{Ie} = -2e [\alpha \cos(\Omega t)(Xx - Yy) - \beta(Xx + Yy - 2Zz)]. \quad (2.29)$$

Here,  $H_I$  is the center of mass Hamiltonian, while  $H_e$  is the Hamiltonian for the electron dynamics, including coupling to the ionic core and the external trapping field.  $H_{Ie}$  accounts for the electron-Ion coupling. While  $H_I$  is equivalent to the Hamiltonian of an ion in a low lying state,  $H_e$  and  $H_{Ie}$  lead to shifts of the electronic levels and modifications to the trapping potential respectively.

**Electronic level shifts**  $H_e$  accounts for the Coulomb interaction between the doubly ionized core and the valence electron, the spin-orbit coupling, and the trap-electron interaction.  $\Omega_{rf}$  does not resonantly drive transitions to adjacent states (see Eq. 2.22), consequently a quasi static approach where the time  $t$  is treated as a parameter only is used. The trap-electron interaction in  $H_e$  is given by:

$$H_{eT} = -e\Phi(r, t) = e\beta (x^2 + y^2 - 2z^2) - e\alpha \cos(\Omega t) \times (x^2 - y^2) \quad (2.30)$$

For states with a large quantum defect  $\delta$  (typically  $S$ ,  $P$  and  $D$ ) which are energetically well isolated from other Rydberg manifolds, it is sufficient to find an effective Hamiltonian for that  $l$ -manifold only, the contribution of other states on this manifold is calculated by perturbation theory. The effective Hamiltonian for the energy shift in second order perturbation theory reads [SK11]

$$H_{eT}^{(2)mm'} = \sum_{\nu} H_{eT}^{(1)m\nu} H_{eT}^{(1)\nu m'} \left[ \frac{1}{2(E_m - E_{\nu})} + \frac{1}{2(E_{m'} - E_{\nu})} \right], \quad (2.31)$$

with

$$H_{eT}^{(1)m\nu} = \langle \Psi_m | H_{eT} | \Psi_{\nu} \rangle. \quad (2.32)$$

The energy shift has a static and an oscillating part due to the static ( $\beta$ ) and oscillating ( $\alpha$ ) electric field. The static part leads to a small energy shift in the order of  $\Delta E_{\beta} = 2\pi \times 1 \text{ kHz}$  for typical experimental parameters. The oscillating shift however, is in the order of  $\Delta E_{\alpha} = 2\pi \times 10 \text{ MHz}$  for trapping parameters targeted in our experiment. The time dependence of this shift leads to an effective line broadening which is a potential issue for narrow bandwidth laser excitation of Rydberg states. The scaling of the energy shift with principal quantum number  $n$  and electric field gradient  $\alpha$  is given by

$$\Delta E \propto C(l) \times \alpha^2 \times n^{11}. \quad (2.33)$$

The constant  $C$  depends on the angular momentum state and can be either negative (e.g.  $S$ ,  $D$  and  $F$  states in  $^{40}\text{Ca}^+$ ) or positive (e.g.  $P$  states in  $^{40}\text{Ca}^+$ ).

**State dependent trapping potential**  $H_{Ie}$  accounts for the electron-Ion coupling and leads to a modification of the effective trapping potential. With the same approximations as in the case of the electron-trap interactions,  $H_{Ie}$  becomes

$$H_{Ie}^{(2)mm'} = R^{\dagger} U_{mm'} R, \quad (2.34)$$

with

$$U_{mm'} = \sum_{\nu} \langle \Psi_m | R_e | \Psi_{\nu} \rangle \langle \Psi_{\nu} | R_e^{\dagger} | \Psi_{m'} \rangle \left( \frac{1}{2(E_m - E_{\nu})} + \frac{1}{2(E_{m'} - E_{\nu})} \right) \quad (2.35)$$

and

$$R_e = 2e \begin{pmatrix} (-\alpha \cos(\Omega t) + \beta) x \\ (\alpha \cos(\Omega t) + \beta) y \\ -2\beta z \end{pmatrix}. \quad (2.36)$$

## 2. Theoretical foundations

The diagonal elements  $U_{mm}$  couple states in a  $(n, l, j)$  subspace and lead to a time averaged energy shift  $\Delta E_x$  as a function of the displacement  $x$  from the trap center, which corresponds to a harmonic potential. While this effect is rather small in z-direction due to  $\alpha \gg \beta$ , it can lead to a significant shift of  $\omega_{x,y}$

$$\Delta\omega_{x,y} \propto \alpha \times n^{7/2}. \quad (2.37)$$

For high lying Rydberg states, the potential is significantly modified by this dipole-trap interaction<sup>2</sup>.

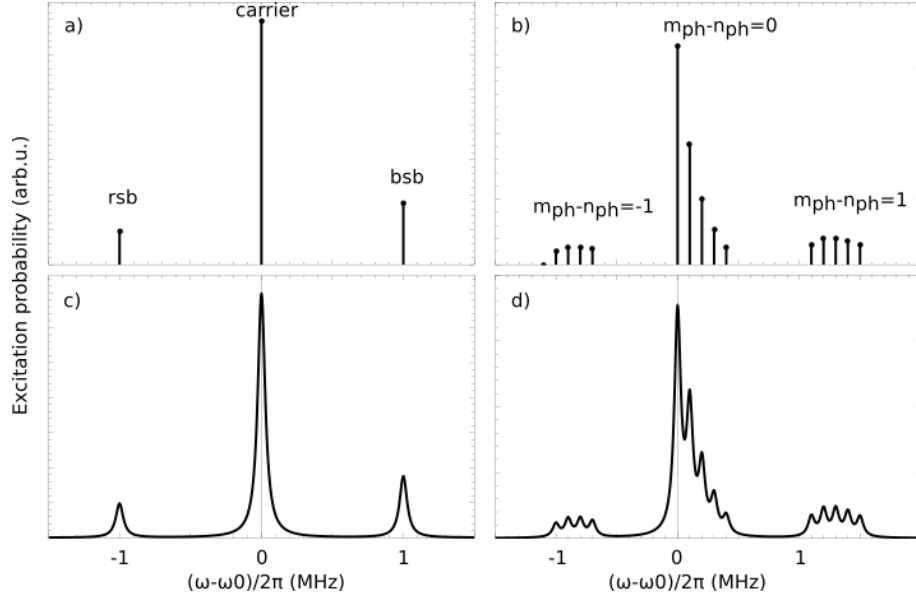


Figure 2.5.: a) Laser excitation of electronically low lying states of an ion in a thermal state with  $\bar{n}_{ph} = 2$ , in a potential of  $\omega_g/2\pi = 1$  MHz and Lamb-Dicke parameter  $\eta = 0.3$ . The typical side band features of spectrally narrow transitions in ion traps are shown. b) Laser excitation of Rydberg states with modified trapping potential. Trap parameters for ground and Rydberg state are  $\omega_g/2\pi = 1$  MHz and  $\omega_{ryd}/2\pi = 1.1$  MHz respectively. Due to  $\omega_g \neq \omega_{ryd}$ , the transition frequency does not only depend on  $\Delta n_{ph}$  but also on the initial state  $n_{ph}$ . A thermal state is a superposition of multiple Fock-states, thus numerous sidebands appear. c) and d) Convolution of the side band structure with a Lorentz distribution corresponding to a lifetime of Rydberg states of  $\tau = 10 \mu s$ .

This state dependent trapping potential affects the excitation of Rydberg states. When exciting an ion from a state  $|g, n_{ph}\rangle$  with phonon number  $n_{ph}$  to an electronically low lying

<sup>2</sup>for example  $\omega_{rad}(4P_{1/2})/2\pi = 2.61$  MHz,  $\omega_{rad}(30P_{1/2})/2\pi = 2.62$  MHz,  $\omega_{rad}(62P_{1/2})/2\pi = 3.73$  MHz for one specific choice of trap operation parameters [Li]

state  $|e, m_{ph}\rangle$ , the resonance is split into a carrier ( $n_{ph} = m_{ph}$ ) at frequency  $\nu_0$  and multiple sidebands ( $n_{ph} \pm \Delta n_{ph} = m_{ph}$ ) at frequencies  $\nu_{sb} = \nu_0 \pm \Delta n_{ph} \times \omega$ . For Doppler cooling temperatures and typical potentials in Paul traps, only a small number of sidebands are present. In contrast, Rydberg states are trapped in a modified potential giving rise to individual transition frequencies  $\nu_{nm}$  for every combination of  $n_{ph}$  and  $m_{ph}$ . The complex resonance structure is illustrated in Fig. 2.5. In order to mitigate this complication, a laser beam with wave vector  $\mathbf{k}$  parallel to the trap axis, coupling only to the axial motion, is best suited for the excitation of trapped ions to Rydberg states as the axial potential is modified only marginally.

### 2.2.3. Coulomb crystals with ions in Rydberg states

In the preceding section we derived fundamental properties of Rydberg ions. We will now discuss the effects of the key features on trapped Coulomb crystals of ions. We start with a discussion of the modified potential which is unique to trapped ions.

Multiple ions, confined in a Paul trap, repel each other due to the Coulomb interaction between charged particles. For low temperatures, as typically reached in experiments with laser cooling this leads to the formation of Coulomb crystals [Win87]. In these crystals, ions have fixed equilibrium positions with inter ion distances of about  $d_{ion} = 3\mu\text{m} - 15\mu\text{m}$ . Ions are structured in 1-D, 2-D or 3-D crystals, depending on the ratio between the potentials  $\omega_x$ ,  $\omega_y$  and  $\omega_z$  as well as the number of ions. The strong Coulomb interaction between individual ions lead to collective vibrational modes similar to phonons in solid state systems. These collective phonon modes provide a versatile tool for controlled interactions between individual ions and thus are of great interest in quantum simulation and quantum information experiments.

Both, the structure and the phonon modes depend on the potential of each individual ion. Exciting one or multiple ions to Rydberg states modifies its potential and changes global properties of the Coulomb crystal.

**Spacial structure of Coulomb crystals** In general the potential energy of a Coulomb crystal with  $N$  ions in the pseudo potential of a Paul trap is given by the sum over each ion's energy in the external potential plus the sum over the pairwise Coulomb potential between all ions [Jam98].

$$E_{pot} = \sum_{i=1}^3 \sum_{k=1}^N \frac{1}{2} m_k \omega_{k,i}^2 r_{k,i}^2 + \sum_{k,l=1, k \neq l}^{N,N} \frac{Q_k Q_l}{8\pi\epsilon_0} \left[ \sum_{i=1}^3 (r_{k,i} - r_{l,i})^2 \right]^{-\frac{1}{2}} \quad (2.38)$$

Here,  $m_k$ ,  $Q_k$ ,  $\omega_k$  and  $r_k$  denote mass, charge, vibrational frequency and position with respect to the trap center of ion  $k$  respectively. In this equation, no assumptions about uniformity of mass, charge and trapping potential for the ions are made. We are particu-

larly interested in the case of uniform mass and charge but modified radial potentials  $\omega_{k,x}$  and  $\omega_{k,y}$  for selected ions.

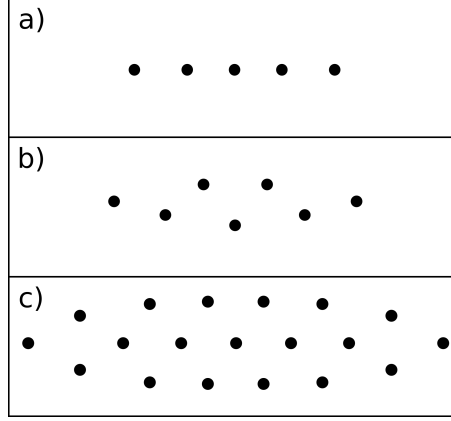


Figure 2.6.: Simulated Coulomb crystals in a potential of  $\omega_z/2\pi = 400$  kHz,  $\omega_x/2\pi = 1$  MHz and  $\omega_y/2\pi = 2.5$  MHz. Increasing the number of ions in the trap induces structural phase transitions from a) a linear 5 ion string to b) a 7 ion zigzag crystal to c) a planar crystal with 19 ions. The strong radial anisotropy restricts ions in a two dimensional plane along  $z$  and  $x$ .

The equilibrium positions of the ions can be determined by calculating the minimum value of  $E_{pot}$ . For typical operation parameters of a linear Paul trap with  $\omega_z \ll \omega_{x,y}$  and few ions, linear strings of ions are formed. Above a threshold [Enz00]

$$\gamma_{crit} = \left( \frac{\omega_z}{\omega_{x,y}} \right)^2 = 2.94(7) \times N^{-1.80(1)} \quad (2.39)$$

a structural transition into a zigzag configuration occurs [Kau12]. Adding even more ion leads to extended 2-D structures as shown in Fig. 2.6 or 3-D crystals [Dre98].

**Modification of the spacial structure by Rydberg ions** Rydberg excitation of ion  $k$  leads to a modified potential  $\omega_{k,i}$  in Eq. 2.38, which in turn leads to a spatial redistribution of the ions. For an anisotropy parameter  $\gamma \approx \gamma_{crit}$  (see Eq. 2.39) the crystal's structure is very sensitive to small changes in the potential. Rydberg excitation of a single ion may induce a structural phase transition. Thus, Rydberg excitation of ions couples the internal state of one ion with the global structure of the ion crystal [Li12] (see chapter 1). In contrast to other impurities like ions with different charge-to-mass ration, the modified potential can be switched by coherent excitation with lasers. In principle, even coherent superpositions of states are possible [Bal12].

**Phonon modes of Coulomb crystals** Thermal energy leads to small oscillations of the ions around their equilibrium position  $\mathbf{r}_k(t) = \mathbf{r}_k^{(0)} + \boldsymbol{\epsilon}_k(t)$ . The vibrations of the individual ions are coupled due to Coulomb interaction, giving rise to collective phonon modes.  $3N$  orthogonal modes exist in a  $N$  ion Coulomb crystal. The Lagrangian of the system reads [Jam98]:

$$\mathcal{L} = \frac{m}{2} \sum_{i=1}^3 \left[ \sum_{k=1}^N (\dot{\epsilon}_{k,i})^2 - \frac{1}{2} \sum_{k,l=1}^N \epsilon_{k,i} \epsilon_{l,i} \left[ \frac{\partial^2 E_{pot}}{\partial x_{k,i} \partial x_{l,i}} \right]_{\epsilon_k = \epsilon_l = 0} \right] \quad (2.40)$$

For a homogenous crystal this expression can be written down explicitly in terms of coupling matrices for radial and axial oscillations [Jam98]. In general one finds that a crystal of  $N$  ions has  $3N$  orthogonal modes of vibration each oscillating at its individual eigenfrequency. For a linear homogenous crystal along the  $z$ -axis, the lowest frequency mode in axial  $z$ -direction and the highest frequency modes in radial  $x$ - and  $y$ -direction consist of in phase oscillation of all ions. All other modes consists of pairwise oscillation with opposite phase, thus canceling out any center-of-mass oscillation of the crystal.

**Modified phonon modes in Coulomb crystals with Rydberg excitations** For Coulomb crystals with Rydberg impurities, which lead to modified radial potentials  $\omega_x$  and  $\omega_y$  for selected ions, Eq. 2.40 may be solved numerically. The obtained radial mode structure can vary widely depending on the vibrational frequencies, the positions and the number of impurities. However, in general two effects are observed: First, the impurity breaks the symmetry of the system, leading to a modified set of eigenmodes. A center-of-mass mode does not exist, but instead multiple modes feature center-of-mass oscillation. Secondly, the coupling of radial oscillation between ions featuring different  $\omega_{x,y}$  is rather weak which leads to localized modes around the impurity or modes which are constrained by impurities. Thus, impurities (e.g. Rydberg excitations) can be used to create specific modes of vibration. We call this method mode-shaping. Examples for linear crystals are shown in Fig. 2.7. The technique is not limited to ion strings but can be used in larger 2-D crystals as well [Nat15] (see chapter 1 and section 5.5.4).

**Dipole-dipole interaction in Coulomb crystals** Concerning the dipole blockade, the situation in an ion trap is very similar to the case of neutral atoms in a periodic trapping potential: Single particles are trapped at a fixed distance  $R$ . In a linear string of ions the minimal distance is given by [Jam98]

$$R_{min} = \left( \frac{Q^2}{4\pi\epsilon_0 m \omega_z^2} \right)^{1/3} \times \frac{2.018}{N^{0.559}} \quad (2.41)$$

For  $^{40}\text{Ca}^+$ ,  $\omega_z/2\pi = 1$  MHz and  $N = 2$  ions, we obtain  $R = 6 \mu\text{m}$ . For distances of this magnitude and Rydberg states accessible in an ion trap the interaction is typically in the

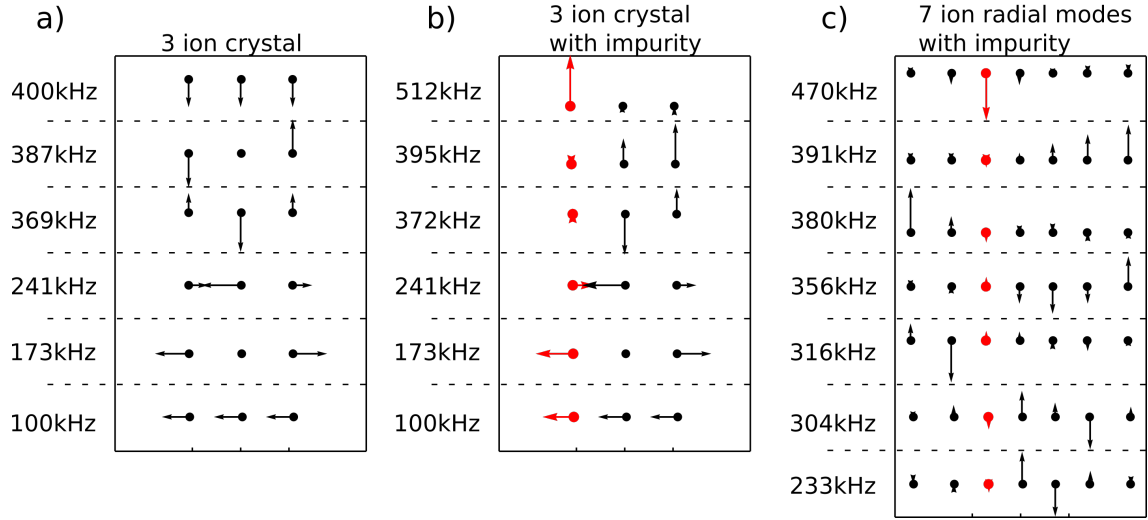


Figure 2.7.: a) Vibrational modes of a three ion crystal without impurity. b) Modes in a crystal with impurity. The impurity is marked by a red dot, arrows indicate amplitude and phase of the oscillation. The vibrational frequencies for a single  $^{40}\text{Ca}^+$  ion are  $\omega_z/2\pi = 100$  kHz,  $\omega_x/2\pi = 400$  kHz and  $\omega_y/2\pi = 600$  kHz. The radial vibrational frequency of the impurity is increased by 30% while the axial potential is unchanged. For the radial modes (x-direction), the oscillation amplitude is large either on the impurity (512 kHz) or on the normal ions (395 kHz and 372 kHz). Due to the broken symmetry all of the radial modes feature some center-of-mass oscillation. c) The radial modes of a seven ion crystal are shown. For the highest frequency mode, the oscillation amplitude is located at the impurity ion (large amplitude) and the adjacent  $^{40}\text{Ca}^+$  ions (smaller amplitudes). The other six modes are located either on one or on the other side of the impurity.

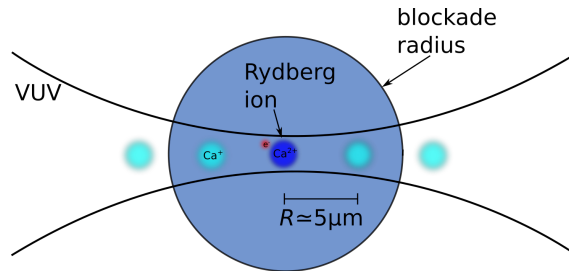


Figure 2.8.: Illustration of the Rydberg blockade in an ion trap. The blockade radius has to be larger than the inter ion distance  $R$  which is typically about  $5 \mu\text{m}$ . Inside the blockade radius, only a single ion can be excited to the Rydberg state.



van-der-Waals ( $\Delta \propto 1/R^6$ ) regime. The interaction energies obtained are  $\Delta/2\pi < 50$  kHz [Li13], which does not allow for high fidelity blockade. Tuning of Förster resonances or the generation of states with a permanent dipole moment would result in  $\Delta \propto 1/R^3$  and interaction energies in the order of  $\Delta/2\pi \approx 10$  MHz. However, Förster tuning with static electric fields is not possible in the case of ions, as the charged particles will always move to a field free position. Instead, microwave dressing of Rydberg states is proposed to generate strong dipole-dipole interaction between ions [Li13]. Here, the transition between two Rydberg states  $|n1, l1\rangle$  and  $|n2, l2\rangle$  is strongly driven with resonant microwave radiation. This results in dressed states  $|+\rangle$  and  $|-\rangle$  with a permanent dipole moment. The interaction between two nearby ions in these dressed states is similar to the interaction in case of a Förster resonance. The interaction strength may exceed  $2\pi \times 1$  MHz for an inter ion distance of  $6 \mu\text{m}$  [Li13].

### 2.3. Atomic properties of $^{40}\text{Ca}^+$ ions

With only one loosely bound valence electron while the other electrons form stable closed shells, the part of the electronic level structure of  $^{40}\text{Ca}^+$  which is accessible by laser illumination is simple. In most experiments working with  $^{40}\text{Ca}^+$ , solely the ground state  $4S_{1/2}$ , the metastable  $3D_j$  states and the short lived  $4P_j$  states are populated. The relevant states for our experiments, are these electronically low lying states together with the Rydberg manifolds  $nP_j$  and  $nF_j$ , depicted in Fig. 2.9.

Property	Value
Ionization threshold	95 752 $\text{cm}^{-1}$ (104.4 nm)
Ion. energy from $3D_{3/2}$	82 102 $\text{cm}^{-1}$ (121.9 nm)
Ion. energy from $3D_{5/2}$	82 041 $\text{cm}^{-1}$ (121.8 nm)
Quantum defect $\delta_S$	1.80
Quantum defect $\delta_P$	1.44
Quantum defect $\delta_D$	0.62
Quantum defect $\delta_F$	0.026

Table 2.2.: Ionization energy [Nat16] and Quantum defects [Dje91] for  $^{40}\text{Ca}^+$ .

One particular feature of  $^{40}\text{Ca}^+$  is the large quantum defect of the  $S$  state which leads to an inverted level structure with the  $4S$  state energetically below the  $3D$  states. Thus, the  $3D$  states have no dipole allowed decay channel, which leads to a very long lifetime ( $\tau \approx 1$  s) of these states. Apart from being ideally suited for quantum logic operations, they can be used as initial states, effectively lowering the energy gap that has to be bridged for Rydberg excitation to  $\lambda \approx 122$  nm.  $^{40}\text{Ca}^+$  has zero nuclear spin and thus no hyperfine splitting is observed. In a magnetic field  $B$ , the Zeeman effect lifts the degeneracy of the various  $m_j$  states which leads to a substructure of  $2j + 1$  Zeeman levels with a frequency

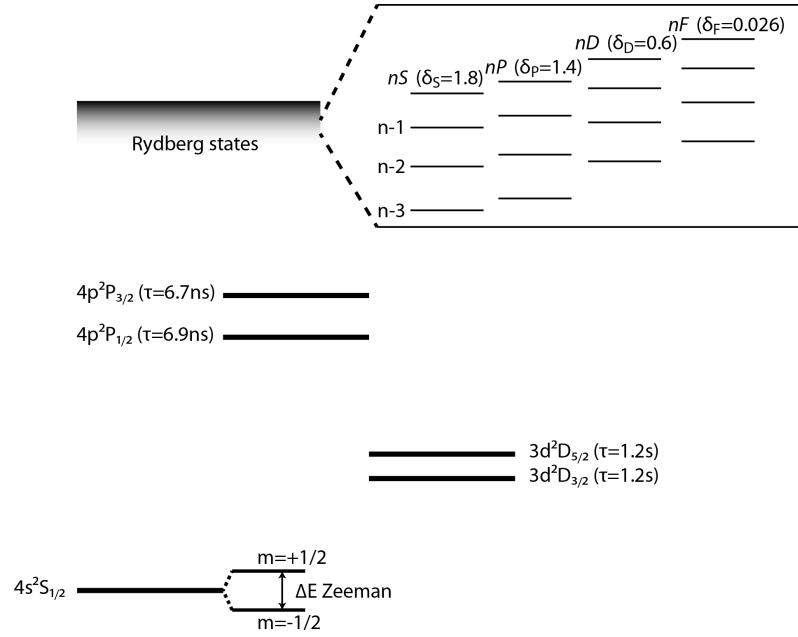


Figure 2.9.: Relevant part of the level scheme of  $^{40}\text{Ca}^+$ . The electronically low lying states are used for cooling, detection, spectroscopy and state preparation. The transition to the short lived  $4P_{1/2}$  state is ideally suited for Doppler cooling and fluorescence detection. The long lived  $3D_j$  states serve as initial states for the Rydberg excitation. The inset shows the Rydberg states with  $l \leq 3$  and their quantum defects. Starting from the  $3D_j$  states we can excite the  $nP$  states and  $nF$  states.

splitting of  $\Delta E = B \times \mu_B \times g_j/h$  with the Bohr magneton  $\mu_B$  and the Lande  $g$  factor  $g_j$ .

The dipole transition  $4S_{1/2} \rightarrow 4P_{1/2}$  at a wavelength of 397 nm is excited with a red detuned laser for Doppler cooling and fluorescence detection of the ion. Scattered photons can be detected with a camera or a photo-multiplier-tube. The  $4P_{1/2}$  state decays to the  $3D_{3/2}$  state with  $p = 0.06435(7)$  [Ram13]. The transition  $3D_{3/2} \rightarrow 4P_{1/2}$  at a wavelength of 866 nm is driven to prevent population from being trapped in the long lived  $3D_{3/2}$  state. The  $3D_{5/2}$  state does not scatter photons during illumination with light at wavelength of 397 nm and 866 nm. This allows for a state sensitive fluorescence detection which distinguishes between ions in the  $3D_{5/2}$  state (dark) and ions in the  $4S_{1/2}$  and  $3D_{3/2}$  states (bright). This scheme allow for the detection of population transfer and is used for the detection of Rydberg excitation (see chapter 6).

The energies of the Rydberg states are determined by the ionization threshold and the quantum defects summarized in Tab. 2.2. Initialization in the metastable  $3D$  states, reduces the energy required for Rydberg excitation significantly. The ionization energies and corresponding wavelengths when starting from the  $3D$  states are added in Tab. 2.2. The radiative lifetimes of Rydberg states of  $^{40}\text{Ca}^+$  can be parametrized [Glu13] as

$$\tau_{n,l} = \tau_l^{(0)} \times n^3 \times \left( 1 + \frac{\tau_l^{(1)}}{n} + \frac{\tau_l^{(2)}}{n^2} + \frac{\tau_l^{(3)}}{n^3} \right). \quad (2.42)$$

The coefficients  $\tau_l^{(i)}$  for  $S$ ,  $P$ ,  $D$  and  $F$  states are given in Tab. 2.3. For Rydberg  $F$  states, lifetimes are in the order of  $\tau \approx 1 \mu\text{s}$ . The radiative lifetime of  $nP$  states is about two orders of magnitude longer. Blackbody radiation is not taken into account by Eq. 2.42 but is expected to have an impact on the lifetime of high lying Rydberg states. Particularly the lifetime of the long live  $nP$  states might be drastically reduced<sup>3</sup>. The transition dipole matrix element to the  $3D$  state can be approximated as [SK11]

$$\mu_{3DnP} = 0.383e \times r_B \times n^{-1.588}, \quad (2.43)$$

with elementary charge  $e$  and Bohr radius  $r_B$ . The dipole matrix element  $\mu_{3DnF}$  for the transition from the  $3D_j$  states to the  $nF$  manifold is about ten times stronger [Li] which corresponds to the shorter lifetime. The Rydberg manifolds  $nS$  and  $nD$  can not be excited from the metastable  $D$  states by a single photon. However they might be excited by two-photon excitation or coupled to the  $nP$  or  $nF$  states by microwave fields. Their lifetimes are about five times longer as compared to the  $nF$  states.

Next to the radiative lifetime, a key parameter is the polarizability of the Rydberg state.  $^{40}\text{Ca}^+$  ions provide state with negative ( $P$ ) and positive polarizability ( $S, D, F$ ). The

<sup>3</sup>We do not have calculations for the lifetime of  $^{40}\text{Ca}^+$  Rydberg states, but from calculations for Rydberg states of neutral alkali-metals we conclude that for Rydberg states with zero temperature lifetime of  $\tau \approx 200 \mu\text{s}$  ( $51P$ ) the lifetime is reduced to about  $\tau = 60 \mu\text{s}$ – $100 \mu\text{s}$  [Bet09]. For states with shorter lifetimes the effects of blackbody radiation are less important

## 2. Theoretical foundations

---

<b>Series</b>	$\tau^{(0)}/ns$	$\tau^{(1)}ns$	$\tau^{(2)}/ns$	$\tau^{(3)}/ns$
$nS$	0.052893	-5.426	13.097	-8.2753
$nP$	1.6187	-3.29	53.02	-520.2
$nD$	0.065904	-1.867	4.704	2.518
$nF$	0.017766	-0.067052	4.1701	-2.6093

Table 2.3.: Parameters for the calculation of radiative lifetimes of Rydberg states of  $^{40}\text{Ca}^+$  according to [Glu13].

polarizability depends strongly on the energetic separation of the state, thus the  $nF$  states, with a quantum defect of  $\delta_F = 0.026$  only, have a much higher polarizability compared to the energetically well isolated states with  $l < 3$ . The polarizability  $\alpha$  of the  $52F$  state [Fel15] is given in Tab.2.4. We use the quantum defects found in [Dje91] and the method developed in [Kos85] to obtain approximate analytical wave functions for computing matrix elements. In the second-order perturbation theory, we set  $m_L = 0$ , which is justified as this state experiences the largest Stark shift for the states of interest. Values for other principal quantum numbers can be estimated with the scaling laws from section 2.1.

<b>State</b>	$\tau (\mu s)$	$\alpha/2 \text{ (MHz/(V/cm)}^2\text{)}$
$52F$	2.5	400
$51P$	204	-37

Table 2.4.: Radiative lifetime  $\tau$  [Glu13] and polarizability  $\alpha$  [Kam14, Fel15] for the Rydberg states  $51P$  and  $51F$ .

The relevant part of the Stark map of  $^{40}\text{Ca}^+$  around the energy of the state  $51F$  is shown in Fig. 2.10. The polarizability of the  $51F$  state is mainly determined by coupling to the close by  $51G$  state. Up to an electric field of 3 V/cm the  $F$  state is well isolated from the  $G$  state and states with  $l > 4$ . Typical fields in the ion trap are below 1 V/cm. The  $nS$ ,  $nP$  and  $nD$  states are energetically by far more isolated due to their larger quantum defect.

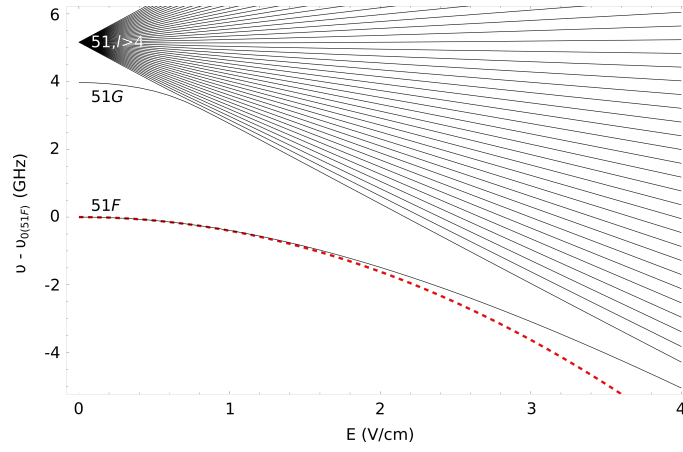


Figure 2.10.: Relevant part of the Stark map of  $^{40}\text{Ca}^+$ . In an electric field, adjacent states are mixed and the Stark eigenstates (black) are generated. Up to a field of 3 V/cm the state corresponding to the  $51F$  state is energetically isolated. For small fields the energy shift is quadratic to the electric field.



## 3. Experimental setup

The experimental setup for the provision of cold  $^{40}\text{Ca}^+$  ions for Rydberg excitation consists of a Paul trap (see chapter 4) inside an ultra high vacuum setup and the required lasers with wavelength in the visible and infrared spectrum. We designed and built this setup and joined it with an existing continuous wave, coherent VUV source which was optimized to provide radiation near 122 nm wavelength for single photon Rydberg excitation of  $^{40}\text{Ca}^+$  ions.

### 3.1. Laser sources for photo-ionization, Doppler cooling, detection and state manipulation

Several laser sources with wavelength in the visible and infrared spectrum are required for ionizing neutral calcium atoms as well as cooling, detection and manipulation of ions inside the Paul trap. The requirements for the lasers depend on their application in the experiment. For the excitation of dipole allowed transitions powers of  $P < 100 \mu\text{W}$  with beam waists of  $w_0 \approx 100 \mu\text{m}$  are sufficient to saturate the transition while illuminating the Coulomb crystal homogeneously. Only moderate frequency stability is required as the resonance width of the respective transitions is  $\Gamma/2\pi \gg 1 \text{ MHz}$ . These beams are easily provided by external cavity diode lasers. On the other hand optical powers of  $P = 1 - 10 \text{ mW}$  and very good frequency stability are needed for coherent operations on the quadrupole transition demanding a more elaborate laser system based on a titanium-sapphire laser.

#### 3.1.1. Photo-ionization of neutral calcium

The Paul trap is loaded by ionizing calcium atoms from a thermal beam. Originally, non-resonant multi-photon ionization with a pulsed laser at 532 nm wavelength<sup>1</sup> was used as illustrated in Fig. 3.1 a. A frequency doubled, Q-switched Nd:YAG laser generates 4 ns pulses with pulse energies up to 12 mJ at a repetition frequency of 10 Hz. While working very stable due to the non-resonant nature of the process and reasonable efficient because of the high intensity in the laser pulse, this scheme has two major disadvantages: First, the required pulse energies of about 10 mJ involve the risk of damaging the ion trap if the laser is not aligned correctly and secondly, all atoms and molecules with a sufficiently low

---

<sup>1</sup>Minilite 1; Continuum lasers

ionization energy are ionized and thus loaded into the Paul trap. While the second point is irrelevant if the trap is operated at pressures  $p \leq 10^{-10}$  mbar, the danger of damaging the trap convinced us to switch to a resonant two photon excitation scheme when we installed the segmented ion trap (T2) made out of gold coated ceramic blades described in section 4.2.

With continuous wave lasers at 423 nm wavelength, resonantly exciting the  $4S \rightarrow 4P$  transition, and 375 nm wavelength, exciting from the  $4P$  state to the ionization continuum, optical powers of  $P = 0.5$  mW are sufficient for efficient photo-ionization. The laser beams are overlapped, coupled into a common single mode fiber<sup>2</sup> and focused by a pair of achromatic doublets<sup>3</sup> into the trap. With optical powers of  $500 \mu\text{W}$  in each beam, focused to  $w_0 \approx 20 \mu\text{m}$ , and an oven current of  $I_{\text{oven}} = 5$  A, we load about 2 ions per minute. We do not observe charging of trap electrodes by the laser radiation. The laser beams are switched by a TTL controlled mechanical shutter [Sin02].

Radiation at 423 nm wavelength is provided by a home built grating stabilized external cavity diode laser<sup>4</sup> in Littrow configuration [Nab12]. Laser diode and external resonator are temperature stabilized, the grating angle is controlled by a micrometer screw<sup>5</sup> and a piezo<sup>6</sup>. The diode is protected against back reflected light with an optical isolator<sup>7</sup>. Detailed information about the resonator mechanics and the electronics for current supply and temperature stabilization<sup>8</sup> can be found in Appendix B. The resonance of the  $4^1S_0 \rightarrow 4^1P_1$  transition is Doppler broadened to  $\sigma \approx 1$  GHz. From the  $4^1P_1$  state, the atoms can be ionized with light at wavelengths  $\lambda < 390$  nm. This transition is not very sensitive to the exact wavelength of the light field, consequently a free running laser diode is used for the generation of radiation near a convenient wavelength of 375 nm<sup>9</sup>.

#### 3.1.2. Diode lasers for cooling, detection and optical pumping

Once we have loaded  $^{40}\text{Ca}^+$  ions into the trap, we want to cool them as well as manipulate and detect their electronic state. The employed transitions near wavelenths of 393 nm, 397 nm, 729 nm, 854 nm and 866 nm are indicated in the  $^{40}\text{Ca}^+$  level scheme in Fig.3.1b.

For Doppler cooling, the transition  $4S_{1/2} \rightarrow 4P_{1/2}$  is excited with a red detuned laser. From the  $4P_{1/2}$  state, ions decay either back to the  $4S_{1/2}$  ground state (probability  $p = 0.93565$  [Ram13]) or to the metastable  $3D_{3/2}$  state ( $p = 0.06435(7)$  [Ram13]). A laser at 866 nm wavelength prevents population from being trapped in the long lived  $3D_{3/2}$  state ( $\tau = 1176(11)$  ms [Kre05]). Ions are detected by imaging their fluorescence light at 397 nm

---

<sup>2</sup>PMC-360SI-2.3-NA012-3-APC-150-P, 60FC-F-4-A6.2S-52; Schäfter + Kirchhoff

<sup>3</sup>ACA254-150-A; Thorlabs

<sup>4</sup>LD 0425 0120, 120mW; Toptica

<sup>5</sup>3/16"-100 Ultra-Fine; Thorlabs

<sup>6</sup>Pst 150/4/5 bs; Piezomechanik GmbH

<sup>7</sup>FR 488/5 S/N 307, 420nm-520nm; GSÄNGER

<sup>8</sup>HTC 1500; wavelength electronics

<sup>9</sup>NDU 4116, 70mW; Nichia



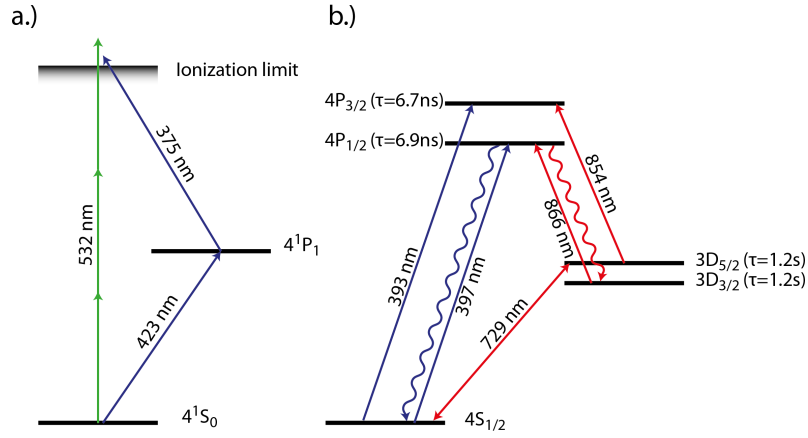


Figure 3.1.: a) Photo ionization of neutral calcium. We use either a non-resonant three-photon process at 532 nm wavelength, or a resonant two-photon scheme. The  $4^1S_0 \rightarrow 4^3P_1$  is excited resonantly with light at 423 nm wavelength before the atom is ionized by a photon at 375 nm wavelength. b) Relevant transitions and wavelength in  $^{40}\text{Ca}^+$ . For Doppler cooling and fluorescence detection, the transitions  $4S_{1/2} \rightarrow 4P_{1/2}$  at a wavelength of 397 nm and  $3D_{3/2} \rightarrow 4P_{1/2}$  at 866 nm wavelength are used. Transitions at wavelengths of 393 nm and 854 nm are used for optical pumping into and out of the  $3D_{5/2}$  dark states. We coherently excite the  $4S_{1/2} \leftrightarrow 3D_{5/2}$  quadrupole transition with light at 729 nm wavelength.

### 3. Experimental setup

---

wavelength to an EMCCD camera (see section 3.2). Since ions in the metastable  $3D_{5/2}$  state do not scatter photons during illumination with light at wavelengths of 397 nm and 866 nm the detection is state selective.

Population can be transferred to the  $3D_{5/2}$  state either directly from the ground state, exciting the quadrupole transition at 729 nm wavelength (see section 3.1.3), or by optical pumping via the  $4S_{1/2} \rightarrow 4P_{3/2}$  transition at 393 nm wavelength followed by a decay to the  $3D_{5/2}$  state. For initialization into the ground state, the two infrared lasers at wavelengths of 854 nm and 866 nm are employed, driving the transitions  $3D_{5/2} \rightarrow 4P_{3/2}$  and  $3D_{3/2} \rightarrow 4P_{1/2}$  respectively.

The light-fields required for the excitation of dipole allowed transitions are generated by grating stabilized diode lasers in Littrow configuration. Two Toptica DL pro lasers at 393 nm<sup>10</sup> and 397 nm<sup>11</sup> wavelength and two home built lasers at 854 nm<sup>12</sup> and 866 nm<sup>13</sup> wavelength (see appendix B) provide optical powers of about 10 mW each. The mechanics and electronics of the infrared lasers are equivalent to the laser described in section 3.1.1. Additionally, they possess two modulation inputs for the diode current required for Pound-Drever-Hall frequency stabilization. With a control voltage at these inputs the current can be modulated by a JFET based circuit from DC to 5 MHz (input 1) and by a bias-Tee designed for frequencies around 25 MHz (input 2). The diodes at 393 nm, 397 nm and 866 nm wavelength are protected against back reflection by optical isolators. All wavelengths are monitored by a wavelength meter<sup>14</sup> with an accuracy of 10 MHz for the infrared and 100 MHz for the blue wavelengths. Long-term drifts of the lasers are compensated automatically by an active frequency stabilization loop based on the wavelength meter measurement.

In order to perform cooling close to the Doppler limit the radiation at 397 nm wavelength should be detuned by  $-\Gamma/2 \approx -2\pi \times 10$  MHz with respect to the  $4S_{1/2} \rightarrow 4P_{1/2}$  transition. Thus, the frequency fluctuation of the laser should be well below a fraction of  $\Gamma/2$  which is realized by stabilizing the lasers at 397 nm and 866 nm wavelength to a medium finesse cavity as illustrated in Fig. 3.2 using a Pound-Drever-Hall (PDH) locking scheme. The cavity consists of mirrors with a reflectivity of 99%<sup>15</sup> at a distance of 100 mm resulting in a finesse of  $\mathcal{F} \approx 300$  and a free spectral range of FSR = 1500 MHz. The mirrors are glued to a low thermal expansion Zerodur<sup>16</sup> spacer. One mirror is mounted on a piezo stack, which enables the tuning of the resonance to the desired wavelength. The piezo stack consists of two ring piezos<sup>17</sup> and is constructed in a way that the thermal expansion of the

---

<sup>10</sup>LD-0395-0120-1, 13mW; Toptica

<sup>11</sup>LD-0397-0030-1, 13mW; Toptica

<sup>12</sup>HL8342MG, 50mW, 852nm; opnext

<sup>13</sup>LD-0870-0100-2, 100mW; Toptica

<sup>14</sup>wavelength meter WSU-10 (infrared) and wavelength meter WSU-7 (blue); Toptica

<sup>15</sup>99% reflectivity for 397nm and 866nm, one curved, one flat; Layertec

<sup>16</sup>ZERODUR; Schott AG

<sup>17</sup>OD18.3, ID16.7, L4 PZ26 Tubes and OD24.4, ID22.4, L4 PZ26 Tubes; Ferroperm piezoceramics

piezos is self-compensating. The piezos are connected to high voltage sources<sup>18</sup> and allow for frequency tuning of the cavity mode over a complete free spectral range. The cavity is positioned in a vacuum housing pumped by a mini ion-getter pump<sup>19</sup> to a pressure of about  $10^{-6}$  mbar. The outside of the stainless steel vacuum vessel is temperature stabilized reducing the long term frequency drift of the cavity.

We generate an error signal by modulating the laser current via the bias-Tee with a voltage controlled oscillator (VCO)<sup>20</sup>, detect the reflected light with a high bandwidth photo-diode<sup>21</sup> and analyze the photo-diode signal with a phase detector<sup>22</sup>. We feed the error signal into a home built, two channel PI-regulator described in appendix B. One channel controls the voltage at the piezo, adjusting the grating angle in the laser and the length of the external cavity, while the other one modulates the diode current, allowing for a high control bandwidth. A laser line-width of well below 1 MHz is achieved with this frequency stabilization which is fully sufficient for all operations on dipole transitions.

The laser beams are switched by acousto-optic modulators<sup>23</sup> (AOMs) ensuring fast switching times  $< 1 \mu\text{s}$  and high repetition rates. The radio-frequency for the operation of the AOMs is provided by VCOs<sup>24</sup>, switched by TTL controlled rf-switches<sup>25</sup> and amplified to 1 W<sup>26</sup> or 2 W<sup>27</sup> for the AOMs working with infrared or blue light respectively. The AOMs switching the beams at 393 nm, 397 nm (Doppler), 854 nm, respectively 866 nm are setup in double pass configuration. The high switching contrast enabled by the double pass configuration ( $P_{on}/P_{off} \approx 10000$ ) is mandatory to ensure that population is not transferred between different quantum states by residual light of a switched off beam. The diffraction efficiency of the AOMs<sup>28</sup> is less important as we require powers of only  $P \approx 100 \mu\text{W}$  at the ion. The AOM switching the  $\sigma$ -polarized beam at 397 nm wavelength is setup in single pass configuration.

The beams are overlapped and coupled into common single mode polarization maintaining fibers (see Fig.3.2) as follows: Beams at 397 nm ( $\sigma$ -pumping) and 393 nm wavelength are overlapped at a polarization beam splitter cube (PBS) and coupled into a common fiber<sup>29</sup>; beams at a wavelength of 854 nm and 866 nm are superimposed at a 50:50 beam-splitter, the resulting beam is subsequently combined with the beam at 729 nm wavelength

<sup>18</sup>PSM10/202P+, HighTek and miniPIA 103; TEM Messtechnik

<sup>19</sup>21/s pump; Varian

<sup>20</sup>ZOS-50+, mini-circuits

<sup>21</sup>1801, DC-125MHz, visible; New Focus (397nm) and home built (866nm)

<sup>22</sup>ZRPD-1+, mini-circuits

<sup>23</sup>BRI-QFZ-80-20-395 (blue) and BRI-TEF-80-20-860 (infrared); Brimrose

<sup>24</sup>ZOS-100+, mini-circuits

<sup>25</sup>ZYSW-2-50DR, mini-circuits

<sup>26</sup>ZHL-3A-S+; mini-circuits

<sup>27</sup>ZHL-1-2W-S; mini-circuits

<sup>28</sup>The AOMs for 397 nm and 393 nm wavelength are polarization sensitive. A double pass configuration where the light's polarization is rotated after the first passing reduces the diffraction efficiency to about 20%

<sup>29</sup>PMC-360SI-2.3-NA012-3-APC-150-P, 60FC-F-4-A6.2S-52, 60 FC-F-A6.2S-52; Schäfter + Kirchhoff

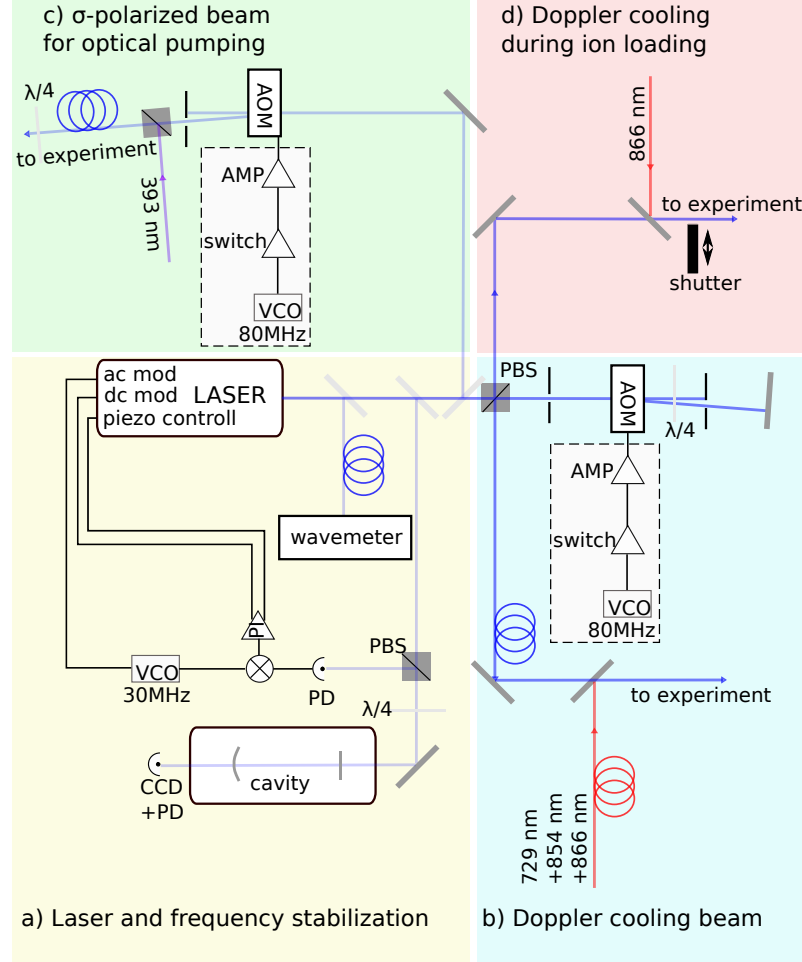


Figure 3.2.: Scheme of the laser-system used for generating light at 397 nm wavelength. a) The ECDL is frequency stabilized to a cavity of finesse  $\mathcal{F} = 300$  and monitored by a wavelength meter. The laser output is split into three beams which are delivered to the ion crystal individually, fully controlled by the experimental control computer. b) One for Doppler cooling and fluorescence detection, c) one for spin initialization and d) one for additional laser cooling during ion loading (d). The beams are switched either by AOMs (b and c) or by a mechanical shutter (d). The setup for the other wavelength is similar to parts (a and b).

at a PBS and coupled into a fiber<sup>30</sup>. The Doppler cooling beam at 397 nm wavelength is delivered to the experiment using a separate fiber<sup>31</sup> and overlapped with the infrared beams right in front of the vacuum chamber.

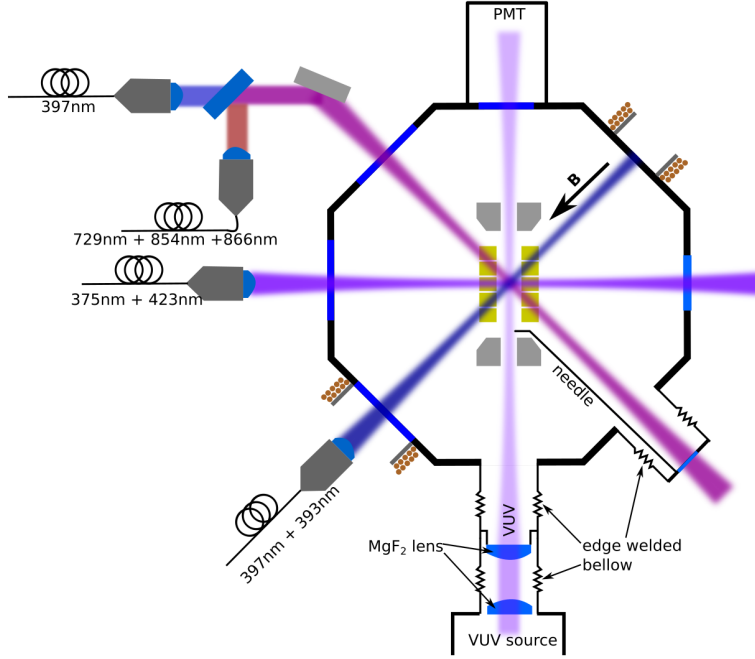


Figure 3.3.: Directions of laser-beams and magnetic field in the ion trap viewed from the top. The VUV beam propagates axially through the trap. Beams for Doppler cooling and optical pumping are delivered to the vacuum vessel by optical fibers and propagate parallel and perpendicular to the magnetic field, featuring a projection on all principal trap axes. The light at 729 nm wavelength is superimposed on the Doppler beam (beam path a), globally illuminating the ion crystal with coupling to all motional modes.

The light is focused onto the ion crystal with the fiber coupling optics. Light at 397 nm, 854 nm and 866 nm wavelength for Doppler cooling and optical pumping propagates perpendicular to the magnetic field and its wave vector  $\mathbf{k}$  exhibits a non-vanishing projection on all principle trap axes. An angle of  $\Theta_{ax,rad1,rad2} = (\pi/4, \pi/3, \pi/3)$  between trap axis and  $\mathbf{k}$  (see Fig. 3.3) provides optimal cooling of all motional modes of the ion.

The 397 nm beam is P-polarized driving  $\pi$ -transitions which keeps the magnetic broadening of the  $4S_{1/2} \rightarrow 4P_{1/2}$  transition used for Doppler cooling to a minimum. The beams at wavelengths of 854 nm and 866 nm are S-polarized, driving  $\sigma^+ + \sigma^-$ -transitions which

<sup>30</sup>PMC-780-5.2-NA012-2-APC-150P (selected fiber with cut-off 708nm), 60FC-F-4-M8-10, 60FC-L-4-M25-02; Schäfter + Kirchhoff

<sup>31</sup>PMC-360SI-2.3-NA012-3-APC-150-P, 60FC-F-4-A6.2S-52, 60 FC-F-A6.2S-52; Schäfter + Kirchhoff

### 3. Experimental setup

allows for efficiently pumping population out of all Zeeman-states of the metastable  $D$  states.

Circular polarized light fields at 393 nm and 397 nm wavelength come in parallel to the magnetic field. The former is used for initialization in one of the  $|4S_{1/2}, \pm 1/2\rangle$  spin states, the later is used for optical pumping to the  $3D_{5/2}$  state. The beams at 375 nm and 423 nm wavelength for photo-ionization propagate through the trap perpendicular to the trap axis.

Initial cooling of hot ionized calcium atoms into the trap, is enhanced with an additional cooling beam with optical power of ( $P \approx 1$  mW), red detuned by about 180 MHz. For this purpose a sample of the beam at 397 nm wavelength is picked up at the PBS in front of the switching AOM, overlapped at a dichroic mirror with a beam at 866 nm wavelength coming from the previously unused port of the 50:50 beam splitter and focused into the trap. This beam is switched by a mechanical shutter.

#### 3.1.3. Narrow bandwidth laser source at 729 nm wavelength

For driving coherent dynamics, resolving motional sidebands and cooling beyond the Doppler limit, the quadrupole transition  $4S_{1/2} \leftrightarrow 3D_{5/2}$  is excited by laser radiation near 729 nm wavelength. The exceptional long lifetime of the  $3D_{5/2}$  state of  $\tau = 1168(9)$  ms [Kre05] corresponds to a very narrow resonance line width.

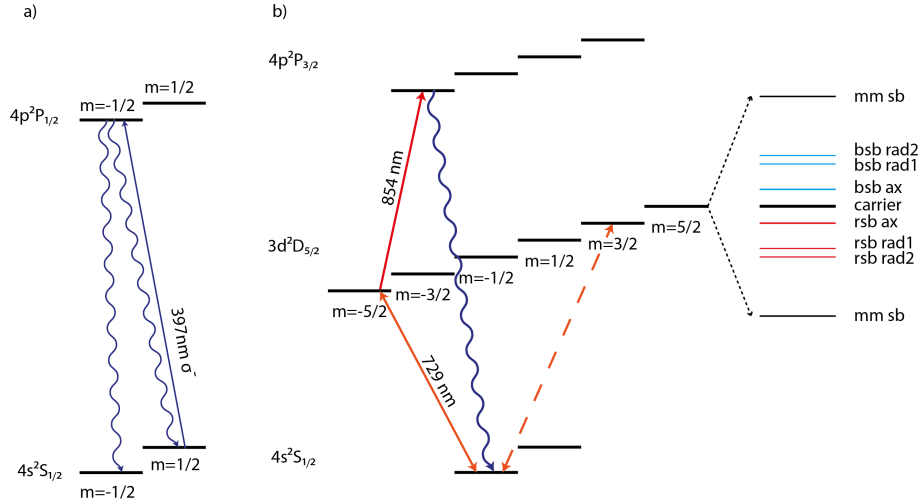


Figure 3.4.: a) Optical pumping into the  $|4S_{1/2}, -1/2\rangle$  state by  $\sigma$ -polarized light at 397 nm wavelength. b) Quadrupole transition  $4S_{1/2} \leftrightarrow 3D_{5/2}$  with Zeeman sub-states, motional sidebands and  $3D_{5/2} \rightarrow 4P_{3/2}$  transition for optical pumping. Our setup allows for excitation of all  $\Delta m = \pm 2$  transitions. Typically we use the  $|4S_{1/2}, -1/2\rangle \leftrightarrow |3D_{5/2}, -5/2\rangle$  transition. The lifetime of the  $3D_{5/2}$  state can be reduced by applying a quench pulse on the  $3D_{5/2} \rightarrow 4P_{3/2}$  transition.

In a magnetic field the  $4S_{1/2}$  and  $3D_{5/2}$  states split up into various Zeeman components

as shown in Fig. 3.4b. A quadrupole transition allows for  $|\Delta m| \leq 2$ , depending on the angle  $\Theta$  between  $\mathbf{k}$  and  $\mathbf{B}$  and the angle  $\Phi$  between the polarization and  $\mathbf{B}$ . Consequently up to 10 different resonances can be observed. Choosing  $\Theta = \pi/2$  and  $\Phi = \pi/2$ , reduces the possible transitions to  $|\Delta m| = 2$  [Roo00]. This configuration has two advantages; first the frequency separation of the remaining resonances is maximized and secondly the  $|\Delta m| = 2$  transitions provide a nearly closed cycle for sideband cooling [Roo99]. The population is initialized in the  $|4S_{1/2}, -1/2\rangle$  state by optical pumping with  $\sigma$ -polarized light at 397 nm wavelength (see Fig. 3.4a).

The spectrally narrow radiation at 729 nm wavelength is generated by a titanium-sapphire laser<sup>32</sup> pumped by a solid state disk laser with intracavity frequency doubling<sup>33</sup> and frequency stabilized to a high finesse cavity<sup>34</sup>. This laser generates light with an output power of about 1.8 W and a line width of  $\Delta\nu \ll 1$  kHz [Mac12].

The laser is shared by multiple experimental setups. It is not operated in the same laboratory as the Rydberg ion experiment, instead the light is delivered to the experiment by a 100 m long single mode fiber<sup>35</sup>. About 50 mW of optical power is delivered to the Rydberg ion experiment. The 100 m long optical fiber introduces phase noise by mechanical and acoustic vibrations in the fiber. In order to preserve the spectral quality of the light, a fiber noise cancellation [Pel13] has been setup, suppressing the noise introduced by the fiber by about 40 dB (see Fig. 3.6). For this purpose the frequency of the light is shifted by 75 MHz with an AOM before it is coupled into the fiber. Part of the light is back reflected and, after being transmitted through the fiber two times, overlapped with the incoming light. The beat signal measured by the photo-diode is given by the sum of the 150 MHz frequency-shift and the phase-noise introduced by the fiber. Phase-locking the beat signal to a stable oscillator at 150 MHz by controlling the AOM's drive frequency results in eliminating the phase noise introduced by the fiber (see Fig. 3.5).

We use an AOM<sup>36</sup>, operated at  $110 \pm 15$  MHz, in double pass configuration for switching, pulse shaping and frequency tuning of the light. The AOM is driven by an amplified<sup>37</sup> versatile frequency generator<sup>38</sup> allowing for amplitude, frequency and phase modulation during and between pulses. The exact pulse-form is transferred to the function generator via USB from the experimental control computer while the pulses are triggered by a TTL signal.

There are two beam-paths available for delivering the light to the ion. For path a the beam is overlapped with the infrared beams at 854 nm and 866 nm wavelength (see section 3.1.2) coupled into a fiber and focused into the ion trap. In this case  $\mathbf{k}$  is perpendicular to

---

<sup>32</sup>Matisse TX; Sirah

<sup>33</sup>Millennia Pro 15s; Spectra Physics

<sup>34</sup>6020 notched cavity  $\mathcal{F}=140000$ ; ATFilms

<sup>35</sup>PMC-630; Schäfter + Kirchhoff

<sup>36</sup>BRI-TEM-110-25-729; Brimrose

<sup>37</sup>ZHL-2-8S; mini-circuits

<sup>38</sup>vfg 150; Toptica

### 3. Experimental setup

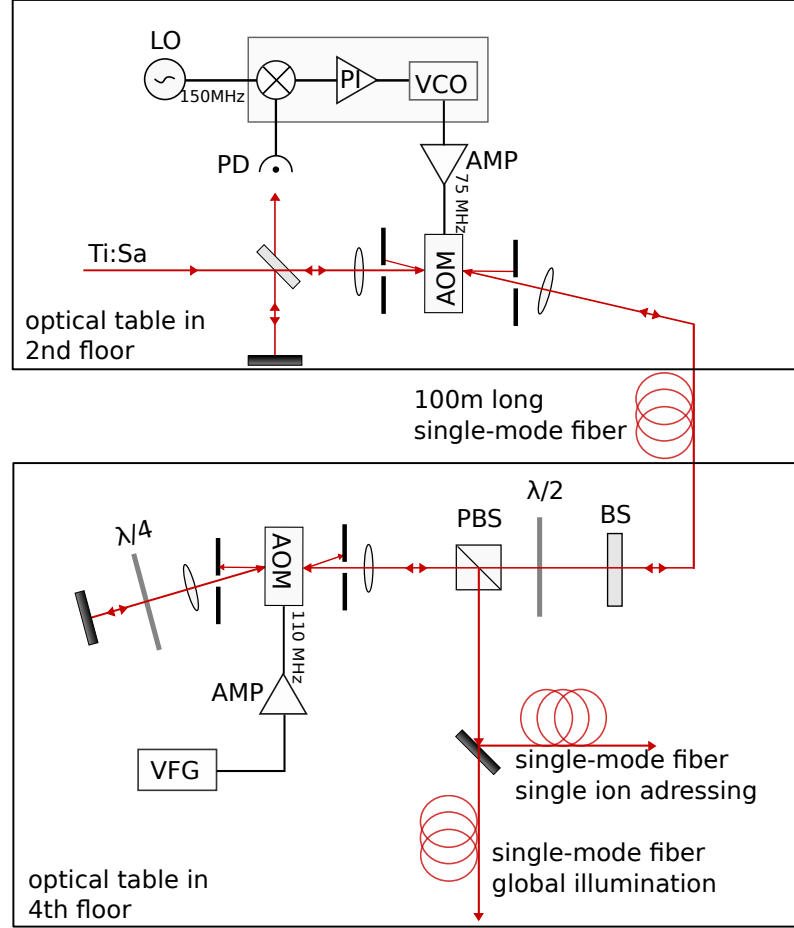


Figure 3.5.: Schematic drawing of the fiber noise cancellation and the pulse shaping setup for light at 729 nm wavelength. Parts of the setup are located on the second floor and connected to our lab on the fourth floor by a single mode fiber. For fiber noise cancellation a sample of the beam coming from the laser is reflected at an AR coated fused silica glass plate and focused on a high bandwidth photo-diode. The frequency of the light is shifted by 75 MHz with an AOM before it is coupled into the fiber. A small part of the transmitted light is reflected and coupled back into the fiber, shifted with the AOM by another 75 MHz, reflected by the same AR coated fused silica plate and overlapped with the non-shifted beam-sample. For switching and pulse shaping an AOM in double pass configuration is used. The pulses are created by an arbitrary wave form generator with USB connection to the experimental control PC. Two fibers deliver the light pulses to the experiment. Figure from Ref. [Pel13].



the magnetic field and has a projection on all principal axes of the trapping potential, which enables spectroscopy of all motional degrees of freedom. The beam waist of  $w_0 \approx 50 \mu\text{m}$  ensures global illumination of the Coulomb crystal. With optical power up to 15 mW, Rabi-frequencies in the order of  $\Omega_0/(2\pi) = 100 \text{ kHz}$  are achieved. We can sideband cool all motional modes using this beam.

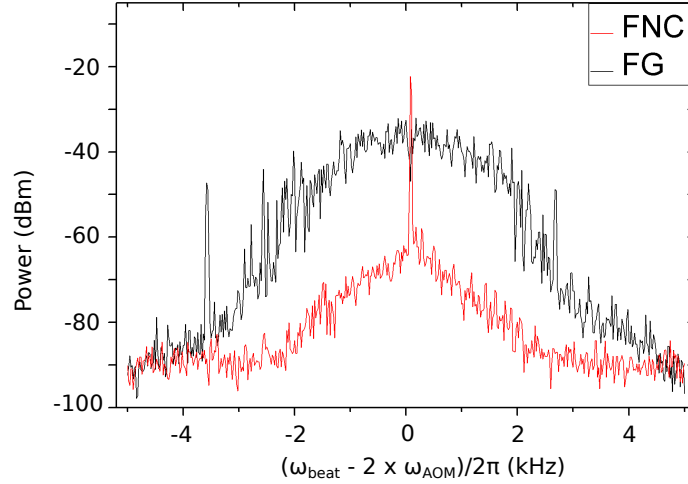


Figure 3.6.: Beat signal between light coming directly from the laser and light transmitted two times through the 100 m single mode fiber as well as an AOM operated at 75 MHz. The signal without fiber noise cancellation (black) has a line width of about 1 kHz (-3 dB). When switching on the fiber noise cancellation, only a narrow central peak remains (red), the noise is suppressed by 40 dB. Figure from Ref. [Pel13].

For beam path b, the beam is coupled into a separate fiber<sup>39</sup> connected to the imaging system. The beam is superimposed to the ions fluorescence image at a dichroic mirror as illustrated in Fig. 3.7 and focused to a spot sizes of about  $4 \mu\text{m}$  by the camera lens. Since the distance between ions is  $d \geq 5 \mu\text{m}$  assuming typical potentials, this beam can be focused on single ions in a Coulomb crystal. Propagating vertically through the trap this beam only couples to the radial motion of the ion. This configuration leads to a Lamb-Dicke parameter independent of the axial potential, which is particularly helpful for spectroscopy in trap T1 (see section 4.1), where the axial vibrational frequency is limited to  $\omega_{ax}/2\pi \approx 120 \text{ kHz}$ . The tight focus leads to a high intensity at the ion ( $I = 4 \times 10^4 \text{ W/m}^2$ ) and fast Rabi-oscillations with  $\Omega_0/(2\pi) > 1 \text{ MHz}$ .

<sup>39</sup>PMC-630-4.2-NA012-3-APC-150-P, 60FC-F-4-M8-10, 60FC-4-M8-10; Schäfter+Kirchhoff

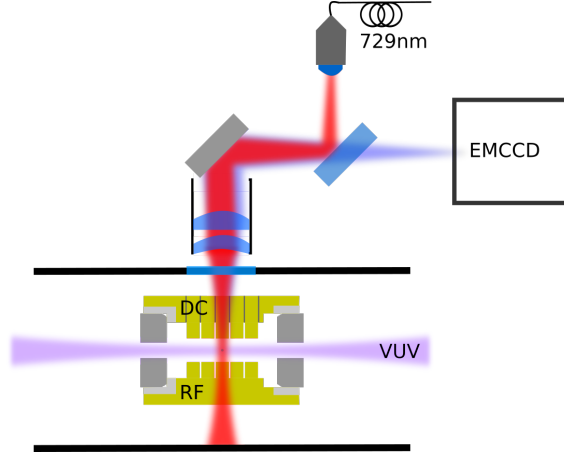


Figure 3.7.: Beam path b) for the light at 729 nm wavelength. The beam is superimposed to the ion's fluorescence image and focused tightly by the imaging lens. This beam propagates vertically through the trap.

## 3.2. Ion imaging

Ions are detected by imaging their fluorescence at 397 nm wavelength to an electron multiplied charged coupled device (EMCCD) camera<sup>40</sup>. The requirements to the imaging system include: Short exposure times for ion detection, high spacial resolution in order to resolve single ions in Coulomb crystals; mechanical stability; independent translation in three dimensions; insensibility to stray light. In addition to using a highly sensitive EMCCD camera this requires an imaging lens with a high numerical aperture and a rigid but adjustable mechanical connection between ion trap, lens and camera.

The imaging lens<sup>41</sup> and camera are mounted on a rigid aluminum profile at a distance of about 1 m with a mirror placed at 45° between lens and camera. The experimentally determined magnification and spacial resolution are  $m = 17.7(1.4)$  and  $d_{min} = 3.2(0.9) \mu\text{m}$  respectively [Nab12]. The system is connected to the ion traps vacuum vessel via a 3-D translation stage<sup>42</sup> and a ball joint. At the side of the EMCCD camera, the system is mounted to the optical table via a combination of linear slider, rotation mount and rocker ensuring the required degrees of freedom. The complete setup is depicted in Fig. 3.8. The beam path is encapsulated in a PVC-tube in order to shield the camera from stray light, additionally a bandpass filter<sup>43</sup> with transmission around 395 nm wavelength is placed in front of the CCD-chip. With this setup we achieve ion detection with exposure times down to  $t_{ex} = 1 \text{ ms}$ .

<sup>40</sup>Andor; IXon3 897; 512x512 pixel; pixel size  $16 \times 16 \mu\text{m}$ ; blue optimized ar coating

<sup>41</sup>Sill Optics GmbH; focal length  $f = 66.8 \text{ mm}$ ; aperture  $D = 38 \text{ mm}$

<sup>42</sup>Thorlabs; PT3, XYZ translation stage

<sup>43</sup>FF01-395/11, transmission 385nm-405nm; Semrock

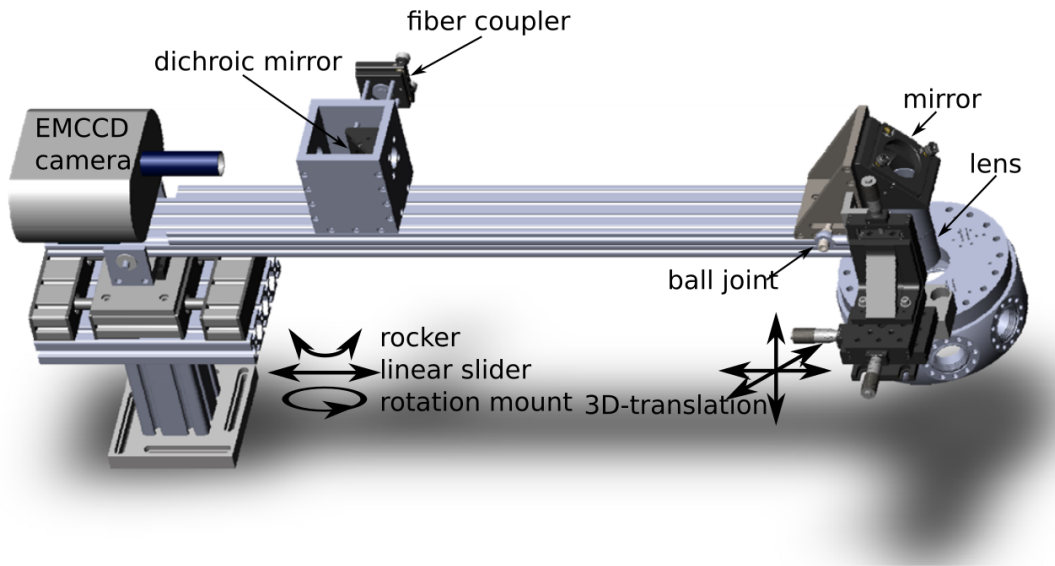


Figure 3.8.: 3D drawing of the imaging system. Camera and lens are connected by a rigid aluminum profile. At the lens' side, the system is fixed to a 3D-translation stage via a ball joint. The camera's side is mounted on a combination of rotating platform, linear slider and rocker to ensure the required degrees of freedom while providing excellent mechanical stability. A dichroic mirror, placed in the beam path at an angle of  $45^\circ$ , allows for superimposing a beam at 729 nm wavelength to the fluorescence image. The ions are imaged through the anti reflex coated viewport integrated in the top flange.

In addition to imaging ions, this system is used for single ion addressing with a laser beam at 729 nm wavelength (see section 3.1.3). A dichroic mirror, transparent for 397 nm wavelength, reflective for 729 nm wavelength, is placed in the imaging path at an angle of  $45^\circ$ . The fiber-coupler for the beam at 729 nm wavelength is mounted on a cage system fixed to the mirror holder. By adjusting the angle of the fiber-coupler and sliding it on the cage system the focus can be aligned to the ion.  $\lambda/2$  and  $\lambda/4$  waveplates allow for adjusting the polarization.

### 3.3. Vacuum ultraviolet light source near 122 nm wavelength

Working with light in the vacuum ultraviolet (VUV) region implies some fundamental differences compared to working with light fields in the visible, infrared or ultraviolet spectrum as typically employed in quantum optics experiments. Particularly the absorption of VUV light by air and the limited availability of optical elements pose considerable challenges for the design of such an experiment. In contrast to most cold ion experiments where the light sources are discrete from the ion or atom trap, in our experiment, the VUV source and the ion trap have to be designed as one integrated apparatus.

The source for continuous wave coherent vacuum ultraviolet radiation we use for driving the transitions to Rydberg states, existed already at the physics department in Mainz. It was developed at the Max-Planck institute for quantum optics [Eik99, Wal01] for the excitation of the Lyman- $\alpha$  transition in hydrogen [Eik01] and improved continuously [Sch09a, Sch10, Kol10, Kol12b, Kol12a]. The VUV source was modified for Rydberg excitation of  $^{40}\text{Ca}^+$  ions by D. Kolbe, M. Stappel and P. Bachor in the group of Prof. J. Walz [Sta15, Bac13]. I did not contribute significantly to its setup, however I briefly describe it in my thesis in order to provide a complete and clear description of the Rydberg ion experiment.

As there are neither transparent gain media nor highly reflective mirrors, the operation of a laser at this wavelength is not possible and consequently one has to rely on sum frequency mixing in nonlinear optical media to generate coherent radiation. We employ four-wave-mixing in a gaseous media. Near resonant light fields matched to the energy levels help to boost the non-linear susceptibility. Suitable resonances for the generation of light near 122 nm wavelength can be found in Hg and result in mixing efficiencies in the order of  $100 \mu\text{W}/\text{W}^3$  [Kol12b] when using a triple resonant four-wave-mixing (FWM) scheme.

The resonances employed in the four-wave-mixing are shown in Fig. 3.9. Lasers at 253.7 nm and 408 nm wavelength resonantly excite the two photon transition  $6^1S \rightarrow 7^1S$ . By choosing a single photon detuning of 133 GHz from the  $6^3P$  level, we avoid population of this state. Tuning the wavelength of the third light field close to one of the resonances  $10^1P$ ,  $11^1P$  or  $12^1P$  yields FWM efficiencies of  $\eta_{\text{FWM}} \approx 100 \mu\text{W}/\text{W}^3$  at wavelengths near 121.26 nm, 122.04 nm or 123.23 nm.

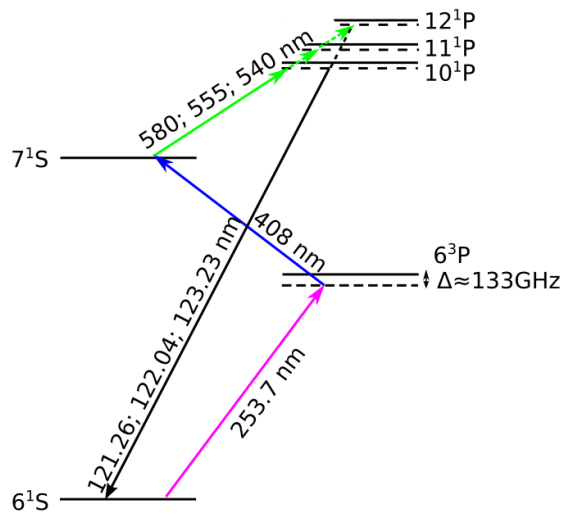


Figure 3.9.: Resonances in mercury used in the four-wave-mixing process. The two photon transition  $6^1S \rightarrow 7^1S$  is excited by the fundamental light fields at 254 nm and 408 nm wavelength. This resonance is essential for efficient four-wave-mixing. The light field near a wavelength of 254 nm is detuned from the  $6^3P$  resonance by about 133 GHz. With two of the fundamental waves fixed to the  $6^1S \rightarrow 7^1S$  transition, the wavelength of the generated VUV light is determined by the third incoming wave.

### 3. Experimental setup

---

The generated VUV power is proportional to the FWM efficiency  $\eta$  and the product of the powers of the fundamental waves:

$$P_{vuv} = \eta_{FWM} \times P_{254nm} \times P_{408nm} \times P_{555nm}. \quad (3.1)$$

Light fields with powers between 150 mW and 2 W generate up to 15  $\mu$ W of VUV light. In addition to high output powers, requirements for the fundamental lasers are:

- Single mode output with high beam quality .
- Narrow spectral bandwidth: The spectral characteristics of the generated VUV light directly depends on the incoming light fields.
- In case of the third laser, mode hope free tunability for the Rydberg spectroscopy.

These requirements are met by frequency stabilized high power solid state lasers in the near infrared with subsequent frequency doubling and frequency quadrupling. An overview over the employed laser systems is given here, for more details see Ref. [Sta15].

Light at 253.7 nm wavelength is generated by frequency quadrupling the output of a cryogenic fiber amplifier [Ste13] running at 1015 nm wavelength. The Yb-fiber is cooled to cryogenic temperatures with liquid nitrogen in order to shift the gain profile to a wavelength of 1015 nm. The fiber amplifier is seeded by a home built external cavity diode laser (ECDL)<sup>44</sup> which is frequency stabilized to a high finesse cavity<sup>45</sup>, resulting in a line width of about 100 kHz. The output power of the diode of about 50 mW is amplified by a tapered amplifier<sup>46</sup> to 1 W. The fiber amplifier generates an output power of 3.5 W at 1015 nm which is coupled into the first frequency doubling resonator built around a lithiumtriborat (LBO) crystal. About 2 W of green light at 507.5 nm are generated and coupled into the second frequency doubling cavity. Featuring a bariumborat (BBO) crystal, up to 300 mW's of ultra violet radiation at 253.7 nm wavelength are generated in this cavity. A fast mechanical shutter is placed in the beam<sup>47</sup>.

The second laser beam required for the two photon  $6^1S \leftrightarrow 7^1S$  transition at a wavelength of 408 nm is generated by a frequency doubled<sup>48</sup> titanium sapphire (Ti:Sa) laser<sup>49</sup>. The laser comes with an integrated cavity for frequency stabilization and features a line width of about 30 kHz according to specifications. The output power is up to 5 W at 816 nm when pumped with 18 W which leads to an optical power of up to 2 W at 408 nm after the frequency doubling resonator.

---

<sup>44</sup>EYP-RWE-1060-00100-0750-SOTO1, 50 mW; Eagleyard

<sup>45</sup>Zerodur spacer in vacuum housing, layertec mirrors, Finesse  $\mathcal{F} \approx 1600$

<sup>46</sup>16073-RTA-1010-2000-CM, 2W, 1010nm; m2kLaser

<sup>47</sup>home built from camera shutter

<sup>48</sup>LBO in PDH stabilized cavity

<sup>49</sup>Matisse TX; Sirah pumped by Verdi V18; Coherent

With two wavelengths fixed to the  $6^1S \leftrightarrow 7^1S$  transition, the sum frequency of the FWM process is determined by the third incoming wave. Utilizing a third resonance in mercury leads to the huge gain in FWM efficiency needed for the experiments. The eligible resonances are  $7^1S \leftrightarrow 12^1P$ , resulting in a VUV wavelength of 121.26 nm used for photo ionization of  $^{40}\text{Ca}^+$ ,  $7^1S \leftrightarrow 11^1P$ , yielding a VUV wavelength of 122.04 nm used for the excitation of Rydberg states around  $n = 52$  (from  $3D_{3/2}$ ) and  $n = 66$  (from  $3D_{5/2}$ ), and  $7^1S \leftrightarrow 10^1P$  for a VUV wavelength of 123.23 nm required for the excitation of Rydberg states  $n = 21$  and  $n = 22$ . The transitions have resonance wavelengths of 540 nm, 555 nm and 580 nm respectively.

The former two are generated by frequency doubling the light from a high power, two stage fiber amplifier [Sta13] with an optical output of 8 W. The light is frequency doubled with a periodically poled lithiumniobat crystal<sup>50</sup> which provides a high doubling efficiency even without a resonator [Sta14]. The two stage Yb-fiber amplifier is seeded by a frequency stabilized ECDL<sup>51</sup> with an output power of about 120 mW.

The gain profile of the Yb-fiber amplifier does not allow for operation at 1160 nm wavelength, thus we built an additional laser setup consisting of a home built ECDL<sup>52</sup> and a subsequent tapered amplifier<sup>53</sup>. This setup generates less optical power (1.5 W) as compared to the fiber amplifier, hence in cavity frequency doubling with a PPLN crystal is used in order to reach sufficient output powers of about 250 mW at 580 nm.

The seeding ECDL's are stabilized to high finesse cavities<sup>54</sup>. The light coupled to the cavity is frequency shifted by a high bandwidth fiber EOM<sup>55</sup>. This setup allows for a modehop free tuning range of the stabilized laser of a few 100 MHz, which is required for Rydberg spectroscopy. For the initial search of Rydberg resonances, an even wider tuning range is necessary which is accomplished by frequency stabilizing the laser to the wavelength meter only.

The beams are superimposed at dichroic mirrors and focused into the mercury vapor cell illustrated in Fig. 3.11. Beam waists of  $w_0 = 6 \mu\text{m}$  (UV),  $w_0 = 14 \mu\text{m}$  (blue) and  $w_0 = 15 \mu\text{m}$  (green/yellow) ensure high intensities in the order of  $10^9 \text{ W/m}^2$ . The mercury is heated to  $100^\circ\text{C}$ – $150^\circ\text{C}$  inside the vacuum chamber in order to achieve high atom density and good phase matching conditions. Water cooled baffles on both sides of the heated cell prevent the Hg vapor from spreading through the vacuum chamber and condensing on the entrance window and magnesium fluoride ( $\text{MgF}_2$ ) lenses. Additionally the optical elements in the beam path are heated while cryo-traps, cooled with liquid nitrogen during operation, prevent contamination of the lenses.

Only a fraction of the optical power is transformed into VUV radiation in the FWM

<sup>50</sup>Magnesium-doped periodically poled lithium niobate crystal (MgO:PPLN)

<sup>51</sup>DL pro, 1110nm, 120 mW; Toptica

<sup>52</sup>LD-1160-TO-200, 1160nm, 200mW, ar-coated; Innolume GmbH

<sup>53</sup>BoosTAPro, 1.5W, 1160nm; Toptica

<sup>54</sup>Zerodur spacer in vacuum housing, layertec mirrors, Finesse  $\mathcal{F} \approx 1600$

<sup>55</sup>NIR-MPX-LN-10, operation wavelength 980 nm-1150 nm, Electro-optic bandwidth 10 GHz; Photoline

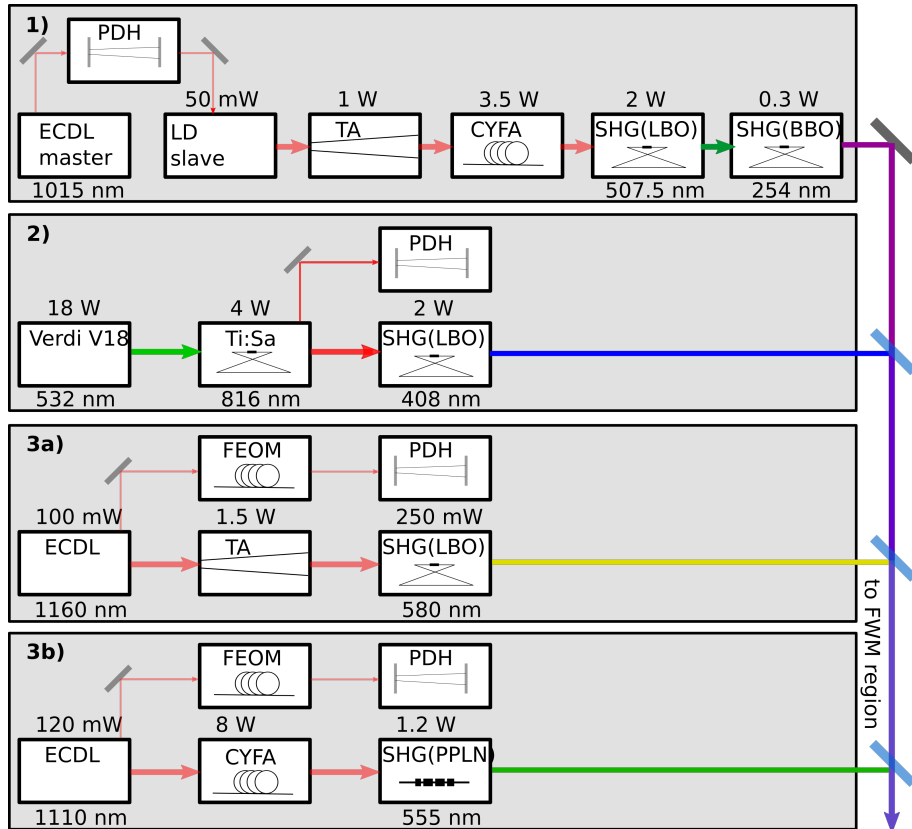


Figure 3.10.: Block diagram of the lasers used to create the fundamental light fields at 254 nm (1), 408 nm (2), 580 nm (3a) and 555 nm (3b) wavelength for the FWM process. The light is generated by frequency doubling (quadrupling) the output of high power infrared lasers. Frequency stabilization to high finesse cavities ensures narrow spectral bandwidth of the outcoming light. Abbreviations used in the plot are; ECDL = external cavity diode laser; TA = tapered amplifier; PDH = Pound-Drever-Hall; (C)YFA = (cryogenic) yttrium fiber amplifier; SHG = second harmonic generation.



process while almost the entire optical power is left in the fundamental light fields. We separate this light from the VUV radiation by making use of the dispersion of  $\text{MgF}_2$ . While the focal length of the lens for the fundamental wavelengths is about 130 mm, the focal length for the light at the sum frequency is significantly shorter. Placing a tiny mirror in the focus of the fundamental beams we reflect them while losing only about a third of the VUV light. A second  $\text{MgF}_2$  lens collimates the beam before it enters the ion trap vacuum chamber and is focused into the trap.

The polarization of the VUV light generated in the FWM process depends on the polarization of the fundamental light fields. All three beams have linear, horizontal polarization, thus VUV light with the same polarization is generated. With the VUV beam propagating axially through the trap and the magnetic field aligned horizontally with an angle of  $\pi/4$  with respect to the axis (see section 3.5), this polarization allows for the excitation of  $\pi$ -transitions and  $\sigma^\pm$ -transitions. However the VUV light passes three  $\text{MgF}_2$  lenses between the mercury cell and the ion crystal. Stress induced birefringence might cause polarization changes. Consequently we have no precise knowledge of the VUV beam's polarization at the ion crystal.

### 3.4. Ultra-high vacuum setup

Operation of an ion trap requires ultra high vacuum (UHV) environment to avoid collisions of cold trapped ions with particles from the thermal background gas. Typically stainless steel conflat flange (CF) hardware with copper gasket seals is used for UHV applications. For the construction of the ion trap only low out-gassing, UHV compatible and non-magnetic materials are used. To achieve pressures of  $p < 10^{-10}$  mbar we require high performance vacuum pumps and a bakeout period during which residuals are evaporated from the surface. Hence, all materials have to be able to withstand temperatures of up to 200 °C for extended periods of time.

An additional challenge in our experiment arises from the fact that VUV radiation is absorbed by air. Consequently the radiation has to be generated in vacuum and the vacuum vessels for the VUV source and the ion trap have to be connected. However, considering the varying requirements for the two vacuum regions; ultra high vacuum ( $p_{ion} < 10^{-10}$  mbar) for the ion trap, high vacuum ( $p_{vuv} < 10^{-6}$  mbar), high partial mercury pressure and frequent venting for the VUV source; a separation of the two regions is mandatory. Building the vacuum setup for the ion trap as small and light as possible was of great importance for two reasons: Space in front of the existing VUV source is restricted, and, for beam alignment, the two parts of the vacuum systems have to be moved with respect to each other. A schematic drawing of the complete setup is shown in Fig. 3.11, a detailed description of the VUV source part of the vacuum can be found in Ref. [Kol10, Sta15]

The vacuum setup for the ion trap is constructed around a compact cylindrical stainless

### 3. Experimental setup

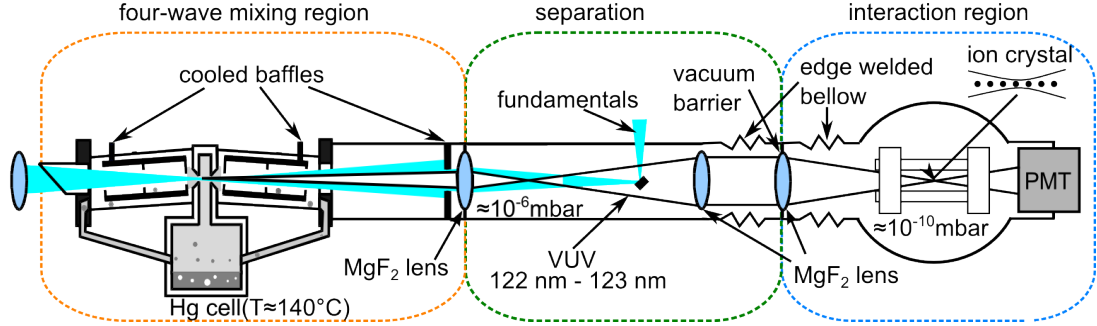


Figure 3.11.: The fundamental laser beams are overlapped at dichroic mirrors and focused into the mercury vapor cell. Cooled metal baffles on both sides of the FWM region prevent the mercury vapor from spreading through the vacuum system. The dispersion of a  $\text{MgF}_2$  lens is used to separate the VUV light from the fundamental waves at a tiny mirror placed in the beam path. The VUV beam is collimated and focused into the ion trap by two more  $\text{MgF}_2$  lenses. The second lens is mounted between two flexible vacuum bellows and serves simultaneously as an airtight vacuum seal between the vacuum regions of the VUV source ( $10^{-6}$  mbar) and the ion trap ( $10^{-10}$  mbar). The VUV beam is transmitted axially through the trap, its power is monitored with a photomultiplier-tube. Figure from Ref. [SK11].

steel vacuum chamber<sup>56</sup> with ports for two CF150 and eight CF40 flanges. The ion trap is mounted on the upper CF150 flange which also provides electrical feed-throughs required for trap operation and optical access for the detection of ions via an integrated fused silica window with 63 mm diameter.

The vacuum vessel is connected to the VUV source via two edge welded bellows with a  $\text{MgF}_2$  lens in between. The  $\text{MgF}_2$  lens is glued to a titanium mount so that it serves simultaneously for focusing the collimated VUV beam into the ion trap and as an airtight barrier between the two vacuum regions. The position of the lens in between two edge welded bellows enables free movement between VUV source, lens and ion trap. The mount of the  $\text{MgF}_2$  lens is fixed to a 2-D translation stage<sup>57</sup> allowing for lateral movement of the lens using fine threaded actuators. The base of the translation stage is fixed rigidly to the ion trap's vacuum vessel. Additionally the ion trap's vacuum vessel is mounted on a 2-D translation stage built by the mechanical workshop (Fig.3.12), allowing for translation transverse to the beam propagating axis.

This setup, sketched in Fig.3.12, allows for precise transverse alignment of the VUV beam while retaining a high beam quality: First the VUV beam is adjusted roughly to the ion trap by vertical and horizontal translation of the ion trap's vacuum vessel. During this

<sup>56</sup>Spherical octagon; kimble physics

<sup>57</sup>linear translation stage M-UMR8.51; Newport

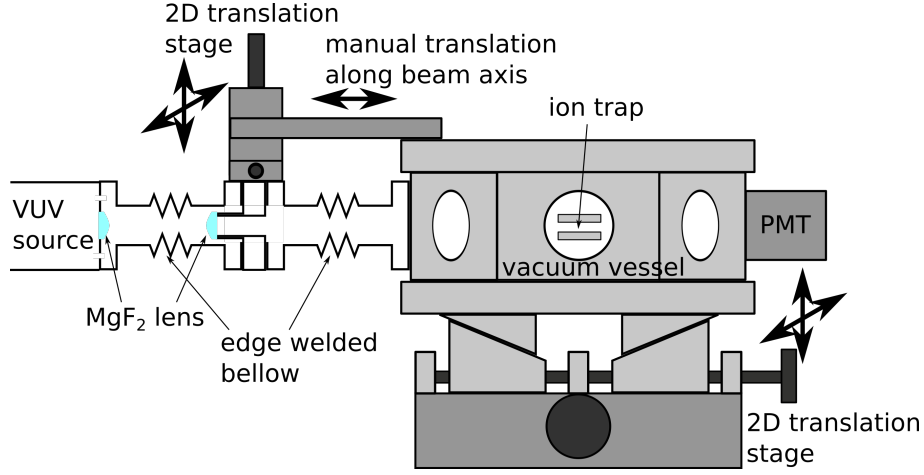


Figure 3.12.: Scheme of the flexible connection of VUV source and ion trap. The focusing  $\text{MgF}_2$  lens is mounted between two edge welded bellows. Transverse to the VUV beam it can be moved by a 2D-translation stage, additionally it can be moved along the beam axis manually. The ion's trap vacuum vessel is mounted on a 2D translations stage allowing for transverse movement as well.

procedure the  $\text{MgF}_2$  lens' position is fixed centrally in front of the VUV source in order to keep geometric aberrations to a minimum. In a second step, we precisely align the beam to the ion crystal using the translation of the  $\text{MgF}_2$  lens; this small change of position has a minor effect on the beam quality only. Due to the Raleigh length of 0.5 mm, axial alignment is much less critical. We move the  $\text{MgF}_2$  lens along the beam propagation axis manually and fix it in the right position.

A  $\text{MgF}_2$  viewport<sup>58</sup> on the opposite end of the vacuum vessel allows for transmission of the beam through the vacuum vessel. We monitor the transmitted VUV power with a photomultiplier<sup>59</sup>. The photomultiplier is used not only for power monitoring but also for the alignment of the VUV beam to the ion crystal. A stainless steel needle with a diameter of  $250\,\mu\text{m}$  and a sharp tip is mounted on an adjustable bellow as depicted in Fig.3.13, allowing us to move the tip either right inside the trap (trap T1) or directly in front of the trap (trap T2)<sup>60</sup>. The cut off of the VUV beam at the needle's tip is measured with the photomultiplier and, by monitoring the needle's position with respect to the trap center, the beam can be aligned to the ion crystal with a precision of about  $30\,\mu\text{m}$  (see section 5.4). During ion trap operation the needle is removed from the trap. A CF16 viewport is placed at the far end of the bellow, allowing for limited optical access.

<sup>58</sup>CF40  $\text{MgF}_2$  viewport, double sided flange; Allectra

<sup>59</sup>R6835; Hamamatsu

<sup>60</sup>Thanks to M. Drewsen for the suggestion

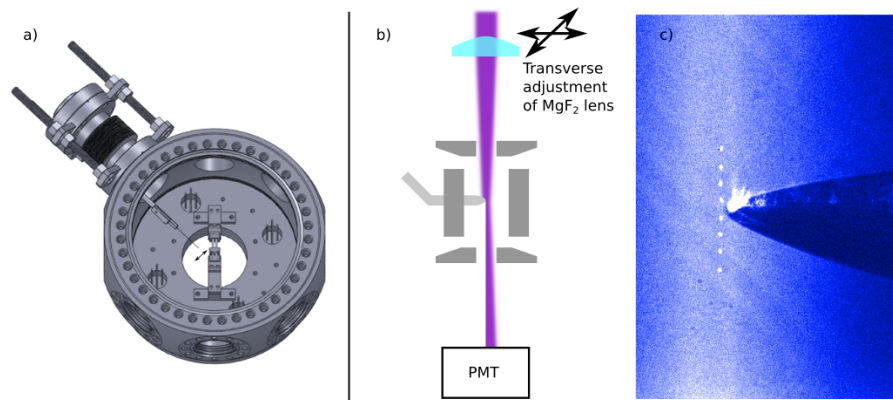


Figure 3.13.: a) Construction drawing of the device for in trap beam waist measurements. A needle with diameter of  $250\,\mu\text{m}$  is mounted on a flexible vacuum below with adjustment screws. It's tip can be moved in and out of the trap. b) Schematic drawing of the beam waist measurement. The needle tip is positioned inside the ion trap. By translating the  $\text{MgF}_2$  lens and measuring the cut off of the VUV beam at the needle with the photomultiplier, the beam waist is determined. c) Superimposed images of the needle tip and an ion crystal. Both images are taken at the same position with the EMCCD camera. Adjusting the needle tip this way allows for aligning the VUV beam to the ion crystal.

Three of the remaining CF40 ports are fitted with anti-reflex coated<sup>61</sup>, fused silica viewports to provide optical access for various laser beams to the ion trap. The vacuum pump is mounted on one of the remaining ports. We opted for a compact, combined ion getter and non-evaporable getter pump<sup>62</sup>. The getter material is placed inside the main vacuum chamber, which ensures efficient pumping close to the ion trap. An all metal vacuum valve<sup>63</sup> and a UHV pressure gauge<sup>64</sup> are mounted via two CF40 Tees. An anti-reflex coated viewport on the far side of the Tee provides optical access to the ion trap. The complete setup is shown in Fig. 3.14.

The system has been vented and baked repeatedly. The glued in MgF<sub>2</sub> lens appeared as a weak spot and failed repeatedly during bake out. However, once the original stainless steel mount was replaced by one made out of titanium (see Fig. 3.12) which has an expansion coefficient similar to MgF<sub>2</sub><sup>65</sup> this problem disappeared.

### 3.5. Magnetic field generation

A well controlled, stable magnetic field is required for the experiment. Its direction provides the quantization axis for optical transitions while its magnitude determines frequency shifts of different states due to the Zeeman splitting. We opted for a horizontal alignment of the magnetic field with an angle of  $\pi/4$  between the magnetic field and the VUV beam. This choice simplifies the operation of the ion trap as laser beams are typically aligned with an angle of  $\pi/4$  to the trap axis, thus either parallel or perpendicular to the magnetic field.

A pair of coils in quasi Helmholtz configuration, sitting on two opposing CF40 ports of the vacuum vessel provide the field(see Fig.3.15). An additional coil, positioned below the vacuum vessel is used for compensation of the earth magnetic field in vertical direction. No compensation is used in horizontal direction perpendicular to the quantization axis as stray fields are small in this direction. The coils, operated with a current of 3 A generate a magnetic field of 0.28 mT.

The stability of the magnetic field is vital for the coherence of the quadrupole transition. For example the  $|4S_{1/2}, -1/2\rangle \leftrightarrow |3D_{5/2}, -5/2\rangle$  transition is shifted by 28 MHz/mT. Using a standard laboratory current supply<sup>66</sup> yields line width of about 50 kHz. With a current stabilization the line width could be reduced to  $< 5$  kHz. Most of the remaining magnetic field noise is at 50 Hz, thus further reduction is possible by triggering the experimental

---

<sup>61</sup>AR coating 11552500230, 390 nm-450 nm and 700 nm-900 nm, temperature 300°C during coating, fused silica viewports may fail; Tafelmaier

<sup>62</sup>NEXTorr D 100-5, SAES Getters

<sup>63</sup>series 54032-GE02-0002, easy close all-metal angle valve; VAT

<sup>64</sup>UHV-24p Bayard-Alpert Gauge Tube; Agilent

<sup>65</sup>Thermal expansion MgF<sub>2</sub>:  $13.7 \times 10^{-6}$  /K (parallel)  $8.9 \times 10^{-6}$  /K (perpendicular) Titanium:  $7.2 \times 10^{-6}$  /K

<sup>66</sup>2225.2; Statron Gerätetechnik GmbH

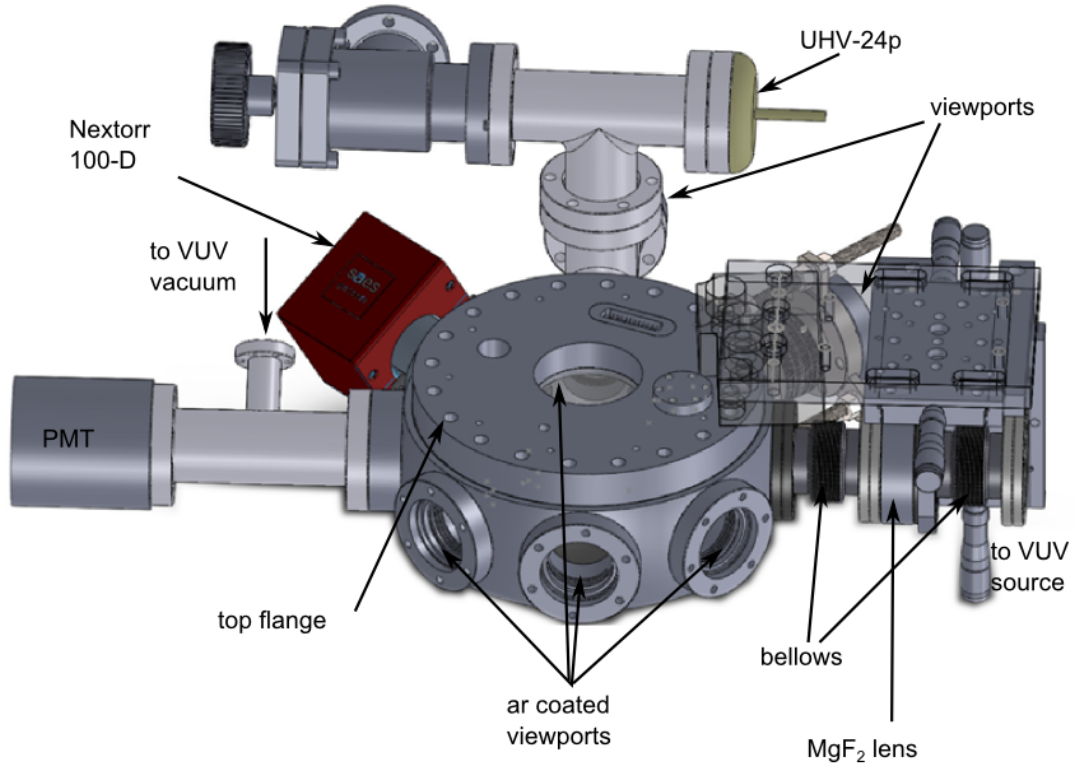


Figure 3.14.: 3D-drawing of the ion trap's vacuum vessel. On the right side, it is connected to the VUV source via two edge welded bellows. The  $\text{MgF}_2$  lens in between these bellows can be moved transverse to the beam with a 2D translation stage. The base of the stage is fixed rigidly to the vacuum vessel (transparent in drawing). The transmitted VUV light is measured with a photomultiplier (PMT), the reducer Tee is required for pumping down the PMT which is not part of the UHV region. The compact vacuum pump (red) reaches directly into the main vacuum chamber. Two CF40 Tees provide ports for a vacuum valve, a pressure gauge and a CF40 viewport. To the right of this construction, the adjustable vacuum bellow for the beam alignment needle is placed. A CF16 viewport allows for optical access from this direction too. Three more anti reflex coated viewports on the front side of the vacuum vessel provide access for the incoming laser beams. The top flange is fitted with a large viewport for ion detection and multiple electrical feed-throughs.

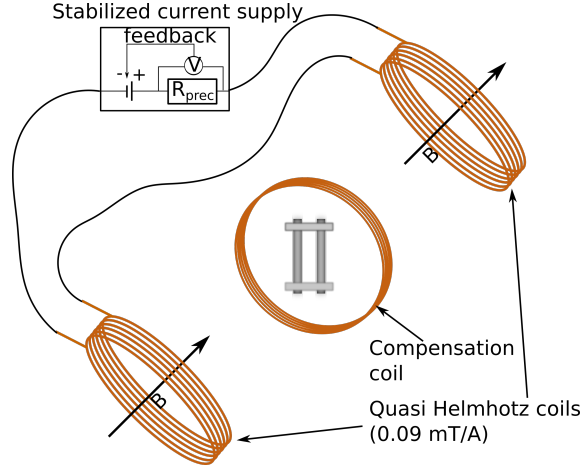


Figure 3.15.: Setup of the coils for the magnetic field. Two coils in quasi Helmholtz configuration generate the quantization field at an angle of  $\pi/4$  with respect to the trap axis. The current supply is stabilized by measuring the voltage drop over a precision resistor  $R_{prec}$ . An additional coil for the compensation of a vertical magnetic field is positioned below the ion trap.

sequence to the 50 Hz line current.

Initially, we discovered a huge stray field of about 1.7 mT at the ion's position, which vanished only after a bake out of the vacuum vessel and a reactivation of the Nextorr pump. The bakeout temperature of about 170 °C is too low to explain the demagnetization, so we conjecture that the getter material of the pump which gets heated to 450 °C was responsible for the stray field. The first bake out and activation was carried out with installed magnets of the ion getter pump, while the following bake outs and activations were always carried out with removed magnets and the stray field never appeared again. We did not do any systematical investigation of this effect, however it seems reasonable to always remove the pumping magnets for activation and bake out.

### 3.6. Computer control

The experiment is controlled by a PC. A software has been developed in our group<sup>67</sup> which provides interfaces for the various hardware devices used in the experiment [Rus12]:

- National Instruments PCI6733 board: Logic TTL signals and analog voltages.
- National Instruments PCI6703 board: Static analog voltages (voltages are not changed during sequences).

<sup>67</sup>master control program (MCP); K. Singer, T. Ruster, V. Kaushal, U. Poschinger et al.

### 3. *Experimental setup*

---

- Andor A-CCI-24 EMCCD-Controller card: Camera control and read out.
- Toptica vfg150: Arbitrary waveform generator.
- FPGA: Analog voltages for Trap T2 and logic TTL signal.
- HighFinesse wavelength meter WSU-10: Reading of wavelength only.

Values for the different devices can be set and read manually, or in realtime sequences. Typically experiments are carried out in sequences finishing with a fluorescence image. The software reads and evaluates the image coming from the EMCCD camera. Results and settings are saved to different text files. The results can be plotted during the experiment. The MCP features a graphical user interface. The modular design allows for modifications according to the requirements of the individual experiment.



## 4. Ion traps for Rydberg excitation

In Paul traps the confining potential is provided by a combination of static and dynamic electric fields with quadrupolar geometry and field gradients in the order of  $\beta = 10^5 \text{ V/m}^2 - 10^7 \text{ V/m}^2$  (static) and  $\alpha = 10^7 \text{ V/m}^2 - 10^9 \text{ V/m}^2$  (dynamic) (see section 2.2.1). For the design of the ion trap for Rydberg excitation of cold ions, we had to consider the unique properties of Rydberg states (see section 2.1), particularly their susceptibility to electric fields.

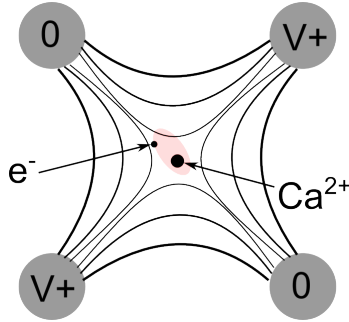


Figure 4.1.: A Rydberg ion in the electric quadrupole field of a Paul trap. The ion is located at the node of the field. The wave function of the doubly charged core in the thermal ground state has a spread of  $X_{ho} = 30 \text{ nm}$  for a trapping potential of  $\omega/2\pi = 1 \text{ MHz}$ . The electronic orbit ( $a_{Ry} \approx 100 \text{ nm}$ ) of the Rydberg state extends even further into the electric field. Thus the ion gets polarized even for perfect compensation. Additional electric fields can shift the ion out of the center and lead to a larger field amplitude.

The ion is localized at the node of the electric quadrupole, its wave function in the trapping potential has a spread in the order of  $X_{ho} = 30 \text{ nm}$ . The electronic wave function, with a spread in the order of  $a_{Ry} = 100 \text{ nm}$ , reaches even further into the electric field as illustrated in Fig. 4.1. While the static part of the field is rather weak that close to the trap center, the oscillating field assumes values of up to  $100 \text{ V/m}$  at a distance of  $100 \text{ nm}$  from the quadrupole node. This field polarizes the Rydberg ion and causes a shift of the excitation energy, broadening of the resonance and a modification to the trapping potential (see section 2.2).

In a real Paul trap additional oscillating fields are generated: Electric stray fields lead to a displacement of the ion out of the radio-frequency node. This effect is particularly prob-

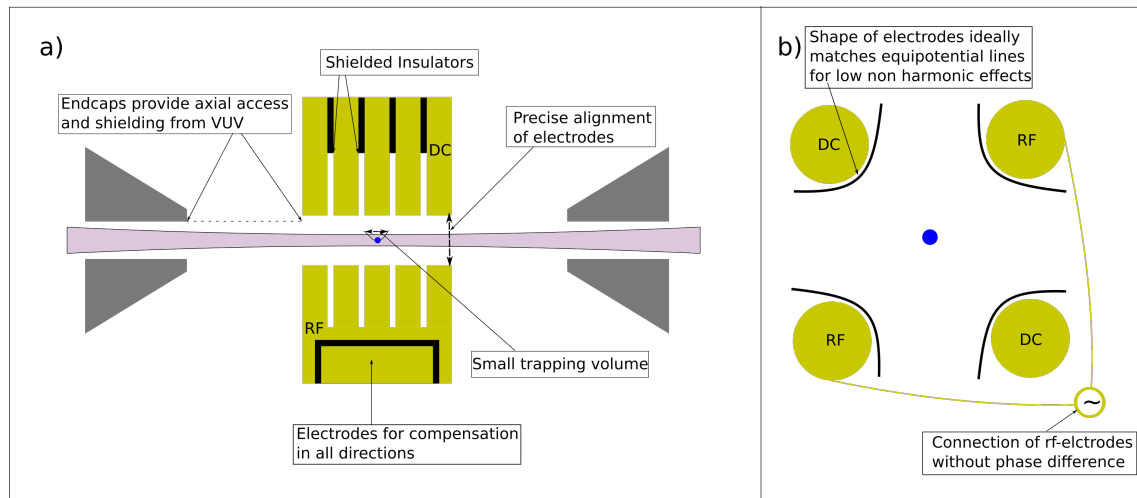


Figure 4.2.: Illustration of key features of a Paul trap for Rydberg excitation of ions (see text for details). a) Viewed from the side. b) Viewed along the axis of the trap.

lematic as the VUV laser generates patch charges on electrode surfaces which results in fluctuating electric stray field. Additionally, a phase difference between the voltage signal at the two diagonally opposing radio-frequency electrodes as well as geometric imperfections of the trap electrodes lead to an oscillating dipole superimposed on the quadrupole field. Considering these issues, the specifications for the ion trap are as follows:

- Axial optical access for the VUV beam.
- A precise assembly minimizes electric fields due to geometric imperfections of the trap. The matching of the static and dynamic minimum of the axial potential is particularly important as any difference leads to axial micro motion which might be hard to compensate by additional static fields.
- Phase differences between the voltage signal on the two radio-frequency electrodes have to be avoided. Oscillating fields generated this way are phase shifted by  $\pi/2$  compared to micro motion due to stray fields and thus can not be compensated with static electric fields.
- In contrast to quantum computing ion trap experiments, operation at a low trap drive frequency  $\Omega_{rf}$  is favorable for Rydberg excitation of ions. On the one hand it allows for operation at lower field gradients as the vibrational frequency of the pseudo potential is proportional to  $\alpha/\Omega_{rf}$  (see section 2.2.1). On the other hand, the phase shift introduced by different signal-paths to the rf-electrodes is reduced by using lower frequencies.

- Dedicated electrodes for compensating stray electric fields in all dimensions are required.
- All surfaces close to the ion have to be shielded from VUV radiation in order to avoid photo induced electrons and patch charges. The contamination of these surfaces (e.g. calcium from the atomic loading beam) must be avoided.

Additionally we discovered that even at pressures  $p \approx 10^{-10}$  mbar atoms from the thermal background gas are ionized by the VUV light and sympathetically cooled into the ion trap where they appear as dark gaps in the Coulomb crystal. In order to reduce this effect a small trapping volume is favorable. The traps used so far fulfill these requirements only partially, consequently we design a new trap for future experiments (see section 8.4).

#### 4.1. Linear rod trap (T1)

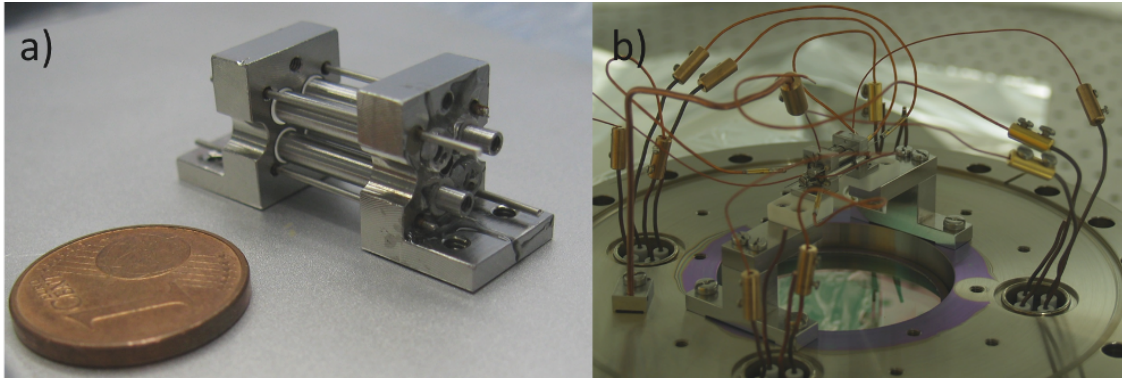


Figure 4.3.: a) Picture of the assembled trap with a one cent coin for size comparison.. b) The trap is mounted on the top-flange of the vacuum vessel, electrically connected to the feed-throughs and isolated from electric ground by Macor spacers. In the experiment the flange is reversed, with the trap positioned centrally under the viewport.

Considering the complexity of the laser system and vacuum setup required for Rydberg excitation we opted for an ion trap as robust possible. The trap consists of four cylindrical electrodes with diameter  $d = 2.5$  mm and two end caps as depicted in Fig. 4.4, all made of stainless steel. The surface to trap-center distance is 1.1 mm, which results in a ratio of 2.3 between electrode diameter and distance. This ratio yields optimal quadrupole approximation of the radial potential and reduces the non-harmonic effects in the trap such as parametric resonances [Den71]. Borosilicate glass tubes with an outer diameter of 2.8 mm and an inner diameter of 1.8 mm are fitted to holes in the end caps. They provide electrically isolated fits for the cylindrical electrodes. The end caps are manufactured

with a precision of 0.05 mm which corresponds to an angle between electrodes of 5 mRad. The distance of 10 mm between the end caps is precisely determined by the length of the thicker central part of the electrodes to  $\Delta d < 0.1$  mm. Four additional electrodes, positioned further away from the trap center, are used for the compensation of electric stray fields. These electrodes are made from stainless steel needles and are electrically isolated from the end caps by PEEK<sup>1</sup> tubes. Axial optical access for the VUV beam is provided by holes with a diameter of 1 mm drilled centrally into the end caps. Recesses at both sides of the end caps allow for optical access with laser beams at an angle of 45° to the trap axis. A 3D-design drawing is shown in Fig. 4.4 while a photograph of the assembled trap is shown in Fig. 4.3.

Electric connections to the electrodes are realized by clamping Kapton-isolated copper cables to the electrodes with M-1.4 sized screws (M-2 for end caps). The compensation electrodes are soldered to copper cables. The ion trap is electrically isolated from the vacuum chamber by Macor spacers. Four feed-throughs<sup>2</sup>, equipped with four copper pins each, provide electrical connections to the outside of the vacuum vessel.

A radio-frequency voltage with an amplitude of up to  $U_{rf} = 300$  V is applied to two diagonally opposing electrodes (rf-electrodes) for radial confinement, while the other two (dc-electrodes) are grounded. The rf-electrodes are connected by a rigid copper bridge, reducing the signal paths difference to  $\Delta l < 4.7$  mm. A common offset voltage is applied to the two dc-electrodes, which lifts the radial degeneracy of the potential.

For the compensation of stray electric fields, we apply a differential voltage to the dc-electrodes as well as individual voltages to the four compensation electrodes. Unfortunately the isolation proved to be insufficient, resulting in short cuts between the end caps and two of the compensation electrodes. However, even with only two remaining compensation electrodes and a differential voltage on the dc-electrodes, two dimensional compensation of electric fields is feasible.

The low noise, high voltage supply for the end caps is built from 0-2 kV voltage modules<sup>3</sup> combined with low pass filters ( $f_c = 50$  Hz) directly at the output of the voltage supply and capacitors at the electric feed-throughs ( $C_1 = 0.22 \mu\text{F}$  and  $C_2 = 4.7$  nF), as close to the ion trap as possible. Bias-Tees integrated in the low pass filters allow for applying various ac-voltage signals. Positive compensation voltages are supplied by the same source while negative voltages are generated by -1.2 kV modules<sup>4</sup>. Low pass filters are installed at the voltage supply side only as noise is less critical on compensation electrodes. All high voltage sources used for ion trap operations are controlled manually.

The low voltages  $U_{dc} \ll 1$  V applied to the dc-electrodes are generated by analog outputs

---

<sup>1</sup>Polyetheretherketon (PEEK)

<sup>2</sup>9216-08-W; Hositrad

<sup>3</sup>PSM10/202P+, HighTek

<sup>4</sup>PPM112, HighTek

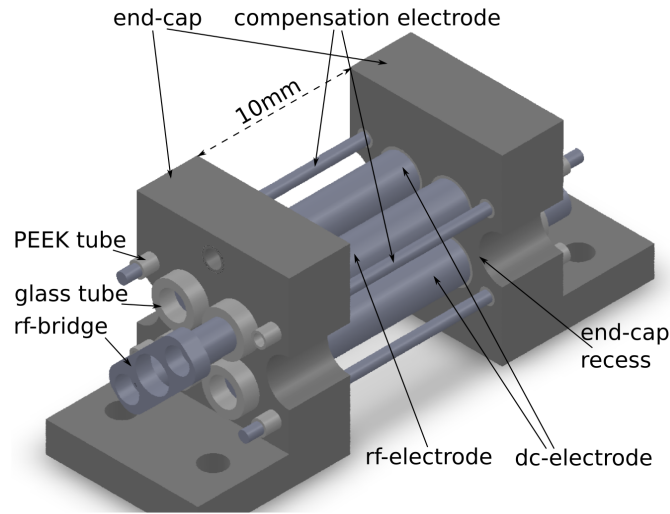


Figure 4.4.: Construction drawing of the linear Paul trap. The trap consists of four cylindrical electrodes and two end caps. Glass tubes provide a precise fit for the cylindrical electrodes as well as electrical insulation between electrodes and end caps. The thin electrodes on the outside of the trap are used for compensation of stray electric fields and are insulated from the end caps by PEEK tubes. A copper bridge of length  $l_{bridge} = 4.7$  mm connects the rf-electrodes. Thus signal path differences are below 4.7 mm. Recesses at the side of the end caps allow for optical access at an angle of  $\pi/4$  with respect to the trap axis. Cylindrical bore holes positioned centrally in the end caps allow for axial access.

of a PCI-6733 board<sup>5</sup>. In order to reduce noise at the electrodes, the signal is decoupled by an instrumental amplifier, divided by a factor of 30 and filtered by additional low pass filters ( $f_c = 110$  Hz) close to the feed-throughs (see Fig. 4.5).

The radio-frequency signal is provided by a signal generator<sup>6</sup> and amplified subsequently<sup>7</sup>. A voltage variable rf-attenuator<sup>8</sup> in between the signal generator and the amplifier, controlled by an analog output of the PCI-6733 board, allows for variation of the rf-amplitude<sup>9</sup>. A helical resonator [Mac59, Nab12] is used for impedance matching the 50 Ohm output of the amplifier to the ion trap. Its resonance frequency can be tuned in a range of  $\Omega_{rf}/2\pi = 3.5 - 10.5$  MHz with a variable capacitor of  $C = 0 - 50$  pF connected in parallel with the ion trap. Rf-amplitudes of up to  $U_{rf} = 300$  V are generated.

With trap operation parameters of  $\Omega_{rf}/2\pi = 3.5 - 10$  MHz and  $U_{rf} = 10 - 300$  V we obtain vibrational frequencies of  $\omega_{rad}/(2\pi) = 0.1 - 1$  MHz. The axial potential is generated by a static voltage applied to the end caps. Voltages between 300 V and 400 V have been used, resulting in potentials of  $\omega_{ax}/(2\pi) = 100 - 120$  kHz.

The atomic beam required for loading of ions into the trap is generated by a Ca-oven. A stainless steel tube with diameter  $d = 2$  mm and wall thickness  $w = 0.05$  mm is filled with calcium pellets. When heated by a current flow of 3.5 A through the thin material, calcium is evaporated which is subsequently ionized inside the trap.

Due to the quadrupole optimized shape of the electrodes, the trap provides stable trapping conditions at high  $q$ -parameters and allows trapping of large two-dimensional and three-dimensional Coulomb crystals as shown in Fig. 4.6. The electrodes are shielded from VUV radiation by the end caps, 5 mm away from the trap center, while the closest insulating surfaces are positioned at an even larger distance.

As stated above, small imperfections in the trap manufacturing process lead to non-perfect alignment of the trap electrodes which causes axial micro motion proportional to  $U_{rf}$  (see Sec. 5.1.1). This axial micro motion cannot be compensated and poses a major drawback of trap T1. Apart from this, the main drawbacks of this trap are low axial vibrational frequencies of  $\omega_{ax}/2\pi \leq 120$  kHz and the trap length of 10 mm, which leads to a high parasitic loading rate of background atoms ionized by the VUV radiation.

## 4.2. Linear segmented micro trap (T2)

Improving the features of trap T1 led to the construction of a new ion trap. Trap T2, a linear Paul trap with segmented electrodes, solves the most serious issues with trap T1, axial micro motion, weak axial potential and high parasitic loading rates. In addition,

---

<sup>5</sup>PCI-6733; National Instruments

<sup>6</sup>8657B; Hewlett-Packard

<sup>7</sup>ZHL-5W-1; mini-circuits

<sup>8</sup>ZX73-2500+; mini-circuits

<sup>9</sup>The introduction of higher harmonics by the attenuator is kept to a minimum by operating it at low power levels and low attenuation

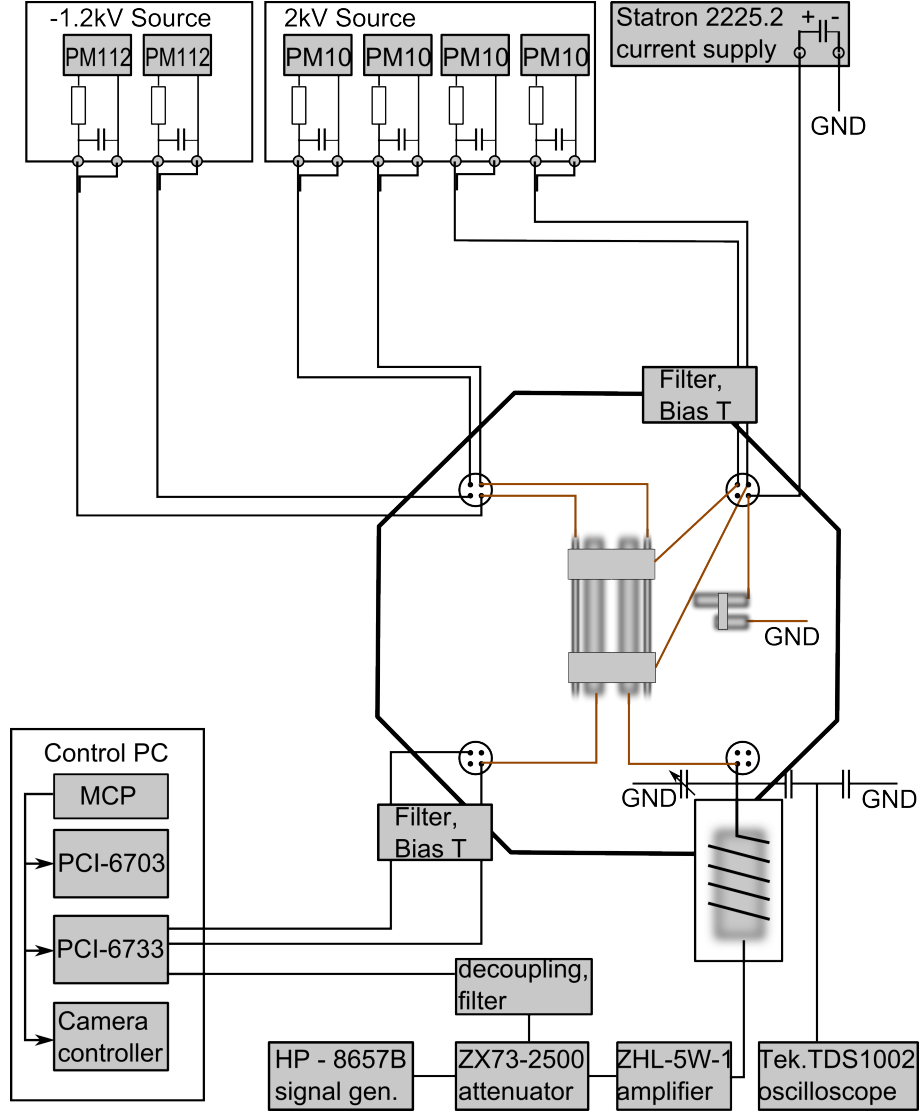


Figure 4.5.: Block diagram of electronics employed for the operation of trap T1. The voltages for end caps and compensation electrodes are provided by manually controlled high voltage sources. Low pass filter close to the feed-throughs reduce noise at the electrodes. A computer controlled analog signal is applied to the dc-electrodes. Low pass filters reduce noise at the electrodes, while a Bias-Tee allows for applying an ac-signal to the electrodes. The rf-frequency is generated by an amplified signal generator. A helical resonator enhances the amplitude up to 300 V. It's resonance can be tuned by a variable capacitor ( $C = 0 - 50 \mu\text{F}$ ), the output is monitored with an oscilloscope. The rf-amplitude is controlled by the computer via a voltage variable attenuator in between the signal generator and the amplifier. The calcium oven is connected to a laboratory current supply operated at 3.5 A.

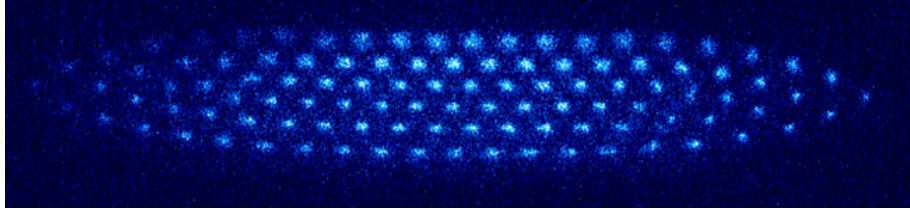


Figure 4.6.: Fluorescence image of a large 2D-Coulomb crystal trapped in trap T1 (106 ions). An additional Doppler cooling beam propagating along the trap axis was used to illuminate the whole crystal. The large trap and the quadrupole optimized shape of the electrodes is essential for trapping and cooling of Coulomb crystals of this size.

the segmented electrodes provide a highly flexible axial potential which allows fast transportation of ion crystals along the trap axis. The design of trap T2 is based on a trap development by Georg Jacob [Keh11, Jac14].

The trap, illustrated in Fig. 4.7 consists of four gold coated ceramic blades glued to an X-shaped titanium mount. The design goal of the titanium mount was to provide the best alignment precision for the electrodes. Electrically insulated end caps, symmetrically placed on both sides of the mounts are used as end stops for radial alignment of the blades. Bore holes in the end caps with 1.5 mm diameter provide axial access for the VUV beam.

The blades (see Fig. 4.9) are laser cut<sup>10</sup> from a 125  $\mu\text{m}$  thick ceramic substrate<sup>11</sup>. Structures down to 30  $\mu\text{m}$  are cut by femtosecond laser pulses. Following this first laser cut, the ceramic blades are sputtered with titanium and subsequently with a 100 nm thick layer of gold. In a last processing step the electrode structure is imprinted on these chips by laser cutting of insulation gaps in the gold coating. For details of the fabrication process see references [Keh11, Sch09b].

The distance of the electrode surface to the trap center is 480  $\mu\text{m}$ . The segment width is 180  $\mu\text{m}$  followed by a 30  $\mu\text{m}$  insulation gap. A total of 11 segments result in a length of the trap of 2.28 mm. The insulation gaps are 500  $\mu\text{m}$  deep, effectively hiding the insulator from the ion and from incoming laser radiation in order to minimize effects of surface patch-charges. The end caps are separated by 12 mm.

The radial confinement is provided by applying a rf-voltage to two diagonally opposing blades (rf-blades). Axial confinement is realized by applying individual voltages to the 11 segments of the dc-blades. This method allows for a high flexibility in generating axial potentials fitting to the experimental requirements. Small effective trapping volumes with the length of approximately one segment width are used while VUV radiation is present in the trap in order to reduce parasitic loading. During loading of  $^{40}\text{Ca}^+$  on the other hand we can use the full length of the trap in order to increase the loading rate. Each

---

<sup>10</sup>Micreon GmbH

<sup>11</sup>Coors ADS996-RES/Al<sub>2</sub>O<sub>3</sub>, 99,6%,; Reinhardt Microtech GmbH



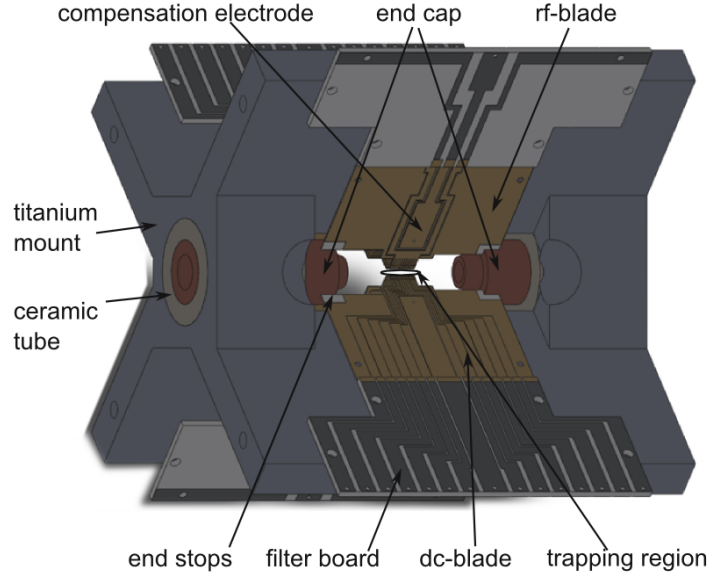


Figure 4.7.: 3D-drawing of the segmented ion trap. Key features are indicated in the drawing. The gold coated ceramic chips are glued to a X-shaped titanium mount. Axial access for the VUV beam is provided by holes in the endcaps. The electrodes are electrically connected to in vacuum low pass filters.

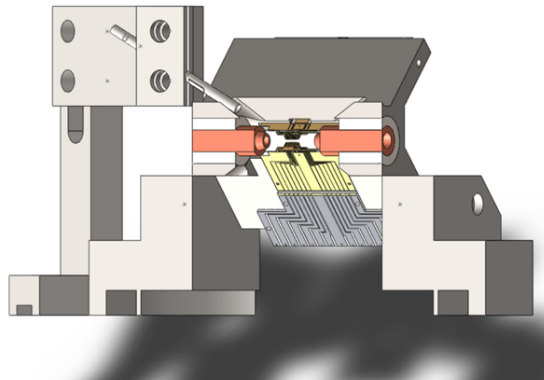


Figure 4.8.: Cut along the axis through a 3D-drawing of the trap with mount and calcium oven.

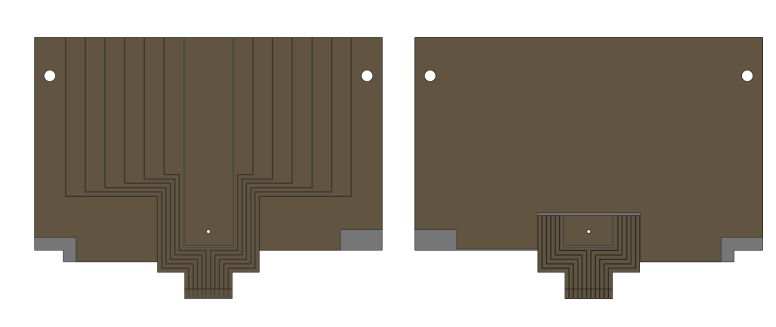


Figure 4.9.: Top (a) and bottom (b) view of a dc-blade. The electrode structure is imprinted by laser cutting of insulation gaps in the gold coated surface. The structure is magnified at the back end of the chip, providing space for the electric connection. Non-coated regions at the corner of the chip ensure electric insulation from the end caps which are used as end stops for the alignment of the blades. Only the front part of the electrode structure is imprinted on the bottom side of the chip. This way a symmetric potential is generated while insulation from the titanium mount is ensured [Keh11].

ceramic blade features an additional electrode for compensation of stray electric fields. Furthermore we use a differential voltage on the dc-segments for compensation.

The calcium oven is rigidly fixed to the top flange (see Fig. 4.8) ensuring precise alignment of the calcium beam. However, the electrodes are not shielded from the atomic beam, consequently their surfaces get contaminated with calcium. We do not switch the calcium oven during the experiment, consequently the oven is operated for about 8 hours per day.

The trap electrodes are electrically connected by bond-wires to in vacuum low pass filters on a ceramic board. Kapton-insulated copper wires, soldered to this filter board, provide the connection to the 25-pin Sub-D feed-through<sup>12</sup>. End caps, compensation electrodes and the calcium oven are connected to a 7-pin feed-through<sup>13</sup>, an additional single pin feed-through is used for the rf-signal<sup>14</sup>.

The 11 dc-segments require an independent voltage supply each. A computer controlled, ultra low noise arbitrary waveform generator with multiple parallel channels has been developed in our group for experiments working on fast ion transport in micro structured ion traps [Wal12, Zie12]. The device features an FPGA for fast generation of waveforms, and one to four digital-to-analog converter boards with 12 outputs each (only one board is used in the Rydberg experiment). Additionally the FPGA controls up to 40 digital TTL outputs. The analog outputs provide -10 V to 10 V adjustable with a precision of  $300 \mu\text{V}$

---

<sup>12</sup>Sub D type 16802-01-W; Hositrad

<sup>13</sup>9294-08-W; Hositrad

<sup>14</sup>9791-08-W; Hositrad

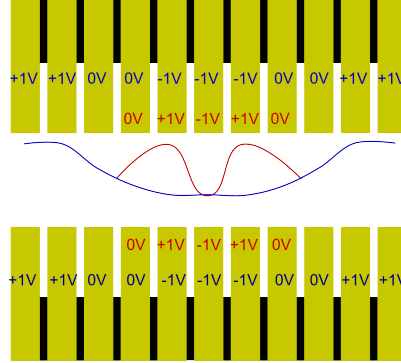


Figure 4.10.: Illustration of the axial potential generated by individual voltages on the segments. A large trapping volume is generated by applying a positive voltage to the outermost electrodes while the three central electrodes are set to negative voltages (blue). Using the three central electrodes only results in a much shorter trapping volume (red). A common offset voltage on all segments determines the splitting of the radial vibrational frequencies.

and an update time of 400 ns. This does not only allow for the flexible shaping of axial potentials but also for fast transportation of ions along the trap axis.

The use of ultra low noise electronics is mandatory to enable low ion heating rates. In addition to the very good noise characteristics of the voltage source [Zie12], we use shielded cables, a 50 kHz CLC- type low pass filter at the electric feed-through and in vacuum filtering (RC type) as close to the trap electrodes as possible.

The compensation electrodes on the rf-blades require higher voltages but are less critical to electric noise. For this purpose we use computer controlled  $\pm 10$  V to  $\pm 100$  V voltage modules<sup>15</sup> with additional low pass filters. The control voltage is supplied by an analog output of the PCI-6733 board, decoupled by an instrumental amplifier.

The rf-electronic is similar to the one used for trap T1 described in section 4.1. We use one of two helical resonators, either with a resonance frequency of  $\Omega_{rf}/2\pi = 6.5$  MHz or with a resonance frequency of  $\Omega_{rf}/2\pi = 14 - 20$  MHz, adjusted with a variable capacitor of  $C = 0 - 50$  pF connected in parallel with the trap. The stability of the rf-amplitude is improved by water cooling the amplifier, reducing temperature induced drifts. The electronics needed for operation of trap T2 are depicted in Fig. 4.11.

Reduced dimensions and more precise manufacturing compared to trap T1 allow for stiffer potentials. The trap is operated at  $\omega_{rad}/(2\pi) = 700$  kHz to  $\omega_{rad}/(2\pi) = 2$  MHz and  $\omega_{ax}/(2\pi) = 250$  kHz to  $\omega_{ax}/(2\pi) = 900$  kHz. The reduced Lamb-Dicke parameters compared to trap T1 improve coherent excitation on the quadrupole transition and allow for resolved sideband cooling on this transition. The reduced trapping volume decreases parasitic loading by VUV radiation by more than one order of magnitude.

<sup>15</sup>PM12-100 $\pm$ ; HighTek

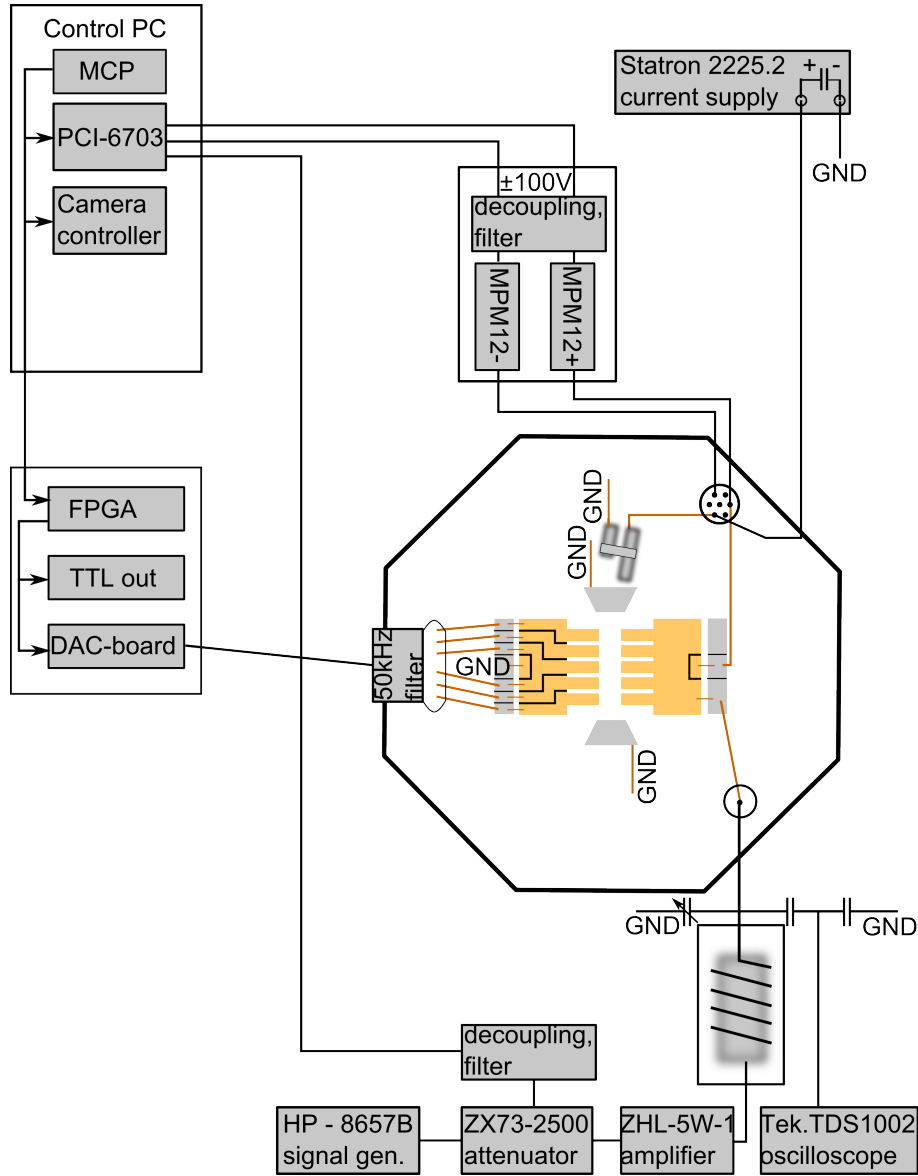


Figure 4.11.: Block diagram of the electronics for operation of trap T2. The rf-signal path and the current supply for the calcium oven are similar to trap T1. Major changes have been made to the dc part of the trap electronics. An FPGA, connected to the experimental control PC via Ethernet, generates waveforms and TTL signals. A low noise DAC board converts these waveforms into voltages for the dc-segments of the trap. A 50 kHz low pass filter at the feed-through and in vacuum low pass filters close to the trap ensure low noise. A computer controlled  $\pm 100$  V module is connected to the compensation electrodes on the rf-blades.

## 5. Trap characterization and preparatory experiments

In this chapter, characterization measurements of both Paul traps are presented. Properties like residual micro motion, heating rates and magnetic field are determined in order to find proper parameters for the Rydberg excitation experiment. Additionally in situ measurements of the VUV beam waist and beam alignment are presented.

We present experimental photo ionization of  $^{40}\text{Ca}^+$  as a first prove of an interaction between the VUV beam and the ion crystal. The mixed ion crystals containing one  $^{40}\text{Ca}^{2+}$  exhibit similar features compared to Coulomb crystals with ions in Rydberg states in so far as the vibrational frequency is altered for a single impurity ion (see section 2.2.2). This allows to study the effects of mode shaping proposed for Coulomb crystals with Rydberg ions in an experimentally more accessible system. Experiments with three respectively six ions in linear configuration and with a large 2D Coulomb crystal containing 24 ions are presented.

### 5.1. Characterization of trap T1

Trap T1 is a linear rod Paul trap with cylindrical electrodes (see section 4.1). Due to the simple and robust construction and the large dimension of the trap, operation is straight forward. Still, characterization measurements have to be performed in order to find optimal parameters for Rydberg excitation. To our knowledge, there are no previous experiments with continuous wave VUV radiation in an ion trap. The VUV radiation may interfere with the ion trapping and has to be investigated thoroughly.

#### 5.1.1. Micro motion detection and compensation

Residual oscillating fields at the ion ( $E_{ion} \times \sin(\Omega_{rf}t)$ ) cause micro motion and contribute to the broadening of the Rydberg resonance via an oscillating Stark shift(see section 2.2).  $E_{ion}$  and the micro motion amplitude are related by

$$x_{mm} = \frac{E_{ion}Q}{\Omega_{rf}^2 m}, \quad (5.1)$$

with charge  $Q$  and mass  $m$ . Consequently, residual fields can be reduced by micro motion compensation. A number of techniques exist for micro motion detection [Ber98,Iba11] out

## 5. Trap characterization and preparatory experiments

of which several are used in our experiment: Spectroscopy of micro motion broadening of the Doppler transition at 397 nm wavelength and the pumping transition at 393 nm wavelength; Resolved spectroscopy of micro motion sidebands on the  $4S_{1/2} \leftrightarrow 3D_{5/2}$  transition; and finally the dependence of the ion's position on the trap drive amplitude.

We compensate the micro motion by static voltages applied to dedicated electrodes and a differential voltage applied to the two dc-electrodes (see section 4.1). Hence, we are restricted to micro motion compensation in radial direction in phase with the trap drive. Axial micro motion introduced by geometrical imperfections in the electrode alignment as well as micro motion due to phase differences between the signals on the rf-electrodes can not be compensated in trap T1.

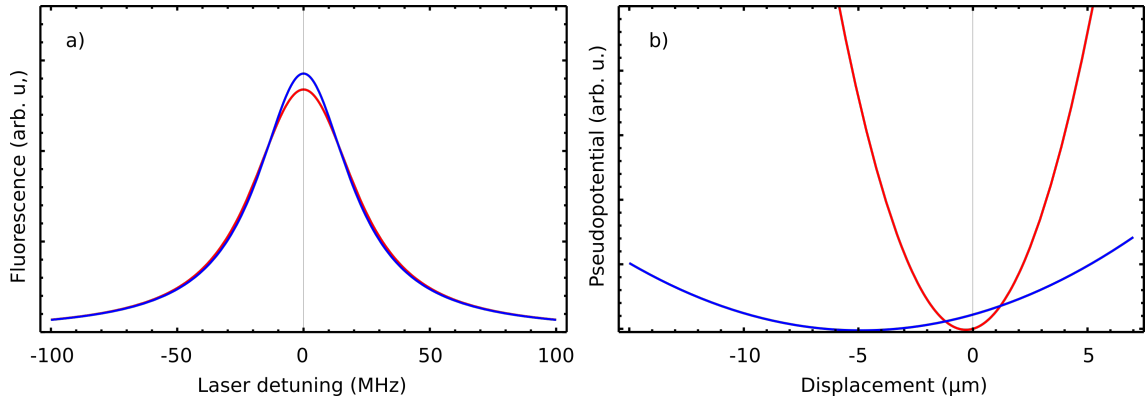


Figure 5.1.: **a)** Resonance of the  $4S_{1/2} \leftrightarrow 4P_{1/2}$  transition with  $\Gamma = 22.3$  MHz with (red) and without (blue) micro motion broadening. Parameters are  $\Omega_{rf}/2\pi = 3.5$  MHz and  $E_{ion} = 30$  V/m. The fluorescence on the side of the resonance ( $\Delta \approx \Gamma$ ) is almost indistinguishable, which makes it difficult to detect the broadening of the Doppler resonance. **b)** Pseudo potential for  $\omega_{rad}/2\pi = 200$  kHz (blue) and  $\omega_{rad}/2\pi = 50$  kHz (red) with an additional static field  $E_{comp} = 0.1$  V/m, corresponding to an oscillating field  $E_{ion} = 0.8$  V/m for the trapping parameters used in the Rydberg excitation experiments. While the potential minimum is only marginally shifted in the case of  $\omega_{rad}/2\pi = 200$  kHz the shift increases to  $5 \mu\text{m}$  for the lowered potential.

We detect radial micro motion in trap T1 by tracking of the ion's position at different rf-amplitudes [Glo15] as illustrated in Fig. 5.1b. This technique is most accurate at low vibrational frequencies as the position shift is given by

$$\Delta x = \frac{2Q}{m\omega_{rad}^2} \times E_{comp}, \quad (5.2)$$

with  $E_{comp}$  denoting the static field that shifts the ion out of position. A reduction of the radial potential to  $\omega_{rad}/2\pi = 50$  kHz leads to a shift of the ion's position of  $50 \mu\text{m}/(\text{V/m})$ . By determination of the horizontal (limited by resolution, precision  $\approx 1 \mu\text{m}$ ) and vertical

position (limited by depth of field, precision  $\approx 10\mu\text{m}$ ) stray fields can be detected in both radial directions with sensitivity of  $E_{comp,h} = 0.02\text{ V/m}$  and  $E_{comp,v} = 0.2\text{ V/m}$ . With trap parameters as employed in the Rydberg experiment of  $\Omega_{rf}/2\pi = 3.5\text{ MHz}$ ,  $\alpha_{rad} = 8 \times 10^6\text{ V/m}^2$  and  $\omega_{rad}/2\pi = 200\text{ kHz}$ , this static field corresponds to a shift of the ion of about  $0.06\mu\text{m}$  ( $0.6\mu\text{m}$ ) in horizontal (vertical) direction and consequently an oscillating Field of  $E_{ion} = 0.5\text{ V/m}$  ( $5\text{ V/m}$ ). The dependence of the ion's position on the rf-amplitude thus allows for fast and precise detection and compensation of radial oscillating fields.

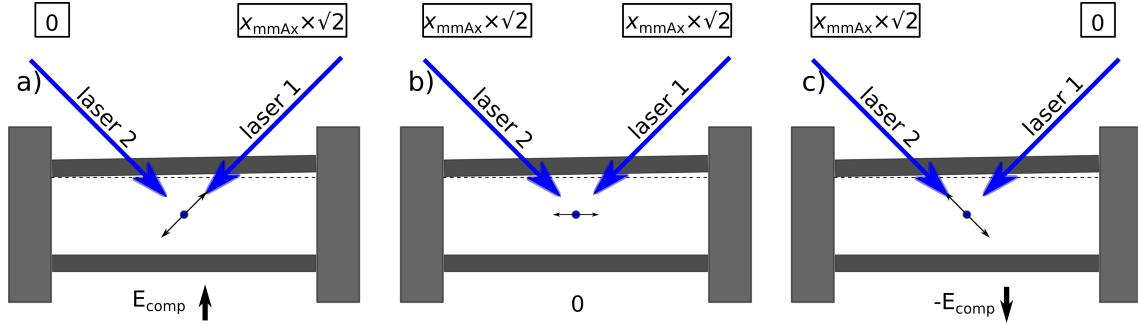


Figure 5.2.: A small misalignment of the electrodes leads to axial micro motion  $x_{mmAx}$ . **b)** With no stray fields present, measuring with probe lasers coming in at an angle of  $\pm\pi/4$  with respect to the trap axis will result in detecting a micro motion amplitude of  $x_{mmAx}/\sqrt{(2)}$ . **a)** and **c)** Applying a static compensation field produces radial micro motion  $x_{mmRad}$  in phase with the axial micro motion. If  $x_{mmAx} = \pm x_{mmRad}$  the projection of the micro motion to the wave vector  $\mathbf{k}$  of one probe laser beam is zero while the projection on the other one is  $x_{mmAx} \times \sqrt{2}$ . The absolute value of the residual electric field is increased by a factor  $\sqrt{2}$  compared to **b)**.

We determine the axial micro motion by measuring the induced Doppler broadening of the dipole allowed transition at 393 nm wavelength with a line width of  $\Gamma/2\pi \approx 20\text{ MHz}$ . Micromotion broadening is described by:

$$g(\omega) = \sum_n \left( J_n^2(\beta_{mm}) \frac{\Gamma}{\Gamma^2 + (\omega_0 + n\Omega_{rf} - \omega)^2} \right), \quad (5.3)$$

with the Bessel functions  $J_n$ , the modulation index  $\beta_{mm} = \mathbf{k}\mathbf{x}_{mm}$ , the natural line width  $\Gamma$ , the laser frequency  $\omega$  and the resonance frequency  $\omega_0$ . The broadening of the dipole transitions at wavelengths of 393 nm and 397 nm with natural line width  $\Gamma/2\pi \approx 20\text{ MHz} \gg \Omega_{rf}/2\pi = 3.5\text{ MHz}$  can be detected for a modulation index  $\beta_{mm} \gg 1$  only (see Fig. 5.1a).

The micro motion in axial direction stems from a misalignment of the electrodes (see section. 4.1) and is proportional to the trap drive amplitude  $U_{rf}$ . Knowledge of the axial

micro motion, which is the main contributor to the residual electric fields at the ion, is necessary. Direct axial access to the trap is blocked by the VUV-source and the photomultiplier, thus we have to deduce the amplitude of the axial micro motion from measurements with a laser beam at an angle of  $\phi = \pi/4$ . Three different compensation voltages are used corresponding to an angle of  $\Theta_{mm393} = (0, \pi/4, \pi/2)$  between the laser beam at 393 nm wavelength and the micro motion (see Fig. 5.2). We measure the line width of the  $4S_{1/2} \leftrightarrow 4P_{3/2}$  transition for each compensation voltage with the wavelength meter and determine 40 MHz FWHM, 55 MHz FWHM and 70 MHz FWHM respectively. From these line width and the trap drive frequency  $\Omega_{rf}/2\pi = 7.25 \text{ MHz}$ <sup>1</sup> we calculate the residual field in axial direction. The resonance line shape with micro motion is given by Eq. 5.3. With  $x_{mm}$  given by Eq. 5.1 we calculate  $E_{ion} = 120 \text{ V/m}$  for a peak to peak rf-voltage of 150 V. With the assumption of  $E_{ion} \propto U_{rf}$  we determine

$$E_{ion} = 0.8(3) \times \frac{U_{rf}}{m}. \quad (5.4)$$

### 5.1.2. Temperature and heating rate measurements

Ions may be heated by electrical noise [Bro15]. This limits the time available for experiments with a cold ion. The temperature of the ion can be measured by spectroscopy on the motional sidebands of the  $4S_{1/2} \leftrightarrow 3D_{5/2}$  transition. The measurement is repeated for various wait times, which in principle allows for the determination of the heating rates of all phonon modes.

In trap T1 we do not resolve the individual sidebands due to low vibrational frequencies. Instead we measured the envelope of the Doppler broadened  $4S_{1/2} \leftrightarrow 3D_{5/2}$  transition at 729 nm wavelength as plotted in Fig. 5.3a. With optimized low pass filters on the dc-electrodes we found that during 60 ms, twice the time we use for the VUV pulse in the Rydberg excitation experiment, the Gaussian line width of the Doppler envelope increases from  $\sigma = 0.73(4) \text{ MHz}$  to  $\sigma = 0.82(5) \text{ MHz}$  only. Assuming that the thermal motion of the ion is fully responsible for this broadening, we calculate approximate temperatures of 1.5 mK and 1.7 mK respectively. We deduce that during 60 ms the ion stays cold enough to not deteriorate experiments.

In the experimental sequence used for Rydberg excitation, we choose a larger detuning of the cooling laser to the  $4S_{1/2} \rightarrow 4P_{1/2}$  transition in order to increase the robustness of the cooling process. Consequently we do not reach very low temperatures in this case. The experimental data of a broadened resonance after Doppler cooling with large detuning is shown in Fig. 5.3b. The fit of a Gaussian distribution to the data yields  $\sigma = 1.3(3) \text{ MHz}$  which corresponds to a temperature of about 4(2) mK.

---

<sup>1</sup>these measurements were carried out at an earlier stage of the experiment when  $\Omega_{rf}/2\pi$  was not yet changed to 3.5 MHz



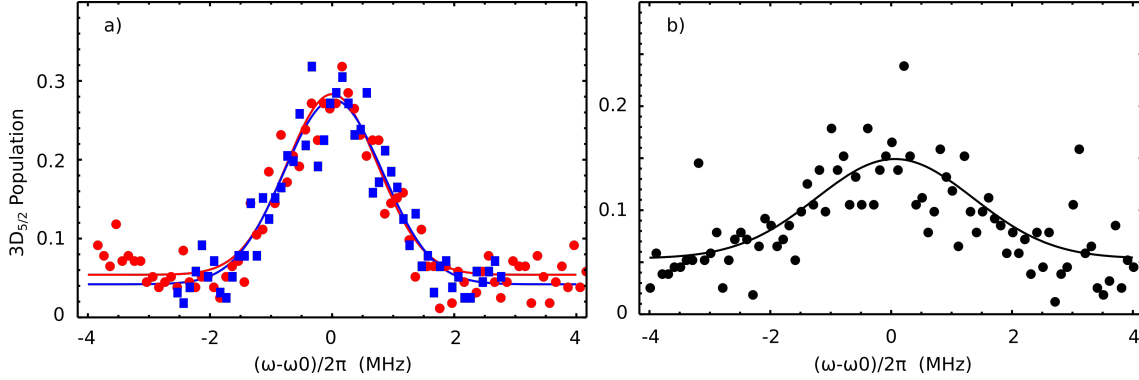


Figure 5.3.: a) Spectrum of the envelope of the motional sidebands on the  $4S_{1/2} \leftrightarrow 3D_{5/2}$  quadrupole transition. Spectrum after Doppler cooling (red) and after an additional wait time of 60 ms (blue). From the fitted Gaussian distributions we obtain  $\sigma = 0.73(4)$  MHz (red) and  $\sigma = 0.82(5)$  MHz (blue). b) The ion is cooled with a far detuned laser. From the Gaussian fit we obtain  $\sigma = 1.3(3)$  MHz which corresponds to a temperature of about 4(2) mK.

### 5.1.3. Ionization of background gas atoms

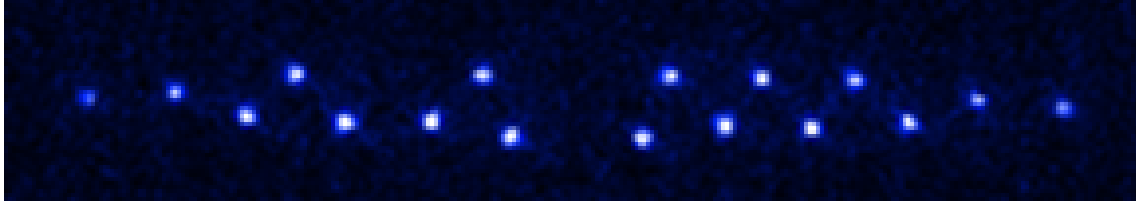


Figure 5.4.: Ionized background atoms sympathetically cooled into the trap lead to dark gaps in the otherwise regularly structured Coulomb crystal of fluorescing  $^{40}\text{Ca}^+$  ions.

The VUV light near 122 nm wavelength ionizes background gas atoms and molecules which are subsequently trapped and sympathetically cooled into the Coulomb crystal. These dark ions appear as gaps in the fluorescence image (see Fig. 5.4), which move around and result in unstable crystals. While we can selectively remove ions with larger mass than  $^{40}\text{Ca}^+$  from the trap by lowering the radial potential the same is not possible for lighter ions. In this case we have to remove the whole crystal from the trap and subsequently load new ions. Using VUV powers of about  $1 \mu\text{W}$  the dark ion loading rate is about  $0.03 \text{ s}^{-1}$ , leading to a large fraction of the experimental time being spend on reloading ions. Furthermore, even before we detect the dark ion, it transfers heat to the Coulomb crystal and disturbs the experiment.

Following these arguments, we have to prevent the ionized background atoms from being

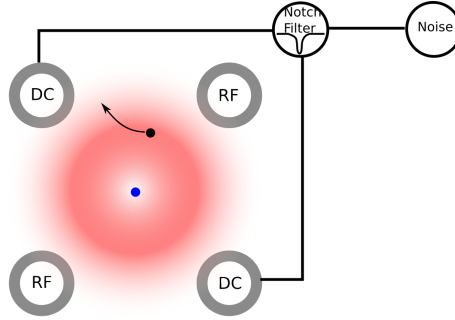


Figure 5.5.: Electric noise with quadrupolar geometry is applied to prevent loading of ions. The noise amplitude is low at the center of the trap and increases towards the outer regions of the trap. Consequently, cold ions are not disturbed, while an ion in the outer region is heated out of the trap. A notch filter, with resonances at the vibrational frequencies of  $^{40}\text{Ca}^+$  further reduces effects on the trapped crystal. The noise is only applied during Doppler cooling.

trapped in the first place. We achieve this by adding electric noise with quadrupolar geometry to the potential which results in a vanishing noise amplitude at the center of the trap where the ion crystal is localized. Parasitically ionized molecules and atoms however, occupy extended orbits far from the center and are heated. Thus, we prevent ions from being cooled into the trap as illustrated in Fig. 5.5. Additionally a notch filter at the vibrational frequencies  $\omega_x$  and  $\omega_y$  reduces the effect on the  $^{40}\text{Ca}^+$  ions.

It is sufficient to apply the noise during Doppler cooling only as sympathetic cooling of an ion into the Coulomb crystal takes much longer than one experimental cycle. Additional Doppler cooling for 1 ms after the noise is switched off ensures that the ion's thermal state during the Rydberg excitation is not influenced negatively.

#### 5.1.4. Spectroscopy on the $4S_{1/2} \leftrightarrow 3D_{5/2}$ transition

Excitation of the  $4S_{1/2} \leftrightarrow 3D_{5/2}$  transition with light at 729 nm wavelength allows for precise spectroscopic determination of the ions motion and the magnetic field on the one hand, and for coherent population transfer to specific Zeeman states of the  $3D_{5/2}$  level on the other hand. It is an important tool for precise spectroscopic investigation of Rydberg resonances starting from the  $3D_{5/2}$  state as well as a mandatory prerequisite for applications of Rydberg ions in quantum simulation or quantum information processing.

In a magnetic field the  $4S_{1/2} \leftrightarrow 3D_{5/2}$  transition splits into 10 Zeeman transition shown in Fig. 5.6. We apply a field of  $B \approx 0.3 \text{ mT}$  perpendicular to the laser beam at 729 nm wavelength. With this geometry, only the  $|\Delta m| = 2$  carriers can be excited. The absolute value of the magnetic field of 0.3 mT represents a good compromise between undesired broadening of dipole transitions and the possibility to resolve different Zeeman carriers of the quadrupole transition.

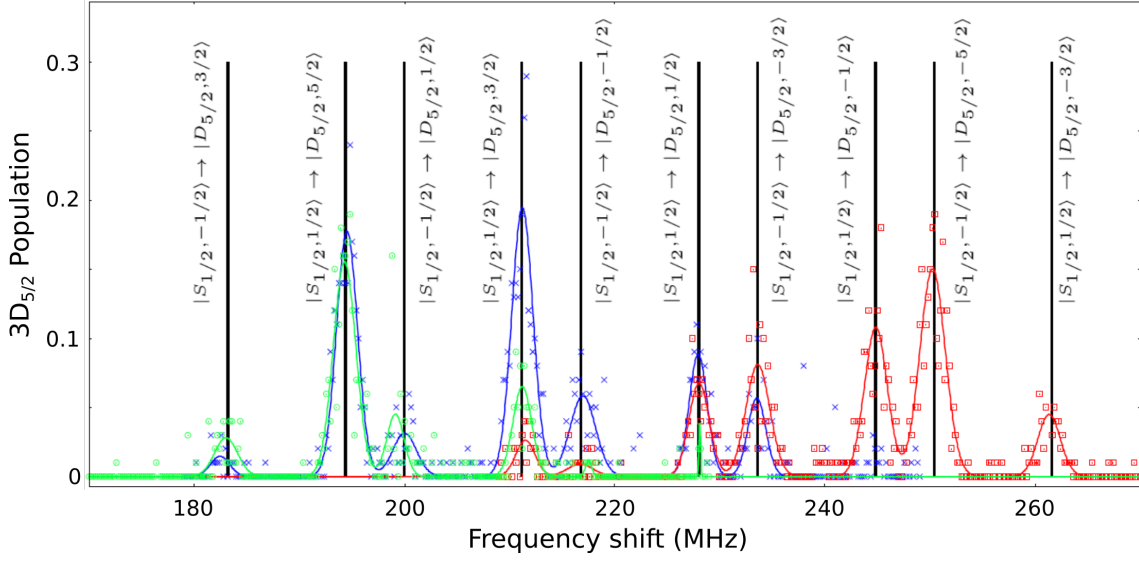


Figure 5.6.: Spectroscopy of all Zeeman transitions in a randomly oriented magnetic field of 1 mT. Subsequently the magnetic field was reduced to 0.3 mT and aligned perpendicular to the wave vector and the polarization of the light at 729 nm wavelength. This reduced the transitions to  $\Delta m = \pm 2$ . (Plot from Ref. [Pel13])

Two laser beams with different wave vectors  $\mathbf{k}$  are available for motional spectroscopy. One is aligned parallel to the Doppler cooling beam, which corresponds to a projection on all principal trap axes while the other one propagates vertically through the trap, thus only couples to the radial motion of the ion (see section 3.1.3). The respective spectra, plotted in Fig. 5.7 clearly show that trap T1 is not ideally suited for resolved sideband spectroscopy. The low vibrational frequency in axial direction leads to  $\sqrt{n}\eta \gg 1$  with Lamb-Dicke parameter  $\eta$  and phonon number  $n$ . Consequently a multitude of motional sidebands appear in the spectrum.

## 5.2. Characterization of trap T2

While trap T1 is simple to operate and suited for first experiments, important limitations, namely the low vibrational frequencies and the presence of axial micro motion, became obvious quickly. Trap T2 was built in order to overcome these limitations and provide better control of the axial potential which is now generated by segmented dc electrodes.

Due to the flexible potential, the trap volume can be fitted to specific requirements. A long trap is used for ion loading while a much shorter trap is used during Rydberg excitation. This way we could drastically reduce parasitic ion loading by VUV radiation. Hence, the use of injected noise (see section 5.1.3) is not necessary.

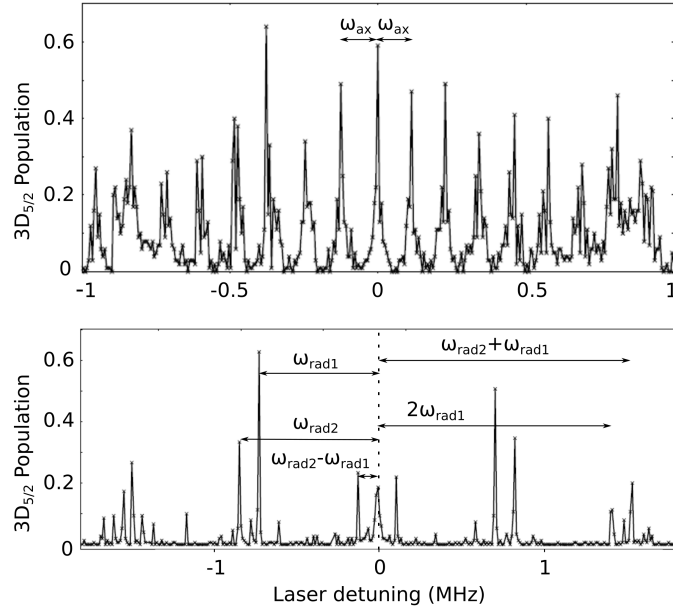


Figure 5.7.: a) Resolved sideband spectrum of the axial motion of a single ion. Due to the low axial vibrational frequency  $\omega_{ax}/2\pi = 120$  kHz which corresponds to Lamb-Dicke parameter of  $\eta = 0.2$ , a multitude of sidebands are observed. b) A spectrum taken with the vertical beam shows a much cleaner signal. The peaks can be clearly assigned to the frequencies of the radial modes  $\omega_{rad1}/2\pi = 720$  kHz,  $\omega_{rad2}/2\pi = 840$  kHz and their combinations. Plot from [Pel13].

### 5.2.1. Micro motion determination by sideband spectroscopy

We measure the micro motion in trap T2 by resolved sideband spectroscopy in three dimensions. For this purpose, the photomultiplier (see section 3.4) has been removed and an additional laser beam at 729 nm wavelength, aligned along the trap axis, has been installed. We measure the modulation index by comparing the Rabi-frequency on the micro motion sideband with the one on the carrier transition (see Eq. 5.3):

$$\frac{J_1(\beta_{mm})}{J_0(\beta_{mm})} = \frac{\Omega_{mm}}{\Omega_{car}}. \quad (5.5)$$

For  $\mathbf{k}\mathbf{x}_{mm} = \beta_{mm} \ll 1$  the Bessel functions can be approximated by  $J_0(\beta_{mm} \approx 1)$  and  $J_1(\beta_{mm} \approx \beta_{mm}/2)$ . Inserting Eq. 5.1 in Eq. 5.5 yields

$$E_{ion} = \frac{2\Omega_{rf}^2 m}{|\mathbf{k}| Q} \times \frac{\Omega_{mm}}{\Omega_{car}}. \quad (5.6)$$

Repetition of the experiment for different axial ion positions yields the axial pseudo potential presented in Fig. 5.8a. In the minimum, no axial micro motion is detected, while at a distance of  $9 \mu\text{m}$  the modulation index is increased to 0.28, which corresponds to a field of  $E_{ion} = 22.5 \text{ V/m}$  and an axial gradient of  $\alpha_{ax} = 2.5 \times 10^6 \text{ V/m}^2$ .

We determine radial micro motion with the same method with a laser beam in radial direction (see section 3.1.3). The data are presented in Fig. 5.8b, we measure a minimal modulation index of  $\beta_{mmRad} = 0.19$ . With  $\Omega_{rf}/2\pi = 6.5 \text{ MHz}$  and  $U_{rf} = 48 \text{ V}$  this corresponds to a minimal residual field of  $E_{min} = 15 \text{ V/m}$ . The reason for residual micro motion even at optimal compensation voltages is most likely a phase difference between the signals on the two rf-electrodes.

While the axial position of lowest micro motion is defined by the geometry of the segmented electrodes and thus stable over extended periods of time, radial micro motion has to be compensated regularly during the experiment, particularly during the use of the VUV laser. For this purpose, the horizontal micro motion is detected by sideband spectroscopy as described above while the vertical micro motion (equivalent to a horizontal displacement) is compensated by tracking the ion's position while varying the rf-amplitude (see section 4.1).

### 5.2.2. Temperature and heating rate measurements

We measure the temperature by comparing the Rabi-oscillations on the red and blue sidebands and the carrier of the  $4S_{1/2} \leftrightarrow 3D_{5/2}$  transition. In the Lamb-Dicke regime, defined by the condition  $\eta^2(2n+1) \ll 1$  the Rabi-frequencies for carrier and sideband transitions are given by [Roo00]:

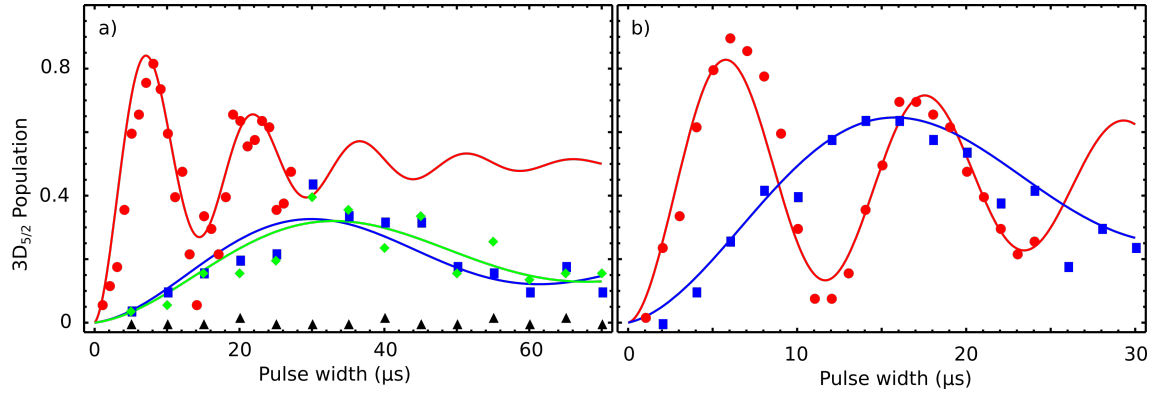


Figure 5.8.: a) Pulse width scan with an axial aligned laser beam on the carrier (red), on the micro motion sideband at the position of minimal axial micro motion (black) and at an axial displacement of  $\pm 9 \mu\text{m}$  (green and blue). For the scan on on the sideband the laser power was increased by a factor of 2.5. Rabi frequencies of  $\Omega_{\text{carrier}}/2\pi = 68 \text{ kHz}$  for the carrier transition and  $\Omega_{\text{mmAx}}/2\pi = 15 \text{ kHz}$  for the sideband transition of the displaced ion are observed. From these values a modulation index of  $\beta_{\text{mmAx}} = 0.28$  at an axial displacement of  $\pm 9 \mu\text{m}$  is deduced. b) Pulse width scan with a radial aligned laser beam on the carrier (red) with  $45 \mu\text{W}$  laser power and on the radial micro motion sideband (blue) with  $640 \mu\text{W}$  laser power for optimal compensation voltages. From the Rabi frequencies of  $\Omega_{\text{car}}/2\pi = 85 \text{ kHz}$  and  $\Omega_{\text{mmRad}}/2\pi = 30 \text{ kHz}$  we deduce a modulation index of  $\beta_{\text{mmRad}} = 0.19$ .

$$\Omega_{car} = \Omega_0(1 - \eta^2 n) \quad (5.7)$$

$$\Omega_{rsb} = \Omega_0 \eta \sqrt{n} \quad (5.8)$$

$$\Omega_{bsb} = \Omega_0 \eta \sqrt{n+1}. \quad (5.9)$$

Here,  $\Omega_0$  denotes the bare Rabi-frequency,  $\eta$  the Lamb-Dicke factor and  $n$  the phonon number. The phonon number distribution for the ion in a thermal state is given by

$$\rho_{th}(n) = \frac{\bar{n}^n}{(\bar{n} + 1)^{n+1}}, \quad (5.10)$$

with  $\bar{n}$  being the mean phonon number of the thermal state. Applying these formulas and taking into account the decoherence rate  $\gamma$  and the detection efficiency  $R_{up}$ , the probability to find the ion in the  $3D_{5/2}$  state after a laser pulse of width  $t$ , is given by

$$\rho D_{car,rsb,bsb}(t) = \frac{1}{2} \times R_{up} \sum_n \rho_{th}(n) (1 - \cos(\Omega_{car,rsb,bsb} t) \times e^{-\gamma t}). \quad (5.11)$$

The fitted data for the axial motion<sup>2</sup> are plotted in Fig. 5.9, similar measurements have been performed on the radial modes. We repeat these measurements for various wait times between cooling and spectroscopy pulse. The results are summarized in Tab. 5.1. The obtained heating rates are not very accurate due to a variety of limitations. First of all, the measurement is performed using a laser beam with a wave vector  $\mathbf{k}$  with angles  $\phi_{ax,rad1,rad2} = (\pi/4, \pi/3, \pi/3)$  with respect to the motional modes in the ion trap. Thus the phonons in the different modes are not measured independently. Furthermore, we assume that the ion is in the Lamb-Dicke regime. Using sideband cooling on all modes and vibrational frequencies of  $\omega_{ax,rad1,rad2}/2\pi = (0.65 \text{ MHz}, 1.2 \text{ MHz}, 1.4 \text{ MHz})$  this assumption is valid directly after cooling. However, after 10 ms of wait time we arrive at  $\eta^2(2n+1) = 0.13$  for the axial mode which results in significant deviations from the approximations in Eq. 5.7.

### 5.3. Single ion addressing on the $4S_{1/2} \leftrightarrow 3D_{5/2}$ transition

The VUV beam propagates on the trap axis and consequently illuminates the Coulomb crystal globally. The excitation of specific ions to Rydberg states thus requires single ion addressing on the  $4S_{1/2} \leftrightarrow 3D_{5/2}$  transition in order to selectively initialize ions which are subsequently excited to the Rydberg state. The single ion addressing beam at 729 nm wavelength is tightly focused by the camera lens with  $NA = 0.27$  and propagates vertically through the trap (see section 3.1.3). The tight focus and the radial alignment allow for single ion addressing at typical trap operation parameters.

---

<sup>2</sup>fit with software RabiMCMC; Ulrich Poschinger

mode	axial	radial 1	radial 2
$\omega/2\pi$ in MHz	0.65	1.2	1.4
$\bar{n}$ wait time 0 ms	2	12	6
$\bar{n}$ wait time 10 ms	22	20	17
$\frac{\gamma}{\bar{n}}$ in $\text{ms}^{-1}$	2	0.8	1.1

Table 5.1.: Summarized results of the temperature measurements in trap T2 at given vibrational frequencies. The obtained heating rates allow for resolved sideband cooling. Rydberg excitation is limited to a few 10 ms before the resonance is significantly broadened by the thermal motion of the ion.

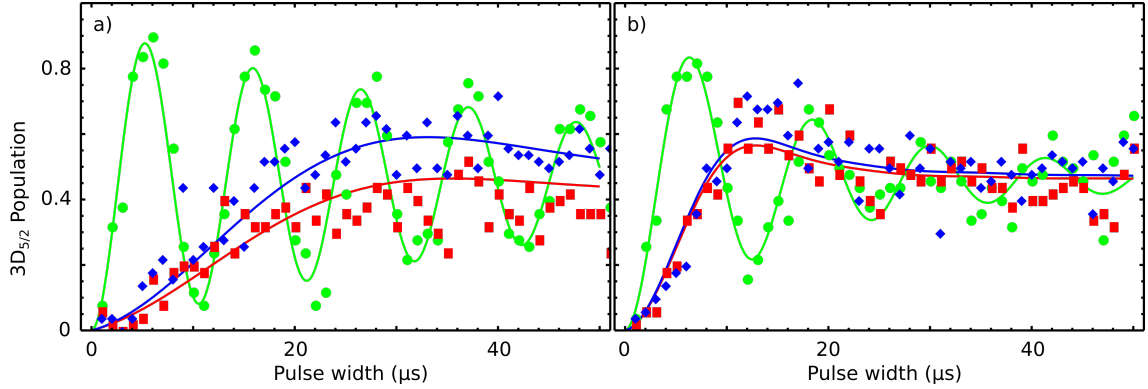


Figure 5.9.: **a)** Rabi-oscillations on the red and blue sideband (red and blue) and the carrier (green). The Rabi-frequency on the carrier  $\Omega_{car}/2\pi \approx \Omega_0/2\pi = 95$  kHz is much higher than on the sidebands  $\Omega_{rsb}/2\pi = 11.4$  kHz  $\approx \Omega_{bsb}/2\pi = 14.7$  kHz. Fitting the data with Eq. 5.11 yields  $\bar{n} = 2$ . The decoherence rate of  $\gamma = 18 \text{ ms}^{-1}$  prevents the observation of oscillation on the sidebands. **b)** The same spectrum with 10 ms wait time in between cooling and spectroscopy pulse. The Rabi-frequencies on the sidebands are increased to  $\Omega_{rsb}/2\pi = \Omega_{bsb} = 36$  kHz. From the fitted data we obtain  $\bar{n} = 22$  which corresponds to a heating rate of 2 phonons/ms.



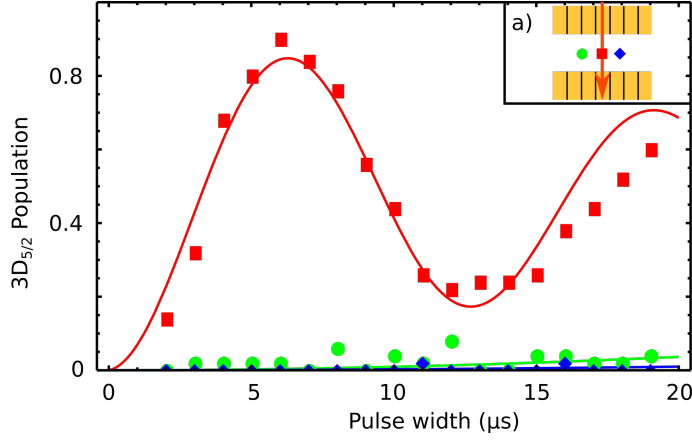


Figure 5.10.: Addressed excitation of the central ion from a three ion string. The central ion (red) flops at a Rabi-frequency of  $\Omega_{add}/2\pi = 80$  kHz. The excitation of the outer ions (green and blue) is negligible. Inset a), illustrates the alignment of laser and ion crystal.

Addressed excitation of the central ion out of a three ion string is presented in Fig. 5.10. We obtain a Rabi-frequency of  $\Omega_{add}/2\pi = 80$  kHz for the addressed ion. The population of both non-addressed outer ions remains small for pulse width  $< 20 \mu\text{s}$ , we estimate a Rabi-frequency of  $\Omega_{non}/2\pi < 3$  kHz. From this data and an axial vibration frequency of  $\omega_{ax}/2\pi = 600$  kHz which corresponds to an inter ion distance of  $d \approx 7 \mu\text{m}$  we calculate a beam waist of  $w_0 = 4 \mu\text{m}$ . Population transfer to the  $3D_{5/2}$  state with a  $\pi$ -rotation on the addressed ion is limited by ion temperature and beam pointing stability to about 85%.

For the addressed excitation of multiple ions, we rely on the capability to transport ions along the traps axis (see section 4.2) instead of steering the laser beam. In Fig. 5.11, the excitation of the two outer ions from a three ion string is plotted. In between laser pulses the ion is shifted by  $2d = 14 \mu\text{m}$  along the trap axis. We apply linear voltage ramps of  $\Delta U = \pm 280$  mV and  $\tau_{\Delta U} = 500 \mu\text{s}$  to trap segments 4 and 8. We obtain Rabi-frequencies of  $\Omega_{add}/2\pi = 35$  kHz for both outer ions and  $\Omega_{non}/2\pi = 3$  kHz for the central ion. The residual excitation of the central ion is caused by two laser pulses in this case.

The transport operations between laser pulses might excite axial motion of ions. We measured the motion by resolved sideband spectroscopy (see section 5.2.2) before and after a pair of transport operations which shifted a single ion by  $14 \mu\text{m}$  and back to the original position. Thermal and coherent motion of the ion increased by  $\Delta\bar{n}_{th} = 7$  and  $\Delta\bar{n}_{coh} = 1.5$  respectively, thus the ion stay sufficiently cold for Rydberg excitation after the transport. With an optimized experimental sequence, transport operations may get faster and introduce less heating [Wal12].

Addressed excitation of single ions is not limited to small ion strings but can be extended to large 2D Coulomb crystals. The excitation of a single ion out of a large 31-ion Coulomb

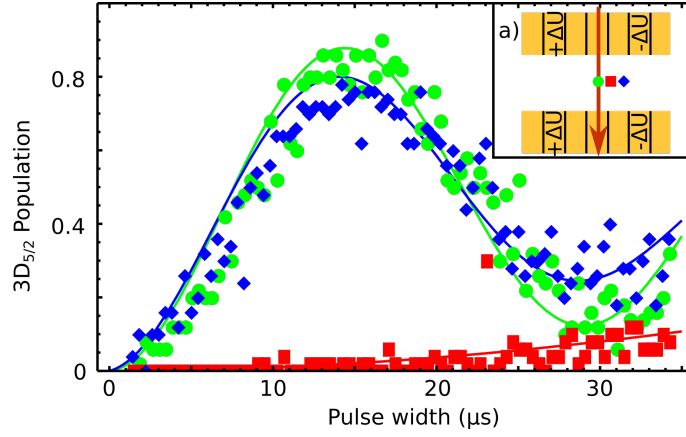


Figure 5.11.: Addressed excitation of the two outer ions (green and blue) from a three ion string. In between laser pulses the ion crystal is shifted by  $2d = 14\,\mu\text{m}$ . Voltage ramps of  $\Delta U = \pm 280\,\text{mV}$  are applied to trap segments 4 and 8 for this purpose.

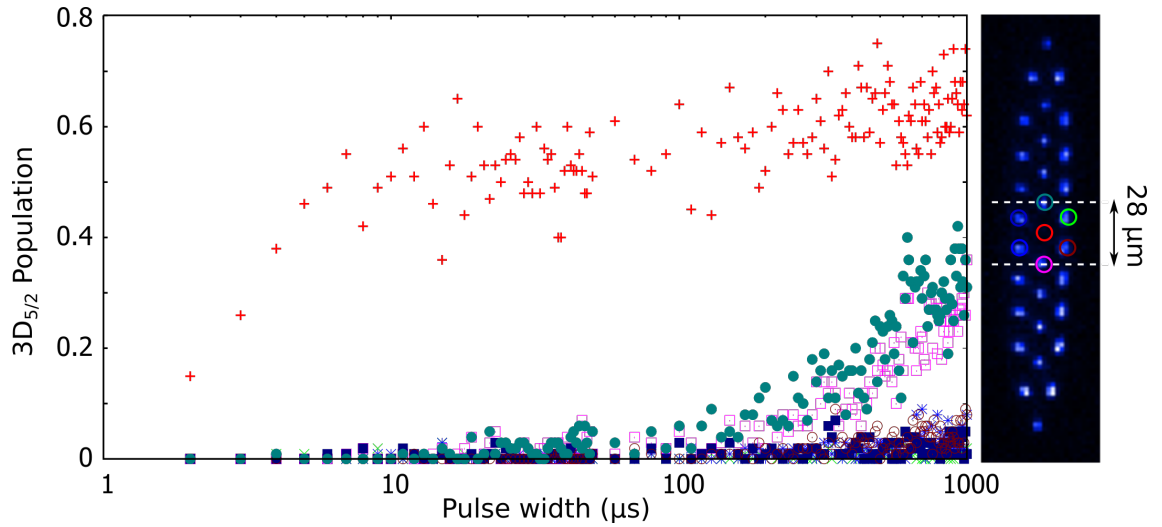


Figure 5.12.: Pulse width scan with the single ion addressing beam. The center ion of the plaquett (red) is addressed by the laser. A pulse of  $\tau \approx 4.5\,\mu\text{s}$  transfers 30% of the population to the  $3D_{5/2}$  state. The other ions are only excited by much longer pulses of  $\tau > 100\,\mu\text{s}$ . The weak potential in trap T1 and the multitude of mode in the large crystal prevent coherent excitation of the addressed ion.

crystal with an inter ion distance of  $d = 14 \mu\text{m}$  confined in trap T1 is presented in Fig. 5.12. The addressed ion is excited to the  $3D_{5/2}$  state with 50% fidelity for pulse width  $\tau < 10 \mu\text{s}$ , while the surrounding ions are not affected at all. Only for much longer laser pulses some excitation of the two adjacent ions on the trap axis is observed.

## 5.4. Characterization of the VUV beam

The power, wavelength, beam shape and beam alignment of the VUV radiation have to be controlled precisely for Rydberg excitation of trapped ions. We monitor the power with a photomultiplier and the wavelength of all fundamental light fields involved in the four wave mixing with a wavelength meter (see section 3.3). We perform knife edge measurements in vacuum by placing a sharp edge or tip into the beam and measuring the transmission with the photomultiplier. A full beam waist characterization has been performed prior to the installation of the ion trap.

Two orthogonal razorblades, mounted on a 2D translation stage, allow for the precise determination of  $w_{0x}$  and  $w_{0y}$ . We repeated this measurement for multiple z-positions in order to completely characterize the VUV beam. This way we optimized the collimation of the beam by the first  $\text{MgF}_2$  lens (see section 3.3) and subsequently measure and optimize the focus of the beam after the second  $\text{MgF}_2$  lens. The beam profile as measured with razorblades in vertical and horizontal directions is plotted in Fig. 5.13. We measure a focus of  $w_{0x} = 12 \mu\text{m}$  and  $w_{0y} = 16 \mu\text{m}$  at a focal length of 160 mm and beam quality parameters of  $M_x^2 = 7.4$  and  $M_y^2 = 9.4$ .

Additionally, in situ measurements are performed regularly, using a needle tip<sup>3</sup> positioned inside the ion trap (see section 3.4). These in situ measurements are particularly important due to drifts in beam pointing and the dispersion of the employed  $\text{MgF}_2$  lens for light near 122 nm wavelength. The in situ measurement is performed at the position of the ion (trap T1) or on the trap axis at a distance of approximately 2 mm from the trap center (trap T2). The restricted space between the trap electrodes does not allow for the use of orthogonal blades, but instead a sharp needle tip is positioned inside the trap. We monitor the needle tip with the detection system and align it with respect to the trap center. From the cutoff of the beam transmission at the tip, the beam waist in vertical and horizontal direction is deduced as illustrated in the insets of Fig. 5.14. In horizontal direction, the curved shape of the needle tip results in a less accurate measurement as compared to using razorblades. However for a beam waist smaller than the radius of curvature of the needle tip, the deviations are acceptable. The data are plotted in Fig. 5.14, we obtain a spot size of  $w_{0x} = 10 \mu\text{m}$  and  $w_{0y} = 11 \mu\text{m}$  in the focus which is in good agreement with the method described above. The beam alignment precision is limited by the accuracy of the needle tip's alignment. In trap T1 the horizontal alignment is limited

<sup>3</sup>acupuncture needle; diameter  $250 \mu\text{m}$

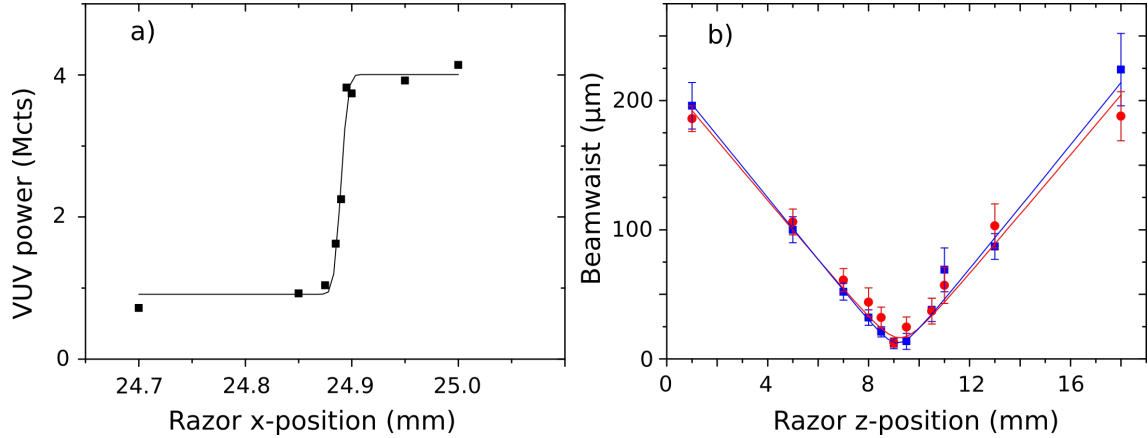


Figure 5.13.: a) A knife edge measurement in the focus of the beam is plotted. Fitting the data with an error function yields the beam waist  $w_0 = 10 \mu\text{m}$  of the Gaussian beam. The beam profile in b) is obtained by repeating this measurement for various  $z$  positions along the beam axis. Fitting with  $w = w_0 \sqrt{1 + (z/z_0)^2}$  results in a focus  $w_{0x} = 12 \mu\text{m}$ ,  $w_{0y} = 16 \mu\text{m}$  and a Rayleigh length  $z_{0x} = 0.5 \text{ mm}$ ,  $z_{0y} = 0.7 \text{ mm}$ . From Rayleigh length and focus we deduce beam quality parameters of  $M_x^2 = 7.4$  and  $M_y^2 = 9.4$ .

only by the resolution of the detection system and thus accurate to a few  $\mu\text{m}$ . The vertical position on the other hand is less accurate (about  $30 \mu\text{m}$ ) as we can only deduce it from the depth of field information. In trap T2, additional uncertainties of about  $20 \mu\text{m}$  in both dimensions arise as the needle is not positioned at the trap center but at a distance of  $2 \text{ mm}$ .

## 5.5. Experiments with doubly ionized $^{40}\text{Ca}^{2+}$ ions

With the photo ionization of trapped  $^{40}\text{Ca}^+$  ions we demonstrate an interaction of the VUV radiation near a wavelength of  $121 \text{ nm}$  and the laser cooled ion crystal for the first time. We generate mixed Coulomb crystals, consisting of  $^{40}\text{Ca}^+$  and  $^{40}\text{Ca}^{2+}$  ions, and investigate their behavior in the Paul trap. The experimental work presented in this section is published in Ref. [Fel14]. It investigates the influence of impurities (e.g. ions with a different vibrational frequency) in Coulomb crystals on structure and vibrational modes. Using mixed crystals with doubly charged ions instead of Rydberg excitations as impurities, we benefit from the effectively infinite lifetime of  $^{40}\text{Ca}^{2+}$  ions as compared to a lifetime of about  $100 \mu\text{s}$  for a Rydberg excitation. We investigate in detail radial modes and configuration changes. The presented experiments with  $^{40}\text{Ca}^{2+}$  ions can be considered as an important step towards mode shaping experiments with Rydberg excitations [Li13]. Still, one important aspect of the proposed mode shaping and ion crystal configuration is

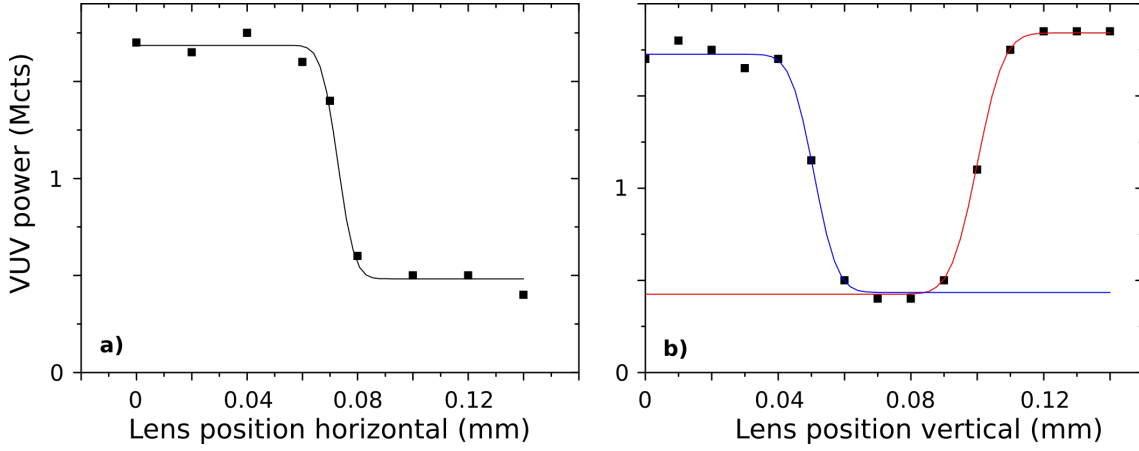


Figure 5.14.: Transmission cutoff at the needle in a) horizontal and b) vertical direction. The data are fitted with error functions in order to obtain the beam waist  $w_{0x} = 10 \mu\text{m}$  and  $w_{0y} = 11 \mu\text{m}$ . a) The beam waist is small as compared to the curvature of the needle tip resulting in an accurate measurement. b) The needle's diameter is given by the distance between the falling and rising edge of the transmission signal.

not captured: Only coherent Rydberg excitation would give complete control over these effects, including superposition states.

Assuming the well justified pseudo potential approximation [Lei03b], a linear Paul trap is fully described by a static potential in axial direction with angular frequency

$$\omega_z = 2\sqrt{q\beta/M} \quad (5.12)$$

and a pseudo potential in radial direction with angular frequency

$$\omega_r = \sqrt{2((q\alpha/(M\Omega))^2 - q\beta/M)}, \quad (5.13)$$

where  $q$  denotes the charge,  $M$  the mass of the ion and  $\alpha, \beta$  the curvature of the dynamic and static electric potential. By applying an offset voltage  $V_{\text{of}}$  to the dc-electrodes an additional static electric potential  $\beta_{\text{rad}}$  is induced and the radial pseudo-potential reads:

$$\omega_{x,y} = \sqrt{2((q\alpha/(M\Omega))^2 - q\beta/M \mp q\beta_{\text{rad}}/M)}. \quad (5.14)$$

From Eq. 5.14 follows that the static ( $\propto \sqrt{q/m}$ ) and dynamic ( $\propto q/m$ ) parts of the potential scale differently with  $q/M$ . The axial vibrational frequency is increased by  $\sqrt{2}$  for  $^{40}\text{Ca}^{2+}$  compared to singly ionized calcium. The relation of the radial vibrational frequencies is more complex due to the combination of dynamic and static parts in the potential. In general, the higher frequency mode is increased by a factor of  $\sqrt{2}$  to 2 while

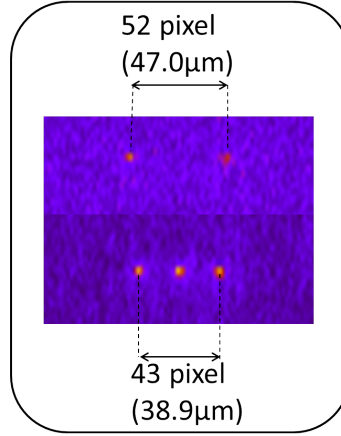


Figure 5.15.: Fluorescence image of a three ion crystal with a  $^{40}\text{Ca}^{2+}$  in the center. Compared to the pure crystal the elongation is increase by 21%. We use this elongation as a tool to detect  $^{40}\text{Ca}^{2+}$  and distinguish is from other impurities.

the lower frequency mode is increased by more than a factor of 2.

The experiments were carried out in trap T1 (see section 4.1), operated at an rf-amplitude of  $U_{\text{rf}} = 100 \text{ V} - 200 \text{ V}$  and a frequency  $\Omega_{\text{rf}}/(2\pi) = 10.66 \text{ MHz}$ . This results in vibrational frequencies for  $^{40}\text{Ca}^+$  of  $\omega_x/(2\pi) = 150 \text{ kHz} - 500 \text{ kHz}$  and  $\omega_y/(2\pi) = 450 \text{ kHz} - 650 \text{ kHz}$ . The end caps are operated at adc voltage of 400 V which yields an axial vibrational frequency of  $\omega_z/(2\pi) = 119 \text{ kHz}$ .

For photo-ionization of  $^{40}\text{Ca}^+$  we first load a linear string of three ions. The ions are pumped to the  $3D_{3/2}$  state by laser light at 397 nm wavelength, before we apply a pulse of VUV light at 121.26 nm wavelength which corresponds to a photon energy slightly above the ionization limit. Since a doubly-charged ion does not resonantly scatter light near 397 nm a successful formation of  $^{40}\text{Ca}^{2+}$  is characterized as a dark gap in the ion crystal. However, such dark gaps may also result from loading of ions from ionized background gas. In order to verify the ionization of a  $^{40}\text{Ca}^+$  and to discriminate  $^{40}\text{Ca}^{2+}$  from accidentally loaded ions of other species we check the length of the crystal ( $\text{Ca}^+ - \text{Ca}^{2+} - \text{Ca}^+$ ), which increases by 21% (see Fig. 5.15) and the lowest frequency axial eigenmode which increases by 15% compared to a pure  $^{40}\text{Ca}^+$  crystal. We produce larger crystals with an impurity ion also starting from a three ion crystal, ionize one of the ions and finally load the desired number of additional  $^{40}\text{Ca}^+$  ions into the trap. This way we make sure that the crystal contains a single  $^{40}\text{Ca}^{2+}$  ion.

### 5.5.1. Vibrational modes of mixed three-ion crystals

The  $^{40}\text{Ca}^{2+}$  impurity leads to modified vibrational modes compared to a pure  $^{40}\text{Ca}^+$  crystal (see section 2.2.3). The broken symmetry of the crystal gives rise to radial modes

which, except for the rocking mode with  $^{40}\text{Ca}^{2+}$  in central position ( $\uparrow \circ \downarrow$ ), are no longer orthogonal to the center of mass mode [Lin13]. Hence, modes can be excited by applying a resonant radiofrequency to one of the dc-electrodes. We concentrate on the radial modes of the crystal since these are the most interesting for mode shaping. The axial modes of a three-ion crystal with  $^{40}\text{Ca}^{2+}$  have been measured previously by Kwapien et al. [Kwa07].

We determine the eigenfrequency of the respective mode by measuring the oscillation amplitude of the ions with respect to the applied radiofrequency at a constant rf-amplitude. The oscillation amplitude results in a smeared out fluorescence image of the ion as the oscillation period is short compared to the camera exposure time. The eigenfrequency of the mode is determined as the central frequency of a Gaussian, fitted to the oscillation amplitude. We avoid non-linear response [Ake10] by keeping a low excitation amplitude. The simulated and measured frequencies are shown in Fig. 5.16 and agree to about 1 kHz, the deviation can be explained by errors in the determination of the eigenfrequency (0.5 kHz) and a drift of the trapping potential between measurement and calibration where the trap frequencies  $\omega_{x,y,z}$  are measured with a single  $^{40}\text{Ca}^+$ . The rf-amplitude  $U_{\text{rf}}$  is not perfectly stable but decreases slowly over time which leads to the observed trapping potential drift of  $\Delta\omega_{x,y}/(2\pi) \approx 10$  kHz over the course of a day. For the highest frequency modes, the  $^{40}\text{Ca}^{2+}$  exhibits an approximately 50 times higher oscillation amplitude than the  $^{40}\text{Ca}^+$ . These could not be measured exactly because the oscillation amplitude of the  $^{40}\text{Ca}^+$  is too small to be detected with the camera. When we increase the rf amplitude the crystal melts due to strong oscillation of the  $^{40}\text{Ca}^{2+}$  ion before we can detect an oscillation of the  $^{40}\text{Ca}^+$  ions.

The zigzag mode of a crystal with  $^{40}\text{Ca}^{2+}$  in outer position (Fig. 5.16c) is shifted to lower frequencies compared to the zigzag mode of a three-ion  $^{40}\text{Ca}^+$  crystal, while the zigzag mode of a crystal with  $^{40}\text{Ca}^{2+}$  in central position (Fig. 5.16a) is shifted to higher frequencies. This result agrees with the observed behavior of the zigzag transition in section 5.5.2.

### 5.5.2. Structural changes in a three-ion crystal by an $^{40}\text{Ca}^{2+}$ impurity

The configuration of an ion crystal in the potential given by Eq. 5.14 is determined by the anisotropy parameters  $\gamma_{x,y} = \omega_z^2/\omega_{x,y}^2$ . For tight radial confinement  $\omega_{x,y} \gg \omega_z$  the ions form a linear string aligned on the  $z$ -axis. Lowering the radial confinement causes a phase transition to a zigzag configuration at  $\gamma = \gamma_{\text{crit}}$  [Enz00, Ulm13, Pyk13]. For  $\gamma_x > \gamma_y$  this zigzag crystal is confined to the  $xz$ -plane which prevents it from rotating around the  $z$ -axis.

From Eq. 5.14 follows that the static ( $\propto \sqrt{q/m}$ ) and dynamic ( $\propto q/m$ ) parts of the potential scale differently with  $q/m$ , resulting in a different  $\gamma$  for  $^{40}\text{Ca}^{2+}$  compared to singly ionized calcium. The values of  $\gamma$  given in this section, always refer to the vibrational frequencies of singly charged  $^{40}\text{Ca}^+$ . To measure the phase transitions of different three-

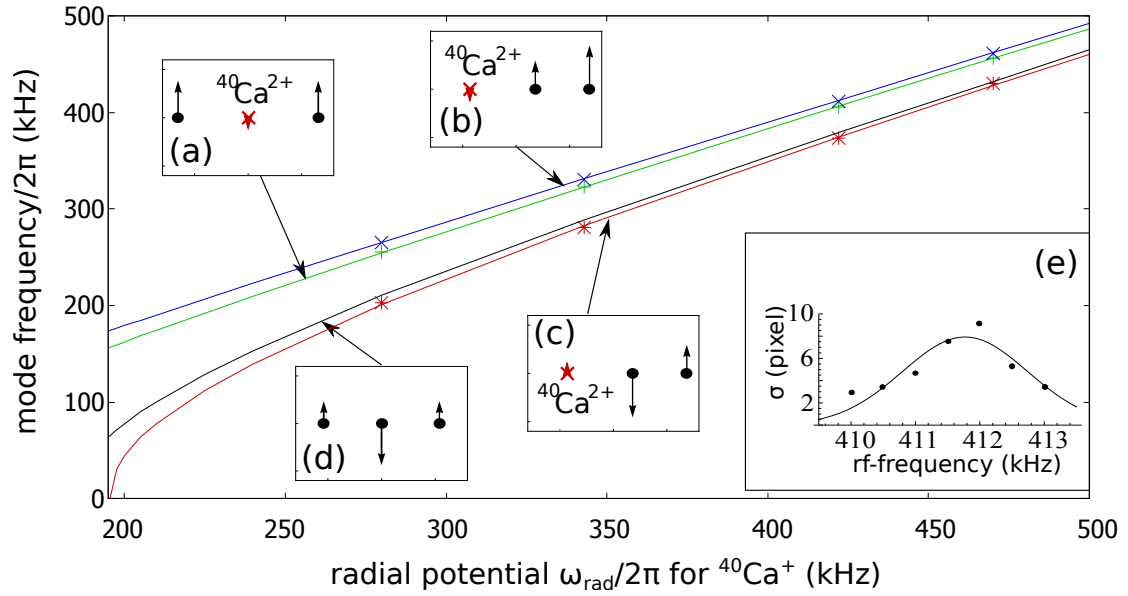


Figure 5.16.: Measured and simulated frequencies of selected modes of mixed ion crystals. Dots represent measured values while lines are from numerical simulations. The small insets (a-c) show the modes which were measured. For comparison the simulated frequency of the zigzag mode (d) without <sup>40</sup>Ca<sup>2+</sup> is also shown. (e) The oscillation amplitude of the ions is plotted for different radiofrequencies. The eigenfrequency is determined as the center frequency of a Gaussian fitted to the oscillation amplitude as a function of the applied rf-frequency. Plot from Ref. [Fel14]



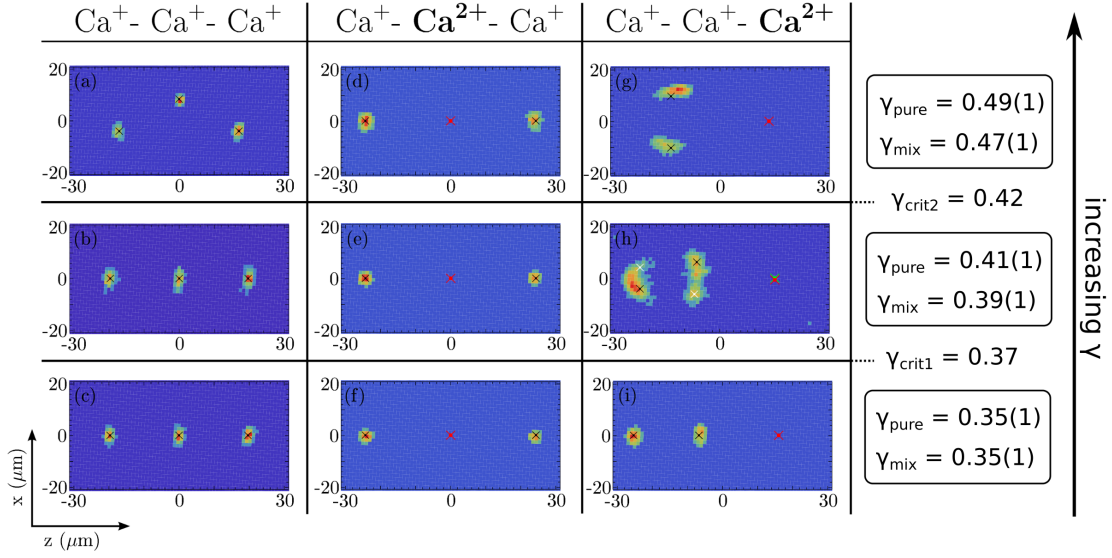


Figure 5.17.: Fluorescence images (a-i) of three-ion crystals, without  $^{40}\text{Ca}^{2+}$  ion and with  $^{40}\text{Ca}^{2+}$  ion in central or outer position, for different anisotropy parameters. Simulated positions are indicated as black ( $^{40}\text{Ca}^+$ ) and red ( $^{40}\text{Ca}^{2+}$ ) crosses. In (h) there are additional crosses in white ( $^{40}\text{Ca}^+$ ) and green ( $^{40}\text{Ca}^{2+}$ ) for the mirrored configuration. The reason for slightly different  $\gamma$  for crystals with ( $\gamma_{\text{mix}}$ ) and without  $^{40}\text{Ca}^{2+}$  ( $\gamma_{\text{pure}}$ ) is a drift of the trapping potential between these measurements. Plot from Ref. [Fel14].

ion crystals the static potentials  $\beta = 14.7(2) \text{ kV/m}^2$  and  $\beta_{\text{rad}} = 37(1) \text{ kV/m}^2$  are kept constant, the values are determined from the oscillation frequency of a single trapped  $^{40}\text{Ca}^+$  ion. The dynamic potential  $\alpha$  is varied using a rf-attenuator.

Measured and simulated configurations of the Coulomb crystal are shown in Fig. 5.17. In the case of a mixed ion crystal  $\gamma_{\text{crit}}$  depends on the position of the  $^{40}\text{Ca}^{2+}$  ion. We observe three different regimes: For  $\gamma < \gamma_{\text{crit1}}$  all crystals are linear strings, for  $\gamma_{\text{crit1}} < \gamma < \gamma_{\text{crit2}}$  only the crystal with  $^{40}\text{Ca}^{2+}$  in outer position is in zigzag configuration while the others are still linear and for  $\gamma > \gamma_{\text{crit2}}$  the crystal with a central  $^{40}\text{Ca}^{2+}$  ion is the last one remaining in the linear configuration. We could not observe a zigzag crystal with  $^{40}\text{Ca}^{2+}$  in central position at all, instead the  $^{40}\text{Ca}^{2+}$  always moves to the outside for  $\gamma \gg \gamma_{\text{crit2}}$ . The theoretical predicted critical anisotropy parameters for the three-ion  $^{40}\text{Ca}^+$  crystal  $\gamma_{\text{crit2}} = 0.42$  and the  $^{40}\text{Ca}^{2+}$  at the outer position  $\gamma_{\text{crit1}} = 0.37$  agree with the experiment.

In order to compare observed ion positions of the three-ion crystal with the simulation, a coordinate conversion is applied to the pictures. The line of sight of the imaging system and the crystal plane normal are under  $45^\circ$ , so the scaling in x- and z-direction is stretched by a factor of  $\sqrt{2}$ . Additionally a deviation of  $3^\circ$  between the crystals center line and the z-direction, due to misalignment of the imaging system, has been taken into account.

After this transformation, the deviation between simulated and measured positions is below  $1\text{ }\mu\text{m}$  for all pictures except for Fig. 5.17g with a deviation of  $3.7\text{ }\mu\text{m}$  and Fig. 5.17h where a fit was not possible. Such deviation may be attributed to a drift of the trapping potential which occurs between calibration and measurement. The additional deviation in Fig. 5.17g can be attributed to a small error in stray field compensation so that the trapping potential minimum is shifted for  $^{40}\text{Ca}^{2+}$  compared to  $^{40}\text{Ca}^+$ .

Close to the critical trap anisotropy, when  $\gamma$  is barely bigger than  $\gamma_{\text{crit}}$ , the potential barrier between mirrored degenerate configurations is small enough to enable the ion to change configurations many times during camera exposure time under Doppler cooling conditions [Rei02]. This results in a broadening of the detected peak, as seen in Fig. 5.17h and prevents exact determination of ion positions.

### 5.5.3. Local modes in linear crystal with $^{40}\text{Ca}^{2+}$ impurity

A long ion string can be divided into separately oscillating parts by impurity ions. Here we use a  $^{40}\text{Ca}^{2+}$  ion, which is subjected to a much stiffer radial confinement in the trap, for the tailoring of radial modes. We prepare a string of five  $^{40}\text{Ca}^+$  and one  $^{40}\text{Ca}^{2+}$  positioned as the third ion in the chain and excite the radial modes. We find that for each mode the oscillation is almost completely restricted to either the upper or the lower ions (see Fig. 5.18).

The measured frequencies and eigenvectors are in good agreement with simulations. The eigenfrequencies of the modes are  $2\pi \times 468\text{ kHz}$  (Fig. 5.18a),  $2\pi \times 463\text{ kHz}$  (Fig. 5.18b),  $2\pi \times 423\text{ kHz}$  (Fig. 5.18c) and  $2\pi \times 403\text{ kHz}$  (Fig. 5.18a) for vibrational frequencies of  $\omega_z = 2\pi \times 119\text{ kHz}$ ,  $\omega_x = 2\pi \times 480\text{ kHz}$  and  $\omega_y = 2\pi \times 630\text{ kHz}$  for a single  $^{40}\text{Ca}^+$  ion. In addition to the observed modes shown in Fig. 5.18 there exists a mode with eigenfrequency  $2\pi \times 1006\text{ kHz}$  where almost exclusively the  $^{40}\text{Ca}^{2+}$  oscillates and a mode with eigenfrequency  $2\pi \times 352\text{ kHz}$  for which the oscillation is localized to the lower sub crystal. Simulations show that for the modes with eigenfrequencies of  $2\pi \times 423\text{ kHz}$  and  $2\pi \times 403\text{ kHz}$  the oscillation amplitude on different sides of the  $^{40}\text{Ca}^{2+}$  differs by a factor of  $\approx 30$  while ions on the same sub-crystal have similar oscillation strength. The results imply that the mode density for the sub-crystals is much lower than for a string of six  $^{40}\text{Ca}^+$  ions trapped in the same potential. The minimal frequency separation for modes on the same sub-crystal is  $2\pi \times 45\text{ kHz}$  compared to  $2\pi \times 15\text{ kHz}$  for a pure  $^{40}\text{Ca}^+$  crystal.

### 5.5.4. Ring modes in planar Coulomb crystals

Localized modes of vibration created by impurities in large Coulomb crystals are of great interest for quantum simulation experiments. One example is the Kagome lattice [Nat15]. In this section, Kagome lattice modes around a single  $^{40}\text{Ca}^{2+}$  impurity in a 2D Coulomb crystal are investigated. A Coulomb crystal consisting of 23  $^{40}\text{Ca}^+$  and one  $^{40}\text{Ca}^{2+}$  ion is trapped and cooled. With vibrational frequencies of  $\omega_z/2\pi = 120\text{ kHz}$ ,  $\omega_x/2\pi = 284\text{ kHz}$

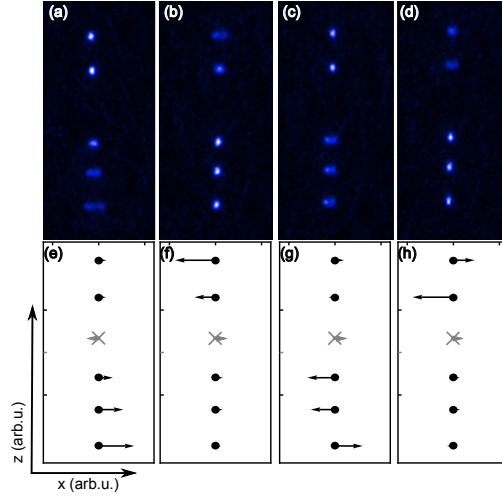


Figure 5.18.: Upper part: Fluorescence images of excited local modes (a-d) in a linear string with  $^{40}\text{Ca}^{2+}$  impurity. The local excitation of ions is observed from the broadening of the ion image in radial direction. The oscillation amplitudes of the ions fit well to the simulated eigenvectors of the modes (e-f). Figure from Ref. [Fel14].

and  $\omega_y/2\pi = 729\text{ kHz}$  for  $^{40}\text{Ca}^+$ , these ions form a two dimensional crystal as shown in Fig. 5.19c. The  $^{40}\text{Ca}^{2+}$  ion is always located on the trap axis as it is confined by a stronger radial potential.

Simulations show that the mode structure of the crystal is divided into lower frequency in-plane modes and higher frequency out-of-plane modes (see Fig. 5.19a). The two modes with eigenfrequencies of  $2\pi \times 890\text{ kHz}$  and  $2\pi \times 1210\text{ kHz}$  feature a strong oscillation amplitude of the  $^{40}\text{Ca}^{2+}$  ion. In particular the highest frequency mode consist of a strong out-of-plane oscillation of the  $^{40}\text{Ca}^{2+}$  ion and a weaker oscillation of the six surrounding ions. With rf-tickling, we could excite the mode at  $\omega/2\pi \approx 1190\text{ kHz}$  (see Fig. 5.19c) but could not show the localized character of the mode. This can be explained as follows: We do not observe the oscillation of the  $^{40}\text{Ca}^{2+}$  ion which does not scatter light, but only the oscillation of the surrounding  $^{40}\text{Ca}^+$  ions which have an oscillation amplitude smaller by about an order of magnitude. In order to see the oscillation of the surrounding ions in the fluorescence image, the amplitude of the resonant rf-field has to be large which leads to a huge oscillation of the  $^{40}\text{Ca}^{2+}$  ion. At amplitudes large enough for detection, the whole ion crystal is disturbed by the oscillating  $^{40}\text{Ca}^{2+}$  ion. A similar observation has been made for the highest frequency modes of much smaller three ion crystals with a  $^{40}\text{Ca}^{2+}$  impurity (see section 5.5.1). With a more sophisticated detection scheme, where the camera is synchronized to the ions oscillation [Roß15], the detection sensitivity may be improved in the future allowing for verification of the localized character of the mode.

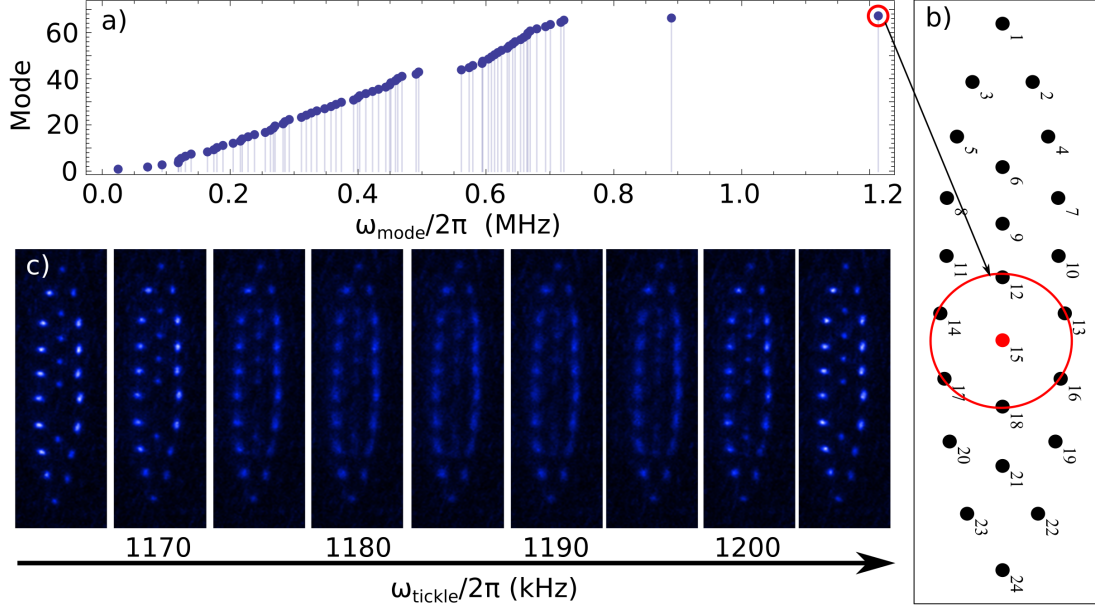


Figure 5.19.: a) Simulated mode spectrum of a 24 ion crystal. The in-plane modes ( $\omega/2\pi = 0 - 500$  kHz) and out-of-plane modes ( $\omega/2\pi = 550 - 750$  kHz) are clearly separated. Due to its higher charge, the  $^{40}\text{Ca}^{2+}$  impurity ion generates modes at much higher frequencies of  $\omega/2\pi = 890$  kHz and  $\omega/2\pi = 1210$  kHz. Rf-excitation of a vibrational mode around  $\omega/2\pi = 1190$  kHz. b) Simulation of the spacial structure of the same crystal ( $\omega_z/2\pi = 120$  kHz,  $\omega_x/2\pi = 284$  kHz,  $\omega_y/2\pi = 729$  kHz). The  $^{40}\text{Ca}^{2+}$  ion at position 15 is indicated by a red dot. We are particularly interested in an out-of-plane mode which has localized amplitude on the  $^{40}\text{Ca}^{2+}$  and the six surrounding ions indicated by the black circle. c) Rf-excitation of a vibrational mode around  $\omega/2\pi = 1190$  kHz in a 24 ion crystal with one  $^{40}\text{Ca}^{2+}$ . The frequency is close to the predicted value of  $\omega/2\pi = 1210$  kHz but the local character of the mode is not observed.

## 6. Rydberg excitation of trapped $^{40}\text{Ca}^+$

As compared to atomic species typically used in neutral atom Rydberg experiments like Rb (ionization threshold  $33691\text{ cm}^{-1}$ ) the energy needed for Rydberg excitation of ions is larger by a factor of two to four, posing a considerable challenge for the development of UV or VUV laser sources at the appropriate wavelength. The ionization thresholds of singly charged ions of the alkali-earth group used in ion trap experiments are given in Tab. 6.1. They range from  $80686\text{ cm}^{-1}$  for  $\text{Ba}^+$  to  $146883\text{ cm}^{-1}$  for  $\text{Be}^+$ , which corresponds to wavelengths of  $123.9\text{ nm}$  -  $68.1\text{ nm}$ .

$\text{Ca}^+$ ,  $\text{Sr}^+$  and  $\text{Ba}^+$  feature long lived  $D$  states which, when employed as an initial state for the Rydberg excitation, effectively lower the required excitation energy. Starting from the  $3D_{3/2}$  or  $3D_{5/2}$  state in  $\text{Ca}^+$  reduces the Rydberg excitation energy to a wavelength in the range of  $122\text{ nm}$  -  $124\text{ nm}$ . This is close to the Lyman- $\alpha$  wavelength in hydrogen at  $121.57\text{ nm}$  wavelength, for which a continuous wave source for coherent radiation is available at our institute. With some modifications (see section 3.3) this laser source is employed for the Rydberg excitation of  $^{40}\text{Ca}^+$  ions.

Ion	$E_{ion}(S)$ ( $\text{cm}^{-1}$ )	$\lambda_{ion}(S)$ (nm)	$E_{ion}(D)$ ( $\text{cm}^{-1}$ )	$\lambda_{ion}(D)$ (nm)
$\text{Be}^+$	146 883	68.1	-	-
$\text{Mg}^+$	121 268	82.5	-	-
$\text{Ca}^+$	95 752	104.4	82 041	121.9
$\text{Sr}^+$	88 965	112.4	74 129	134.9
$\text{Ba}^+$	80 686	123.9	75 011	133.3

Table 6.1.: Ionization wavelengths and energies for singly charged alkali-earth ions from the ground state and, if available, from the metastable  $D$  state [Nat16].

Experiments were carried out in two linear Paul traps described in Chapter 4. The VUV beam (see section 3.3) propagates axially through the trap. A scheme of the trap with all relevant laser beams is presented in Fig. 6.1.

For an estimation of the Rydberg excitation rates we need, in addition to the VUV intensity, the transition dipole moment  $\mu$  and the line width  $\Gamma$  of the broadened resonance. The transition dipole moment to low lying states scales with  $n^{-3/2}$  (see section 2.1) and can be approximated for the transition from the metastable  $3D$  states to the Rydberg  $P$  manifold by [SK11]

$$\mu_{3DnP} = 0.383e \times r_B \times n^{-1.588} \quad (6.1)$$

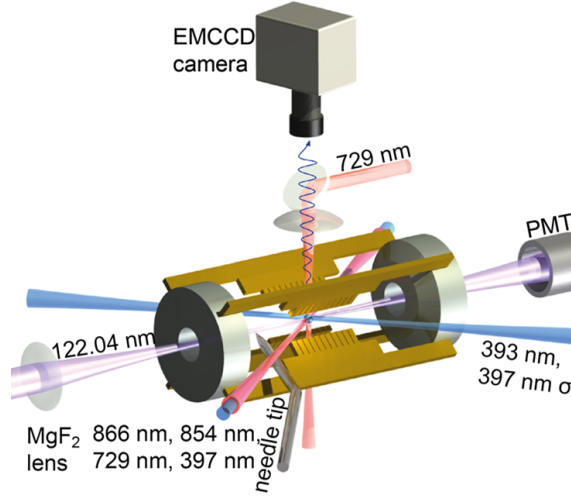


Figure 6.1.: Sketch of the trap and the relevant laser beams. The VUV beam propagates axially through the trap, it's power is monitored with a photomultiplier. Laser beams at wavelengths of 393 nm, 397 nm, 729 nm, 854 nm and 866 nm are available for the manipulation of the low lying electronic states of  $^{40}\text{Ca}^+$ . A tightly focused beam at 729 nm wavelength allow for individual addressing of single ions. Fluorescence at 397 nm wavelength is imaged to an EMCCD camera. Figure from Ref. [Fel14].

resonance	wavelength	FWM efficiency	VUV power
$3D_{5/2} \rightarrow 22F$	123.256 nm	$6 \mu\text{W}/\text{W}^3$	$0.15 \mu\text{W}$
$3D_{3/2} \rightarrow 52F$	122.042 nm	$70 \mu\text{W}/\text{W}^3$	$8 \mu\text{W}$
$3D_{3/2} \rightarrow 53F$	122.033 nm	$20 \mu\text{W}/\text{W}^3$	$2 \mu\text{W}$
$3D_{5/2} \rightarrow 66F$	122.041 nm	$140 \mu\text{W}/\text{W}^3$	$15 \mu\text{W}$
$3D_{3/2} \rightarrow 23P$	123.218 nm	$90 \mu\text{W}/\text{W}^3$	$2 \mu\text{W}$
$3D_{3/2} \rightarrow 53P$	122.046 nm	$20 \mu\text{W}/\text{W}^3$	$2 \mu\text{W}$

Table 6.2.: Approximate values for FWM efficiency and VUV power at wavelengths of selected transitions. Both, FWM efficiency and power of the fundamental fields are subjected to fluctuations, in the table maximal values are given. In day to day use the available power is typically a factor of 2 to 10 lower. In general, the power of the fundamental wave at 580 nm used for generation of VUV light near 123 nm is about a factor of five lower than the power at 555 nm wavelength, used for generation of VUV light near 122 nm wavelength. The VUV power at the ion is lower by a factor of 6 compared to the VUV power generated in the mixing region due to losses induced by optical elements. This factor is included in the values given in the last column of the table.

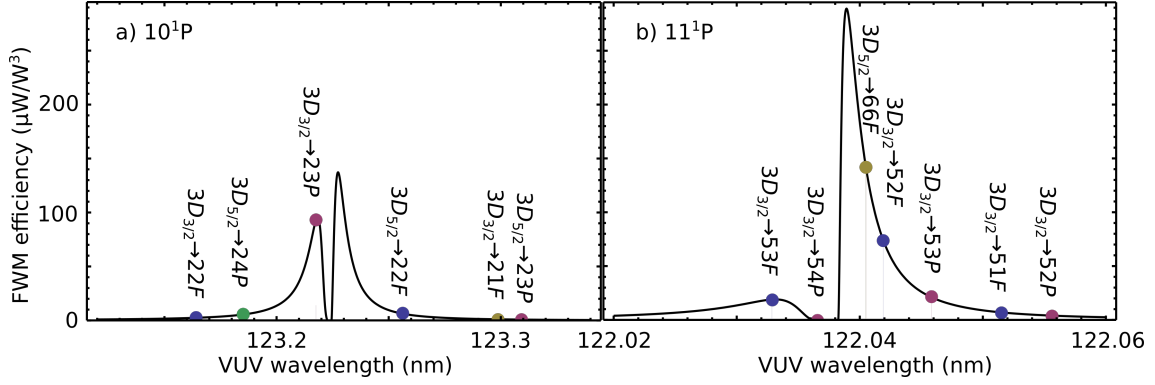


Figure 6.2.: Calculated four-wave-mixing efficiency around the  $10^1P$  (a) and  $11^1P$  (b) resonance. Transitions to Rydberg states are indicated. The symmetry of the resonances can be tuned by the beam parameters of the fundamental waves to a certain extent in order to optimize the efficiency at the wavelength of Rydberg resonances.

with the elementary charge  $e$  and the Bohr radius  $r_B$ . The transition dipole moment for the transition from the  $3D$  states to Rydberg  $F$  states of the same principal quantum number is about ten times larger [Li]. The scattering cross section for light at frequency  $\omega$  is given by

$$\sigma = \mu^2 \times \frac{2\omega_0^3}{3\epsilon_0\hbar c^3} \times \frac{\lambda^2}{4} \times g(\omega). \quad (6.2)$$

Here,  $g(\omega)$  denotes the line shape function of the resonance,  $\omega_0$  the resonance frequency of the transition,  $\epsilon_0$  the vacuum electric permittivity,  $\hbar$  the Planck constant,  $c$  the speed of light and  $\lambda$  the wavelength of the light. The excitation rate  $R$  is calculated from the cross section as

$$R = \sigma \times \frac{Int}{\hbar\omega}, \quad (6.3)$$

with  $Int$  denoting the laser intensity at the ion. In Fig. 6.3, excitation rates in dependence of beam waist and beam alignment for the transitions to various Rydberg states are plotted. The rates for each resonance were calculated using the VUV power given in Tab. 6.2.

Initialization of the ion in the metastable  $3D_{3/2}$  or  $3D_{5/2}$  state, not only results in a more accessible transition wavelength but also allows for simple and efficient detection of the Rydberg excitation. The modified electron shelving scheme (see section 2.3) is based on the discrimination between states that scatter light, ( $4S_{1/2}$ ,  $3D_{3/2}$ ) and a dark state that does not scatter photons during Doppler cooling ( $3D_{5/2}$ ). Rydberg excitation, followed by a decay back to the (meta)stable states, will lead to a population transfer between

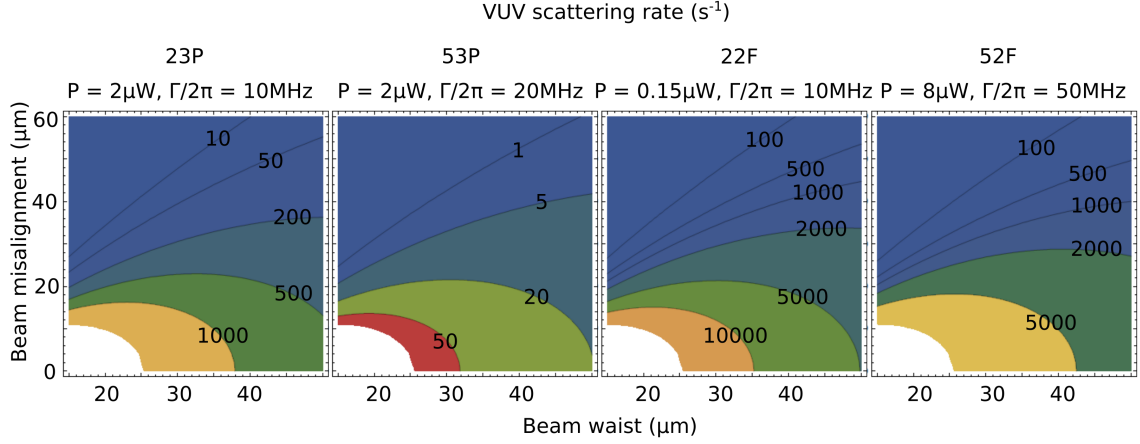


Figure 6.3.: Excitation rates to various Rydberg states at optimal VUV power. Different line widths are estimated for the individual transitions due to the difference in polarizability of Rydberg states. The excitation of Rydberg  $F$  states is easier due to the large transition dipole moment. With a beam waist of  $30\ \mu\text{m}$  and a beam adjustment precision of  $20\ \mu\text{m}$ , the excitation rate of all four states is sufficient to be detected in the experiment.

these states. Subsequently we determine the population of these states by a fluorescence measurement. Depending on the initial state ( $3D_{3/2}$  or  $3D_{5/2}$ ) and the target Rydberg state ( $nP$  or  $nF$ ) we use different variations of this scheme. The detection efficiency is determined by the branching ratio out of the initial state and varies between  $p_P \approx 1/2$  for  $P$  state detection and  $p_F \approx 1/16$  for  $F$  state detection. Using the electron shelving for the detection of the Rydberg state, we benefit from the much longer lifetime of the metastable states ( $\tau \approx 1\text{ s}$ ) as compared to the Rydberg states. This allows for a fluorescence detection with an exposure time of a few ms, and results in near unity fidelity for the discrimination between bright and dark states [Sau86]. Consequently, even if we use only a single ion, very low Rydberg excitation rates in the order of  $1\text{ s}^{-1}$  can be detected.

### 6.1. Rydberg excitation to the states $52F$ , $53F$ and $66F$

The results presented in this section are published in Ref. [Fel15]<sup>1</sup>. Ions are initialized in the metastable  $3D_{3/2}$  or  $3D_{5/2}$  state before they are excited to the  $52F$  and  $53F$  (from  $3D_{3/2}$ ), or respectively  $66F$  (from  $3D_{5/2}$ ), state with vacuum ultraviolet radiation near a wavelength of  $122\text{ nm}$ .

The state  $52F$  has been excited in trap T1 operated at a trapping potential of  $\omega_{ax,rad}/(2\pi) =$

<sup>1</sup>The discrepancy in the principal quantum numbers of the excited states compared to the ones given in the paper are due to additional information that was gained by the excitation of the state  $22F$ . A detailed explanation is given in appendix A



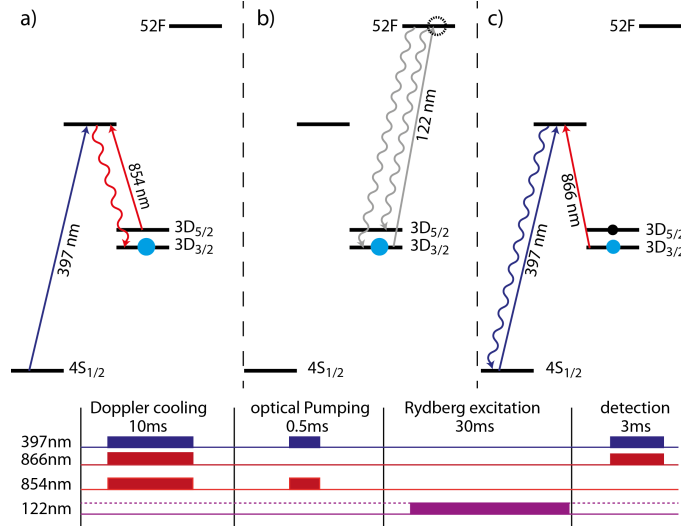


Figure 6.4.: Pulse sequence and level scheme for the excitation and detection of the Rydberg states  $52F$  and  $53F$ . The ions are initialized in the  $3D_{3/2}$  state. A 30 ms VUV pulse excites the ion to the  $52F$  state from where it decays either back to the initial  $3D_{3/2}$  state or to the  $3D_{5/2}$  state (probability  $p \approx 1/16$ ). Successful Rydberg excitation is indicated by population of the dark state.

(90, 200) kHz and a trap drive frequency of  $\Omega_{rf}/2\pi = 3.5$  MHz. The Rydberg states  $52F$ ,  $53F$  and  $66F$  have been excited in trap T2 operated at  $\omega_{ax,rad}/(2\pi) = (270, 700)$  kHz and a trap drive frequency of  $\Omega_{rf}/2\pi = 6.5$  MHz. Measurements have been performed with single ions and, in order to speed up data acquisition, with linear three-ion and five-ion crystals. The experimental sequence used for excitation of  $52F$  and  $53F$  is illustrated in Fig. 6.4.

- i) Initialization by optical pumping to the  $3D_{3/2}$  state (lifetime: 1176(11) ms [Kre05]).
- ii) VUV excitation by a 30 ms pulse. The Rydberg state then decays and within 30 ms is either back in the initial state or the  $3D_{5/2}$  (lifetime: 1168(9) ms [Kre05]) the detection efficiency is therefore dominated by the branching fractions out of the initial state.
- iii) Detection: Under resonant excitation with laser light at 397 nm and 866 nm the ion emits no fluorescence light, if the Rydberg excitation in (ii) was successful. The transition resonances to  $52F$  and  $53F$  are shown in Fig. 6.5.

We observe Rydberg excitation to the  $52F$  state at 122.041 913(5) nm wavelength and to the  $53F$  state at 122.032 384(10) nm wavelength. The line width of the excitation to the  $52F$  varies between 60 MHz and 400 MHz full-width at half-maximum (FWHM), depending on the trap control parameters. For the  $F$  resonances the branching ratio between the decay from the Rydberg state into the  $3D_{5/2}$  and  $3D_{3/2}$  state is estimated to be about 7%, using data from lower-lying Rydberg states [Nat16]. Thus our detection efficiency is limited to about 7%. In addition to the population transfer, double ionization followed by ion loss, is observed on resonance in  $\sim 0.3\%$  of the Rydberg excitations.

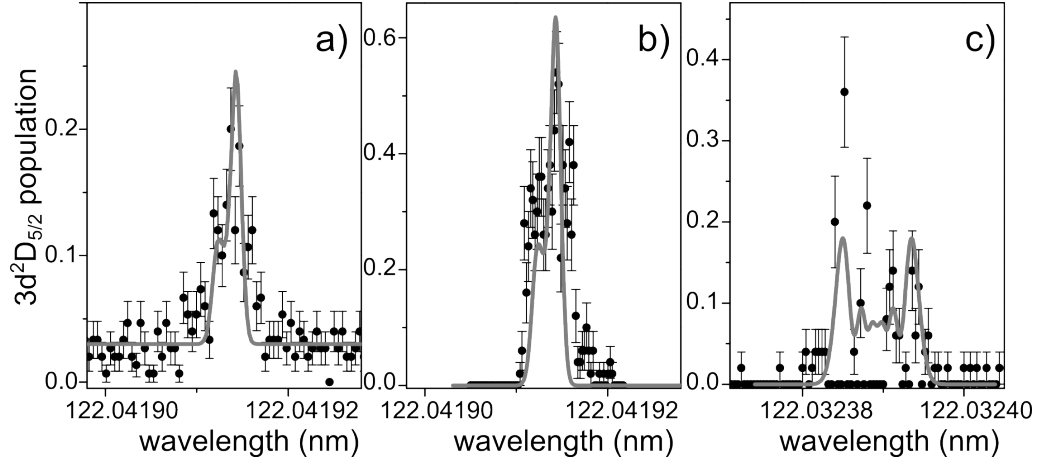


Figure 6.5.: a) and b): Rydberg excitation from the  $3D_{3/2}$  to the  $52F$  state, at a VUV power of  $\approx 0.5 \mu\text{W}$  and 30 ms pulse duration. The trap (trap T1) is operated at motional frequencies of  $\omega_{ax,rad}/(2\pi) = (90, 200)$  kHz. Different peak heights are due to variations of the VUV power and alignment for different measurement runs. a) Ground state population is optically pumped to the  $3D_{5/2}$  state after the Rydberg excitation. The line width is  $\simeq 60$  MHz full-width-at-half-maximum (FWHM). b) No optical pumping, only the direct population transfer to  $3D_{5/2}$  is observed. c) Excitation from the  $3D_{3/2}$  to the  $53F$  state in trap T2, operated at motional frequencies of  $\omega_{ax,rad}/(2\pi) = (270, 700)$  kHz. The line shape model includes broadening by thermal excitation, magnetic field, micro motion and Stark effect. Measurements were performed with a single ion, 150 cycles for each data point in a), while for b) and c) each data point is obtained from 50 cycles, the error bars depict the quantum projection noise. Plot from Ref. [Fel14].

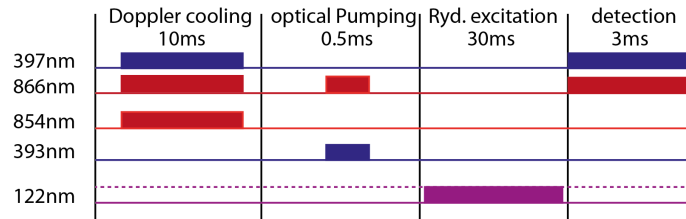


Figure 6.6.: Pulse sequence for the excitation of  $66F$ . In contrast to the sequences for the excitation of the states  $52F$  and  $53F$ , the ions are initialized to the  $3D_{5/2}$  state by optical pumping with the laser at 393 nm wavelength.

Higher lying Rydberg states are searched with a similar detection sequence. For a similar wavelength as compared to the transitions  $3D_{3/2} \rightarrow 52F$ , the initialization of ions in the  $3D_{5/2}$  state gives access to Rydberg states with principal quantum numbers around  $n = 66$ . The sequence is illustrated in Fig. 6.6. We do not observe population transfer exceeding the 3% background caused by the finite lifetime of the  $3D_{5/2}$  state. However, we see significantly increased ion loss rates, as in the case of the other resonances, between wavelengths of 122.040 46 nm and 122.040 55 nm. We ascribe this ion loss to the excitation of the  $66F$  state at 122.040 50(5) nm wavelength. The resonance was scanned in 50 MHz steps with 50 cycles at each frequency.

In both traps we have observed that the excitation of high lying Rydberg states with  $n > 50$  becomes unstable after several months of experimenting. Contamination of electrode surfaces by Ca from the loading atomic beam might be an explanation for this behavior; as the work function of Ca is much smaller compared to Au, we expect a high flux of electrons from contaminated surfaces, accelerated by the rf-trap. These electrons may perturb the highly susceptible Rydberg states preventing us from observing the resonance. For future experiments we plan to use an optimized trap (see section 8.4). The electrodes of this optimized trap T3 are completely shielded from the calcium beam and the VUV beam in order to avoid VUV-induced photo-emission of electrons close to the trapped ions.

## 6.2. Excitation to the Rydberg state $22F$

In this section, excitation to the Rydberg state  $22F$  is presented, the results are published in Ref. [Bac16]. With polarizability scaling as  $n^7$ , energy difference between adjacent states as  $n^3$  and spread of the wave function as  $n^2$ , this state is much less influenced by the trap field and other perturbations as compared to the state  $52F$  (see sections 6.4 and 2.2), which allows for a more systematic investigation of related effects. We can start from an undisturbed situation and increase the perturbation in controlled steps.

The lower polarizability of the  $22F$  state allows for the operation of the trap at higher vibrational frequencies of  $\omega_i/2\pi \approx 1$  MHz and, correspondingly, lower Lamb-Dicke parameters  $\eta$ . This enables us to combine the coherent excitation of the  $4S_{1/2} \leftrightarrow 3D_{5/2}$  quadrupole transition at 729 nm wavelength with Rydberg excitation near 123 nm wavelength and provides an extended tool-box for the experiment [Lei03a]. Initialization of ions via coherent excitation of the  $4S_{1/2} \leftrightarrow 3D_{5/2}$  instead of incoherent optical pumping is a step towards Rydberg quantum logic with trapped ions. The sharp  $4S_{1/2} \leftrightarrow 3D_{5/2}$  resonance allows for the initialization of ions into specific Zeeman states of the  $3D_{5/2}$  state (see Fig. 6.7). On the one hand this leads to a narrower Rydberg resonance, as less Zeeman transitions are involved, on the other hand this enables a new detection scheme, in which a change of the magnetic quantum number  $m$  induced by the Rydberg excitation, is detected. Compared to the detection technique which we used in previous experiments [Fel15] (see section 6.1), where we observe a change in the total angular momentum  $j$ , this new method

is more efficient by about a factor of 5. This enabled us to reduce the VUV-pulse time to 1.5 ms. All experiments with the Rydberg state  $22F$  have been performed in trap T2.

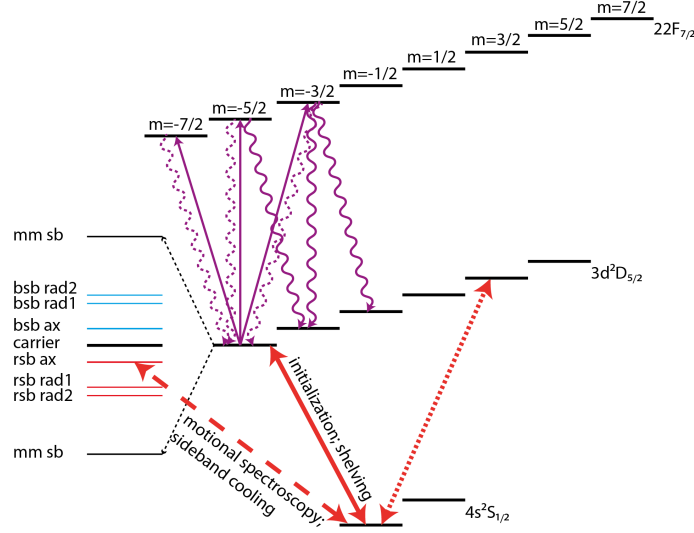


Figure 6.7.: Zeeman structure of the  $3D_{5/2}$  state and the Rydberg state  $22F_{7/2}$ . The ion is initialized by a  $\pi$ -rotation on the  $4S_{1/2} \leftrightarrow 3D_{5/2}$  transition (red arrow). Alternatively, initialization to other Zeeman states is possible (red dotted arrow). Subsequently the ion is excited to the  $22F$  state with VUV light. The  $4S_{1/2} \leftrightarrow 3D_{5/2}$  transition is used for precise spectroscopy of the magnetic field, as well as the thermal motion and micro motion of the ion (red dashed arrow). Figure from Ref. [Bac16]

The coherent excitation of the  $4S_{1/2} \leftrightarrow 3D_{5/2}$  transition is used not only for the initialization of the ions but also for extending the experimental control during the Rydberg excitation experiment (see section 5.2). Micro motion compensation can be executed more precisely by resolved spectroscopy on the micro motion sidebands. Furthermore, we can perform resolved sideband cooling using the narrow line width of the quadrupole transition.

### 6.2.1. Zeeman-state selective initialization, excitation to $22F$ and detection

In a magnetic field the degeneracy of the Zeeman states is lifted by

$$E_z = \mu_B \times g_j \times B \quad (6.4)$$

with the Bohr magneton  $\mu_B$  and the Lande g-factor  $g_j$ . After sideband cooling the axial motion to  $n_{ph} = 4(2)$  phonons, we initialize the ion in the states  $|3D_{5/2}, \pm 5/2\rangle$  with a  $\pi$ -rotation on the qubit transition. We reach about 90% population transfer with a

single  $\pi$ -rotation which is limited by the residual axial and radial motion of the ion. In contrast to the sharp  $4S_{1/2} \leftrightarrow 3D_{5/2}$  resonance, the resonance width for the transition to the Rydberg  $22F$  state is much broader due to the comparatively short lifetime of this state ( $\tau \approx 200$  ns [Glu13]), the thermal motion of the ion and the line width of the VUV radiation. In the  $F_{7/2}$  manifold a magnetic field of  $B = 0.28$  mT yields a frequency splitting of 4.5 MHz. Consequently we do not resolve the individual Zeeman states of the  $22F$ , but the VUV radiation at 123.256119(5) nm wavelength induces transitions with  $\Delta m = -1, 0, 1$ . This results in population transfer out of the initial Zeeman state which indicates successful excitation. The experimental sequence is illustrated in Fig. 6.8.

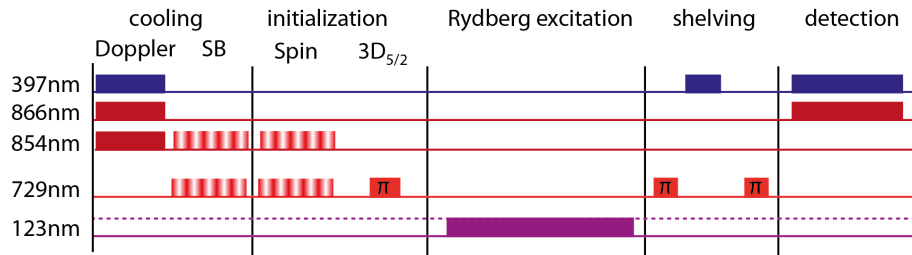


Figure 6.8.: a) Ions are initialized with a  $\pi$ -pulse on the  $|4S_{1/2}, \pm 1/2\rangle \leftrightarrow |3D_{5/2}, \pm 5/2\rangle$  transition. b) A VUV pulse of 1.5 ms excites ions to the Rydberg states, from where they decay rapidly back to the  $3D_{5/2}$ . c) A  $\pi$ -pulse on the  $|4S_{1/2}, \pm 1/2\rangle \leftrightarrow |3D_{5/2}, \pm 5/2\rangle$  transition rotates population that did not change the Zeeman state back to the ground state. d) Optical pumping with light at 397 nm, hides the ground state population in the  $3D_{3/2}$  state. e) An additional pulse on the  $|4S_{1/2}, \pm 1/2\rangle \leftrightarrow |3D_{5/2}, \pm 5/2\rangle$  transition increases the fidelity of the shelving further to  $> 95\%$ . f) Light at wavelength of 397 nm and 866 nm is switched on for the fluorescence detection. Figure from Ref. [Bac16]

The observed resonances are composed of two Zeeman transition each, as illustrated in Fig. 6.9. From the initial states  $|3D_{5/2}, +5/2\rangle$  and  $|3D_{5/2}, -5/2\rangle$  transitions with  $\Delta m = (-1, 0)$  and  $\Delta m = (0, +1)$  are detected. The transitions to the extreme  $m$  states  $|3D_{5/2}, \pm 7/2\rangle$  are excited but do not change the Zeeman state and consequently are not detected.

The data presented in Fig. 6.10 shows the transition resonances for the initial states  $|3D_{5/2}, +5/2\rangle$  and  $|3D_{5/2}, -5/2\rangle$ . We fit a model function consisting of a Gaussian distribution for each Zeeman transition to the data. The Zeeman splitting is given by the magnetic field of  $B = 0.28(1)$  mT which has been measured by spectroscopy on the  $4S_{1/2} \leftrightarrow 3D_{5/2}$  transition. The line width  $\sigma_m$  and the relative strength  $C_{m, \Delta m}$  of each individual Zeeman transition are obtained by fitting the data. We determine  $\sigma_{+5/2} = 4.8(3)$  MHz,  $C_{+5/2, -1} = 0.19(3)$  and  $C_{+5/2, 0} = 0.32(3)$  for transitions from  $m = +5/2$  and  $\sigma_{-5/2} = 3.9(3)$  MHz,  $C_{-5/2, +1} = 0.27(3)$  and  $C_{-5/2, 0} = 0.22(3)$  for transitions from  $m = -5/2$ . The model function agrees with the data, which corroborates our

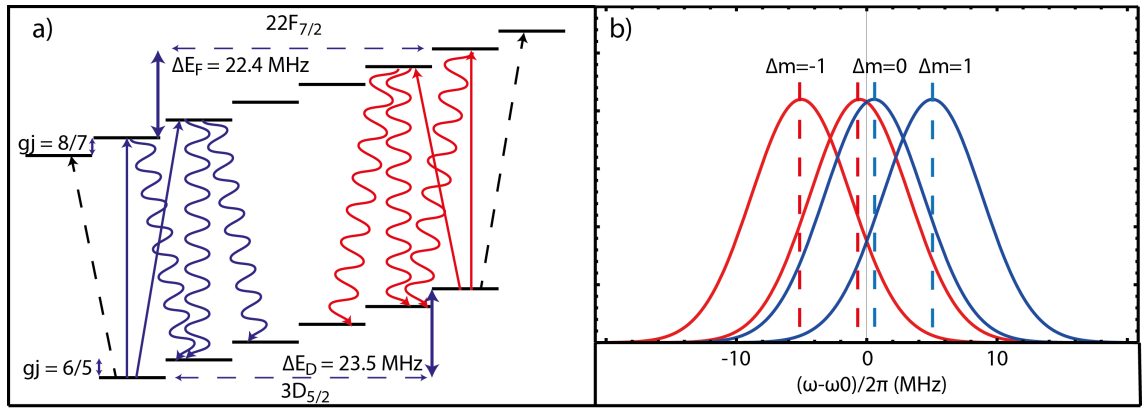


Figure 6.9.: a) Transitions between individual Zeeman state which are excited and detected in the experiment. Transitions to the  $|22F_{7/2}, \pm 7/2\rangle$  states (black dashed arrow) are excited but not detected as they decay back to the initial state. Consequently, transitions with different  $\Delta m$  are detected for initialization in different Zeeman states. This asymmetric excitation and the  $g_j$ -factors of  $g_j(F_{7/2}) = 8/7$  and  $g_j(D_{5/2}) = 6/5$  lead to a frequency shift of the observed resonance. b) Frequency splitting of transition between individual Zeeman states in a field of 0.28 mT. The observed resonances are the sum of the red resonances for the initial state  $|3D_{5/2}, +5/2\rangle$  and the sum of the blue resonances for the initial state  $|3D_{5/2}, -5/2\rangle$ .

assumptions about the excitation and detection of Zeeman transitions. Transitions with different  $\Delta m$  are detected with similar probability. The experimentally determined line widths of  $\sigma_{+5/2} = 4.8(3)$  MHz and  $\sigma_{-5/2} = 3.9(3)$  MHz are large as compared to the natural line width of  $\Gamma/2 = 0.4$  MHz [Glu13] which indicates broadening by thermal motion of the ion and VUV laser line width.

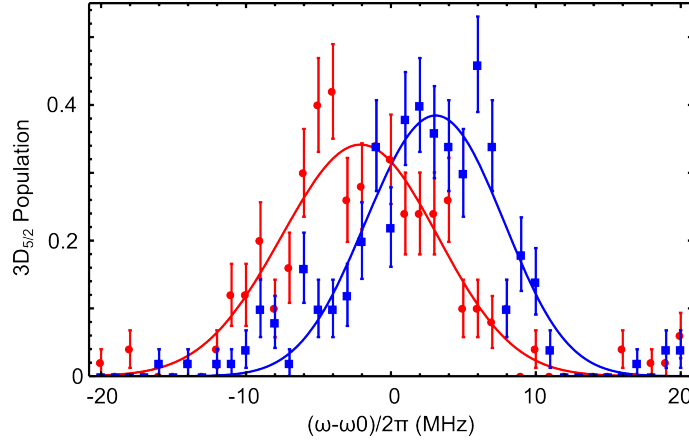


Figure 6.10.: Experimental data of the  $|3D_{5/2}, \pm 5/2\rangle \leftarrow 22F$  resonance. Each data point is obtained by 50 cycles, the error bars depict the quantum projection noise. Solid lines represent a fit of a model function (see text) to the experimental data. The model function, which includes Zeeman splitting in a magnetic field of  $B = 0.28(1)$  mT agrees with the data.

### 6.3. Quantum defect and principal quantum numbers

We excited the Rydberg states  $22F$ ,  $52F$ ,  $53F$  and  $66F^2$ . The transition wavelengths and energies from the  $4S_{1/2}$  ground state are summarized in Tab.6.3. Measured frequencies of 411 042 130 MHz for the  $4S_{1/2} \leftrightarrow 3D_{5/2}$  transition [Chw09] and 1 819 599 MHz for the  $3D_{5/2} - 3D_{3/2}$  fine structure splitting [Yam08] have been used in the data analysis.

The energy levels for Rydberg states are calculated by the Rydberg formula

$$E_{n,\delta} = IP - \frac{R_\infty}{1 + \frac{m_e}{m_{\text{Ca}^+}}} \times \frac{Z^2}{(n - \delta)^2}, \quad (6.5)$$

where  $R_\infty$  is the Rydberg constant,  $m_e$  is the electron mass,  $m_{\text{Ca}^+}$  is the mass of the calcium ion,  $Z$  is the charge-state, and  $n$  is the principal quantum number. In addition to these constants the energy depends on the principal quantum number  $n$ , the quantum defect  $\delta$ , and the ionization potential  $IP$  which can be obtained by fitting Eq.6.5 to the

<sup>2</sup>In Ref. [Fel15] we attributed the excited resonances to  $51F$ ,  $52F$  and  $64F$  but the additional data for the  $22F$  resonance implies that  $52F$ ,  $53F$  and  $66F$  is correct. For details see Appendix A

state	$\lambda D_{3/2}(\text{nm})$	$\lambda D_{5/2}(\text{nm})$	$\Delta E \text{ (cm}^{-1}\text{)}$
$22F$	–	123.256 119(5)	94842.764(3)
$52F$	122.041 913(5)	–	95589.258(3)
$53F$	122.032 384(10)	–	95595.656(7)
$66F$	–	122.040 50(5)	95650.901(33)

Table 6.3.: Transition vacuum wavelengths, and energies from the  $4S_{1/2}$  ground state for all Rydberg states excited in our experiment.

measured data points. As we have measured resonance frequencies to a few different Rydberg states only, we have to employ additional information from theory and former experiments in order to obtain an unambiguous result. From earlier experiments [Xu98] and theory [SK11] we know that the ionization potential is approximately  $95750 \text{ cm}^{-1}$ , while theory [Dje91] provides the quantum defects  $\delta_F = 0.026$  and  $\delta_P = 1.44$  for  $F$  states and  $P$  states, respectively. With this information, the lowest observed state can be clearly identified as  $22F$ . Subsequently the other states are identified as  $52F$ ,  $53F$  and  $66F$  as plotted in Fig. 6.11.

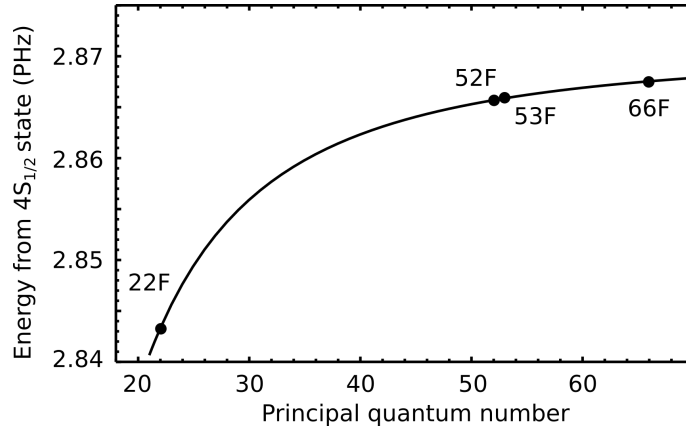


Figure 6.11.: Measured ground state energies of the excited Rydberg states and fitted Rydberg formula. On this scale no deviation is observed. Error bars are smaller than plot markers.

For a precise determination of the quantum defect, we have to take into account that  $\delta$  is not constant but weakly dependent on  $n$  [Dje91] and approximated by the power series:

$$\delta F(n) = 0.025947 - \frac{0.15336}{n^2} + \frac{4.40639}{n^4} - \frac{61.2766}{n^6} \quad (6.6)$$

With this power series we calculate a quantum defect of  $\delta_{F22} = 0.2565$  and  $\delta_{F52} = 0.02589$ . The difference to  $\delta_0$  corresponds to a frequency deviation of 600 MHz at  $n = 22$  which is much larger than the uncertainty of our measurement. Due to the limited



tunability of our VUV-source, we have not measured enough resonance frequencies to fit  $\delta$  as a power series of  $n$ . We solve this problem by taking the small varying part of  $\delta$  from theory and obtain only the much larger constant part  $\delta_0$  from the fit. As plotted in Fig. 6.12, we find excellent agreement between experimental data and theory for the excitation energies of the states  $22F$ ,  $52F$  and  $66F$  but a large deviation for the energy of the  $53F$  state. Obviously, further measurements have to be carried out to investigate this discrepancy but for now it seems reasonable to doubt the measured excitation frequency of the  $53F$  state. We do not consider it for the determination of  $\delta$  and  $IP$ . The experimentally determined values of  $\delta$  and  $IP$  are summarized in Tab. 6.4.

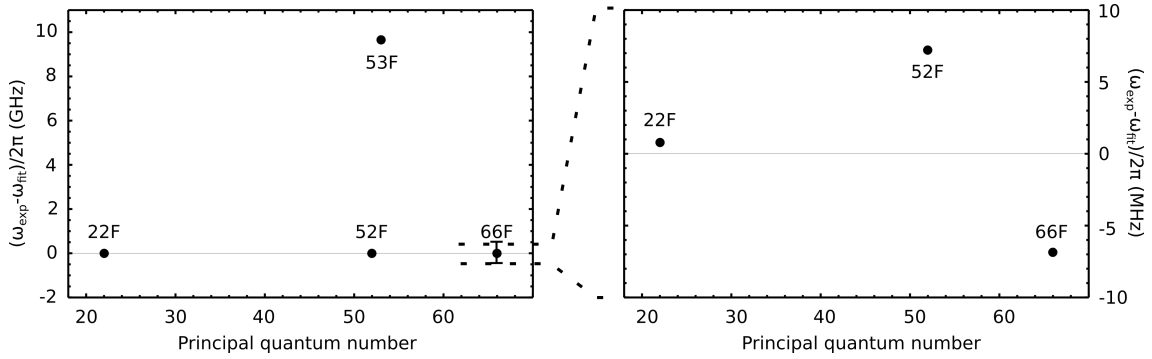


Figure 6.12.: a) Frequency deviation of the measured resonances from the fitted Rydberg formula. The deviation for the  $53F$  resonance is about three orders of magnitude bigger than for the other resonances, consequently this measurement was not used for the evaluation. Error bars for  $22F$ ,  $52F$  and  $53F$  are smaller than plot markers. b) Magnified plot of the frequency deviation for the three remaining Rydberg resonances. Error bars (not plotted) are larger than plot range.

$\delta_{0\text{Theo}}$	0.02595
$\delta_{0\text{Exp}}$	0.02545(10)
$IP(\text{cm}^{-1})$	95751.747(3)

Table 6.4.: Quantum defects of the excited state and the ionization potential obtained from the fit. The fitted constant part  $\delta_{0\text{Exp}}$  is close to the theory value [Dje91].

## 6.4. Line shape of the Rydberg resonance in the trap field

In order to model the observed resonance lines to the  $52F$  state, the electric field, the motional state of the ion and the magnetic field are taken into account. The oscillating electric field in the Paul trap polarizes the highly susceptible Rydberg state, and leads to

a shifted and broadened resonance. We investigate the shape of the resonance at different electric fields and fit it with a theoretical model.

Due to fabrication imperfections in the geometry of trap T1, the ion is exposed to an alternating electric field proportional to the trap drive amplitude (see Section 5.1.1)

$$E_{geom} = 0.8(3) \times \frac{U_{rf}}{\text{m}} \times \sin \Omega_{rf} t, \quad (6.7)$$

where  $U_{rf}$  is the radio frequency voltage at the trap drive frequency  $\Omega_{rf}$ . In comparison, additional fields  $E_{charge}$  in radial direction due to charging of electrodes by scattered VUV light are about an order of magnitude smaller when compensated optimally.

The oscillating field  $E_{geom}$  points in the axial direction along the VUV beam, and leads to a modulation of the Rydberg energy due to the electric polarizability  $\alpha$ , and, in addition, to a modulation of the Doppler effect due to the induced micro motion. The instantaneous resonance frequency reads:

$$\omega(t) = \omega_0 + \mathbf{k} \mathbf{x}_{mm} \Omega_{rf} \sin \Omega_{rf} t - \frac{\alpha E_{geom}^2}{2} \cos^2 \Omega_{rf} t. \quad (6.8)$$

Here,  $\omega_0$  is the bare resonance frequency,  $\mathbf{k}$  is the wave number of the laser along the motion of the ion,  $E_{geom}$  is the electric field amplitude and  $\mathbf{x}_{mm}$  is the micro motion amplitude. From this equation we can derive the temporal shape of the resonance laser field

$$\begin{aligned} E_{res}(t) &\propto e^{-i\omega_0 t} e^{i2\beta_\alpha \Omega_{rf} t} \\ &\times \sum_n J_n(\beta_{mm}) e^{in(\Omega_{rf} t + \frac{\pi}{2})} \\ &\times \sum_m (-1)^m J_m(\beta_\alpha) e^{2im\Omega_{rf} t}. \end{aligned} \quad (6.9)$$

In this equation we define the modulation index in the Bessel functions  $J_n(\beta)$  due to the axial micro motion by  $\beta_{mm} = kx_{mm}$  and due to the oscillating Stark shift by  $\beta_\alpha = \alpha E_{geom}^2 / 8\Omega_{rf}$ . The second exponent in Eq. (6.9) denotes a static frequency shift due to the fact that the modulated Stark shift can only reduce the transition frequency to the  $F$  states. It is apparent that the lineshape comes from a complicated interplay from the sidebands at  $n \times \Omega_{rf}$  caused by the micro motion and the sidebands at  $2n \times \Omega_{rf}$  caused by the oscillating Stark shift.

The time dependent energy shift due to Stark effect and Doppler effect as well as the corresponding sideband structure is illustrated in Fig. 6.13. We do not resolve these sidebands experimentally due to various additional broadening mechanisms. Thermal ion motion at  $T \approx 5$  mK, as determined from the Doppler broadening of the  $4S_{1/2} \leftrightarrow 3D_{5/2}$  transition (see section 5.1.2) and the magnetic field of  $B = 0.45$  mT, determined from the

Zeeman splitting of the  $4S_{1/2} \leftrightarrow 3D_{5/2}$  transition, lead to a broadening of about 10 MHz. Thus, the line shape observed in the experiment is a convolution of Eq. 6.9 and a Gaussian distribution with  $\sigma = 10$  MHz. As the Paul trap is operated at  $\Omega_{rf}/2\pi$  between 3.5 MHz and 5.2 MHz, the sidebands are not resolved in the spectrum.

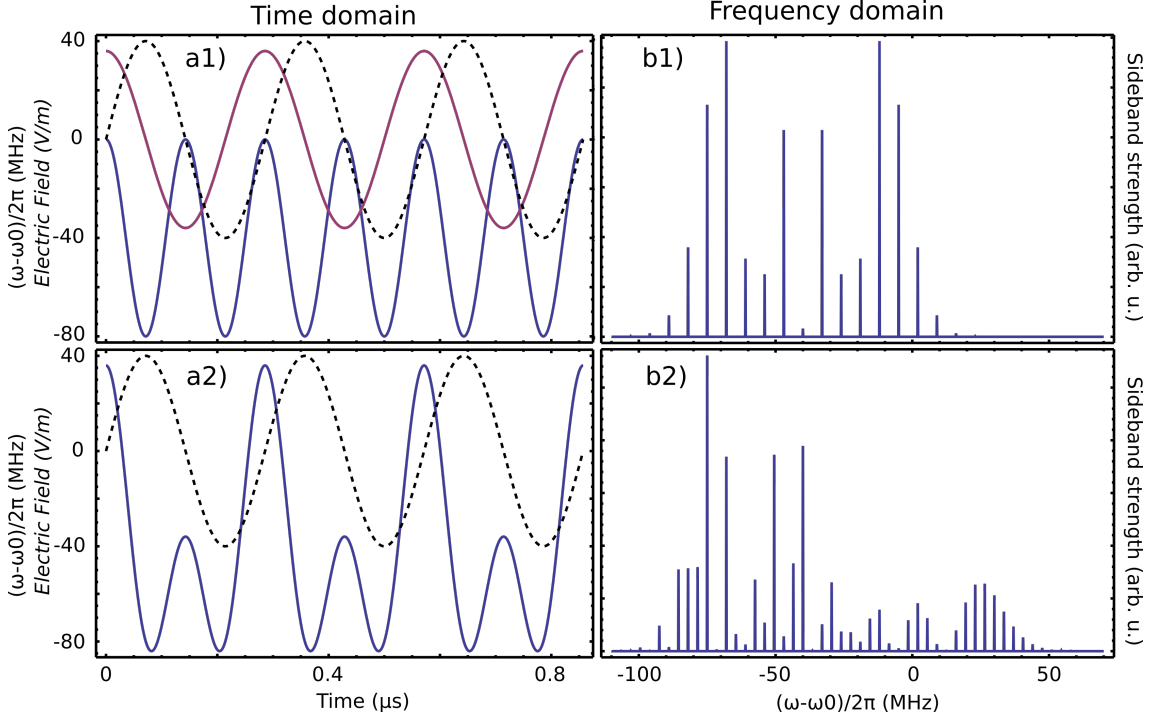


Figure 6.13.: Energy shifts due to Doppler effect and Stark effect in time (a) and frequency (b) domain for a field amplitude  $E_0 = 40$  V/m, oscillation frequency  $\Omega_{rf}/2\pi = 3.5$  MHz and polarizability  $\alpha/2 = 500$  MHz/(V/cm)<sup>2</sup>. In a1) the oscillating electric field (black, dashed) the Stark shift (blue) and the Doppler shift (red) are plotted. The Doppler shift has a phase shift of  $\pi/2$  with respect to the electric field. Consequently, the influence of the Doppler effect is strongest when the Stark effect is zero and vice versa. In a2) the combined shift of Doppler effect and Stark effect is plotted. The line is clearly asymmetric. b1) Side band structure caused by the Stark effect. Sidebands at  $2n \times \Omega_{rf}$  arise symmetrically around the shifted center. b2) Combining both effects leads to additional sidebands at  $n \times \Omega_{rf}$ , the line becomes asymmetric as in a2).

With the known electric field amplitude  $E_{geom}$  we estimate the polarizability  $\alpha$  from a fit of our model to the observed resonance line shape, the data is presented in Fig. 6.14. The experimentally determined  $\alpha/2 = 5_{-3}^{+7} \times 10^2$  MHz/(V/cm)<sup>2</sup> is in agreement with the polarizability of the  $52F$  state,  $\alpha_{52F}/2 \approx 4 \times 10^2$  MHz/(V/cm)<sup>2</sup> obtained from second-order perturbation theory and neglecting spin-orbit coupling (see section 2.3).

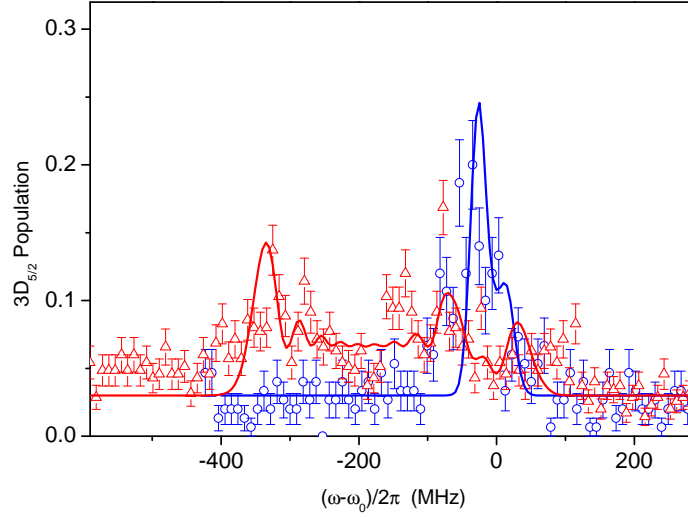


Figure 6.14.: Experimental data (trap T1) of the  $3D_{3/2}$  to  $52F$  resonance with  $E_{geom} = 24 \text{ V/m}$  (blue) and  $E_{geom} = 84 \text{ V/m}$  (red). Fitting the data with our line shape model, we determine  $\alpha_{52F}/2 = 5^{+7}_{-3} \times 10^2 \text{ MHz}/(\text{V/cm})^2$  for the polarizability. Measurements were performed with one ion and 150 cycles per data point for the resonance at  $24 \text{ V/m}$  (blue) while at  $84 \text{ V/m}$  (red) a five ion crystal and 70 cycles per data point were used. The error bars depict the quantum projection noise.

In trap T2, axial micro motion is negligible, but residual electric fields  $E_{charge}$  generated by charging the surface of the trap electrodes with VUV radiation are stronger as compared to trap T1 due to a smaller distance from the ion. The field thus points in the radial direction and line broadening by micro motion in the direction of the VUV beam is small while the Stark effect remains the dominant line broadening effect. As this stray field  $E_{charge}$  is subjected to drifts during the run of the experiment we have not used it for polarizability measurements.

#### 6.4.1. Polarizability of the $22F$ state in an oscillating field

So far we analyzed the influence of the oscillating field on the Rydberg resonance  $52F$ . However, due to the low trap drive frequency, the high polarizability and the huge resonance broadening we were not able to resolve the side band structure predicted by our model. With the lower lying Rydberg state  $22F$  the polarizability is supposed to be reduced by a factor of 400. For polarization measurements we can still generate Stark sidebands by intentionally shifting the ion out of the radiofrequency node. We shift the

ion by voltages  $U\Delta_{dc}$  and  $U\Delta_{rf}$  applied to the compensation electrodes and measure the modulation index due to the induced micro motion by sideband spectroscopy with the vertical aligned beam at 729 nm wavelength. The data are plotted in Fig. 6.15, see section 5.2.1 for more details about the measurement technique. We choose the ratio between  $U\Delta_{dc}$  and  $U\Delta_{rf}$  so that the shift is purely horizontal. A shift in horizontal direction perpendicular to the trap axis corresponds to an oscillating field in vertical direction as illustrated in the inset of Fig. 6.15. The resulting micro motion is perpendicular to the laser beams for Doppler cooling and optical pumping as well as to the VUV-beam, thus it does not influence the experiment. From the experimental data we obtain an oscillating field of  $E_{osc} = 22000(1000) \times U\Delta_{dc}/\text{m}$ .

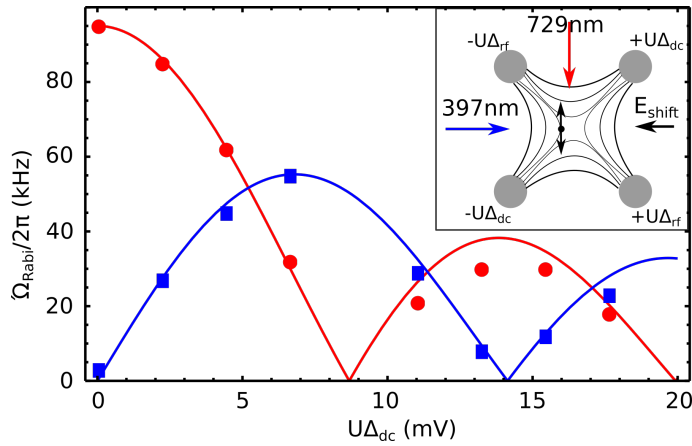


Figure 6.15.: Voltages  $U\Delta_{dc}$  and  $U\Delta_{rf}$ , applied to the compensation electrodes shift the ion out of the radiofrequency node of the trap. The micro motion can be measured with the vertically aligned beam at 729 nm wavelength. The plot shows  $\Omega_{rabi}/2\pi$  for the carrier transition (red data points) and the first micro motion sideband (blue data points). We obtain the modulation index which corresponds to the field strength by fitting Bessel functions to the experimental data. A voltage of  $U\Delta_{dc} = 10 \text{ mV}$  corresponds to a modulation index of  $\eta = 2.7$  and a field amplitude of 220 V/m.

The direct field measurement is limited to small fields for two reasons: First, the tuning range of the AOM frequency allows for measuring the carrier and the first micro motion sideband only and secondly, the horizontal displacement of the ion out of the tightly focused laser beam leads to a reduced intensity for large fields. Consequently we measured the modulation index at low fields and extrapolated the values to high fields.

We employ the same experimental sequence as in section 6.2 for Rydberg excitation at optimal compensation (amplitude  $< 50 \text{ V/m}$ ) and in an oscillating field of 680(30) V/m. The experiment is carried out with a trap drive frequency of  $\Omega_{rf}/2\pi = 6.5 \text{ MHz}$  resulting in Stark sidebands spaced by 13 MHz (see Eq. 6.9). From the data presented in Fig. 6.16

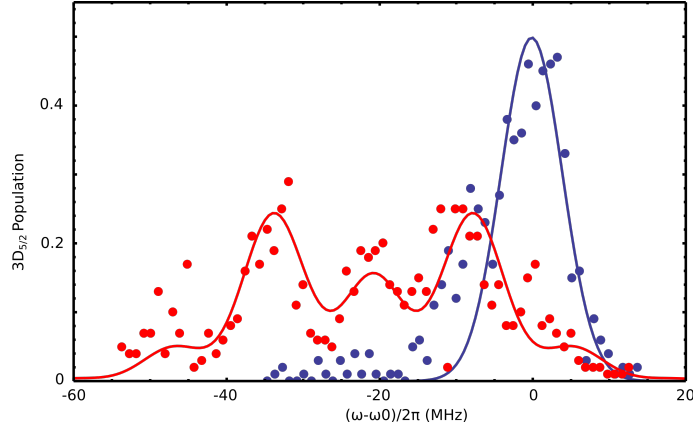


Figure 6.16.: Lineshape of the  $22F$  resonance at optimal compensation (black) and at an electric field amplitude of  $680(30)$  V/m. The sideband structure predicted by our model is observed but not fully resolved. From the fitted model function we obtain a polarizability of  $\alpha/2 = 0.9(2)$  MHz/(V/cm) $^2$ .

we obtain a polarizability of  $\alpha/2 = 0.9$  MHz/(V/cm) $^2$  which is in good agreement with theoretical predictions (see section 2.3) and the experimental value for the Rydberg state  $52F$  (see section 6.1). We observe hints of the predicted sideband structure but the resonance broadening by thermal motion, laser line width and magnetic field prevents us from fully resolving it. In principal it should be easy to increase the trap drive frequency and correspondingly the sideband spacing. Instead we find a sharp decrease of our detection efficiency if we increase the trap drive frequency to  $\Omega_{rf}/2\pi = 20$  MHz. Closer examination reveals that the decay to different Zeeman-states of the  $3D_{5/2}$  decreases, while the decay to the  $3D_{3/2}$  state increases. We attribute this behavior to a mixing of the the  $22F_{5/2}$  and  $22F_{7/2}$  states induced by the field at frequency  $\Omega_{rf}$ . The frequency difference between fine structure states can be calculated by [SK11]

$$\Delta\omega/2\pi = \frac{R_\infty}{1 + \frac{m_e}{m_{\text{Ca}^+}}} \times \frac{Z^2}{(n-\delta)^2} \left( \frac{\alpha_{ls}Z^2}{(n-\delta)(j+1/2)} - \frac{\alpha_{ls}Z^2}{(n-\delta)(j'+1/2)} \right) \quad (6.10)$$

with fine structure constant  $\alpha_{ls}$  and total angular momentum  $j$  and  $j'$ . When neglecting a possible difference in the quantum defect we obtain  $\Delta\omega_{5/2,7/2}/2\pi = 22$  MHz which is in accordance with our explanation. This effect has to be investigated more thoroughly in the future.

## 6.5. Addressed Rydberg excitation in a linear crystal

For advanced experiments using Rydberg excitations as a tool in quantum simulation or quantum computing it will be necessary to excite specific ions out of a large Coulomb crystal to Rydberg states. Instead of addressing single ions with a focused and steered VUV-beam, we initialize selected ions to the  $3D_{5/2}$  state with the tightly focused beam at 729 nm wavelength (see section 3.1.3) - only those ions will undergo excitation to the Rydberg level, even though the VUV beam illuminates the entire ion crystal. This concept has important advantages: First, the  $3D_{5/2}$  state lives for  $\tau = 1168(9)$  ms [Kre05] such that we have sufficient time for pulses and transport or separation sequences to initialize and configure multiple ions (see section 5.3) before a single VUV pulse excites all  $D$ -state ions at once. Secondly it is technically simple to address ions with a laser beam at 729 nm wavelength while it would be much more challenging to rapidly steer the VUV beam on single ions and finally the excitation dynamics become very complicated using a beam with a wave vector in radial direction due to the different radial vibrational frequencies for an ion in the ground-state compared to an ion in the Rydberg-state (see section 2.2.2).

For this experiment we operate the trap drive at a radio frequency of  $\Omega_{rf}/2\pi = 20$  MHz in order to generate a stable potential for multiple ions in a linear string. Vibrational frequencies of  $\omega_{rad}/2\pi = 1.5$  MHz and  $\omega_{ax}/2\pi = 600$  kHz were obtained. The latter corresponds to an inter ion distance of  $d \approx 7 \mu\text{m}$  for a three ion crystal.

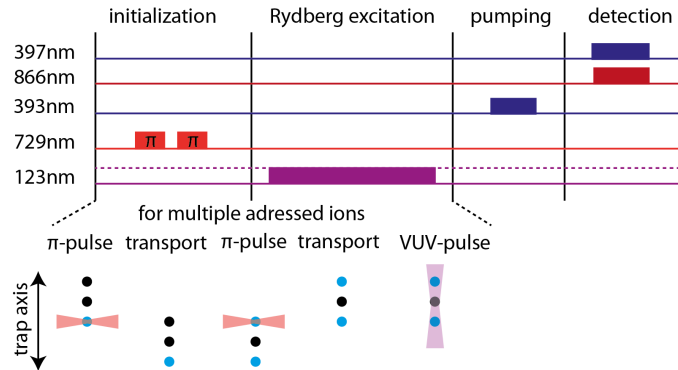


Figure 6.17.: Sequence for the addressed Rydberg excitation of ions. Initialization is performed by addressed  $\pi$ -rotations on individual ions. In case of addressed excitation of multiple ions, the ions are initialized serially, applying a transport sequence between each pulse. The following Rydberg excitation is done on all initialized ions at once. See text for details. Figure from Ref. [Bac16]

The pulse sequence used for the addressed excitation of one ion, or two ions, in a crystal of three ions is illustrated in Fig. 6.17. a) After Doppler cooling, two  $\pi$ -pulses on different Zeeman transitions are used for the initialization of each ion in order to increase the population transfer to  $> 90\%$ . b) A VUV pulse of  $t = 5$  ms excites the ions on

the  $3D_{5/2} \rightarrow 22F$  transition, a fraction of the excited ions decay to the  $3D_{3/2}$  state. c) Ground state population of all ions is pumped to the  $3D_{5/2}$  state with 90% fidelity. d) The initialized and the non-initialized ions are in the dark state ( $3D_{5/2}$ ), only ions excited to Rydberg states and decayed to the  $3D_{3/2}$  scatter photons during illumination with light at 397 nm wavelength. Only about 90% of the ground state population end up in the  $3D_{5/2}$  state after pumping with light at 393 nm wavelength while 10% decays to the  $3D_{3/2}$  state. While this only has a small effect for the addressed ions as they are predominantly in the  $3D_{5/2}$  or  $3D_{3/2}$  state at this point, it leads to a background of 10% for the non addressed ions to be in the 'bright' state. This effect is accounted for by adding 8% constant background to the data of the addressed ions, so that far from resonance the background signal is identical for all ions.

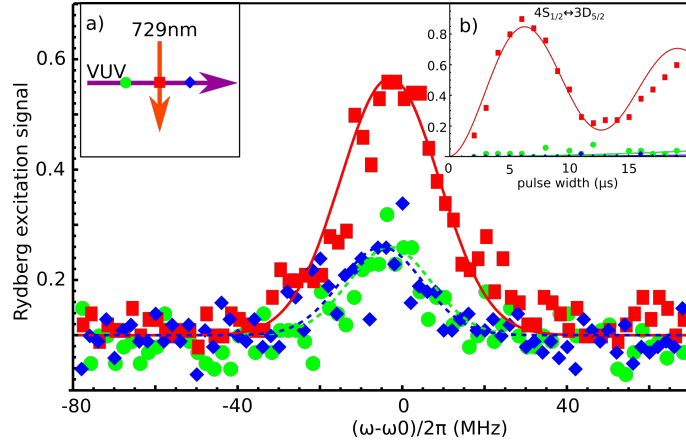


Figure 6.18.: Addressed Rydberg excitation of the central ion out of a linear three ion crystal. The ratio for Rydberg excitation on the addressed to the non addressed ions is about 3 with subtracted background signal. A constant background of 8% was added to the data of the addressed ion to account for this systematic error (see explanation in text). Inset a) shows the geometry of the beams with respect to the ion chain. Inset b) shows addressed excitation of the  $4S_{1/2} \leftrightarrow 3D_{5/2}$  transition. The Rabi-frequency on the central ion is  $\Omega_{\text{rabi}}/2\pi = 80$  kHz while the excitation of the outer ions remains negligible. Plot from Ref. [Bac16]

The measured resonance with central ion addressed is shown in Fig. 6.18. The excitation rate on the addressed ion is about three times higher compared to the non addressed ion. The Rabi oscillations on the  $4S_{1/2} \leftrightarrow 3D_{5/2}$  transition are shown in inset b) of Fig. 6.18. During the time needed for a  $\pi$ -rotation on the addressed central ion, the excitation of the outer ions remains negligible. Still, residual Rydberg excitation of the non-addressed ions is observed. This behavior can be explained by the fact that we do not switch the VUV beam, but instead the VUV pulse width is determined by the time between



initialization and detection. In contrast to the measurements presented in section 6.2.1, all ions (addressed and non-addressed) which have not been excited to Rydberg states are in the  $3D_{5/2}$  state during detection. Consequently they can be excited during detection and decay to a bright state. Switching the VUV beam with an electro optical modulator may solve this problem and allow for better addressing fidelity limited only by the quality of the initialization.

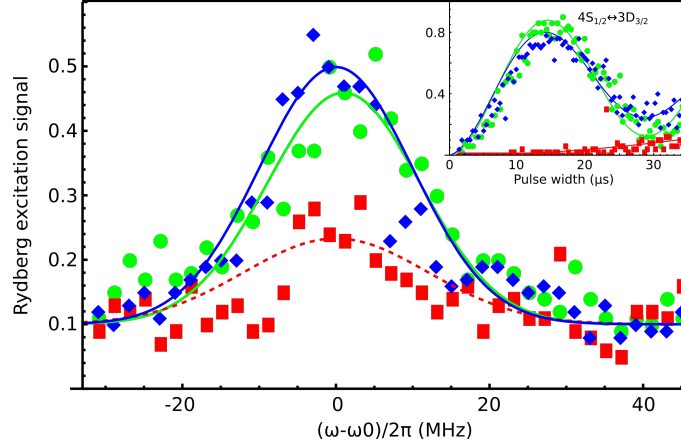


Figure 6.19.: Addressed Rydberg excitation of both outer ions in a linear three ion crystal. The ratio for Rydberg excitation on the addressed to the non addressed ions is about 2.8 with subtracted background signal. A constant background of 8% was added to the data of the addressed ions. The inset shows the coherent population transfer on the addressed  $4S_{1/2} \leftrightarrow 3D_{5/2}$  transition. Even with pulses on both outer ions the excitation of the non-addressed central ions remains negligible. Plot from Ref. [Bac16]

Multiple ions can be addressed by using transport operations in between laser pulses (see section 5.3). We can move the ion crystal along the trap axis by modifying the dc part of the trap potential. Voltage ramps of  $\Delta V = \pm 280\text{mV}$  on segments 4 and 8 have been used to displace the crystal by  $14\text{ }\mu\text{m}$  in  $500\text{ }\mu\text{s}$ . In inset b) of Fig. 6.19 the Rabi oscillations on the  $4S_{1/2} \leftrightarrow 3D_{5/2}$  transition are shown. Compared to the sequence for a single addressed ion, neither the contrast of the oscillation for the addressed ion is reduced, nor the unwanted excitation of the non-addressed ion is increased by the transport operations.

The measured resonance with outer ions addressed is presented in Fig. 6.19. In between laser pulses, the crystal is moved along the trap axis to superimpose the selected ion with the fixed  $729\text{ nm}$  beam. Once all addressed ions are initialized in the  $3D_{5/2}$ , a single VUV pulse excites them to the Rydberg state. In principle this approach is scalable to long ion chains and even to two dimensional ion crystals as long as Rydberg excitation is restricted to ions on the trap axis.



## 7. Conclusion

In conclusion, we excited Rydberg states of trapped and laser cooled ions for the first time ever. In order to accomplish this, we built a compact ion trap apparatus with vacuum vessel, diode lasers for photo ionization of neutral calcium and for cooling, optical pumping, and fluorescence detection of  $^{40}\text{Ca}^+$  ions. We integrated spectrally narrow radiation from an existing titanium:sapphire laser for the coherent excitation of the long lived  $3D_{5/2}$  state. Furthermore, we built a detection system for the ions fluorescence based on an EMCCD camera and control electronics for the Paul trap, the lasers and the camera. We successfully connected this ion trap apparatus with the existing continuous wave VUV source.

Two different Paul traps, a simple mm-sized rod trap (T1) for initial experiments, and an advanced segmented micro trap (T2) have been built and employed in the experiment. We demonstrated basic ion trap techniques such as Doppler cooling, optical pumping, fluorescence detection and micro motion compensation as well as more advanced techniques such as resolved sideband spectroscopy on the  $4S_{1/2} \leftrightarrow 3D_{5/2}$  quadrupole transition and addressed excitation of single ions in large Coulomb crystals for both traps. Additionally, we demonstrated sideband cooling of all motional modes to mean phonon numbers of  $\bar{n}_{ax} = 2$ ,  $\bar{n}_{rad1} = 6$  and  $\bar{n}_{rad2} = 12$  and coherent state preparation by a  $\pi$ -rotation to the  $3D_{5/2}$  state with a fidelity  $F > 90\%$ . The combination of coherent excitation and single ion addressing on the  $4S_{1/2} \leftrightarrow 3D_{5/2}$  transition with the elementary ion transport operations enabled by the segmented electrode structure in trap T2, allowed for the selective excitation of multiple ions in linear ion strings.

We characterized the VUV beam and aligned it to the trap center with the help of a needle tip which can be moved into the ion trap. Two  $\text{MgF}_2$  lenses focus the VUV beam to a waist of  $w_{0x} = 12\,\mu\text{m}$  and  $w_{0y} = 16\,\mu\text{m}$ . Optical powers of  $P_{VUV} > 1\,\mu\text{W}$  at a wavelength near 122 nm result in ionization of background atoms which are subsequently loaded into the ion trap. We demonstrated techniques to prevent the parasitic loading of ionized background atoms into the Paul trap and achieved demonstrated stable ion trap operation with optical powers of  $P_{VUV} > 1\,\mu\text{W}$  in the VUV beam.

By photo ionization of trapped  $^{40}\text{Ca}^+$  with light near 121 nm wavelength we showed an interaction of the VUV beam with the trapped ions for the first time. The  $^{40}\text{Ca}^{2+}$  ions exhibit a modified potential similar to ions excited to Rydberg states. Hence, experiments with  $^{40}\text{Ca}^{2+}$  impurity ions in Coulomb crystals with up to 24 ions, allowed for a preliminary investigation of the proposed schemes for mode shaping and structural phase transitions.

## 7. Conclusion

---

We excited trapped ions to the Rydberg states  $22F$ ,  $52F$ ,  $53F$  and  $66F$  and detected the excitation with a modified electron shelving scheme which allows for detection of very low excitation rates. Starting from the metastable  $3D$  states we measured resonance wavelengths of 123.256 119(5) nm ( $3D_{5/2} \rightarrow 22F$ ), 122.041 913(5) nm ( $3D_{3/2} \rightarrow 52F$ ), 122.032 384(10) nm ( $3D_{3/2} \rightarrow 53F$ ) and 122.040 50(5) nm ( $3D_{5/2} \rightarrow 66F$ ). From these experimental data we calculated energies of 94 842.763(3) cm<sup>-1</sup> ( $22F$ ), 95 589.258(3) cm<sup>-1</sup> ( $52F$ ), 95 595.656(7) cm<sup>-1</sup> ( $53F$ ) and 95 650.901(33) cm<sup>-1</sup> ( $66F$ ) with respect to the ground state. Fitting the Rydberg formula to these data points yields an ionization potential of 95 751.747(3) cm<sup>-1</sup> and a quantum defect of  $\delta 0 = 0.02545(10)$  which is in agreement with the theory value for the quantum defect of the  $F$  states of  $\delta 0 = 0.02595$  [Dje91]. We investigated the line shape of the transition to the states  $22F$  and  $52F$  in the oscillating potential of the Paul trap and developed a line shape model which takes into account the polarizability of the Rydberg state and the micro motion of the ion. We obtained values of  $\alpha_{52F}/2 = 5_{-3}^{+7} \times 10^2$  MHz/(V/cm<sup>2</sup>) and  $\alpha_{22F}/2 = 0.9(2)$  MHz/(V/cm<sup>2</sup>) which is in agreement with a scaling of  $\alpha \propto n^7$ . We combined excitation of the Rydberg state  $22F$  with resolved sideband cooling and coherent excitation of the initial  $3D_{5/2}$  state. The initialization into single Zeeman states of the  $3D_{5/2}$  state by  $\pi$ -rotations on the quadrupole transition allowed for the implementation of an improved detection scheme as well as for a rough investigation of the Zeeman structure of the Rydberg state. We selectively excited the central and the two outer ions of a three-ion string to the Rydberg state  $22F$ , using a combination of addressed initialization on the  $4S_{1/2} \leftrightarrow 3D_{5/2}$ , ion shuttling, and global illumination with the VUV beam.

This experimental work demonstrates the feasibility of Rydberg excitation of laser cooled ions in Paul traps. Hence, it paves the way towards a novel platform of Rydberg matter, where the key features of Rydberg states, high polarizability, long lifetimes and long range interactions, are combined with the outstanding control over quantum states in trapped ion crystals.

## 8. Outlook

While we excited and investigated Rydberg states of trapped ions, substantial advances are required in order to fully exploit the unique features of Rydberg ions.

### 8.1. Spectroscopy of Rydberg $P$ states

In the experiments presented in this thesis, Rydberg  $F$  states have been excited. These states are suitable for spectroscopy experiments and have the advantage of a large transition dipole moment to the initial  $3D_{3/2}$  states. However, for advanced experiments it will be advantageous to employ Rydberg  $P$  states which have longer radiative lifetimes, lower polarizabilities, and feature narrower transition resonances as illustrated in Fig. 8.1. Consequently the next step in the experiment should be the excitation of Rydberg  $P$  states.

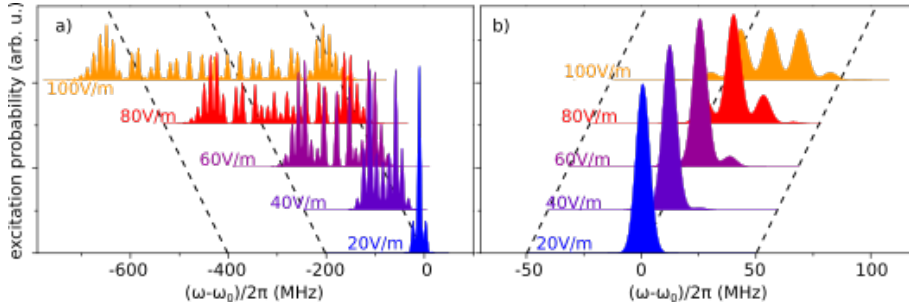


Figure 8.1.: Resonance shape of the transitions to  $51F$  (a) and  $51P$  (b) in an oscillating field of various amplitude. Cooling to the Doppler limit and a trap drive frequency of  $\Omega_{rf}/2\pi = 6.5$  MHz is assumed. The influence of the oscillating field is much less pronounced for the  $51P$  state.

**Excitation of the state  $23P$**  The first Rydberg  $P$  state we aim to excite will be  $23P$ . The exact excitation wavelength of this state will allow us to deduce the quantum defect of the  $P$  manifold, which will in turn simplify the search for higher lying  $P$  states around  $n = 53$  which we will start subsequently.

The excitation wavelength of about 123.218 nm for the transition  $3D_{3/2} \rightarrow 23P$  is very close to the  $10^1P$  resonance in mercury. The four-wave-mixing efficiency at this wavelength

is about  $90 \mu\text{W}/\text{W}^3$  compared to about  $6 \mu\text{W}^3$  for the resonance wavelength of the  $3D_{3/2} \rightarrow 22F$  transition. Thus, the increased VUV power compensates for the transition dipole moment  $\mu_{3DnP}$  which is smaller by a factor of ten compared to the dipole matrix element  $\mu_{3DnF}$  for the transitions to  $F$  states. With the ionization threshold obtained from our previous measurement the resonance wavelength is determined by the quantum defect of the  $P$  manifold which is calculated to be  $\delta_{P32} = 1.4358$  and  $\delta_{P12} = 1.4396$  [SK11]. However, given the energy gap of about 2.8 THz between two adjacent states of the same angular momentum quantum number, an uncertainty of 0.01 in the quantum defect leads to a deviation of 28 GHz from the calculated resonance frequency, thus we expect to search in a frequency range of a few 10 GHz.

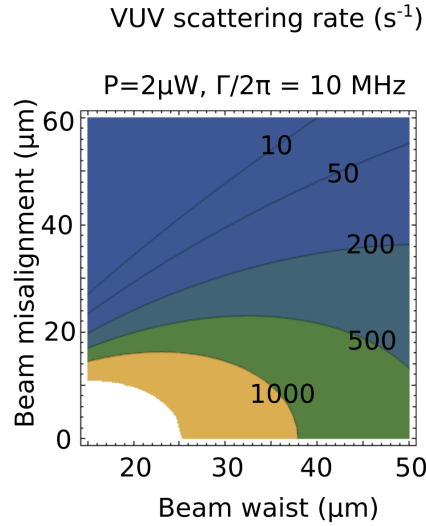


Figure 8.2.: Excitation rate of the state  $23P$ . With a beam waist of  $50 \mu\text{m}$  we are located at the right side of the plot. Excitation rates are sufficient for detection even at a beam misalignment of about  $50 \mu\text{m}$ .

In order to make the search as efficient as possible, we will first adjust the VUV-beam to the ion with the help of the  $22F$  resonance which can be done with  $\mu\text{m}$  precision. We increased the beam size at the ion to about  $50 \mu\text{m}$ , thus we decrease the influence of small beam pointing fluctuations. The increased beam waist removes the need to repeat the frequency scan for different beam positions, while the intensity is still sufficient for decent excitation rates as shown in Fig. 8.2.

The excitation and detection sequence illustrated in Fig. 8.3 is similar to the ones used for the excitation of Rydberg  $F$  states. Detection efficiency is quite high as more than 50% of the excited population ends up in the ground state [Li] which is subsequently pumped by light at 393 nm wavelength to the dark  $3D_{5/2}$  state. On the down side, the necessary optical pumping step at the end of the excitation pulse implies that spontaneous decay of

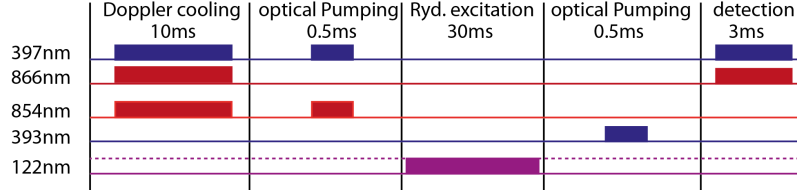


Figure 8.3.: Excitation and detection sequence for the  $3D_{3/2} \rightarrow 23P$  resonance. Ions are initialized in the  $3D_{3/2}$  state by optical pumping. After the VUV pulse, the fraction of the population that decayed to the ground state (direct and via the Rydberg state) is optically pumped to the dark state  $3D_{5/2}$ .

the metastable  $3D_{3/2}$  state leads to a background signal of about  $\tau_{vuv}/\tau_{3Dj}$ , thus about 3% for a 30 ms VUV-pulse. Still, the calculated excitation rate is much bigger than the spontaneous decay so that detection of the Rydberg excitation should be feasible.

**Excitation of high lying  $P$  states around  $n = 53$**  Calculations for the state  $23P$  yield a lifetime of  $\tau = 18 \mu\text{s}$  [Glu13] and a polarizability of  $\alpha/2 = 0.14 \text{ MHz}/(\text{V}/\text{cm})$  [Kam14] (see section 2.3). For experiments which aim to exploit the dipole dipole interaction between ions at about  $5 \mu\text{m}$  distance or the state dependent potential for mode shaping, these values might be insufficient and the excitation of higher lying Rydberg state is required. The excitation wavelength for the transition  $3D_{3/2} \rightarrow 53P$  is in the vicinity of the  $11^1P$  resonance in mercury. A four-wave-mixing efficiency of  $20 \mu\text{W}/\text{W}^3$  is reached. Once the exact quantum defect for the  $P$  states is known, the transition wavelength for these state can be calculated very accurately which should greatly simplify our search.

## 8.2. Dispersive measurement of Rydberg states

So far, Rydberg states were excited resonantly. An alternative detection method we plan to implement is the measurement of a line shift induced by off-resonant VUV-radiation. As we can measure the  $4S_{1/2} \leftrightarrow 3D_{5/2}$  transition very accurately using a spin echo sequence, even small energy shifts of the  $3D_{5/2}$  state could be observed.

The pulse sequence we may use for this measurement is illustrated in Fig. 8.4. The VUV radiation is only switched on between the spin-echo pulse and the second  $\pi/2$ -pulse. We need to switch the VUV laser rapidly for this experiment. Currently we integrate an electro optical modulator switching the fundamental light field at 580 nm wavelength, into the experiment. With an optical power of  $P_{vuv} = 0.15 \mu\text{W}$  (see chapter 6) and a beam waist of  $w_0 = 15 \mu\text{m}$  (see section 5.4), we expect a Rabi frequency of  $\Omega_0/2\pi = 200 \text{ kHz}$ . The induced line shift of the  $3D_{5/2}$  state is given by

$$\Delta\omega = \frac{\Omega_0^2}{4\Delta}. \quad (8.1)$$

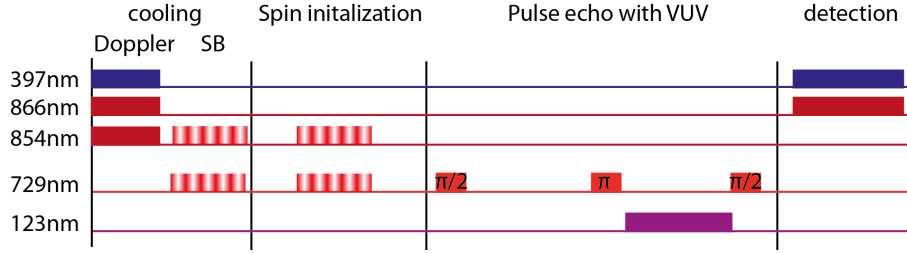


Figure 8.4.: Pulse sequence for the dispersive measurement of Rydberg states. After side-band cooling close to the thermal ground state the ion is initialized to the state  $|4S_{1/2}, -1/2\rangle$ . A  $\pi/2$ -pulse on the qubit transition generates a superposition of  $|4S_{1/2}, -1/2\rangle$  and  $|3D_{5/2}, -5/2\rangle$ . During a wait time  $\tau_{se}$ , a phase between the ion's superposition state and the laser field is accumulated. An intermediate  $\pi$ -pulse flips the direction of the rotation, followed by a second wait time  $\tau_{se}$ , during which the VUV radiation is switched on, and finally another  $\pi/2$ -pulse. If the same phase is accumulated during both wait times, the latter  $\pi/2$ -pulse rotates the population back to the  $|4S_{1/2}, -1/2\rangle$  state. However, if the energy of the  $|3D_{5/2}, -5/2\rangle$  state is shifted by the near resonant VUV radiation, the accumulated phase will change. Consequently the second  $\pi/2$  rotation will be out of phase, which can be detected by a population transfer to the  $|3D_{5/2}, -5/2\rangle$  state.

For a detuning of  $\Delta/2\pi = 10$  MHz we calculate a line shift of  $\Delta\omega/2\pi = 1$  kHz.

### 8.3. Microwave spectroscopy of Rydberg states

Microwave mixing of Rydberg states is proposed to be a very versatile tool [Mül08, Li14]. Resonant microwave coupling of two Rydberg states generates a strong dipole-dipole type interaction between ions (see chapter 1), while at the same time it allows for tuning the polarizability of the mixed state. When mixing the Rydberg  $P$  state (negative polarizability) with the  $S$  state or  $D$  state (positive polarizabilities), it allows even for a cancellation of the polarizability to first order.

Transition	$\omega_{MW}/2\pi$
$22F \leftrightarrow 22G$	47 GHz
$52F \leftrightarrow 52G$	3.6 GHz
$53P \leftrightarrow 52D$	36 GHz
$53P \leftrightarrow 53S$	71 GHz

Table 8.1.: Microwave frequencies for selected transitions, calculated with the theoretical quantum defects [Dje91].

In a first step towards this goal, we will perform microwave spectroscopy between dif-



ferent Rydberg states. Possible transitions in an accessible frequency region are the  $F$  to  $G$  transition for the low lying Rydberg states and the  $P$  to  $D$  or  $P$  to  $S$  transitions for higher lying states. Selected transition frequencies are given in Tab.8.1.

## 8.4. Optimized new trap design

In both traps we have observed that excitation of high lying Rydberg states with  $n > 50$  becomes unstable after several months of experimenting (see section 6.1). Consequently we have developed a new trap T3 for future experiments with high lying Rydberg states. For trap T3 we keep the overall design of an X-shaped segmented blade trap but change the form of the blades, the end caps and the calcium oven. The key features of trap T3 (illustrated in Fig.8.5) are:

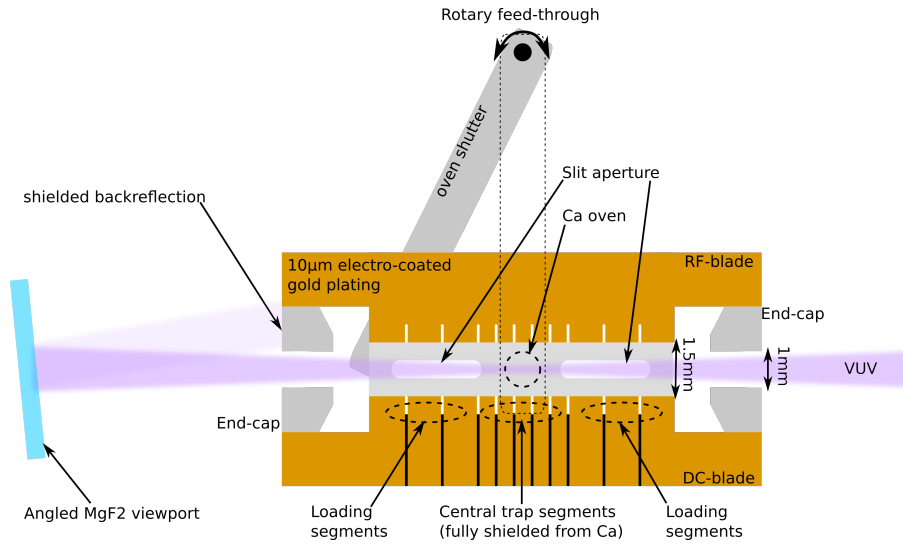


Figure 8.5.: Illustration of the key feature of trap 3. The electrodes are well shielded from the VUV beam by the end-caps. An oven shutter, as well as a slit aperture prevent contamination of the electrode surface from the loading atomic beam.

- Major changes have been made to the ceramic blades and the end caps. We increase the distance of the electrode surface to the trap center from  $480 \mu\text{m}$  to  $750 \mu\text{m}$ , while we increase the radius of the holes in the end caps from  $750 \mu\text{m}$  to  $500 \mu\text{m}$ . Thus, the electrodes are shielded from scattered VUV light more efficiently. The width of the segments has been changed compared to trap T2 (see Fig.8.6): Five central electrodes with a width of  $0.5 \text{ mm}$  constitute the interaction region, where ions are excited to Rydberg states. On each side of this central region, three wider electrodes ( $1 \text{ mm}$ ) constitute the loading regions, where Ca atoms are ionized and cooled into the trap.

- The ceramic chips, sputtered with a thin layer of gold, will get an additional  $10\text{ }\mu\text{m}$  thick electro-coated gold coating. The heating rate of a segmented micro trap, operated in our group, could be reduced by more than two orders of magnitude with this technique [Kau15]. A similar reduction for trap T3 would allow for ground state cooling of all motional modes.
- For trap T2, the ceramic blades were glued to the titanium mount. Due to its high fluidity, glue can creep in between the blade and the titanium mount, which leads to a deterioration of the alignment. The new blades will be screwed to the mount to avoid this issue.
- One possible source for stray light on the trap electrodes is the back reflection of the VUV beam at the  $\text{MgF}_2$  viewport and the photomultiplier at the rear of the vacuum vessel. We redesigned these parts of the vacuum setup. All reflecting surfaces are tilted with respect to the trapping axes, thus deflecting the beam away from the trap (see Fig. 8.5).
- We improved the Ca-oven in order to avoid contamination of the trap electrodes with Ca. A double slit aperture (width  $300\text{ }\mu\text{m}$ ) fixed to the X-shaped titanium mount shields the electrodes from the loading atomic beam. The slit is interrupted in the central part, thus completely shielding the experimental region of the trap. The use of a dedicated loading zone, well separated from the experimental region ensures that no atomic calcium can contaminate the well shielded electrodes in the experimental region.
- The dedicated loading zone allows for ion loading in parallel to the experimental sequence. That way, if an ion is lost during Rydberg excitation we can quickly reload from the reservoir.
- An oven shutter, actuated with a rotational feed-through<sup>1</sup> can shut the Ca-oven completely when it is not used. Thus, the electrode contamination will be reduced further.
- Due to the increased ion-electrode distances, higher voltages will be required for trap operation. For a voltage of  $U_{dc} = -1\text{ V}$  at the center segment and an rf-amplitude of  $U_{rf} = 100\text{ V}$  simulations [Sin10] yield axial and radial gradients of  $\beta = 2.5 \times 10^5\text{ V/m}^2$  and  $\alpha = 6.8 \times 10^7\text{ V/m}^2$ . These values are about a factor of three lower compared to trap T2. Still, vibrational frequencies of  $\omega_{ax}/2\pi \approx 1\text{ MHz}$  and  $\omega_{rad}/2\pi \approx 2\text{ MHz}$  appear feasible in trap T3.

With these improvements we are confident that stable excitation of high lying Rydberg  $P$  states will be possible.

---

<sup>1</sup>rotary feedthrough

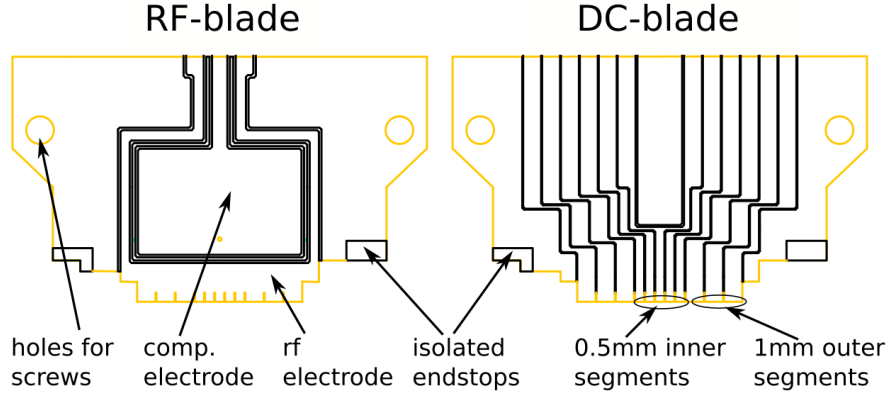


Figure 8.6.: Drawing of rf-blade and dc-blade of trap 3. The segments have been significantly modified, five inner segments with a width of 0.5 mm form the experimental region. On each side of this region, three wider electrodes (width 1 mm) form independent loading regions. In contrast to trap T2, the dc-blade does not feature a dedicated compensation electrode. In this direction compensation can be achieved by a differential voltage applied to the segments.

## 8.5. Investigation of two-step Rydberg excitation of $^{40}\text{Ca}^+$ ions.

Two-step Rydberg excitation with UV lasers [Hen16] might be an alternative option for future experiments. Excitation from the metastable  $3D_{5/2}$  state to Rydberg  $nS$  or  $nD$  states via the intermediate state  $5P_{3/2}$  requires light at wavelengths of 213 nm and 290 nm - 295 nm. While deep in the UV region of the electromagnetic spectrum, these light fields can be generated with commercially available laser systems.

For fast entangling gate operations via dipole blockade, Rabi-frequencies in the order of several MHz are required. Even faster Rabi-frequencies might allow for operations faster than the trap drive frequency  $\Omega_{rf}$ . When triggered to the trap drive signal, the excitation could be carried out at the same rf-phase and consequently at the same electric field each time. Combined with a digital trap drive (see section 8.6), even excitation during a field free time could be considered.

With the current VUV source, the generation of optical powers of about  $2\text{ }\mu\text{W}$  seems to be feasible at the resonance wavelength of the  $3D_{3/2} \rightarrow 53P$  transition. With the dipole transition matrix element  $\mu_{3D53P}$  [SK11] and a beam waist of  $w_0 = 12\text{ }\mu\text{m}$  (see section 3.3), a Rabi-frequency of  $\Omega_0/2\pi \approx 23\text{ kHz}$  may be achieved. On the other hand, two photon excitation with optical powers of 25 mW at 213 nm wavelength and 100 mW at 290 nm wavelength, focused to a beam waist of  $10\text{ }\mu\text{m}$  results in a Rabi-frequency of  $\Omega_0/2\pi = 14\text{ MHz}$  as shown in Fig. 8.7. A single photon detuning of  $\Delta_1/2\pi = 3.2\text{ GHz}$  prevents population of the short lived  $5P_{3/2}$  state. Dipole matrix elements for the single

photon transitions are estimated by using values from Ref. [Saf11] (scaled with  $n^{-1.5}$  for the Rydberg states).

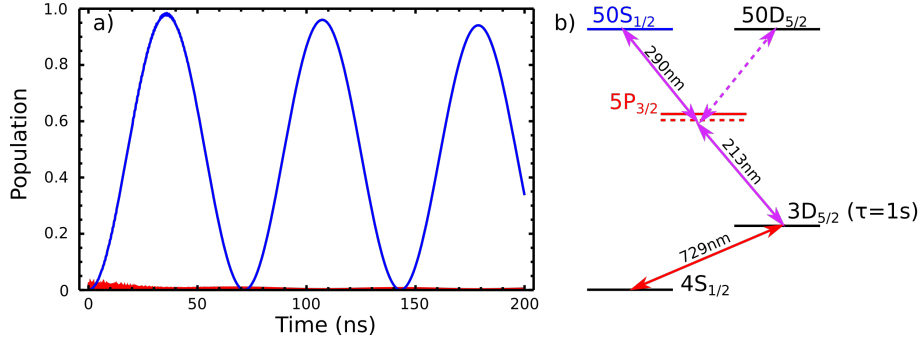


Figure 8.7.: a) Dynamics on the two-photon transition  $3D_{5/2} \leftrightarrow 50S_{1/2}$  via the intermediate level  $5P_{3/2}$ . The population of the state  $50S_{1/2}$  (blue) flops at  $\Omega_0/2\pi = 14$  MHz. A one-photon detuning of  $\Delta_1/2\pi = 3.2$  GHz ensures low population of the intermediate  $5P_{3/2}$  state (red). Consequently, population transfer with a fidelity of about 98% may be achieved. b) Employed states for the two-photon excitation. The excitation starts from the metastable  $3D_{5/2}$  state. A light field at 213 nm wavelength off-resonantly couples the  $3D_{5/2}$  to the  $5P_{3/2}$  state. A second light field near 290 nm wavelength couples the intermediate state to the Rydberg  $nS$  or  $nD$  states.

The laser radiation for the  $3S_{5/2} \leftrightarrow 5P_{3/2}$  transition at 213 nm wavelength can be generated by a frequency quadrupled Titanium:Sapphire laser. The light near 290 nm wavelength has to be tuned to the respective Rydberg resonance. A laser system which consists of a fiber amplifier operated at 1550 nm wavelength and a Titanium:Sapphire laser operated at 925 nm-950 nm wavelength, a frequency mixing stage and a subsequent frequency doubling stage would allow for a wide wavelength tunability. Consequently many different Rydberg states could be excited. Using counter-propagating beams would reduce the Doppler broadening by the thermal motion of the ion significantly which reduces the requirements on ground-state cooling of the ions. Particularly for experiments with larger ion crystals this might be useful.

On the downside of this excitation scheme, we can not excite the long lived  $nP$  states by two-photon excitation from the  $D$ -states. As the  $P$ -states exhibit a lifetime which is longer by about one order of magnitude compared to  $S$ -states and  $D$ -states [Glu13] (see section 2.3), they are particularly well suited for mode shaping experiments where the lifetime of the Rydberg ion must be long compared to its oscillation period in the trap. Other disadvantages are the use of UV-beams with high optical powers in the trap which might generate patch charges on electrode surfaces and the generation of unwanted Stark shifts on the ground state due to the strong light fields.

## 8.6. The potential of digital trap operation for Rydberg excitation of ions

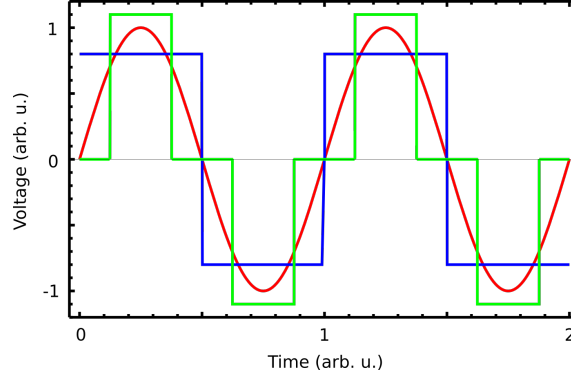


Figure 8.8.: Voltage signal for a sinusoidal (red), two-step (blue) and three-step (green) trap drive. The two-step signal yields a constant absolute value of the field strength, thus avoiding an oscillating stark shift. Instead the Rydberg resonance is shifted by a constant value. The three-step signal features periods of zero field strength. Rydberg excitation during these periods is similar to Rydberg excitation of non-trapped atoms.

The ponderomotive potential in Paul traps is generated by a sinusoidal rf-signal applied to the electrodes (see section 2.2.1). However, in general other periodic signals will result in a ponderomotive potential as well. The use of a digital trap drive where the voltage signal is assembled from two or more time steps with constant voltage [Ber08, Mar12, Ban13], is particularly interesting for Rydberg excitation of ions. In a configuration with just two steps ( $\pm V$ ), illustrated in Fig. 8.8, the absolute value of the electric field is constant. As the Stark effect scales quadratically with the field strength, this results in a constant shift of the excitation wavelength but no resonance broadening. Another option is a three step configuration where in between the steps at  $\pm V$ , zero voltage is applied for a time. The Rydberg excitation could then be carried out during this field free time.



## A. Assignment of Rydberg states and quantum defects

In Ref. [Fel15] we assigned principal quantum numbers of  $n = (51, 52, 64)$  to the experimentally determined resonances at wavelengths of 122.041 913(5) nm, 122.032 384 nm (from  $3D_{3/2}$ ) and 122.040 50(5) nm (from  $3D_{5/2}$ ). These quantum numbers were obtained by fitting the data with the Rydberg formula, while limiting our parameter region to values of  $\delta$  close to the theoretical value for the quantum defect [Dje91] and values of the ionization potential IP close to earlier experimental results [Xu98]. The experimental data deviated from a fit with a common quantum defect by up to  $3\sigma$  as shown in Fig. A.1a. We concluded that there might be issues with single channel quantum defect theory [Sea83] and consequently reported no value for the quantum defect.

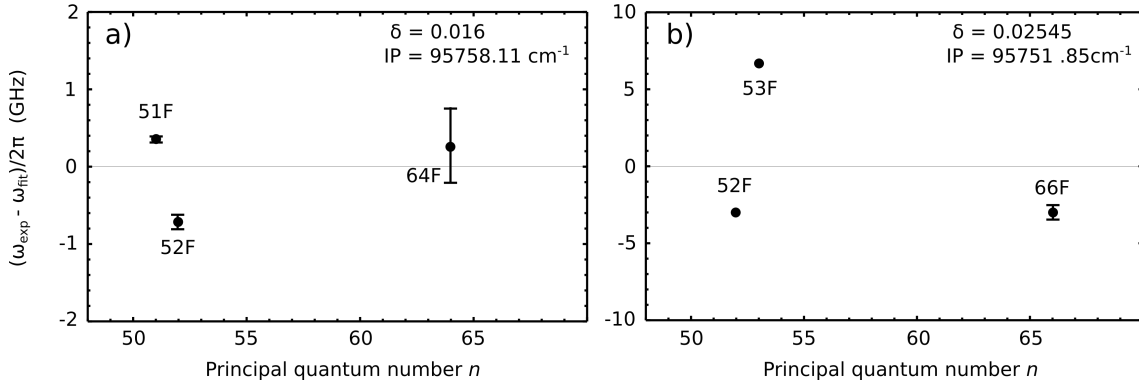


Figure A.1.: a) Principal quantum numbers assigned as in Ref. [Fel15]. The uncertainties of the measurement are 100 MHz for 51F, 200 MHz for 52F and 1 GHz for 64F. Principal quantum numbers of  $n = (51, 52, 64)$  and a quantum defect of  $\delta = 0.016$  yield the best agreement with the experimentally determined resonance wavelength. Still, the deviance is much bigger than explained by experimental uncertainties. We concluded that there might be an issue with quantum defect theory for Rydberg states of  $^{40}\text{Ca}^+$  and did not report a quantum defect. b) With a quantum defect of  $\delta = 0.02545$ , close to the value from theory [Dje91] and principle quantum numbers  $n = (52, 53, 66)$ , the agreement between experimental data and fit is much worse, resulting in deviations of up to 7 GHz. Error bars smaller than plot markers are not shown.

After publication of Ref. [Fel15], we determined the wavelength for the transition  $3D_{5/2} \rightarrow 22F$  to 123.256 119(5) nm. The energy of this state deviates by about 200 GHz from energy calculated from the high lying Rydberg states (see Fig. A.2a). With the assumption that the principle quantum numbers are instead  $n = (22, 52, 53, 66)$ , the fit agrees with the experimental data of  $22F$ ,  $52F$  and  $66F$ . Only the energy of the state  $53F$  deviates by about 9 GHz as shown in Fig. A.2b. We assume that some error must have occurred in the measurement of  $53F$ . Unfortunately we are not able to repeat the measurement for the  $53F$  states at the moment due to technical issues (see section 8.4). As soon as these issues are solved we will repeat the spectroscopy of the high lying Rydberg states in order to determine if an error in the measurement is responsible for the frequency deviation or if there are really deviations from single channel quantum defect theory in  $^{40}\text{Ca}^+$ .

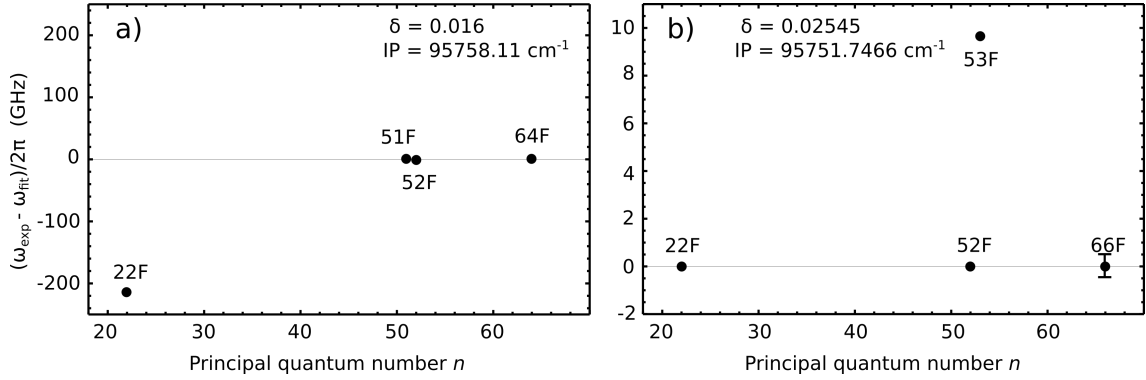


Figure A.2.: a) The experimentally determined energy of the  $22F$  state does not agree with the values of  $n = (51, 52, 64)$  presented in Ref. [Fel15]. The deviation of 200 GHz is about 2000 times larger than the experimental uncertainty. The assignment of  $n = 22$  for this state is unambiguous since frequency separation from adjacent  $F$  states is in the order of 3 THz. b) Principal quantum numbers  $n = (22, 52, 53, 66)$  and a quantum defect close to the theory value [Dje91] of  $\delta = 0.02545$  yields almost perfect agreement of the experimentally determined energies of  $22F$ ,  $52F$  and  $66F$  with the fit. For the energy of the state  $53F$ , a deviation of about 9 GHz is observed. We conclude that some error might have occurred in the measurement. Consequently, the data from state  $53F$  is not taken into account for further data evaluation. Error bars smaller than plot markers are not shown.



## B. Home built external cavity diode lasers



Figure B.1.: Render graphic of the home built external cavity diode laser. The cavity mechanics consist of a baseplate allowing for vertical adjustment of the grating with a fine threaded screw (Thorlabs; Ultra fine hex adjuster 3/16 100), a diode mount and a grating mount allowing for horizontal alignment of the grating via a fine threaded screw (Thorlabs; Ultra fine hex adjuster 3/16 100) and a piezo (Piezomechanik; PSt 150/4/5 bs). These parts are manufactured from nickel silver. The light is collimated by a collimation tube (Thorlabs; LT110P-B with standard lens (IR) and A110TM-A (423 nm)) and diffracted by a holographic grating (Thorlabs; visible holographic grating 1200/mm (IR) and 240/mm (423 nm)). Next to the collimation tube a temperature sensor (Conrad Elektronik; NTC 10k) is installed. A Peltier-element (Conrad Elektronik; Quick Cool  $30 \times 30 \times 3.8$  mm 8.6 V), positioned in between laser housing and cavity allows for temperature stabilization of the latter. The housing is made from anodized aluminium.

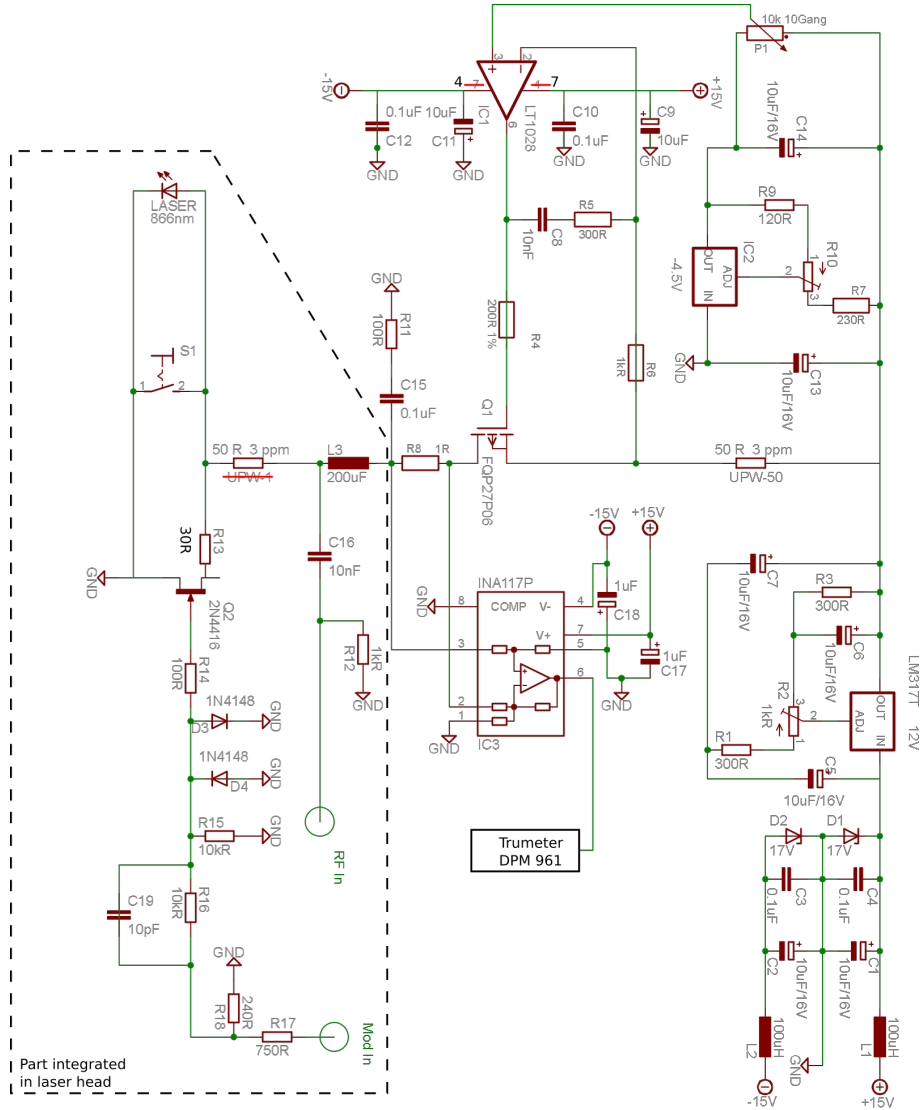


Figure B.2.: Circuit diagram of the stable current source used for operation of the laser. The current can be modulated by a Bias-Tee and a JFET. The modulation part is integrated in the laser head. For more details and characterization measurements see Ref. [Nab12]



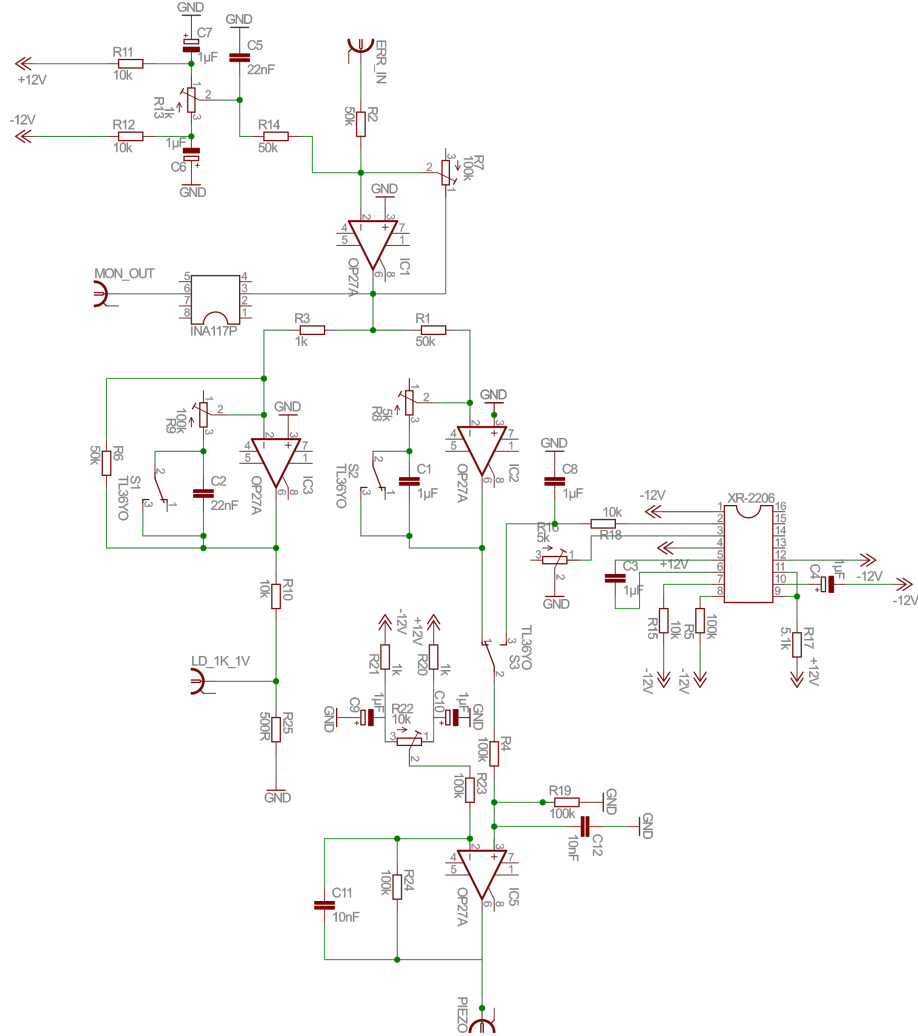


Figure B.4.: Circuit diagram of the stabilization electronics. Two separate PI channels are connected to the piezo and the current modulation input of the laser respectively. An additional signal generator and set point adjustment in the piezo part allows for scanning and manual wavelength adjustment.

## C. List of publications

### **Rydberg excitation of trapped cold ions: a detailed case study**

F. Schmidt-Kaler, T. Feldker, D. Kolbe, J. Walz, M. Müller, P. Zoller, W. Li and I. Lesanovsky

*New Journal of Physics* **13**, 075014 (2011)

doi: 10.1088/1367-2630/13/7/075014

### **Mode shaping in mixed ion crystals of $^{40}\text{Ca}^{2+}$ and $^{40}\text{Ca}^+$**

T. Feldker, L. Pelzer, M. Stappel, P. Bachor, R. Steinborn, D. Kolbe, J. Walz and F. Schmidt-Kaler

*Applied Physics B* **114**, 11 (2014)

doi: 10.1007/s00340-013-5673-1

### **Rydberg Excitation of a Single Trapped Ion**

T. Feldker, P. Bachor, M. Stappel, D. Kolbe, R. Gerritsma, J. Walz and F. Schmidt-Kaler

*Physical Review Letters* **115**, 173001 (2015)

doi: 10.1103/PhysRevLett.115.173001

### **Towards Rydberg quantum logic with trapped ions**

P. Bachor, T. Feldker, J. Walz and F. Schmidt-Kaler

arXiv:1602.05006[quant-ph] (2016)

Accepted for publication in *Journal of Physics B*



# Bibliography

- [Ake10] N. Akerman, S. Kotler, Y. Glickman, Y. Dallal, A. Keselman, and R. Ozeri, *Single-ion nonlinear mechanical oscillator*, Phys. Rev. A **82**, 061402 (2010).
- [Bac13] P. Bachor, *Frequenzstabilisierung von Lasersystemen zur Rydberganregung von Calciumionen*, Master's thesis, Johannes-Gutenberg Universität, Mainz (2013).
- [Bac16] P. Bachor, T. Feldker, J. Walz, and F. Schmidt-Kaler, *Towards Rydberg quantum logic with trapped ions*, arXiv:1602.05006 (2016).
- [Bal12] J. D. Baltrusch, C. Cormick, and G. Morigi, *Quantum quenches of ion Coulomb crystals across structural instabilities*, Phys. Rev. A **86**, 032104 (2012).
- [Ban13] S. Bandelow, G. Marx, and L. Schweikhard, *The 3-state digital ion trap*, Int. J. Mass Spectrom. **353**, 49 (2013).
- [Bar15] D. Barredo, H. Labuhn, S. Ravets, T. Lahaye, A. Browaeys, and C. S. Adams, *Coherent Excitation Transfer in a Spin Chain of Three Rydberg Atoms*, Phys. Rev. Lett. **114**, 113002 (2015).
- [Ben08] J. Benhelm, G. Kirchmair, C. F. Roos, and R. Blatt, *Towards fault-tolerant quantum computing with trapped ions*, Nat. Phys. **4**, 463 (2008).
- [Ber98] D. J. Berkeland, J. D. Miller, J. C. Bergquist, W. M. Itano, and D. J. Wineland, *Minimization of ion micromotion in a Paul trap*, J. Appl. Phys. B **83**, 5025 (1998).
- [Ber08] A. Berton, P. Traldi, L. Ding, and F. L. Brancia, *Mapping the Stability Diagram of a Digital Ion Trap (DIT) Mass Spectrometer Varying the Duty Cycle of the Trapping Rectangular Waveform*, J. Am. Soc. Mass Spectrom. **19**, 620 (2008).
- [Ber12] A. Bermudez, J. Almeida, K. Ott, H. Kaufmann, S. Ulm, U. Poschinger, F. Schmidt-Kaler, A. Retzker, and M. B. Plenio, *Quantum magnetism of spin-ladder compounds with trapped-ion crystals*, New. J. Phys. **14**, 093042 (2012).
- [Bet08] H. A. Bethe and E. E. Salpeter, *quantum mechanics of one- and two-electron atoms*, Dover, New York, 2008, dover ed.

- [Bet09] I. I. Beterov, I. I. Ryabtsev, D. B. Tretyakov, and V. M. Entin, *Quasiclassical calculations of blackbody-radiation-induced depopulation rates and effective lifetimes of Rydberg  $nS$ ,  $nP$ , and  $nD$  alkali-metal atoms with  $n \leq 80$* , Phys. Rev. A **79**, 052504 (2009).
- [Bla67] J. M. Blatt, *Practical Points Concerning the Solution of the Schrödinger Equation*, J. Comput. Phys. **1**, 382 (1967).
- [Bla08] R. Blatt and D. J. Wineland, *Entangled states of trapped atomic ions*, Nature (London) **453**, 1008 (2008).
- [Bla12] R. Blatt and C. F. Roos, *Quantum Simulation with trapped ions*, Nat. Phys. **8**, 277 (2012).
- [Bro15] M. Brownnutt, M. Kumph, P. Rabl, and R. Blatt, *Ion-trap measurements of electric-field noise near surfaces*, Rev. Mod. Phys. **87**, 1419 (2015).
- [Bru94] M. Brune, P. Nussenzweig, F. Schmidt-Kaler, F. Bernardot, A. Maali, J. M. Raimond, and S. Haroche, *From Lamb Shift to Light Shifts: Vacuum and Subphoton Cavity Fields Measured by Atomic Phase Sensitive Detection*, Phys. Rev. Lett. **72**, 3339 (1994).
- [Bru96] M. Brune, F. Schmidt-Kaler, A. Maali, J. Dreyer, E. Hagley, J. M. Raimond, and S. Haroche, *Quantum Rabi Oscillation: A Direct Test of Field Quantization in a Cavity*, Phys. Rev. Lett. **76**, 1800 (1996).
- [Cho10] C. W. Chou, D. B. Hume, J. C. J. Koelemeij, D. J. Wineland, and T. Rosenband, *Frequency Comparison of Two High-Accuracy  $Al^+$  Optical Clocks*, Phys. Rev. Lett. **104**, 070802 (2010).
- [Chw09] M. Chwalla, J. Benhelm, K. Kim, G. Kirchmair, T. Monz, M. Riebe, P. Schindler, A. S. Villar, W. Hänsel, C. F. Roos, R. Blatt, M. Abgrall, G. Santarelli, G. D. Rovera, and P. Laurent, *Absolute Frequency Measurement of the  $^{40}Ca^+ 4s^2S_{1/2} - 3d^2D_{5/2}$  Clock Transition*, Phys. Rev. Lett. **102**, 023002 (2009).
- [Cir95] J. I. Cirac and P. Zoller, *Quantum computation with cold ions*, Phys. Rev. Lett. **74**, 4091 (1995).
- [Den71] D. R. Denison, *Operating Parameters of a Quadrupole in a Grounded Cylindrical Housing*, J. of Vac. Sci. and Tech. **8**, 266 (1971).
- [Dje91] M. T. Djerdar, *Atomic parameters for transitions involving Rydberg states of singly ionized alkaline earths*, Journal de Physique II **1**, 1 (1991).



- 
- [Dre98] M. Drewsen, C. Brodersen, L. Hornekær, and J. S. Hangst, *Large Ion Crystals in a Linear Paul Trap*, Phys. Rev. Lett. **81**, 2878 (1998).
- [Eik99] K. S. E. Eikema, J. Walz, and T. W. Hänsch, *Continuous Wave Coherent Lyman-alpha Radiation*, Phys. Rev. Lett. **83**, 3828 (1999).
- [Eik01] K. S. E. Eikema, J. Walz, and T. W. Hänsch, *Continuous Coherent Lyman-alpha Excitation of Atomic Hydrogen*, Phys. Rev. Lett. **86**, 5679 (2001).
- [Enz00] D. G. Enzer, M. M. Schauer, J. J. Gomez, M. S. Gulley, M. H. Holzscheiter, P. G. Kwiat, S. K. Lamoreaux, C. G. Peterson, V. D. Sandberg, D. Tupa, A. G. White, R. J. Hughes, and D. F. V. James, *Observation of Power-Law Scaling for Phase Transitions in Linear Trapped Ion Crystals*, Phys. Rev. Lett. **85**, 2466 (2000).
- [Fan70] U. Fano, *Quantum Defect Theory of  $l$  Uncoupling in  $H_2$  as an Example of Channel-Interaction Treatment*, Phys. Rev. A **2**, 353 (1970).
- [Fel14] T. Feldker, L. Pelzer, M. Stappel, P. Bachor, R. Steinborn, D. Kolbe, J. Walz, and F. Schmidt-Kaler, *Mode shaping in mixed ion crystals of  $^{40}\text{Ca}^{2+}$  and  $^{40}\text{Ca}^+$* , Appl. Phys. B. **114**, 11 (2014).
- [Fel15] T. Feldker, P. Bachor, M. Stappel, D. Kolbe, R. Gerritsma, J. Walz, and F. Schmidt-Kaler, *Rydberg Excitation of a Single Trapped Ion*, Phys. Rev. Lett. **115**, 173001 (2015).
- [För65] T. Förster, *Delocalized excitation and excitation transfer*, in: *Modern quantum Chemistry, Istanbul Lectures: Part III: Action of Light and Organic Crystals*, Academic Press, New York, 1965.
- [Gaë09] A. Gaëtan, Y. Miroshnychenko, T. Wilk, A. Chotia, M. Viteau, D. Comparat, P. Pillet, A. Browaeys, and P. Grangier, *Observation of collective excitation of two individual atoms in the Rydberg blockade regime*, Nat. Phys. **5**, 115 (2009).
- [Gal88] T. F. Gallagher, *Rydberg atoms*, Rep. Prog. Phys. **51**, 143 (1988).
- [Gal94] T. F. Gallagher, *Rydberg Atoms*, Cambridge University Press, Cambridge, 1994.
- [Ger10] R. Gerritsma, G. Kirchmair, F. Zähringer, E. Solano, R. Blatt, and C. F. Roos, *Quantum simulation of the Dirac equation*, Nature (London) **463**, 68 (2010).
- [Ger11] R. Gerritsma, B. P. Lanyon, G. Kirchmair, F. Zähringer, C. Hempel, J. Casanova, J. J. Garcia-Ripoll, E. Solano, R. Blatt, and C. F. Roos, *Quantum simulation of the Klein paradox*, Phys. Rev. Lett. **106**, 060503 (2011).

- [Glo15] T. F. Gloger, P. Kaufmann, D. Kaufmann, M. T. Baig, T. Collath, M. Johanning, and C. Wunderlich, *Ion-trajectory analysis for micromotion minimization and the measurement of small forces*, Phys. Rev. A **92**, 043421 (2015).
- [Glu13] I. L. Glukhov, E. A. Nikitina, and V. D. Ovsiannikov, *Lifetime of Rydberg States in Ions of the Group II Elements*, Opt. Spectrosc. **115**, 9 (2013).
- [Hei07] R. Heidemann, U. Raitzsch, V. Bendkowsky, B. Butscher, R. Löw, L. Santos, and T. Pfau, *Evidence for Coherent Collective Rydberg Excitation in the Strong Blockade Regime*, Phys. Rev. Lett. **99**, 163601 (2007).
- [Hen16] M. Hennrich, *Realization of Trapped Strontium Rydberg Ions*, <http://lxqo.uibk.ac.at/en/research/rydberg.html> (2016).
- [Iba11] Y. Ibaraki, U. Tanaka, and S. Urabe, *Detection of parametric resonance of trapped ions for micromotion compensation*, Appl. Phys. B **105**, 219 (2011).
- [Ise10] L. Isenhower, E. Urban, X. L. Zhang, A. T. Gill, T. Henage, T. A. Johnson, T. G. Walker, and M. Saffman, *Demonstration of a Neutral Atom Controlled-NOT Quantum Gate*, Phys. Rev. Lett. **104**, 010503 (2010).
- [Jac14] G. Jacob, K. Groot-Berning, S. Wolf, S. Ulm, L. Couturier, U. G. Poschinger, F. Schmidt-Kaler, and K. Singer, *Single particle microscopy with nanometer resolution*, arXiv:1405.6480 (2014).
- [Jak00] D. Jaksch, J. I. Cirac, P. Zoller, S. L. Rolston, R. Côté, and M. D. Lukin, *Fast Quantum Gates for Neutral Atoms*, Phys. Rev. Lett. **85**, 2208 (2000).
- [Jam98] D. F. V. James, *Quantum dynamics of cold trapped ions with application to quantum computation*, Appl. Phys. B **66**, 181 (1998).
- [Jur14] P. Jurcevic, B. P. Lanyon, P. Hauke, C. Hempel, P. Zoller, R. Blatt, and C. F. Roos, *Quasiparticle engineering and entanglement propagation in a quantum many-body system*, Nature (London) **511**, 202 (2014).
- [Kam14] A. A. Kamenski and V. D. Ovsiannikov, *Formal approach to deriving analytically asymptotic formulas for static polarizabilities of atoms and ions in Rydberg states*, J. Phys. B **47**, 095002 (2014).
- [Kau12] H. Kaufmann, S. Ulm, G. Jacob, U. Poschinger, H. Landa, A. Retzker, M. B. Plenio, and F. Schmidt-Kaler, *Precise Experimental Investigation of Eigenmodes in a Planar Ion Crystal*, Phys. Rev. Lett. **109**, 263003 (2012).
- [Kau15] H. Kaufmann, *Johannes Gutenberg Universität, Mainz: private communication* (2015).

- 
- [Keh11] A. Kehlberger, *Entwicklung und Aufbau einer neuartigen Ionenfalle*, Master's thesis, Johannes-Gutenberg Universität, Mainz (2011).
- [Kie02] D. Kielpinski, C. R. Monroe, and D. J. Wineland, *Architecture for a Large-Scale Ion-Trap Quantum Computer*, Nature (London) **417**, 709 (2002).
- [Koc78] P. M. Koch, *Resonant States in the Nonperturbative Regime: The Hydrogen Atom in an Intense Electric Field*, Phys. Rev. Lett. **41**, 99 (1978).
- [Kol10] D. Kolbe, *Effizientes Vierwellenmischen durch Ausnutzen von Resonanzen in Quecksilber*, Ph.D. thesis, Johannes-Gutenberg Universität, Mainz (2010).
- [Kol12a] D. Kolbe, M. Scheid, and J. Walz, *Influence of the  $6^1S_0 - 6^3P_1$  resonance on continuous Lyman- $\alpha$  generation in mercury*, Appl. Phys. B **113**, 559 (2012).
- [Kol12b] D. Kolbe, M. Scheid, and J. Walz, *Triple Resonant Four-Wave Mixing Boosts the Yield of Continuous Coherent Vacuum Ultraviolet Generation*, Phys. Rev. Lett. **109**, 063901 (2012).
- [Kos85] V. A. Kostelecký and M. M. Nieto, *Analytical wave functions for atomic quantum-defect theory*, Phys. Rev. A **32**, 3243 (1985).
- [Kre05] A. Kreuter, C. Becher, G. P. T. Lancaster, A. B. Mundt, C. Russo, H. Häffner, C. F. Roos, W. Hänsel, F. Schmidt-Kaler, R. Blatt, and M. S. Safronova, *New experimental and theoretical approach to the  $^3d_2D$ -level lifetimes of  $^{40}\text{Ca}^+$* , Phys. Rev. A **71**, 032504 (2005).
- [Kwa07] T. Kwapień, U. Eichmann, and W. Sandner, *Sympathetic cooling of laser-produced doubly charged ions in a few-ion crystal*, Phys. Rev. A **75**, 063418 (2007).
- [Lan11] B. P. Lanyon, C. Hempel, D. Nigg, M. Müller, R. Gerritsma, F. Zähringer, P. Schindler, J. T. Barreiro, M. Rambach, G. Kirchmair, M. Hennrich, P. Zoller, R. Blatt, and C. F. Roos, *Universal Digital Quantum Simulation with Trapped Ions*, Science **334**, 57 (2011).
- [Lei03a] D. Leibfried, R. Blatt, C. Monroe, and D. J. Wineland, *Quantum dynamics of single trapped ions*, Rev. Mod. Phys. **75**, 281 (2003).
- [Lei03b] D. Leibfried, B. DeMarco, V. Meyer, D. Lucas, M. Barrett, J. Britton, W. M. Itano, B. Jelenkovic, C. Langer, T. Rosenband, and D. J. Wineland, *Experimental demonstration of a robust, high-fidelity geometric two ion-qubit gate*, Nature (London) **422**, 412 (2003).
- [Li] W. Li, *Univ. Nottingham, U.K.: private communication*.

- [Li12] W. Li and I. Lesanovsky, *Electronically Excited Cold Ion Crystals*, Phys. Rev. Lett. **108**, 023003 (2012).
- [Li13] W. Li, A. W. Glaetzle, R. Nath, and I. Lesanovsky, *Parallel execution of quantum gates in a long linear ion chain via Rydberg mode shaping*, Phys. Rev. A **87**, 052304 (2013).
- [Li14] W. Li and I. Lesanovsky, *Entangling quantum gate in trapped ions via Rydberg blockade*, Appl. Phys. B **114**, 37 (2014).
- [Lin13] Y. Lin, J. P. Gaebler, T. R. Tan, R. Bowler, J. D. Jost, D. Leibfried, and D. J. Wineland, *Sympathetic Electromagnetically-Induced-Transparency Laser Cooling of Motional Modes in an Ion Chain*, Phys. Rev. Lett. **110**, 153002 (2013).
- [Lud15] A. D. Ludlow, M. M. Boyd, J. Ye, E. Peik, and P. O. Schmidt, *Optical atomic clocks*, Rev. Mod. Phys. **87**, 637 (2015).
- [Luk01] M. D. Lukin, M. Fleischhauer, R. Côté, L. M. Duan, D. Jaksch, J. I. Cirac, and P. Zoller, *Dipole Blockade and Quantum Information Processing in Mesoscopic Atomic Ensembles*, Phys. Rev. Lett. **87**, 037901 (2001).
- [Mac59] W. W. Macalpine and R. O. Schildknecht, *Coaxial Resonators with Helical Inner Conductor*, Proceedings of the IRE **47**, 2099 (1959).
- [Mac12] T. Macha, *Frequenzstabilisierung eines Titan-Saphir-Laser und Verbesserung von Qubits mit  $\text{Ca}^+$  - Ionen*, Master's thesis, Johannes Gutenberg Universität, Mainz (2012).
- [Mal15] K. M. Maller, M. T. Lichtman, T. Sia, Y. Sun, M. J. Piotrowicz, A. W. Carr, L. Isenhower, and M. Saffman, *Rydberg-blockade controlled-NOT gate and entanglement in a two-dimensional array of neutral-atom qubits*, Phys. Rev. A **92**, 022336 (2015).
- [Mar12] F. Martinez, S. Bandelow, G. Marx, and L. Schweikhard, *Production of multiply-charged metal-cluster anions in Penning and radio-frequency traps*, AIP Conf. Proc. **1521**, 230 (2012).
- [Mes85] D. Meschede, H. Walther, and G. Müller, *One-Atom Maser*, Phys. Rev. Lett. **54**, 551 (1985).
- [Mon16] T. Monz, D. Nigg, E. A. Martinez, M. F. Brandl, P. Schindler, R. Rines, S. X. Wang, I. L. Chuang, and R. Blatt, *Realization of a scalable Shor algorithm*, Science **351**, 1068 (2016).

- 
- [Mül08] M. Müller, L. Liang, I. Lesanovsky, and P. Zoller, *Trapped Rydberg ions: from spin chains to fast quantum gates*, New J. Phys. **10**, 093009 (2008).
- [Nab12] J. Naber, *Aufbau und Betrieb einer Paulfalle zur Rydberganregung von Ionen*, Master's thesis, Johannes-Gutenberg Universität, Mainz (2012).
- [Näg99] H. C. Nägerl, D. Leibfried, H. Rohde, G. Thalhammer, J. Eschner, F. Schmidt-Kaler, and R. Blatt, *Laser addressing of individual ions in a linear ion trap*, Phys. Rev. A. **60**, 145 (1999).
- [Nat15] R. Nath, M. Dalmonte, A. W. Glaetzle, P. Zoller, F. Schmidt-Kaler, and R. Gerritsma, *Hexagonal plaquette spin-spin interactions and quantum magnetism in a two-dimensional ion crystal*, New J. Phys. **17**, 065018 (2015).
- [Nat16] National Institute of Standards and Technology, *Atomic Spectra Database*, <http://www.nist.gov/pml/data/asd.cfm> (2016).
- [Pel13] L. Pelzer, *Ionisation von  $^{40}\text{Ca}^+$  und Untersuchung gemischter  $^{40}\text{Ca}^+ / ^{40}\text{Ca}^{2+}$ -Ionenkristalle*, Master's thesis, Johannes-Gutenberg Universität, Mainz (2013).
- [Pey12] T. Peyronel, O. Firstenberg, Q. Y. Liang, S. Hofferberth, A. V. Gorshkov, T. Pohl, M. D. Lukin, and V. Vuletic, *Quantum nonlinear optics with single photons enabled by strongly interacting atoms*, Nature (London) **488**, 57 (2012).
- [Pyk13] K. Pyka, J. Keller, H. L. Partner, R. Nigmatullin, T. Burgmeister, D. M. Meier, K. Kuhlmann, A. Retzker, M. B. Plenio, W. H. Zurek, A. Campo, and T. E. Mehlstäubler, *Topological defect formation and spontaneous symmetry breaking in ion Coulomb crystals*, Nat. Commun. **4**, 2291 (2013).
- [Rai01] J. M. Raimond, M. Brune, and S. Haroche, *Manipulating quantum entanglement with atoms and photons in a cavity*, Rev. Mod. Phys. **73**, 565 (2001).
- [Ram13] M. Ramm, T. Pruttivarasin, M. Kokish, I. Talukdar, and H. Häffner, *Precision Measurement Method for Branching Fractions of Excited  $P_{1/2}$  States Applied to  $^{40}\text{Ca}^+$* , Phys. Rev. Lett. **111**, 023004 (2013).
- [Rei02] D. Reiß, K. Abich, W. Neuhauser, C. Wunderlich, and P. E. Toschek, *Raman cooling and heating of two trapped  $\text{Ba}^+$  ions*, Phys. Rev. A **65**, 053401 (2002).
- [Rem90] G. Rempe, F. Schmidt-Kaler, and H. Walther, *Observation of Sub-Poissonian Statistics in a Micromaser*, Phys. Rev. Lett. **64**, 2783 (1990).
- [Rie04] M. Riebe, H. Häffner, C. F. Roos, W. Hänsel, J. Benhelm, G. P. T. Lancaster, T. W. Körber, C. Becher, F. Schmidt-Kaler, D. F. V. James, and R. Blatt, *Deterministic quantum teleportation with atoms*, Nature (London) **429**, 734 (2004).

- [Roo99] C. Roos, T. Zeiger, H. Rohde, H. C. Nägerl, J. Eschner, D. Leibfried, F. Schmidt-Kaler, and R. Blatt, *Quantum State Engineering on an Optical Transition and Decoherence in a Paul Trap*, Phys. Rev. Lett. **83**, 4713 (1999).
- [Roo00] C. F. Roos, *Controlling the quantum state of trapped ions*, Ph.D. thesis, Leopold-Franzens-Universität, Innsbruck (2000).
- [Roß15] J. Roßnagel, S. T. Dawkins, K. N. Tolazzi, O. Abah, E. Lutz, F. Schmidt-Kaler, and K. Singer, *A single-atom heat engine*, Science **352**, 325 (2015).
- [Rus12] T. Ruster, *Schneller Transport von kalten gefangenen Ionen*, Master's thesis, Johannes-Gutenberg Universität, Mainz (2012).
- [Rus14] T. Ruster, C. Warschburger, H. Kaufmann, C. T. Schmiegelow, A. Walther, M. Hettrich, A. Pfister, V. Kaushal, F. Schmidt-Kaler, and U. G. Poschinger, *Experimental realization of fast ion separation in segmented Paul traps*, Phys. Rev. A **90**, 033410 (2014).
- [Saf10] M. Saffman, T. G. Walker, and K. Mølmer, *Quantum information with Rydberg atoms*, Rev. Mod. Phys. **82**, 2313 (2010).
- [Saf11] M. S. Safronova and U. I. Safronova, *Blackbody radiation shift, multipole polarizabilities, oscillator strengths, lifetimes, hyperfine constants, and excitation energies in  $Ca^+$* , Phys. Rev. A **83**, 012503 (2011).
- [Sau86] T. Sauter, W. Neuhauser, R. Blatt, and P. E. Toschek, *Observation of Quantum Jumps*, Phys. Rev. Lett. **57**, 1696 (1986).
- [Sch05] P. O. Schmidt, T. Rosenband, C. Langer, W. M. Itano, J. C. Bergquist, and D. J. Wineland, *Spectroscopy Using Quantum Logic*, Science **309**, 749 (2005).
- [Sch09a] M. Scheid, D. Kolbe, F. Markert, T. Hänsch, and J. Walz, *Continuous-wave Lyman- $\alpha$  generation with solid-state lasers*, Optics Express **17**, 11274 (2009).
- [Sch09b] S. A. Schulz, *Scalable Microchip Ion Traps for Quantum Computation*, Ph.D. thesis, Universität, Ulm (2009).
- [Sch10] M. Scheid, *Einfluss der  $6^1S-6^3P$  Resonanz auf die Lyman- $\alpha$  Erzeugung in Quecksilber*, Ph.D. thesis, Johannes-Gutenberg Universität, Mainz (2010).
- [Sch15a] P. Schauß, J. Zeiher, T. Fukuhara, S. Hild, M. Cheneau, T. Macrì, T. Pohl, I. Bloch, and C. Gross, *Crystallization in Ising quantum magnets*, Science **347**, 1455 (2015).

- 
- [Sch15b] H. Schempp, G. Günter, S. Wüster, M. Weidemüller, and S. Whitlock, *Correlated Exciton Transport in Rydberg-Dressed-Atom Spin Chains*, Phys. Rev. Lett. **115**, 093002 (2015).
- [Sea83] M. J. Seaton, *Quantum defect theory*, Rep. Prog. Phys. **46**, 167 (see page 237) (1983).
- [Sen15] C. Senko, P. Richerme, J. Smith, A. Lee, I. Cohen, A. Retzker, and C. Monroe, *Realization of a Quantum Integer-Spin Chain with Controllable Interactions*, Phys. Rev. X **5**, 021026 (2015).
- [Sin02] K. Singer, S. Jochim, M. Mudrich, A. Mosk, and M. Weidemüller, *Low-cost mechanical shutter for light beams*, Rev. Sci. Instrum. **73**, 4402 (2002).
- [Sin04] K. Singer, M. Reetz-Lamour, T. Amthor, L. G. Marcassa, and M. Weidemüller, *Suppression of Excitation and Spectral Broadening Induced by Interactions in a Cold Gas of Rydberg Atoms*, Phys. Rev. Lett. **93**, 163001 (2004).
- [Sin10] K. Singer, U. G. Poschinger, M. Murphy, P. Ivanov, F. Ziesel, T. Calarco, and F. Schmidt-Kaler, *Colloquium: Trapped ions as quantum bits: Essential numerical tools*, Rev. Mod. Phys. **82**, 2609 (2010).
- [SK03] F. Schmidt-Kaler, H. Häffner, M. Riebe, S. Gulde, G. P. T. Lancaster, T. Deuschle, C. Becher, C. F. Roos, J. Eschner, and R. Blatt, *Realization of the Cirac-Zoller controlled-NOT quantum gate*, Nature (London) **422**, 408 (2003).
- [SK11] F. Schmidt-Kaler, T. Feldker, D. Kolbe, J. Walz, M. Müller, P. Zoller, W. Li, and I. Lesanovsky, *Rydberg excitation of trapped cold ions: a detailed case study*, New J. Phys. **13**, 075014 (2011).
- [Sta13] M. Stappel, R. Steinborn, D. Kolbe, and J. Walz, *A high power, continuous-wave, single-frequency fiber amplifier at 1091 nm and frequency doubling to 545.5 nm*, Laser Phys. **23**, 075103 (2013).
- [Sta14] M. Stappel, D. Kolbe, and J. Walz, *Continuous-wave, double-pass second-harmonic generation with 60% efficiency in a single MgO:PPLT crystal*, Opt. Lett. **39**, 2951 (2014).
- [Sta15] M. Stappel, *Eine vakuumultraviolette Laserquelle zur Rydberganregung von Calciumionen*, Ph.D. thesis, Johannes-Gutenberg Universität, Mainz (2015).
- [Ste13] R. Steinborn, A. Koglbauer, P. Bachor, T. Diehl, D. Kolbe, M. Stappel, and J. Walz, *A continuous wave 10 W cryogenic fiber amplifier at 1015 nm and frequency quadrupling to 254 nm*, Optics Express **21**, 22693 (2013).

- [Ton04] D. Tong, S. M. Farooqi, J. Stanojevic, S. Krishnan, Y. P. Zhang, R. Côté, E. E. Eyler, and P. L. Gould, *Local Blockade of Rydberg Excitation in an Ultracold Gas*, Phys. Rev. Lett **93**, 063001 (2004).
- [Ulm13] S. Ulm, J. Roßnagel, G. Jacob, C. Degünther, S. T. Dawkins, U. G. Poschinger, R. Nigmatullin, A. Retzker, M. B. Plenio, F. Schmidt-Kaler, and K. Singer, *Observation of the Kibble-Zurek scaling law for defect formation in ion crystals*, Nat. Commun. **4**, 2290 (2013).
- [Urb09] E. Urban, T. A. Johnson, T. Henage, L. Isenhower, D. D. Yavuz, T. G. Walker, and M. Saffman, *Observation of Rydberg blockade between two atoms*, Nat. Phys. **5**, 110 (2009).
- [Vog06] T. Vogt, M. V. Viteau, J. Zhao, A. Chotia, D. Comparat, and P. Pillet, *Dipole Blockade at Förster Resonances in High Resolution Laser Excitation of Rydberg States of Cesium Atoms*, Phys. Rev. Lett. **97**, 083003 (2006).
- [Wal01] J. Walz, A. Pahl, K. S. E. Eikema, and T. W. Hänsch, *The first continuous coherent Lyman- $\alpha$  source*, Nuclear Physics A **692**, 163 (2001).
- [Wal12] A. Walther, F. Ziesel, T. Ruster, S. T. Dawkins, K. Ott, M. Hettrich, K. Singer, F. Schmidt-Kaler, and U. Poschinger, *Controlling Fast Transport of cold Trapped Ions*, Phys. Rev. Lett. **109**, 080501 (2012).
- [Wil10] T. Wilk, A. Gaëtan, C. Evellin, J. Wolters, Y. Miroshnychenko, P. Grangier, and A. Browaeys, *Entanglement of Two Individual Neutral Atoms Using Rydberg Blockade*, Phys. Rev. Lett. **104**, 010502 (2010).
- [Win87] D. J. Wineland, J. C. Bergquist, W. M. Itano, J. J. Bollinger, and C. H. Manney, *Atomic-Ion Coulomb Clusters in an Ion Trap*, Phys. Rev. Lett. **59**, 2935 (1987).
- [Xu98] C. B. Xu, X. P. Xie, R. C. Zhao, W. Sun, P. Xue, Z. P. Zhong, W. Huang, and X. Y. Xu, *Study on ionic Rydberg states of calcium*, J. of Phys. B **31**, 5355 (1998).
- [Yam08] R. Yamazaki, H. Sawamura, K. Toyoda, and S. Urabe, *Stimulated Raman spectroscopy and the determination of the D-fine-structure level separation in  $^{40}\text{Ca}^+$* , Phys. Rev. A **77**, 012508 (2008).
- [Zie12] F. Ziesel, *Quantum State Manipulation and Dynamics in Micro Ion Traps*, Ph.D. thesis, Universität, Ulm (2012).
- [Zim78] M. L. Zimmerman, J. C. Castro, and D. Kleppner, *Diamagnetic Structure of Na Rydberg States*, Phys. Rev. Lett. **40**, 1083 (1978).
- [Zim79] M. L. Zimmerman, M. G. Littman, M. M. Kash, and D. Kleppner, *Stark structure of the Rydberg states of alkali-metal atoms*, Phys. Rev. A **20**, 2251 (1979).



# Danksagung

Die Fertigstellung dieser Arbeit wäre ohne die Unterstützung von vielen, direkt oder indirekt am Projekt beteiligten, Personen nicht möglich gewesen. Mein Dank gilt vor allem Prof. Ferdinand Schmidt-Kaler dem Initiator des Forschungsprojektes. Er ermöglichte es mir meine Arbeit in diesem spannenden Gebiet der Physik durchzuführen. Bedanken möchte ich mich auch für das ausgezeichnete Arbeitsumfeld und die stets gute Betreuung. Ebenso möchte ich mich bei Prof. Jochen Walz bedanken, in dessen Laboren das Experiment aufgebaut wurde. Ohne die dort vorhandene VUV Laserquelle und ohne seine Erfahrung in diesem Bereich der Physik wäre das Projekt nicht realisierbar gewesen.

Ebenso gilt mein Dank:

- Meinen Kollegen Patrick Bachor und Matthias Stappel für die gute Zusammenarbeit und die vielen gemeinsam im Labor verbrachten Stunden.
- Julian Naber und Lennart Pelzer, deren Diplomarbeiten ich betreuen durfte, für ihren überdurchschnittlichen Einsatz und ihre Arbeit am Experiment.
- Daniel Kolbe der wichtige Beiträge zum Aufbau der VUV Quelle geleistet hat und von dem ich insbesondere am Anfang meiner Arbeit viel gelernt habe.
- Allen Kollegen am Institut für die gute Zeit die ich hier hatte, den Erfahrungsaustausch und die vielen anregenden Diskussionen.
- Allen Mitarbeitern der mechanischen Werkstatt im Institut, ohne die die vielen für das Experiment benötigten Spezialanfertigungen nicht realisierbar gewesen wären.
- Sowie allen weiteren Mitarbeitern des Instituts und Kollaborationspartnern außerhalb der Universität die zum Gelingen dieser Arbeit auf die ein oder andere Weise beigetragen haben.

# Thomas Feldker

---

---

## Persönliche Daten

Name **Thomas Feldker**  
Geboren am **29.3.1984 in Köln**  
Nationalität **Deutsch**  
Familienstand **Ledig**

---

## Hochschulstudium

seit 2/2011 **Beginn der Promotion.**  
Johannes Gutenberg Universität Mainz, Physik  
Titel: Rydberg Excitation of Trapped Ions  
Betreuer: Prof. Dr. Ferdinand Schmidt-Kaler

10/2008–6/2010 **Physik (M.Sc.).**  
Technische Universität Darmstadt; Gesamtnote: Sehr gut (1,1)  
**Master Thesis.**  
Prof. Dr. Gerhard Birkel  
*Experimente mit Isotopenmischungen  
von kalten, metastabilen Neonatomen*  
Note: Sehr gut (1,0)

10/2004–6/2008 **Physik (B.Sc.).**  
Technische Universität Darmstadt; Gesamtnote: Gut  
**Bachelor Thesis.**  
Prof. Dr. Gerhard Birkel  
*Durchstimmverhalten von gitterstabilisierten Diodenlasern*  
Note: Sehr gut (1,0)

8/2007–5/2008 **Auslandsstudium.**  
Kungliga Tekniska högskolan, Stockholm

---

## Schule, Zivildienst

1994–2003 **Schillergymnasium, Köln.**  
Abitur, Gesamtnote: 1,2

9/2003–7/2004 **Städtische Schule für Geistig Behinderte.**  
Betreuung einer Klasse